Development of Novel pH-Sensitive Dyes for Early Stage Wound Infection Detection and Monitoring

DISSERTATION

zur Erlangung des Grades eines Doktors

der Naturwissenschaften

vorgelegt von

M.Sc. Aswathi Syam

eingereicht bei der Naturwissenschaftlich-Technischen Fakultät

der Universität Siegen

Siegen 2025

Betreuer und erster Gutachter
Prof. Dr. Holger Schönherr
Universität Siegen

Zweiter Gutachter
Prof. Dr. Heiko Ihmels
Universität Siegen

Tag der mündlichen Prüfung
17. Dezember 2025

"I am among those who think that science has great beauty. A scientist in his laboratory is not only a technician: he is also a child placed before natural phenomena which impress him like a fairy tale."

- Marie Curie

Table of Contents

Zusammenfassung V

Abstract VII

List of Abbreviations and Acronyms IX

1 Introduction and Motivation 1

2 State of Knowledge 5

2.1 Wound Infection and the Role of pH 5

2.2 pH-Sensitive Fluorophores 6

2.2.1 Acidity Constant, pK_a 7

2.2.2 Colorimetric pH Indicators 8

2.2.3 Common Fluorophores Used in pH Sensing 9

2.3 Solvatochromism of Dyes 13

2.3.1 Solvent Effects on Absorption 13

2.3.2 Solvent Effects on Fluorescence 14

2.3.3 Solvent Parameters 16

2.4 Polymer-Based Systems as Dye Carriers 17

2.4.1 Amphiphilic Block Copolymer Vesicles 17

2.4.2 Chitosan 19

2.5 Methods Used to Analyze Fluorescent Dyes 21

2.5.1 Ultraviolet-visible (UV-VIS) Spectrophotometry 21

2.5.2 Determination of Fluorescence Quantum Yields 22

2.5.3 Determination of Fluorescence Lifetime 24

3 Synthesis and Characterization of Novel pH-Sensitive Carborhodol Dyes 29

3.1 Introduction and Objective 29

3.2 Results and Discussion 32

3.3 Conclusion and Outlook 40

3.4 Experimental Section 41

3.4.1 Equipment 41

3.4.2 Synthesis 42

4 pH-Dependent Photophysical Properties of Carborhodol Dyes 59
4.1 Introduction and Objective 59
4.2 Results and Discussion 61
4.2.1 Absorption Properties 61
4.2.2 Fluorescence Properties 64
4.2.3 Photostability Assessment 74
4.3 Conclusion and outlook 78
4.4 Experimental Section 79
4.4.1 Equipment 79
4.4.2 Materials and Methods 79
5 Solvatochromic Behavior of Carborhodol Dyes 83
5.1 Introduction and Objective 83
5.2 Results and Discussion 85
5.2.1 Solvent-Dependent Absorption and Emission of the Basic Form of Carborhodols 86
5.2.2 Solvent-Dependent Absorption and Emission of the Acidic Form of Carborhodols 91
5.2.3 Solvent-Dependent Fluorescence Lifetime of the Basic Form of Carborhodols 98
5.3 Conclusion and Outlook 102
5.4 Experimental Section 103
5.4.1 Equipment 103
5.4.2 Materials and Methods 103
6 Encapsulation of pH-Sensitive Dyes in Poly(ethylene glycol)-*block*-poly(lactic acid) Vesicles for Sensing Applications 105
6.1 Introduction and Objective 105
6.2 Results and Discussion 107
6.2.1 Hydrophilicity of Dyes 107
6.2.2 Synthesis of Amphiphilic PEG-*b*-PLA Block Copolymers 108
6.2.3 Encapsulation of Reporter Dyes 110

6.3 Conclusion and Outlook 116
6.4 Experimental Section 117
6.4.1 Equipment 117
6.4.2 Materials and Methods 118
7 pH-Responsive Chitosan-Based Hydrogels for Detecting Wound Infections 121
7.1 Introduction and Objective 121
7.2 Results and Discussion 123
7.2.1 Coupling of Carborhodol Dyes to Chitosan Hydrogel 123
7.2.2 Photophysical Properties of Dye-Coupled Chitosan Films 126
7.2.3 Coupling of Rhodamine-Based ATTO Dyes to Chitosan Hydrogels 133
7.3 Conclusion and Outlook 135
7.4 Experimental Section 136
7.4.1 Equipment 136
7.4.2 Materials and Methods 137
8 Conclusion and Outlook 141
References 143
Appendix 155
Chapter 3: Synthesis and Characterization of Novel pH-Sensitive Carborhodol Dyes 155
Chapter 4: pH-Dependent Photophysical Properties of Carborhodol Dyes 173
Chapter 5: Solvatochromic Behavior of Carborhodol Dyes 183
Chapter 6: Encapsulation of pH-Sensitive Dyes in poly (ethylene glycol)-*block*-poly (lactic acid) Vesicles for Sensing Applications 187
Chapter 7: pH-responsive Chitosan-Based Hydrogels for Detecting Wound Infections 191
Acknowledgements 197

Zusammenfassung

Wundinfektionen im Frühstadium sind schwer zu erkennen. Eine rechtzeitige Diagnose verbessert jedoch die Heilungsergebnisse erheblich und verringert das Risiko von Narbenbildung oder systemischen Komplikationen. Gesunde Haut ist leicht sauer (durchschnittlicher pH-Wert ~4,7), während chronische oder infizierte Wunden alkalisch bleiben (7,15–8,9) und während der Heilung allmählich wieder sauer werden. Die Echtzeitüberwachung des pH-Werts von Wunden hat sich als wertvolles Instrument zur Verfolgung des Heilungsfortschritts, zur Frühwarnung vor möglichen bakteriellen Infektionen und zur Reduzierung unnötiger Antibiotikatherapien erwiesen.

pH-empfindliche Farbstoffe, die innerhalb von Trägermaterialien sichtbare Farbveränderungen durchlaufen, stellen einen einfacheren und kostengünstigeren Ansatz für die Überwachung des pH-Werts von Wunden dar. Aktuelle pH-Indikatoren leiden jedoch unter geringer Lichtbeständigkeit und Farbstoffauswaschung, was ihre praktische Anwendung einschränkt. Diese Arbeit präsentiert die Konzeption, die Synthese und die funktionelle Bewertung von Carborhodol-Farbstoffen, die als lichtbeständige Alternativen zu herkömmlichen pH-Indikatoren entwickelt und für den physiologischen pH-Bereich optimiert wurden.

Neun neue Carborhodole wurden aus ihren jeweiligen Carbopyronin-Vorläufern durch hydrolytische Desaminierung synthetisiert, wobei strukturelle Modifikationen vorgenommen wurden, um die Photostabilität, Löslichkeit und das Biokonjugationspotenzial zu verbessern. Die Farbstoffe weisen unterschiedliche pH-abhängige optische Eigenschaften auf, mit pK_a-Werten im physiologisch relevanten Bereich (5–7). Die Deprotonierung führt zu einer Erhöhung der Absorption, der Quantenausbeute und der Fluoreszenzlebensdauer, was eine empfindliche Detektion von pH-Änderungen sowohl im kolorimetrischen als auch im fluorogenen Modus ermöglicht. Im Vergleich zum Standardindikator Fluorescein und dem gängigen biologischen Marker Cy5 weisen Carborhodole eine überlegene Photostabilität auf und beseitigen damit eine wesentliche Einschränkung bestehender Sonden. Darüber hinaus zeigen die basischen Formen einen ausgeprägten positiven Solvatochromismus, was auf ihre Eignung als polaritätsempfindliche Sonden hinweist.

Um praktische Anwendungen zu demonstrieren, wurden die Farbstoffe in polymerbasierte Systeme eingebaut. Die Einkapselung in PEG-*b*-PLA-Vesikel führte zu einer Zunahme der Fluoreszenzintensität bei steigendem pH-Wert, während die kovalente Aufbringung auf Chitosan-Filme zu Hydrogel-Verbänden führte, die eine reversible Echtzeit-pH-Überwachung innerhalb des für Wunden relevanten Bereichs ermöglichten. Diese Hybridmaterialien verbinden hohe Stabilität und Biokompatibilität mit pH-abhängigen Farbänderungen, die mit

bloßem Auge unter Umgebungslicht sichtbar sind, und einer unter UV-Beleuchtung mit dem Auge leicht erkennbaren Fluoreszenzaktivierung. Damit zeigen sie die erfolgreiche Übertragung der Eigenschaften molekularer Farbstoffe auf funktionelle biomedizinische Plattformen und unterstreichen ihr Potenzial für intelligente Wundverbände und verwandte Diagnosegeräte.

Abstract

Early-stage wound infections are challenging to detect; however, a timely diagnosis significantly improves healing outcomes and reduces the risk of scarring or systemic complications. Healthy skin is mildly acidic (average pH ~4.7), while chronic or infected wounds remain alkaline (7.15–8.9) and gradually return to acidic during healing. Real-time monitoring of wound pH has emerged as a valuable tool for tracking the progression of healing, providing an early warning of potential bacterial infection, and reducing unnecessary antibiotic therapy.

pH-sensitive dyes that undergo visible color changes within carrier materials present a simpler and cost-effective approach for wound pH monitoring. Current pH indicators, however, suffer from low photostability and dye leaching, limiting their practical use. This work presents the design, synthesis, and functional evaluation of carborhodol dyes, developed as photostable alternatives to conventional pH indicators, optimized for the physiological pH range.

Nine novel carborhodols were synthesized from their respective carbopyronine precursors through hydrolytic deamination, with structural modifications designed to enhance photostability, solubility, and bioconjugation potential. The dyes exhibit distinct pH-dependent optical properties, with pK_a values in the physiologically relevant range (5–7). Deprotonation leads to increases in absorption, quantum yield, and fluorescence lifetime, enabling sensitive detection of pH changes by both colorimetric and fluorogenic modes. Compared to the standard indicator fluorescein and the common biological label Cy5, carborhodols display superior photostability, addressing a key limitation of existing probes. Additionally, the basic forms exhibit pronounced positive solvatochromism, indicating their utility as polarity-sensitive probes.

To demonstrate practical applications, the dyes were incorporated into polymer-based systems. Encapsulation in PEG-*b*-PLA vesicles resulted in an increase in fluorescence intensity with rising pH levels, whereas covalent grafting to chitosan films yielded hydrogel dressings capable of reversible, real-time pH monitoring within the wound-relevant range. These hybrid materials combine high stability and biocompatibility, with pH-dependent color changes visible to the naked eye under ambient light, and fluorescence turn-on readily detectable by the eye under UV illumination, showing the successful translation of molecular dye properties into functional biomedical platforms, and highlighting their promise for smart wound dressings and related diagnostic devices.

List of Abbreviations and Acronyms

A	Absorbance
a.u.	Arbitrary units
AFM	Atomic force microscopy
AN	Gutmann acceptor number
aq.	Aqueous (solution)
ATR	Attenuated total reflection
b	Block
BCP	Block copolymer
BODIPY	Boron-dipyrromethene
χ^2	Chi-squared (goodness of fit)
COSY	Correlation spectroscopy (1H–1H)
cru	Constitutional repeating unit
CS	Chitosan
Cy5	Cyanine dye 5
Da	Dalton
DCC	*N*,*N*-dicyclohexylcarbodiimide
DCE	1,2-dichloroethane
DDQ	2,3-Dichloro-5,6-dicyano-1,4-benzoquinone
DFT	Density functional theory
DIPEA	*N*,*N*-diisopropylethylamine
DLS	Dynamic light scattering
DMF	*N*,*N*-dimethylformamide
DMSO	Dimethyl sulfoxide
DN	Gutmann donor number
ε	Molar absorption coefficient
EDG	Electron-donating group
$E_T(30)$	Dimroth-Reichardt solvent polarity parameter
EtOAc	Ethyl acetate
EWG	Electron-withdrawing groups
FESEM	Field emission scanning electron microscopy
Φ_{fl}	Fluorescence quantum yield
FLIM	Fluorescence lifetime imaging microscopy
FRET	Fluorescence resonance energy transfer

FTIR	Fourier transform infrared spectroscopy
FWHM	Full width at half maximum
h	Hours
HMBC	Heteronuclear multiple bond correlation (1H–13C)
HOMO	Highest occupied molecular orbital
HPLC	High performance liquid chromatography
HSQC	Heteronuclear single quantum coherence (1H–13C)
IC	Internal conversion
ICT	Intramolecular CT
IR	Infrared
ISC	Intersystem crossing
LCMS	Liquid chromatography–mass spectrometry
λ_{em}	Emission wavelength(s)
λ_{exc}	Excitation wavelength
log K_{ow}	Octanol–water partition coefficient (logarithmic form)
LSER	Linear solvation energy relationship
LUMO	Lowest unoccupied molecular orbital
max.	Maximum
μ_e	Dipole moment of the excited state
MeCN	Acetonitrile
min	Minute(s)
M_n	Number average molar mass
μ_s	Dipole moment of the ground state
Mw	Weight average molar mass
MWCO	Molecular weight cut-off
NHS	N-hydroxysuccinimidyl
NIR	Near-IR
$\tilde{\nu}_{max}$	Wavenumber
NMR	Nuclear magnetic resonance
p	Packing parameter
PBS	Phosphate buffered saline
PCL	Poly(caprolactone)
PEG	Poly(ethylene glycol)
PET	Photoinduced electron transfer
PLA	Poly(lactic acid)
r.t.	Room temperature

rpm	Revolutions per minute
SA	Catalán's solvent acidity scale
SB	Catalán's solvent basicity scale
SdP	Solvent dipolarity parameter
SEC	Size-exclusion chromatography
SNARF	Seminaphthorhodafluors
SP	Solvent polarizability parameter
τ	Fluorescence lifetime
TBDMS	Tert-butyldimethylsilyl
TCSPC	Time-correlated single photon counting
TD-DFT	Time-dependent density functional theory
TFA	Trifluoroacetic acid
THF	Tetrahydrofuran
TICT	Twisted ICT
TMEDA	Tetramethylethylenediamine
t_R	Retention time (HPLC)
UV	Ultraviolet
VIS	Visible
wt%	Weight percent

1 Introduction and Motivation

Hospital-acquired infections (nosocomial infections) and chronic wound infections, particularly in immunocompromised, immunosuppressed, or diabetic patients, represent a major global health challenge.[1,2] These complications result in higher morbidity and mortality rates and impose substantial costs on the healthcare system.[3,4] Conventional diagnostic approaches, such as standard bacterial cultures and testing, are slow (taking up to 48 hours) and conducted in laboratories separate from the patient.[5] The prevalence of skin wounds in everyday life, along with their high occurrence rate, has a significant social and economic impact worldwide.[6] Early diagnosis of pathogenic infections offers several benefits, including reducing unnecessary or prolonged antibiotic use, thereby limiting the risk of antimicrobial resistance, fewer unnecessary dressing changes, which can reduce the risk of reinfection, and overall lower healthcare costs.[7,8] Consequently, there is an urgent need for new strategies to monitor wound conditions during treatment without removing the wound dressing.

Wound healing is a complex process, and pH is a key indicator of the wound's state. Healthy skin has an average pH of 4.7, i.e., below 5.[9] When the skin is damaged, the underlying tissue, which has a pH of 7.4, becomes exposed, creating conditions favorable for bacterial growth.[10] Infections can raise the wound pH above 7.4 due to the production of alkaline byproducts by bacteria.[11] Persistently elevated pH levels at later stages strongly indicate a chronic wound, which typically ranges from pH 7.15 to 8.9, and the pH will return to acidic during the wound healing.[12] Therefore, a pH-dependent point-of-care method would enable immediate diagnosis through the real-time display of pH changes within a wound dressing.

Over the past decade, a variety of devices have been developed for wound pH monitoring, including flex-circuit inductive transducers,[13] optical sensors based on chemical dyes,[14] pH-sensitive electrodes,[15] and carbon quantum dots.[16] However, these methods often rely on advanced technologies, which can increase production costs. Conventional glass pH probes, on the other hand, provide only localized measurements, lacking the ability to capture complex data across the entire wound area.[17] Alternatively, using pH-sensitive dyes that change color in the visible spectrum is a straightforward method for tracking pH levels.

Natural dyes, including anthocyanins,[18–22] anthraquinone,[23] green tea extract,[24] and curcumin,[25,26] as well as synthetic dyes such as phenol red, and rosolic acid[27] have been investigated for their incorporation into polymers to develop pH-sensitive films for detecting wound infections. However, these dyes suffer from poor photostability and generally function as simple absorbance-based indicators, rather than enabling more sensitive and accurate fluorescence-based sensing.[28–31] Additionally, the coloration of natural dyes depends on the source of extraction, which limits reproducibility.[32] Similarly, the pyranine-benzalkonium ion

pair has been investigated as a fluorescent ratiometric probe for wound pH detection, but its application is hindered by dye leaching from the system, reducing stability and reliability.[33]

Fluorescein and its derivatives are the most widely used fluorescent pH indicators; however, their tendency to photobleach limits long-term applications.[34,35] To address this drawback, seminaphthorhodafluors (SNARF) were developed as an intracellular pH probe. Compared to fluoresceins, SNARFs display improved photostability and pH-dependent dual-emission properties, enabling sensitive ratiometric measurements.[36] Nevertheless, most commercially available SNARFs exhibit pK_a values above 7, which restricts their suitability for monitoring pH changes characteristic of wound environments.[37]

In this context, rhodol dyes represent promising alternatives. As structural hybrids of fluorescein and rhodamine, rhodols often combine enhanced photostability with pK_a values in the range of 4.5–7, making them well-suited for biomedical sensing.[38] Despite being first described in the 19th century, rhodols have been less extensively studied than other xanthene chromophores. Importantly, core-modified rhodols frequently display superior photophysical properties compared to their parent scaffolds, although their synthesis is more challenging.[39]

Carborhodols, a distinct subclass of rhodol derivatives, were first synthesized by Sednev et al. in 2013,[40] with an alternative route reported by Jia et al. in 2018.[41] Beyond these studies, no synthetic approaches have been described, and their application as pH-responsive probes remains unexplored. Preliminary investigations suggest that carborhodols exhibit pH equilibria similar to classical rhodols; however, their potential for ratiometric sensing or integration into bioresponsive materials has not been systematically evaluated. To address this gap, an alternative synthetic strategy was employed in this thesis, yielding nine novel carborhodol derivatives. As members of the xanthene dye family, these compounds are generally considered biocompatible, making them attractive candidates for biomedical sensing platforms.[42]

This work aims to develop novel, photostable, and pH-sensitive fluorescent dyes (pK_a 5–7) and incorporate them into polymer-based systems to create smart wound dressings for continuous monitoring of wound healing and infection.

The main objectives are:

- To design, synthesize, and characterize novel photostable, pH-sensitive carborhodol dyes with pK_a values in the range of 5–7 (Chapter 3).
- To investigate the pH-dependent photophysical properties of the synthesized carborhodols to evaluate their potential as colorimetric and fluorogenic probes (Chapter 4). Specific aims include:
    - Determination of their pK_a values from pH-dependent absorption spectra.
    - Investigation of their emission properties, including fluorescence quantum yield and fluorescence lifetimes, in acidic and basic forms.

- To assess the photostability of acidic and basic forms of carborhodols to evaluate their suitability for long-term pH monitoring (Chapter 4).
- To analyze the absorption, emission, and fluorescence lifetimes of the acidic and basic forms of carborhodols in solvents of varying polarity to elucidate how the local environment influences their photophysical properties (Chapter 5).
- To chemically or physically incorporate selected carborhodol candidates into polymersomes or polymer networks to test their application in pH-responsive wound dressings (Chapters 6 & 7).

The overview of each main chapter of the thesis is presented in Figure 1.1.

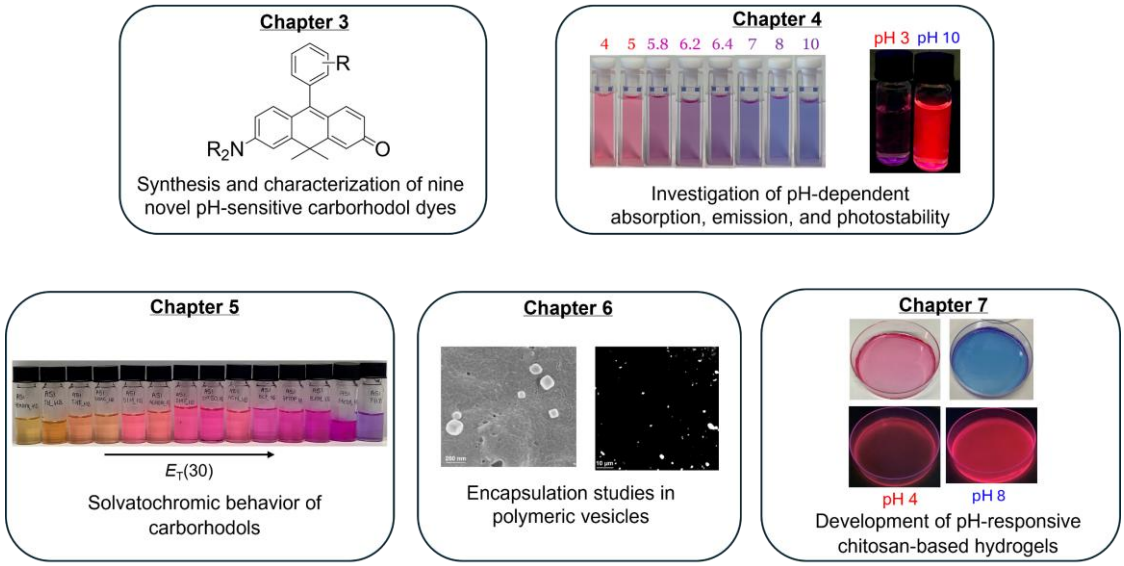

Figure 1.1: Schematic overview of the thesis chapters.

In this thesis, Chapter 3 outlines the synthesis and structural characterization of nine novel carborhodol derivatives, obtained via hydrolytic deamination of the corresponding carbopyronine precursors. Structural modifications were introduced to enhance photostability, solubility, and bioconjugation potential. This synthetic strategy provides access to two major dye classes: carborhodols and carbopyronines.

Chapter 4 focuses on the pH-dependent photophysical behavior of carborhodols. The dyes exhibit changes in absorption and fluorescence properties, including intensity, quantum yield, and lifetime, under varying pH conditions, with pK_a values in the physiological range (5-7). These measurements are used to evaluate their suitability as colorimetric and fluorogenic sensors, with potential relevance to biomedical sensing. Carborhodols are also compared to the conventional indicator fluorescein and the common biological label Cy5 in terms of photostability.

Chapter 5 presents studies on the solvatochromic behavior of the acidic and basic forms of carborhodols. Absorption, emission, and fluorescence lifetime measurements in solvents of

varying polarity reveal how the solvent environment affects the photophysical properties, with the basic form showing pronounced positive solvatochromism. These results provide insight into the dye's potential as polarity-sensitive probes.

Chapters 6 and 7 focus on the integration of carborhodols into functional material systems. Chapter 6 explores dye encapsulation within vesicles formed from the amphiphilic block copolymer poly(ethylene glycol)-*block*-poly(lactic acid) (PEG-*b*-PLA), examining how the hydrophilicity and charge of the dye influence retention within the vesicle. Hydrophilicity is quantified using octanol-water partition coefficients ($\log K_{ow}$), and the pH-dependent fluorescence behavior of dye-encapsulated vesicles is characterized. Chapter 7 describes the immobilization of carborhodols onto chitosan films to create hydrogel-based wound dressings capable of reversible, real-time pH monitoring. These hybrid materials combine high photostability, biocompatibility, and dual-mode optical sensing.

Overall, this work establishes carborhodol dyes as versatile, tunable, and photostable pH-responsive probes. By integrating molecular design with material platforms, this thesis demonstrates the potential of carborhodol dyes for biomedical and environmental sensing, particularly in the development of smart wound dressings.

2 State of Knowledge

In 1909, Sørensen introduced the concept of pH as the negative logarithm of the hydrogen ion concentration($pH = -\log [H^+]$), with values typically ranging from 0 to 14.[43] The pH plays a significant role in many areas, such as determining food quality,[44] skin protection barrier,[45] accessibility of nutrients in soils,[46] and body fluid balance regulation.[47] The pH level is a vital indicator of the abnormal status of human organs, including the tumor microenvironment.[48] The pH of bodily fluids, including tears, urine, sweat, and saliva, has been used to diagnose some disorders.[49]

2.1 Wound Infection and the Role of pH

The pH of the wound is an important parameter influencing microbial colonization, metabolic activities, protease activity, and tissue regeneration.[50] Under normal conditions, the skin surface exhibits an acidic milieu with a pH below 5.[9] This acidic environment serves as a natural barrier against microbial colonization. When the skin is damaged, exudate will appear at the wound site, and its pH value changes along with several pathological changes, including inflammation, collagen synthesis, and angiogenesis.[51]

A temporary drop in pH occurs during the healing of acute wounds. The blood vessels in the local tissue of the wound contract during inflammation, reducing the blood supply and resulting in a deficiency of nutrients and oxygen, and at the same time, glycolysis increases lactic acid and CO_2, leading to a decreased pH.[17] An acidic pH in the wound facilitates many aspects of the natural healing process.[52] A low pH enhances oxygen release through the Bohr effect, as hydrogen ions bind to hemoglobin, causing a conformational change in the protein and reducing its oxygen-binding affinity.[53] As a result, oxygen is more readily released into the surrounding tissues. This effect increases the available tissue concentration of oxygen at the wound edge, specifically at the frontier of migrating epithelium. Subsequently, fibroblast proliferation, angiogenesis, and collagen synthesis are improved, thus promoting optimal healing conditions.[54]

If pathogens are present in the wound, they digest the wound's endogenous extracellular matrix and produce ammonia, which makes the wound alkaline.[45] If no appropriate measures are taken, neutrophils will rapidly aggregate and release excessive elastase, a serine protease that helps degrade damaged extracellular matrix components, allowing new tissue formation.[55] The excessive elastase will interact with necrotic and inactivated tissues in the wound, leading to increased metabolic load at the injury and prolonged wound healing.[12] The pH value of chronic wounds can range from 7.15 to 8.9,[12] which further fosters bacterial proliferation.[55]

Most pathogenic bacteria thrive in environments with a pH above 6. *Staphylococcus aureus*, a common wound pathogen, proliferates at pH levels between 7.0 and 7.5.[50] Thus, pH is a reliable indicator of wound status, with fluctuations in pH predicting the chances of healing, infection, and deterioration (Figure 2.1).[56]

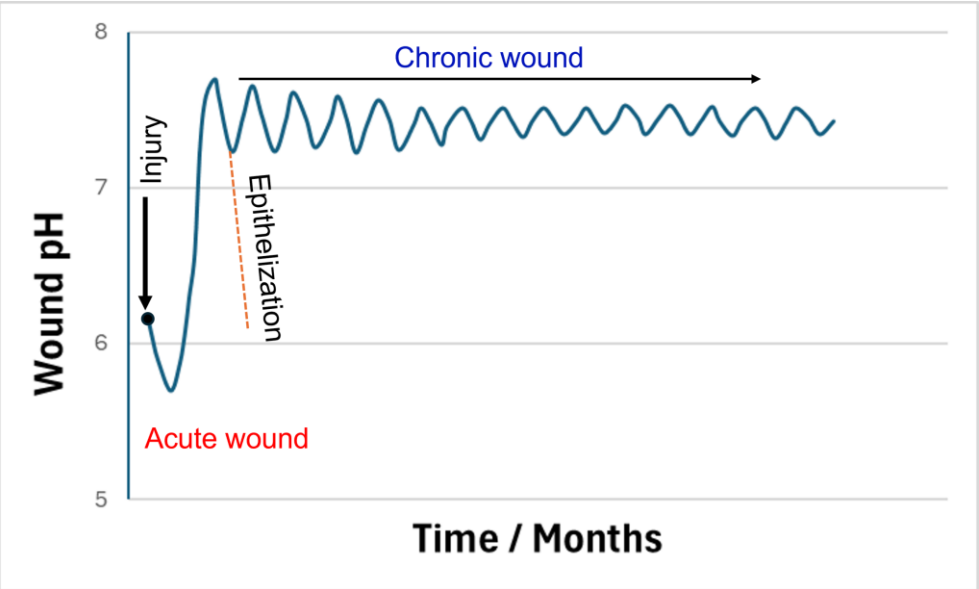

Figure 2.1. Change in pH value in the acute and chronic wound microenvironment over time. Wound healing begins during the epithelialization phase, adapted from Schneider et al.[17], with permission from Springer Nature.

2.2 pH-Sensitive Fluorophores

Absorption and fluorescence are fundamental photophysical processes widely used in spectroscopy, sensing, and imaging applications. These phenomena occur when molecules interact with light, leading to electronic transitions and energy release. A Perrin-Jablonski diagram can explain the processes associated with a molecule's light absorption (Figure 2.2).

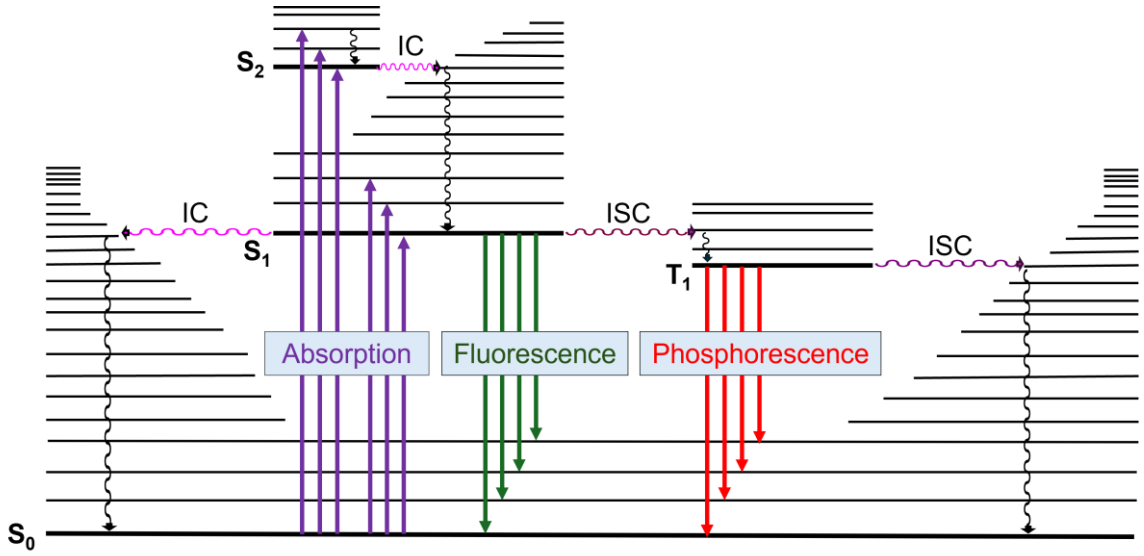

Figure 2.2. Jablonski diagram, demonstrating the origin and positions of absorption, emission, and phosphorescence bands.

Jablonski diagram demonstrates the relative positions of molecular energy levels and the photophysical processes that occur after photon absorption. When a photon is absorbed by the molecule in the singlet ground state S_0, the system is excited to a higher electronic state S_n. Then, the molecule undergoes a vibrational relaxation to the lowest vibrational level of S_1. Afterward, several processes can occur to relax the singlet ground state.[57]

One of the radiative transitions is fluorescence, which occurs from S_1 to S_0.[58] The emitted photons possess lower energy than the absorbed photons, which accounts for the Stokes shift, defined as the difference between the maximum of absorption and emission bands.[59] Other deactivation processes include internal conversion (IC) and intersystem crossing (ISC). IC refers to a non-radiative transition between two electronic states of the same spin multiplicity, converting the electronic energy of the initial state into the vibronic energy of the final state, thus moving the system to a higher vibronic state, followed by a vibrational relaxation.[60] ISC, on the other hand, involves a non-radiative transition between two isoenergetic vibrational levels linked to electronic states of different multiplicities. Unless there is a strong spin-orbit coupling, this process is formally prohibited and proceeds slowly. Heavy elements like Br, Se, I, and Pb promote intersystem crossing by increasing spin-orbit coupling.[61] Phosphorescence refers to the $T_1 \rightarrow S_0$ transition that is accompanied by the emission of a photon.[58]

All deactivation processes reduce the probability of the radiative $S_1 \rightarrow S_0$ transition, thereby diminishing the fluorescence quantum yield (Φ_{fl}). Φ_{fl} is the fraction of the number of photons emitted vs absorbed. An ideal fluorophore should be bright, and its brightness (signal strength) is defined as the product of fluorescence quantum yield and the extinction coefficient.[62]

Dyes that exhibit changes in the aforementioned processes with variations in pH are extensively used in research. Such pH-sensitive dyes offer superior sensitivity and responsiveness compared to traditional electrochemical methods such as pH electrodes.[63]

2.2.1 Acidity Constant, pK_a

The pK_a is an important parameter that determines the optimal pH sensing range of a pH-sensitive dye. Each pH-sensitive dye has a specific pK_a, making them valuable tools for monitoring pH in various environments.[64] Consider a dye molecule DH that can be deprotonated to D^- in an aqueous solution:

$$DH + H_2O \leftrightharpoons D^- + H_3O^+ \qquad \text{(Eq. 2.1)}$$

The protonated and deprotonated forms exhibit changes in their electronic structures, resulting in shifts in absorption or fluorescence spectra.[65] The concentration of water in Eq. 2.1 remains essentially constant, so the expression for the equilibrium constant of the reaction is defined as K_a, the acidity constant.[66]

$$K_a = \frac{[\mathrm{D}^-][\mathrm{H_3O}^+]}{[\mathrm{DH}]} \quad \text{(Eq. 2.2)}$$

The logarithmic form of the equation is the Henderson-Hasselbalch equation (Eq. 2.3). When the pH is equal to the pK_a, the concentration of the protonated (DH) and deprotonated (D^-) species will be the same.[66]

$$\mathrm{p}K_a = \mathrm{pH} - \log\frac{[\mathrm{D}^-]}{[\mathrm{DH}]} \quad \text{(Eq. 2.3)}$$

Dyes can be chemically modified to tune their pK_a values, allowing their use in different environments, e.g., acidic compartments such as lysosomes, neutral cytosol, or alkaline extracellular fluids.[67] Introducing electron-withdrawing groups near an acidic site stabilizes the conjugate base (D^-) via inductive or resonance effects.[68] Thus, with increased stability of D^-, K_a increases and pK_a decreases (Eq. 2.2). For example, introducing halogen groups to fluorescein (**1**) produced the Oregon green series (**2**), and the pK_a drops from 6.4 to around 4.8; therefore, these indicators are useful for measuring pH in acidic cellular environment compartments.[69] Contrarily, an increase in the electron-donating groups destabilizes the conjugate base, or stabilizes the protonated form, and the pK_a increases.[70]

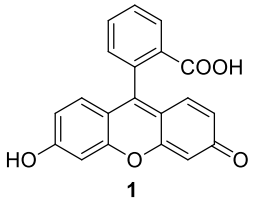

1

Fluorescein

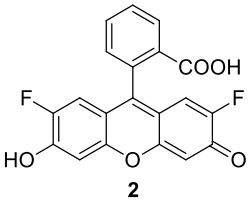

2

Oregon Green 488

The pH-sensitive probes can either change color (colorimetric), fluorescence (emission intensity, wavelength, or fluorescence lifetime), or both color and fluorescence in response to pH variations.

2.2.2 Colorimetric pH Indicators

Colorimetric indicators undergo visible color changes due to structural changes in their molecular forms, often caused by protonation or deprotonation of specific functional groups such as phenols, carboxylic acids, or amines.[71] Phenolphthalein is a well-known example among colorimetric indicators. Phenolphthalein is colorless in acidic conditions but turns pink when pH rises to 8-9. The lactone form of phenolphthalein **3** is stable in the acid range, but at pH 8-9, the gamma-lactone ring is broken, and molecule **4** with the characteristic chromophore of the triphenylmethane dyes results, which is pink due to extended conjugation (Scheme 2.1).[72]

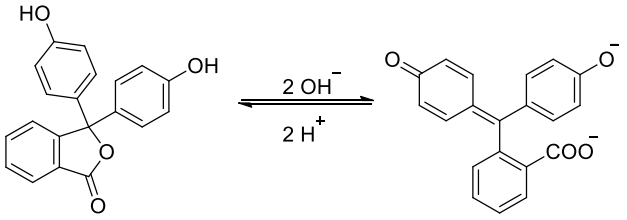

3 **4**

Colorless Pink

Scheme 2.1. Protonation and deprotonation equilibrium of phenolphthalein.

Another example of a colorimetric indicator includes 4,(4-nitrophenoxy)benzeneamine) derived azo dye **5**. This azo dye undergoes a bathochromic shift of 122 nm from acidic to basic conditions, changing from yellow (399 nm) to red (521 nm). The pH range in which the dye is most sensitive is 7.9–10.4. After deprotonation, the dye forms a phenoxide ion **6**, which increases conjugation. The increased electron delocalization stabilizes the excited state, lowers the energy gap, and causes the absorption to shift to longer wavelengths (bathochromic shift).[73]

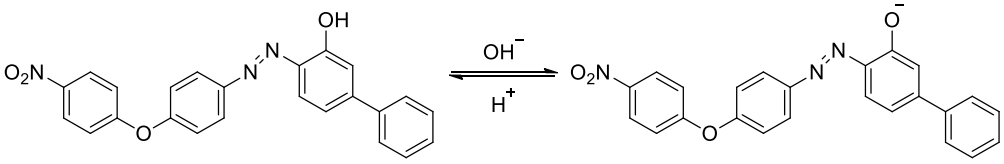

5 **6**

Yellow Red

Scheme 2.2. Protonation and deprotonation equilibrium of the azodye **5**.

2.2.3 Common Fluorophores Used in pH Sensing

The determination of pH via fluorescence is often more accurate, as emitted light is measured more sensitively than absorption.[74] This is particularly important when measuring in biological samples, where either a lower concentration or amount of pH sensor is required, or an early response is needed.[74] In the following section, the major classes of pH-sensitive fluorescent dyes will be discussed.

2.2.3.1 Fluorescein Derivatives

Fluorescein and its derivatives are widely used fluorescent pH indicators. Fluorescein exists in four molecular structures, depending on the pH. The four protolytic forms are cationic, neutral, anionic, and dianionic.[75] The absorption spectra of fluorescein derivatives show a blue shift and a decreased absorptivity with decreased pH. The fluorescence intensity decreases with a decrease in pH, but the band shape and wavelength are mostly unaffected.[75] For biological applications, carboxyfluorescein is commonly used as it is better retained in cells due to the presence of an extra negative charge compared to fluorescein. However, both fluorescein

derivatives rapidly leak from cells, making it very difficult to determine whether the observed decrease in cellular fluorescence arises from the formation of acidic cations or is merely a consequence of dye efflux. This prevents the accurate quantification of pH.[76] The 2′,7′-bis-(2-carboxyethyl)-5-(and-6-) carboxyfluorescein (BCECF) (**7**) and its membrane-permeable acetoxymethyl ester derivatives are the most used fluorescent probes for monitoring intracellular pH, with a pK_a of 7. Once inside the cell, the free form of the dye is well retained due to the presence of four to five negative charges at physiological pH.[77] Additionally, BCECF conjugated to dextran exhibits high levels of intracellular retention, enhancing its utility for long-term measurements.[78] However, despite this improved retention, a significant limitation of fluorescein-based dyes is their lack of photostability.[79] Furthermore, their fluorescence intensity is concentration-dependent, so when the dye accumulates, the observed fluorescence changes may reflect local dye concentration variations rather than true pH fluctuations.[80]

2.2.3.2 Seminaphthorhodafluors (SNARF)

The seminaphthorhodafluors (SNARF) dyes were developed as pH indicators for the purpose of measuring intracellular pH.[36] These are types of benzo[c]xanthene dyes with a pK_a range of 7.5 – 7.9.[81] Like fluorescein, the molar absorptivities of SNARFs are highest under basic conditions, and their absorbance maxima shift to the red. However, unlike most fluorescein-based pH indicators, these dyes are characterized by higher photostability and a pH-dependent band shape or wavelength of the fluorescence spectrum. This enables ratiometric measurements using the much more sensitive fluorescence spectroscopy to determine the pH.[36] For example, both the acidic and basic forms of the dye are excited at a particular wavelength simultaneously, while the ratio of the two fluorescence intensities is correlated with the pH of the medium.[81] Since the pK_a of SNARF derivatives is above 7.5, it is unsuitable for measuring intracellular pH below 7, assessing wound status, etc. However, the pK_a of these dyes can be lowered by introducing electron-withdrawing groups. For example, C-SNARF-4F is prepared by fluorinating the benzo[c]xanthene ring system, which results in a pK_a of approximately 6.4, making it more suitable for detecting lower pH values.[82] Additionally, the fluorescence characteristics of SNARF derivatives, such as C-SNARF-1 (**8**), can be significantly influenced by factors like temperature and the surrounding environment.[36]

2.2.3.3 Rhodols

Rhodol is a hybrid fluorophore derived from rhodamine and fluorescein.[83] They share the same backbone as rhodamine dyes; however, one dialkylamino group in rhodamines is substituted with oxygen.[84] These dyes exhibit significantly higher photostability and longer practical observation times compared to fluorescein derivatives, and are suitable for pH measurements

in acidic environments with pK_a values typically ranging from 4.5 to 7.[38] They exhibit significant changes in absorbance spectra as the pH varies, possess higher absorption coefficients, and are well-suited for dual excitation ratiometric pH measurements.[74] The conjugate of rhodol **9** with ethylenediamino-ouabain (ouabain is a glycosylated steroid) has been utilized for investigating the pH values in the acidic microenvironment of the cardiac glycoside-binding site of Na^+/K^+-ATPase, which shows the highest fluorescence in its basic form and significantly lower fluorescence in its acidic form.[85]

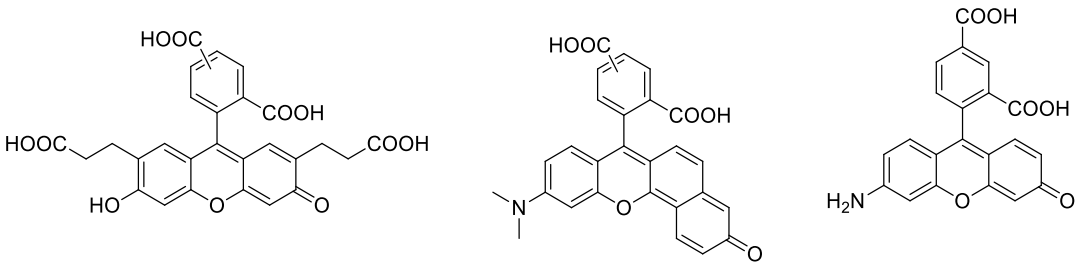

7 BCECF **8** C.SNARF-1 **9** Rhodol

2.2.3.4 Fluorescence On/Off Probes

Several signal-conversion mechanisms, such as Förster resonance energy transfer (FRET), intramolecular charge transfer (ICT), photo-induced electron transfer (PET), and restriction of intramolecular motion (RIM), can be utilized to design turn-on probes for acidic environments.

The non-fluorescent spirocyclic xanthene-based probes, which open upon protonation, resulting in a highly fluorescent form, are an excellent example of RIM-based pH sensing.[86] Fluorescein, Rhodol, and rhodamine-based spirolactone or spirolaclam probes are extensively studied, and the fluorescent form of these possesses all the desirable photophysical characteristics of their parent.[86] The pH-responsiveness of rhodamine spirolactams (RSLs) can be tuned by increasing the steric bulk near the spirolactam nitrogen.[87] Stratton et al. investigated a series of 19 aniline-derived RSLs and found that the pK_a value increases as the substituent size and the electron-withdrawing character increase.[88] Both the steric and electronic stabilization of the protonated spirocyclic intermediate form of the RSLs, making them less likely to donate protons, results in a higher pK_a.[88] A significant disadvantage is that it sometimes requires an organic co-solvent for ratiometric sensing in an aqueous environment, due to the potential for ring opening in the absence of a low pH, resulting from the polar protic nature of the environment.[89]

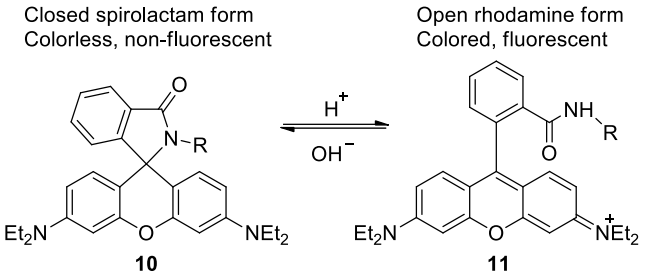

Scheme 2.3. Spirolactam equilibrium of rhodamine (R = aniline) derivatives.

The simple BODIPY-linked aniline (Scheme 2.4) can serve as an example of H^+ monitoring involving PET.

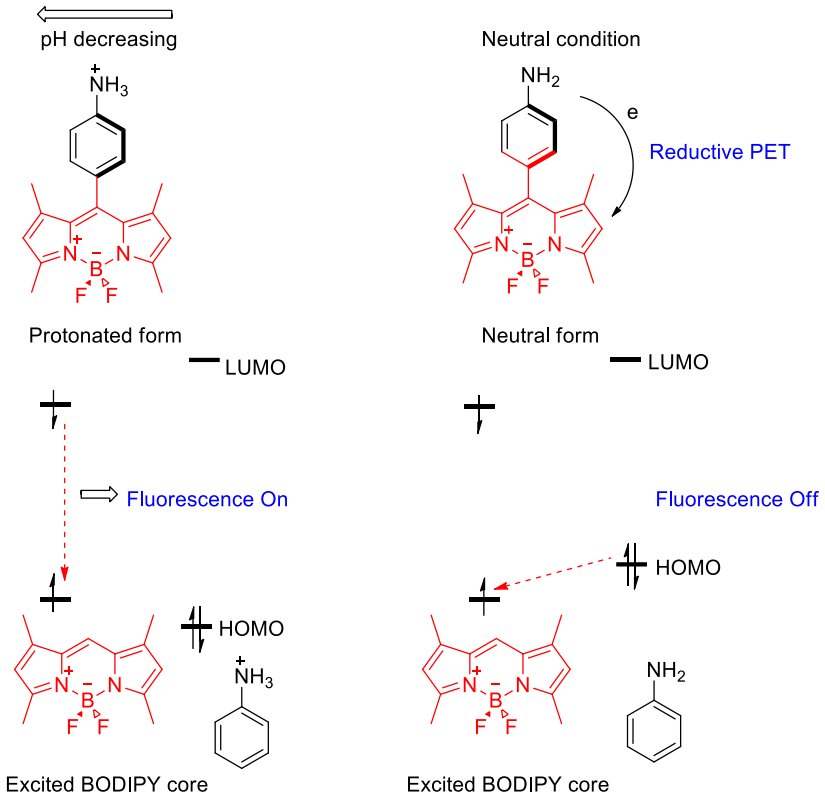

Scheme 2.4. Mechanism of photoinduced electron transfer (PET) between the BODIPY moiety and the phenylamino unit in protonated form (left) and neutral form (right).

In photoexcited BODIPY, the intramolecular electron transfer from the phenylamine to the BODIPY is energetically favorable, and fluorescence of the BODIPY moiety is quenched through PET. In an acidic environment, protonation introduces a positive charge on the nitrogen atom, leading to a reduced highest occupied molecular orbital HOMO energy level, which restricts the PET process and restores fluorescence in the BODIPY moiety. The probe shows more than 500-fold enhanced fluorescence when the pH is shifted from 4.12 to 1.42.[90]

2.3 Solvatochromism of Dyes

The absorption or fluorescence spectrum of a molecule shifts depending on the surrounding solvent. In 1922, Hantzsch introduced the term solvatochromism to describe the changes observed in the UV-Vis absorption spectra of dyes when the solvent is varied.[91] Solvent-dependent spectral shifts result from solute-solvent interactions. These interactions can be classified into non-specific interactions, such as dispersion or dipole forces, and specific interactions, including hydrogen bonding or charge transfer.[92] The polarity of solvents can preferentially stabilize either the ground or excited state, leading to different energy level gaps and thus a solvent-dependent absorption or emission spectrum.

2.3.1 Solvent Effects on Absorption

An increase in solvent polarity can cause the absorption band to shift to shorter wavelengths (blue or hypsochromic shift), known as negative solvatochromism, or to longer wavelengths (red or bathochromic shift), referred to as positive solvatochromism.[93] (Figure 2.3)

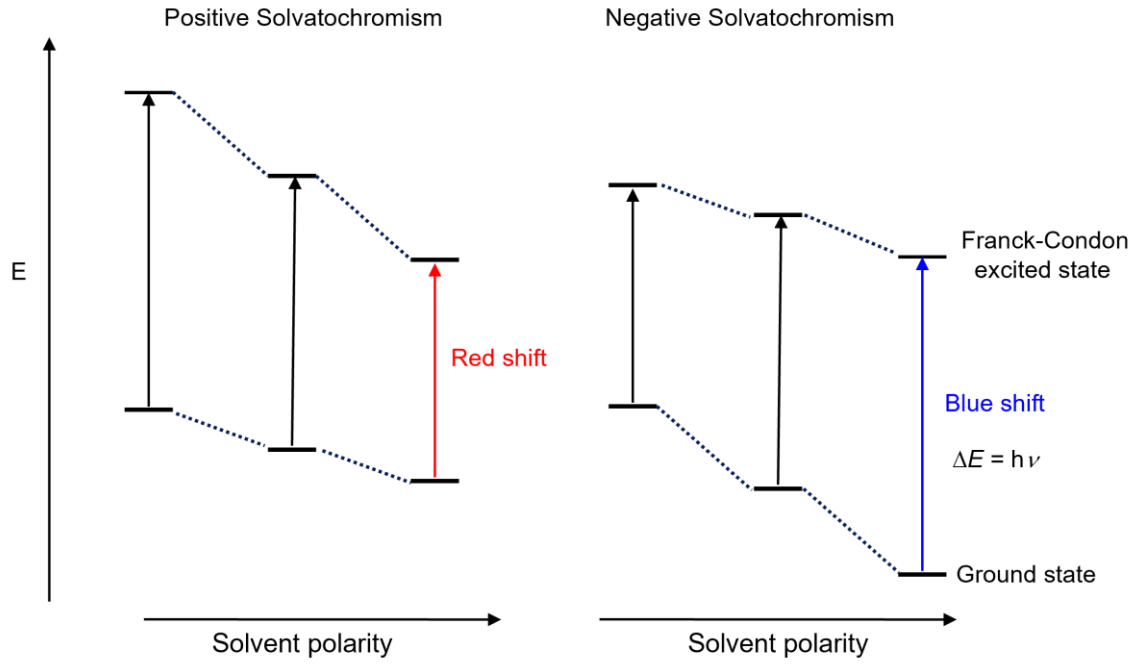

Figure 2.3. Positive (left) and negative (right) solvatochromatic shifts in terms of electronic transition energy, adapted from Reichardt et al.[93], with permission from John Wiley and Sons.

The red-shifted absorption observed in a polar solvent arises from the greater stabilization of the Franck-Condon excited state compared to the ground state.[93] Such positive solvatochromism is commonly seen in donor-acceptor substituted dyes. For example, in the case of imine dye **12**, a HOMO-LUMO transition (π–π*) involving an internal charge transfer from the *N*,*N*-dimethylaminophenyl electron donor to the nitrothienyl electron acceptor group

leads to an increase in the dipole moment of the excited state (μ_e) compared to the ground state (μ_g).[94] The polar solvent molecules interact with the solute, stabilizing its excited state and reducing the energy required for excitation.[95] The energy gap between the ground and excited state decreases, causing a bathochromic (red) shift in the absorption spectrum.[95]

Conversely, if the excited state is less stable than the ground state (i.e., $\mu_g > \mu_e$), more energy is needed to excite the molecule, and this increases the energy gap between the two states, causing a hypsochromic (blue) shift in the absorption spectrum.[95] Reichardt's dye (2,6-Diphenyl-4-(2,4,6-triphenyl-1-pyridinio)phenolate) (**13**) is a classic example of a dye showing large negative solvatochromism. This betaine dye exhibits a large permanent dipole moment in the ground state ($\mu_g \approx 15$ Debye). It contains an extensively polarizable π-electron system with 44 π-electrons, making it suitable for registering dispersion interactions. The phenolate oxygen in Reichardt's dye serves as a strong electron pair donor center, allowing interactions with hydrogen bond donor solvents and Lewis acids. As solvent polarity increases, the highly dipolar ground state undergoes greater stabilization through solvation compared to the less dipolar Franck-Condon excited state and results in negative solvatochromism.[96]

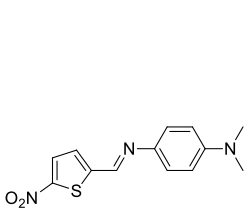

12

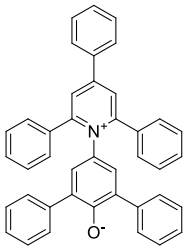

13

2.3.2 Solvent Effects on Fluorescence

If the relaxation time for the rearrangement of the solvent molecules surrounding the solute in the Franck-Condon excited state (τ_R) is significantly less than the finite lifetime of the molecule in the excited state (τ_e), the solvent molecules can reorient after electronic excitation, leading to a relaxed excited state (S_1) with a new solvation equilibrium. The fluorescence occurs from this equilibrium state at room temperature. There is also a Franck-Condon ground state (S'_0) after emission, which exists briefly until the solvent molecules reorganize to the equilibrium arrangement for the ground state.[93] The energy of the relaxed excited state (S_1) decreases with increasing strength of solute/solvent interaction. In the case of a fluorophore with $\mu_e > \mu_g$, S_1 is more stabilized by polar solvents, which results in a red shift and the corresponding Stokes shift of the emission band.[97] (Figure 2.4)

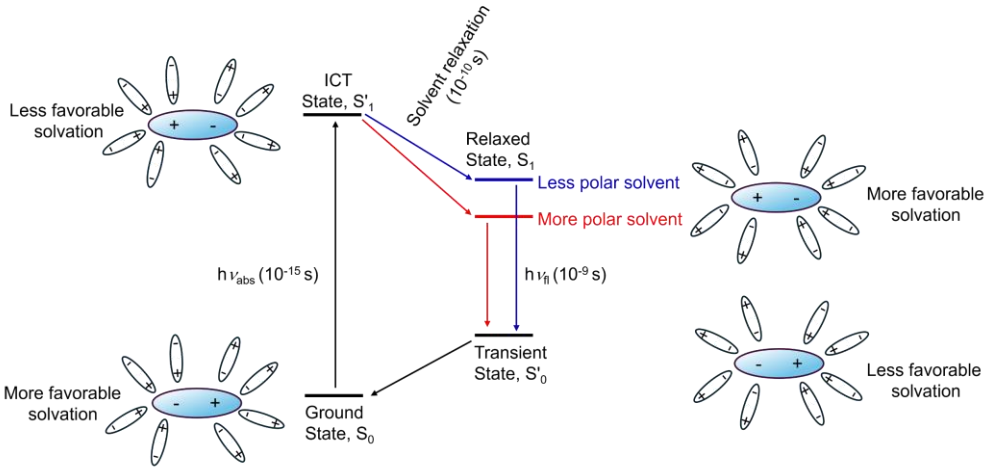

Figure 2.4. State diagram of the photoexcitation and the deactivation pathways of a dipolar fluorophore in a more and less polar solvent, adapted from Reichardt et al.[93], with permission from John Wiley and Sons.

Interactions between the excited-state molecules and the surrounding solvent often influence the emission properties of fluorophores.[93] In protic solvents, strong hydrogen bonding can lower the energy of the excited state, causing a red shift in the fluorescence emission.[98] The electronic effects of substituents also play an important role; as polarity increases, electron-donating groups on the fluorophore tend to stabilize the excited state, leading to red-shifted emission. In contrast, electron-withdrawing groups may destabilize the excited state in polar environments, resulting in a blue shift.[99] Additionally, in viscous solvents, the restricted motion of the fluorophore reduces non-radiative energy loss by limiting intramolecular rotation, which extends the fluorescence lifetime.[100]

Sasaki et al. showed the effect of solute molecules conformational restrictions (torsion) in solvatochromism. They found that the twisted conformations are more sensitive to changes in solvent polarity by investigating the push-pull biphenyl analogues (4-(*N*,*N*-dimethylamino)-4-formylbiphenyl) with a modulated dihedral angle of the aryl-aryl bond, using methyl groups **14** or a bridged structure **15**. The increased torsion between the *N*,*N*-dimethylaniline donor and the benzaldehyde acceptor enhances the polarization of the twisted intramolecular charge transfer (TICT) excited state, resulting in pronounced positive solvatochromism. Compound **14** (with $R^1 = R^3 = CH_3$ and $R^2 = R^4 = H$) exhibited a more substantial solvatochromic shift than well-known polarity-sensitive dyes like Prodan.[101]

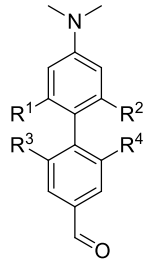

14

R^1, R^2, R^3, R^4 = CH_3 or H

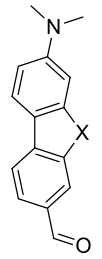

15

X = $C(CH_3)_2$ or $-CH_2CH_2-$

2.3.3 Solvent Parameters

Various solvent polarity scales and solvatochromic parameters have been developed to quantify and compare solvent effects.[102] One of the well-established measures is the $E_T(30)$ scale, which was developed based on the solvent-dependent shifts of the absorption maximum of Reichardt's dye **13** and its large negative solvatochromism.[103] The $E_T(30)$ values represent the molar transition energies (in kcal/mol) of Reichardt's dye (Betaine 30) (Eq. 2.4), where *h, c,* and N_A denote Planck's constant, the speed of light, and Avogadro's constant, respectively. Additionally, λ_{max} indicates the wavelength, while $\tilde{\nu}_{max}$ refers to the wavenumber of the long-wavelength absorption maximum for Reichardt's dye, and high $E_T(30)$ value indicates a high polarity solvent.[104]

$$E_T(30) = hc\tilde{\nu}_{max}N_A = \frac{28591}{\lambda_{max}} \qquad \text{(Eq. 2.4)}$$

The $E_T(30)$ scale is normalized to the E_T^N scale, with dimensionless values ranging from 0 (for tetramethylsilane) to 1 (for water).[105] However, the $E_T(30)$ scale is based on a single empirical parameter and uses only one probe, so it assumes that the nature and strength of the solute–solvent interactions observed for the indicator dye are comparable to those experienced by the solute of interest, and this assumption may not always hold.[97]

Apart from the $E_T(30)$ scale, many other multiparameter solvent polarity scales have been introduced to quantitatively assess the solvent/solute interaction and the resulting spectral shifts.[106] The effect of solvent polarity on the absorption or emission spectra and Stokes shifts is interpreted utilizing linear solvation energy relationship (LSER) using a Kamlet-Taft Equation.[107] (Eq. 2.5)

$$\nu = \nu_0 + s\pi^* + b\beta + a\alpha \qquad \text{(Eq. 2.5)}$$

Where ν is the solute property, ν_0 is the value of ν in a non-interacting reference solvent or in the gas phase, π^* is a measure of both dipolarity and polarizability,[108] α[109] and β[109] represent a solute's ability to donate or accept hydrogen bonds, respectively. The coefficients s, b, and a are the relative susceptibilities of the solvent-dependent solute property to the corresponding

solvent parameters (α, β, and π^*).[110] While the Kamlet-Abboud-Taft model uses a single parameter (π^*) to describe both dipolarity and polarizability, Catalán later proposed two separate scales: one for dipolarity (SdP)[111] and another for polarizability (SP),[112] allowing these two solvent effects to be considered independently. Additionally, the Gutmann donor number (DN) and acceptor number (AN) are used to describe the nucleophilic and electrophilic nature of solvents,[113] and the acid-base behavior of solvents can be evaluated using Catalán's solvent acidity (SA)[114] and basicity (SB)[115] scales.

2.4 Polymer-Based Systems as Dye Carriers

2.4.1 Amphiphilic Block Copolymer Vesicles

Polymers are large macromolecules made up of repeating building blocks called monomers. When the polymer chain is composed of only one type of monomer, it is known as a homopolymer. In contrast, copolymers are formed from two or more distinct monomers linked together within the same chain. If these different monomers are grouped into distinct sections, the polymer is called a block copolymer (BCP). When one monomer is completely polymerized before introducing the second monomer, the resulting structure contains two distinct segments and is called a diblock copolymer.[116] An amphiphilic diblock copolymer consists of a hydrophilic and a hydrophobic segment. A typical example is poly (ethylene glycol)-*block*-poly (lactic acid) (PEG-*b*-PLA), where the PEG segment is hydrophilic, and the PLA segment is hydrophobic.[117]

Amphiphilic block copolymers have attracted significant attention due to their ability to self-assemble into well-defined nanostructures in aqueous environments. This behavior primarily arises from the differences in solubility or hydrophilicity between the constituent blocks.[118] They form ordered structures such as spheres, cylinders, lamellae, vesicles, and many other complex forms of assemblies.[119] A molecule's packing parameter (p) determines its probable self-assembled structure. The dimensionless p is defined in equation 2.6. where v_c is the volume of the hydrophobic segment, a_0 is the optimal area of the head group, and l_c is the length of the hydrophobic segment (Figure 2.5).

$$p = \frac{v_c}{a_0 l_c} \qquad \text{(Eq. 2.6)}$$

Spherical micelles typically form when $p \leq 1/3$. As p increases to the range $1/3 < p \leq 1/2$, cylindrical, also known as worm-like or rod-like micelles, are obtained. Vesicles are seen for $1/2 < p < 1$, while for $p = 1$, lamellar structures are formed.[120] (Figure 2.5)

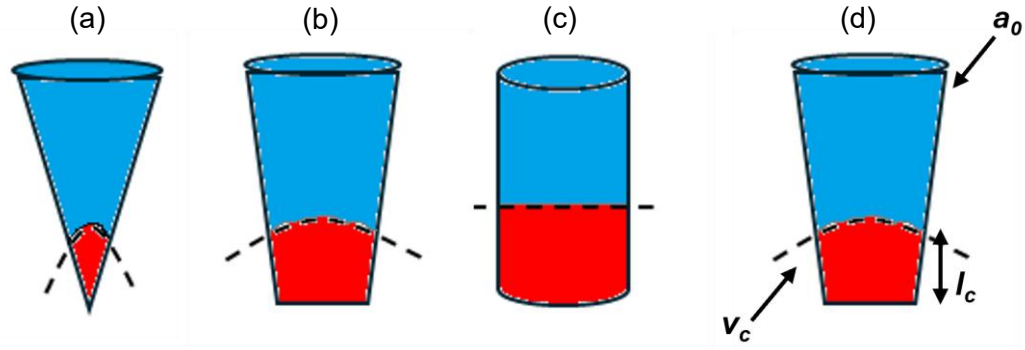

Figure 2.5. Simplified schematic illustration of AB diblock copolymer morphologies: (a) sphere, (b) cylinder, (c) lamella, or vesicle, (d) Parameters of Eq. 2.6 are shown in the cylinder assembly. Hydrophilic block A is represented in blue, and the hydrophobic block B is in red, with dashed lines indicating the interface between the two domains in each morphology. Adapted from Mai et al.[119], with permission from the Royal Society of Chemistry.

Among these assemblies, the BCP vesicles, first introduced in 1995 by the groups of Eisenberg[120] and Meijer[121], have attracted significant research interest and are now extensively investigated for their applications as versatile carriers in biomedical and nanotechnological fields.[122]

Vesicles with well-defined morphologies are commonly prepared using either a solvent-switch method or film rehydration followed by extrusion to control size distribution.[123] In contrast, giant unilamellar vesicles can be generated through electro formation.[124]

The technique used in this thesis is the solvent-switch method. In this approach, the BCP is first dissolved in a water-miscible organic solvent capable of solubilizing both hydrophilic and hydrophobic segments, such as tetrahydrofuran or 1,4-dioxane. Subsequently, a selective non-solvent, typically water or an aqueous buffer that preferentially interacts with the hydrophilic block, is gradually added to the stirring solution of the BCP in organic solvent.[125] Self-assembly into vesicles occurs to minimize energetically unfavorable hydrophobic–water interactions.[122] After several hours of stirring to allow for structural equilibration, excess water is added to freeze the vesicular structure. Finally, residual organic solvent and unassembled BCP are removed by dialysis against water to yield purified vesicles.[125]

If the BCP does not dissolve in water-miscible organic solvents but is soluble in a water-immiscible solvent with chloroform, vesicle formation can still occur through a reversed self-assembly technique by adding the organic BCP solution to the stirring aqueous phase (3:1 v/v), such as with hyaluronic acid-block-poly (lactic acid) (HYA-*b*-PLA) vesicle formation.[126]

The resulting vesicles are composed of hollow spheres featuring a hydrophobic wall along with hydrophilic coronas on both the inside and outside.[127] This enables the transportation of both hydrophilic and hydrophobic cargo molecules in an aqueous environment. Hydrophilic cargos are encapsulated inside the central aqueous cavity or adsorbed to the hydrophilic

corona, whereas the hydrophobic molecules are typically embedded in the hydrophobic membrane core.[128] (Figure 2.6).

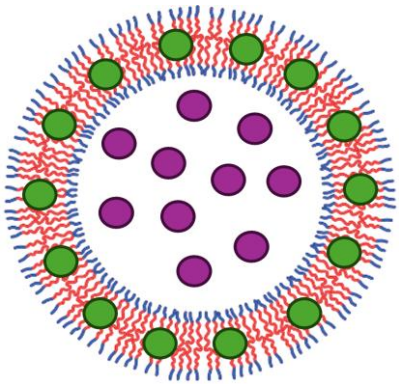

Figure 2.6. Schematic illustration of a polymeric vesicle. The hydrophilic block is shown in blue, and the hydrophobic block is shown in red. Entrapped hydrophilic cargo is illustrated in magenta, while hydrophobic cargo is in green.

Block copolymers have been developed to react to different kinds of stimuli for the delivery of stored cargo to the target area for therapeutic and diagnostic applications. These stimuli or triggers can be physical, chemical, and biological in nature. Physical triggers include temperature,[129] light,[130] ultrasound,[131] or electric and magnetic fields.[132] Chemical triggers can be changes in pH,[133] ionic strength,[134] or oxidation.[135] Enzymes[136] and metabolites[137] are examples of biological triggers. For example, Proteinase K, a readily available model enzyme for the proteinase produced by *Pseudomonas aeruginosa,*[138] can degrade the vesicles of PEG-*b*-PLA by facilitating the hydrolysis of PLA,[139] subsequently releasing their cargo during this process.

2.4.2 Chitosan

Chitin is a naturally occurring polysaccharide composed of *β*-(1→4)-linked N-acetyl-D-glucosamine units.[140] It was first described by Henri Braconnot in 1811, and its name is derived from the Greek term *chiton*, meaning a protective covering, highlighting its early identification in the exoskeletons of fungi, shells, and bones.[141] Similar to the role of cellulose in plants, chitin provides mechanical strength to cell walls in lower animals and plants with nitrogen-rich diets.[142] Chitin exists in nature as ordered crystalline microfibrils and is the second most abundant polymer after cellulose.[142] Although chitin is widely distributed in nature, its primary industrial sources are marine crustaceans, particularly shrimp and crabs.[143] During the production of chitin, mineral components, such as calcium carbonate, are first removed using dilute acid solutions, followed by alkaline extraction to solubilize proteins. Bleaching is often employed to eliminate pigments and enhance purity and visual quality.[144]

Chitosan is produced by the deacetylation of chitin through alkaline hydrolysis at elevated temperatures or enzymatic hydrolysis using enzymes such as chitin deacetylase, during which

acetamide groups are cleaved to yield the deacetylated polymer.[145] The degree of deacetylation varies from 56% to 99% depending on the production method and species.[146] Rouget first discovered chitosan by heating chitin in an alkaline medium in 1859.[147] Hoppe-Seyer later named it chitosan, but its chemical structure was not clarified until 1950.[148]

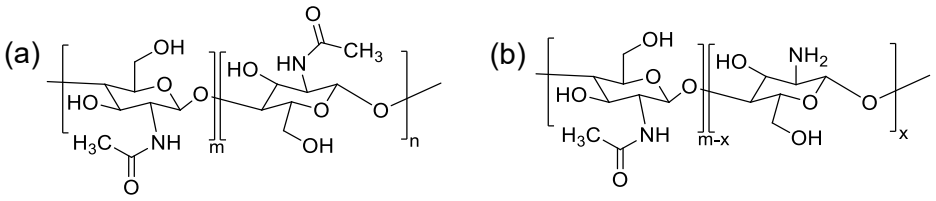

Figure 2.7. Chemical structures of (a) chitin and (b) chitosan.

Chitosan is a biocompatible, nontoxic linear aminopolysaccharide with a high nitrogen content and a rigid D-glucosamine backbone, contributing to its high crystallinity and hydrophilic nature.[149] It is biodegradable as it contains breakable glycosidic bonds.[150] Both amine and hydroxyl groups provide multiple reactive sites for chemical modification and cross-linking.[151–154] While it is insoluble in water and most organic solvents, it dissolves readily in dilute aqueous acids due to protonation of its amino groups (pK_a ~6.2).[155] Chitosan exhibits significant intermolecular hydrogen bonding, resulting in high viscosity in solutions.[156] As a cationic biopolymer with high charge density, carrying one positive charge per glucosamine unit, chitosan interacts with negatively charged entities such as sialic acid residues in mucin, contributing to its mucoadhesive properties.[157,158] It also binds to anionic components of microbial cell membranes and biofilms, leading to membrane disruption and antimicrobial activity.[159–161] Chitosan promotes hemostasis by adsorbing red blood cells and platelets at the site of bleeding, facilitating platelet aggregation and thrombus formation.[162] Additionally, its strong chelating ability toward various metal ions enables its application in metal ion removal and recovery across diverse industrial processes.[163]

Chitosan has gained significant attention for its remarkable physicochemical and biological properties, making it suitable for various applications, including wound healing,[164–168] drug delivery systems,[169,170] biomedical applications,[171] tissue engineering,[172,173] cosmetology,[174] food packaging,[175] wastewater treatment,[176] beverage clarification,[177] and localized antimicrobial therapy.[178]

2.4.2.1 Chitosan Hydrogels

A hydrogel is a polymeric structure composed of chains crosslinked through non-covalent and/or covalent bonds to form a three-dimensional network that exhibits no flow when in a steady state.[179] These structures possess the ability to retain large amounts of water, causing the swelling of the structure.[180] Gels are biphasic: the consistency of a gel is provided by the solid phase, which absorbs a tremendous amount of liquid and remains insoluble, and in

hydrogels, the liquid phase is water.[181] These hydrogels are called physical gels if the origin of the network is due to physical phenomena (phase separation, sol-gel transition, etc.), which is reversible, and called chemical gels if the network is due to chemical cross-linking, which is irreversible.[182] The biopolymer chitosan can form hydrogels in response to slight pH or ionic strength changes. Reversible non-covalent interactions, including electrostatic attractions, hydrophobic forces, hydrogen bonding, and the formation of crystalline regions between polymer chains, primarily mediate the gelation of physical chitosan hydrogels.[183] Chitosan films can be created by spin-coating chitosan solutions onto substrates like silicon wafers and glass[184] or by drop-casting on polystyrene, followed by drying.[185]

Chitosan-based hydrogels are compatible with living tissues and are widely employed in biomedical applications, including scaffolding materials for tissue engineering,[186] biodegradable sutures,[187] membranes for hemodialysis,[188] wound and burn care.[189]

2.5 Methods Used to Analyze Fluorescent Dyes

2.5.1 Ultraviolet-visible (UV-VIS) Spectrophotometry

Studying pH-sensitive dye usually begins with a simple observation of color changes at different pH levels. To evaluate the response more accurately, a quantitative method is needed. For this purpose, UV-VIS spectroscopy is often employed, which records the absorbance of ultraviolet and visible light across a range of wavelengths. The specific wavelengths that are absorbed can be directly related to the perceived color of the compound.[190]

As a beam of light passes through a solution, it becomes attenuated due to partial absorption by the molecules present in the solution. The absorbance (*A*, also known as optical density) and transmittance (*T*) can be determined by measuring the intensity of light before and after it passes through the sample.[191] The Beer-Lambert law, shown in Equation 2.7, describes a linear relationship between absorbance and the product of the molar absorptivity (*ε*), concentration (*c*), and path length (*d*).

$$A = -\log(T) = \log\left(\frac{I_0}{I}\right) = \varepsilon\, c\, d \qquad \text{(Eq. 2.7)}$$

ε is a wavelength-dependent constant that reflects the probability of an electronic transition. This probability is governed by spectroscopic selection rules, particularly the conservation of spin multiplicity. Allowed transitions, such as $\pi \rightarrow \pi^*$ in conjugated organic dyes, are more probable and exhibit high *ε* values.[192] For highly concentrated dye solutions, if concentration-dependent reactions or aggregation occur, the *ε* of the resulting species, such as reaction products or dimers, must be considered.[193]

2.5.2 Determination of Fluorescence Quantum Yields

The fluorescence quantum yield (Φ_{fl}) is the ratio of the number of photons emitted to the number of photons absorbed (Eq. 2.8).[58]

$$\Phi_{\mathrm{fl}} = \frac{no.of\ photons\ emitted}{no.of\ photons\ absorbed} \qquad \text{(Eq. 2.8)}$$

Φ_{fl} primarily depends on the molecular structure of the dye, but is also influenced by external factors such as temperature,[194] viscosity,[195] polarity,[196] and pH[197] of the environment. The environment of a fluorophore can consist of solvent molecules or other dissolved substances, as well as coupled biomolecules or a cell membrane. Changes in fluorescence intensity allow the fluorescent dye to act as a molecular probe, providing insights into specific properties of the surrounding environment.[198]

2.5.2.1 Absolute and Relative Methods

The determination of Φ_{fl} is primarily achieved through two methods: absolute determination and relative determination. If every absorbed photon were re-emitted as fluorescence, the quantum yield would be 1 or 100%. In practice, however, non-radiative deactivation pathways always compete with fluorescence, causing a portion of the absorbed energy to be dissipated as heat. This heat release forms the basis for absolute quantum yield measurements using calorimetric techniques, such as the thermal blooming method.[199] While effective, these approaches require sophisticated experimental setups and rely on a solid theoretical framework for accurate design and interpretation of the results.[200]

For relative determination, the unknown quantum yield of a fluorophore is measured by comparing it to the known quantum yield of a standard or reference dye under the same experimental conditions, such as the geometry of the beam path (e.g. 90° or front face arrangement), detector gain, and the slit width (or bandpass) in a fluorescence spectrometer. In this thesis, Φ_{fl} is determined using the relative method. For accurate determination, both the sample and reference should exhibit identical absorption at the excitation wavelength, ensuring they absorb the same number of photons. The quotient of the integrated fluorescence spectra (*Int* = area of the fluorescence band) of both solutions, recorded under the same experimental conditions, gives the ratio of the quantum yields for both dyes, allowing for the straightforward calculation of the unknown quantum yield. Suppose different solvents are to be used for the sample and reference because of variations in solubility; this must be considered by incorporating the two refractive indices *n* in the calculation. The Φ_{fl} is given by Eq. 2.9, where Φ_S and Φ_R are the fluorescence quantum yields of the sample and reference, respectively. Int_S and Int_R represent the integrated fluorescence emission (area under the emission band) of

the sample and reference. A_S and A_R are the absorbance at the excitation wavelength, and n_S and n_R are the refractive indices of the solvent used for the sample and the reference.[198]

$$\Phi_S = \Phi_R \times \frac{Int_S}{Int_R} \times \frac{1 - 10^{-A_R}}{1 - 10^{-A_S}} \times \frac{{n_S}^2}{{n_R}^2} \quad \text{(Eq. 2.9)}$$

Additionally, to minimize reabsorption effects, the absorbance of the solution in a 1 cm cuvette should be kept below 0.05 for the determination of Φ_{fl}. At higher concentrations, internal filter effects can occur, which significantly falsify the measurement. In highly concentrated samples, the excitation light cannot fully penetrate the solution, thereby reducing the excitation of molecules located deeper in the cuvette. Also, some of the emitted fluorescence may be reabsorbed by other dye molecules in the path before reaching the detector. As a result, the recorded emission spectrum may appear artificially reduced, particularly on the short-wavelength side. It is also essential to consider how temperature affects the measurement results.[201]

2.5.2.1.1 Excitation Wavelength Selection in Relative Methods

The excitation wavelength of the sample and reference can be selected in two ways. One approach is to choose the wavelength at which the long-wavelength absorption bands of the sample and reference intersect. At this intersection point, both dyes exhibit equal absorbance despite their individual absorption maxima differing slightly. This is illustrated in Figure 2.8a: at 513.1 nm, the intersection of the absorption spectra of the sample (**ATTO 532** carboxy) and the reference (**ATTO 488** carboxy), both solutions show identical absorbance values (0.0183). Excitation of both sample and reference at this wavelength ensures equal photon absorption by both dyes, allowing for a more accurate and direct comparison of their fluorescence quantum yields.

The second approach involves exciting each dye at its respective absorption maximum. To ensure a valid comparison, both the sample and reference must exhibit identical absorbance at their individual excitation wavelengths. As shown in Figure 2.8b, **ATTO 532** carboxy and **ATTO 488** carboxy show the same absorbance value (0.0420) at 532 nm and 500 nm, respectively, and are chosen for the excitation. When using this method, it is essential to correct for differences in excitation light intensity at the two selected excitation wavelengths.[202] Modern fluorescence spectrometers address this issue by utilizing a calibrated photodiode to monitor the wavelength-dependent intensity of the excitation source and any fluctuations over time. This correction must be activated in the instrument software before data acquisition, as it cannot be applied after measurement. Additionally, the selected detection range should cover the entire emission profile of the fluorophore.[203]

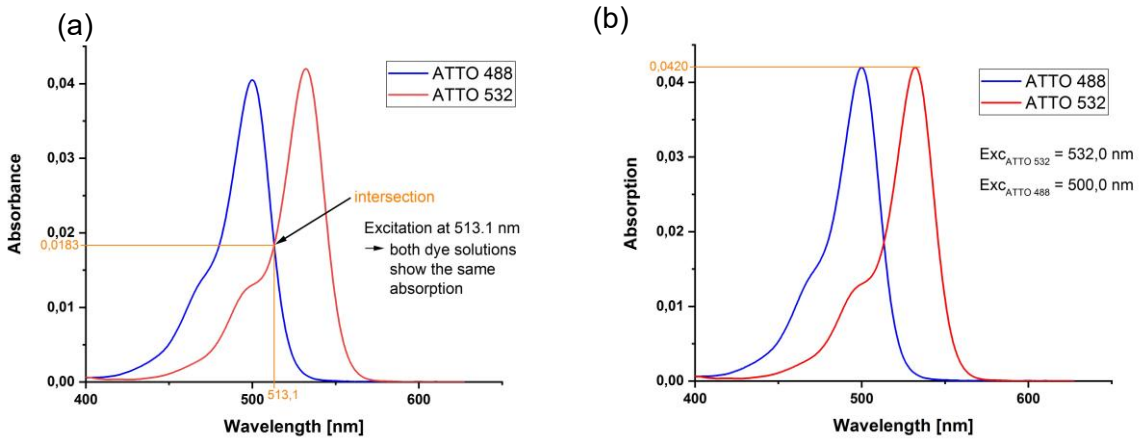

Figure 2.8. Absorption spectra of **ATTO 488** carboxy (blue) and **ATTO 532** carboxy (red) in PBS buffer. The spectra illustrate (a) identical absorbance at the intersection wavelength (513.1 nm) and (b) identical absorbance at the respective absorption maxima. Reprinted with permission from ATTO-TEC GmbH.[203]

2.5.3 Determination of Fluorescence Lifetime

Fluorescence lifetime (τ) refers to the time it takes for the number of excited molecules (n_1) to decrease to 1/e (about 37%) of its initial value. This is given by equation 2.10, where $n_1(t)$ denotes the number of excited-state molecules at time t, $n_1(0)$ is the initial population of excited molecules immediately after excitation, t is the elapsed time, and τ represents the fluorescence lifetime.[58] The time a photon stays in an excited state depends on the environment of the fluorescent probe, such as the solvent, temperature, and pH.[204]

$$n_1(t) = n_1(0)e^{(-t/\tau)} \qquad \text{(Eq. 2.10)}$$

The τ values for the fluorescent dyes were determined using the time-correlated single photon counting (TCSPC) technique. In this method, the sample is irradiated with periodic laser pulses, which serve as the start time. Fluorescence photons are emitted after excitation, and the exact period is measured until the first photon reaches the detector; this point is set as the end time. This time interval corresponds to the fluorescence lifetime (Figure 2.9).

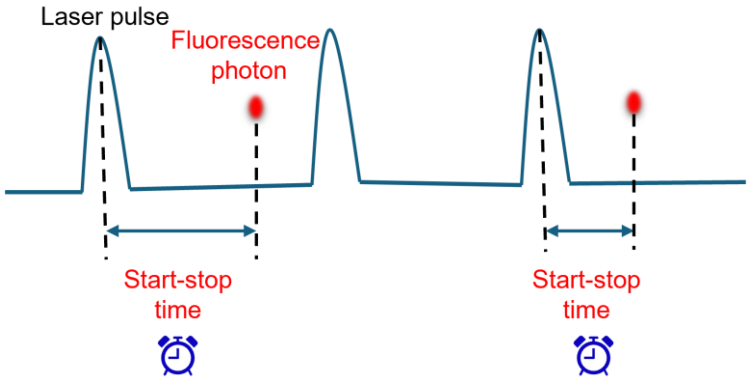

Figure 2.9. Principle of TCSPC: A laser pulse marks the start time, and the arrival of single photons at the detector defines the end time; the interval between them corresponds to the fluorescence lifetime (τ). Adapted from M. Wahl[205], with permission from PicoQuant GmbH.

By repeating this process over many excitation-emission cycles and collecting a statistically significant number of photon arrival times, a histogram of photon counts versus time is generated, from which the fluorescence decay profile can be reconstructed.[205]

Detectors and electronics have a dead time, during which no photon can be registered for at least a few nanoseconds after a photon event. TCSPC systems are typically designed to register about one photon per cycle. At a higher rate, the system often registers the first photon but misses the subsequent ones. This leads to an overrepresentation of early photons in the histogram, an effect known as pile-up, which significantly affects accuracy.[206]

In this thesis, the fluorescence lifetimes of the pH-sensitive dyes in solution were measured using a TemPro lifetime spectrometer. Typically, intense laser or semiconductor diodes are used as the excitation light source. In TemPro, a nano LED serves as the light source, with the wavelength selected based on spectral data. Additionally, choosing an appropriate cut-off filter helps to block scattered excitation light from reaching the detector.

The sample solutions are prepared with an absorbance of less than 0.1 at the 1 cm cuvette to prevent reabsorption and concentration quenching. It is also essential to keep the count rate below 2% of the repetition rate of the pulsed excitation light to avoid pile-up, and the detection time frame should be sufficiently long (≥10000 counts). The counting rate can be lowered by diluting the sample, inserting a neutral density filter in the excitation path to reduce light intensity, or by using a filter with a longer wavelength cut-off in the emission channel to limit the detected wavelength range.

To determine the instrument response function, which reflects the performance of the detection electronics, a scattering solution such as 0.01% Ludox AS40 colloidal silica in water is measured. This reference measurement can be used later during data analysis to correct for instrumental effects. The fluorescence decay of the sample is then fitted to a mathematical model. Theoretically, fluorescence decay follows a mono-exponential function, as expected for a first-order process similar to radioactive decay. However, a higher exponential curve can also yield a better fit for the measured points. This may be the case, for example, when multiple fluorescent species with varying lifetimes are present or when one species exists in two environments.[206] For multi-component processes, a multi-exponential fit is expected. The time-dependent fluorescence decay, $A(t)$, can be described as a sum of exponential functions (Eq. 2.11), where τ_i and a_i are the lifetime and amplitude of the i^{th} component, respectively

$$A(t) = \sum_i a_i * exp\left(\frac{-t}{\tau_i}\right) \qquad \text{(Eq. 2.11)}$$

Figure 2.10 illustrates an example of the lifetime measurement of a batch of **ATTO 647 N** carboxy using the TemPro device. A bi-exponential decay with χ^2 = 1.06 and a standard deviation uniformly distributed was selected as the most suitable fit. Here, the dominant lifetime component (3.55 ns) accounted for over 95% of the total amplitude, while the minor component

(1.77 ns) contributed less than 5%. Also, fitting the data with a mono-exponential model yielded a comparable χ^2 value of 1.08 and a lifetime of 3.5 ns, indicating that the inclusion of the minor component had minimal impact on the overall fit quality. Therefore, the lifetime of the dominant component, 3.5 ns, with a relative amplitude of 95.97%, is considered to represent the fluorescence decay time of **ATTO 647N** carboxy in aqueous solution (PBS, pH 7.4) at 22 °C.

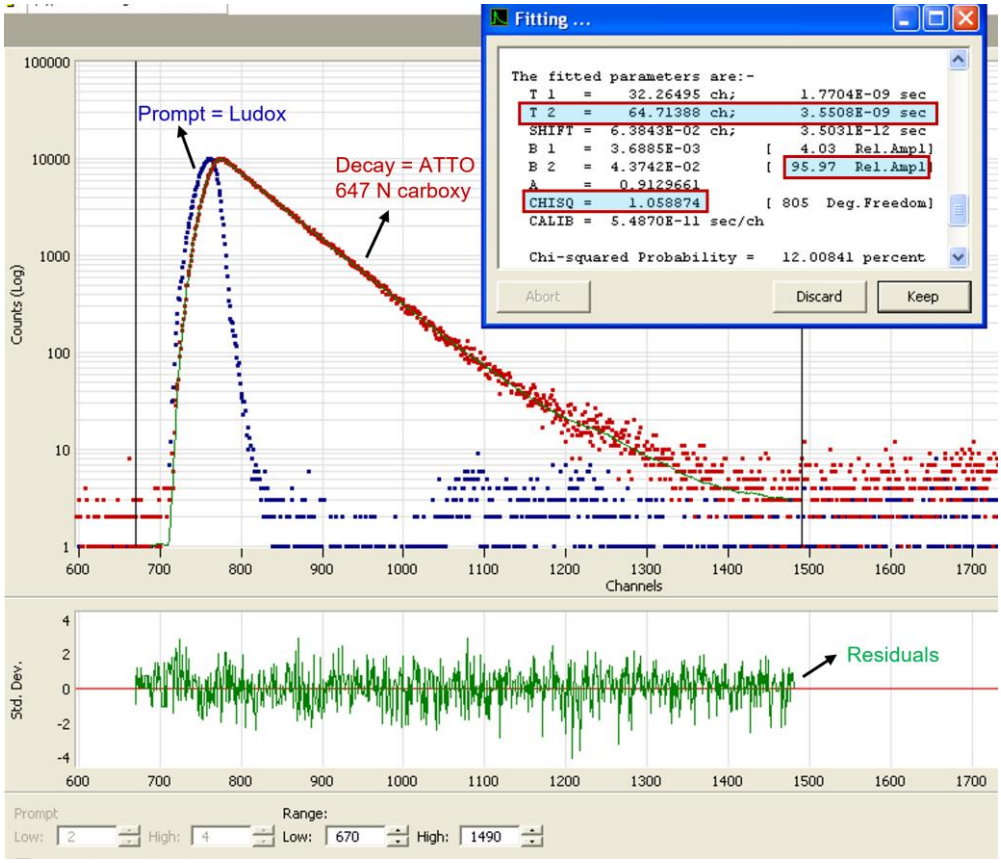

Figure 2.10. Fluorescence decay of **ATTO 647N** carboxy (red) fitted with a bi-exponential model. The prompt signal was recorded using Ludox (blue). Residuals indicate good fit quality (χ^2 = 1.06). The plot was generated from DAS analysis software (Horiba Scientific).

For the lifetime determination of carborhodols in chapters 4 and 5, biexponential fitting was employed. Although biexponential fitting was applied to the fluorescence decay data, the dominant component consistently exhibited a relative amplitude exceeding 95%. The lifetime associated with this major component was nearly identical to the value obtained from mono-exponential fitting. Therefore, the lifetime of the dominant species was used to represent the system's decay behavior. The minor component, contributing less than 5%, was considered negligible in this context. Details of the exceptions can be found in the respective chapter.

2.5.3.1 Fluorescence Lifetime Imaging Microscopy

For the fluorophore incorporated into polymer networks, Fluorescence Lifetime Imaging Microscopy (FLIM) is used to determine the lifetime of the fluorophore. The measurement of fluorescence lifetime using fluorescence decay curves with a confocal microscope is known as

FLIM, and lifetimes obtained at the pixel level are color-coded to create visual images. As a result, FLIM provides data on the spatial distribution of a fluorescent molecule, alongside details about its nano environment.[207] Fluorescence decay curves can be obtained through TCSPC. To implement time-domain detection in FLIM, a pulsed light source, such as a pulsed laser, should be installed on the microscope. For detection in scanning microscopy modes, a photomultiplier tube (PMT) along with dedicated TCSPC electronics or a gated detection system is required.[208] The sample, usually fixed on a glass slide, is illuminated with a pulsed laser that has a specific wavelength and pulse rate. A selected region of the sample is scanned line by line, and TCSPC histograms are generated for each pixel. Details of FLIM measurements with dye-incorporated hydrogel will be discussed in more detail in Chapter 7.

3 Synthesis and Characterization of Novel pH-Sensitive Carborhodol Dyes

The substitution of one of the amine groups in carbopyronine dyes with an oxygen atom yields the hybrid carborhodol dye. This chapter describes the design and synthesis of nine novel carborhodol dyes through hydrolytic deamination of carbopyronine precursors in aqueous hydroxide solutions. This one-step transformation requires the presence of a dimethyl amino group at one terminal position of the carbopyronine chromophore. Halogenated derivatives were synthesized to enhance photostability, while carboxylic acid-functionalized compounds were converted into reactive esters suitable for bioconjugation. Quinoline-derived units were introduced to increase molecular rigidity and improve photophysical properties. Additionally, the introduction of sulfonic acid groups enhanced the hydrophilicity of the dye. Notably, this synthetic approach also enables the simultaneous formation of carborhodol and carborhopyronine products, thereby increasing overall synthetic efficiency and utility.[i]

3.1 Introduction and Objective

Asymmetric hybrid fluorophores are created by combining structural motifs from two or more symmetric dyes, often resulting in novel properties that are not present in the original parent compounds.[209] One such example is the carborhodol dye, which arises from the combination of fluorescein and carbopyronine scaffolds (Figure 3.1).[40] The replacement of the oxygen atom at the C-10 position with a quaternary carbon results in an orange-red emission, thereby reducing cellular autofluorescence, making the uncharged carborhodol dyes particularly well-suited for microscopy applications compared to conventional xanthene dyes.[210]

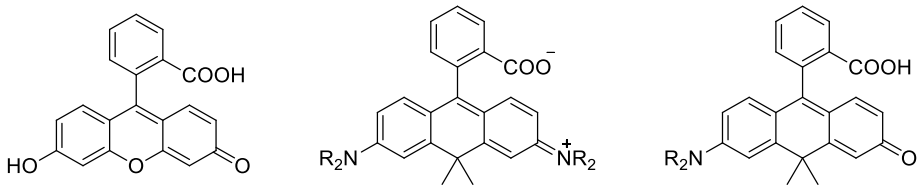

Fluorescein Carbopyronine Carborhodol

Figure 3.1. General structures of fluorescein, carbopyronine, and carborhodol.

The symmetrical nature of xanthene dyes allows for their one-pot synthesis from phthalic anhydride and two equivalents of either a 3-dialkylaminophenol (used for rhodamine)[211] or a

[i] The carbopyronine precursors **AZ 229**, **AZ 234**, **AZ 43**, **AZ 481**, and **AZ 129** were synthesized by Dr. Alexander Zilles (ATTO-TEC GmbH) and were directly used for the conversion. The re-synthesis of **AZ 233** was carried out as part of this thesis.

resorcinol (used for fluorescein).[212] The synthesis of carborhodol dyes requires the introduction of a carbon bridge to the asymmetrically substituted substrate, which makes it challenging and requires a multi-step process.[39] The synthesis of carborhodols was first reported by Sednev et al. in 2013 (Scheme 3.1).[40] They performed a twelve-step synthesis that begins with the coupling of 3-bromoanisole (**1**) and 4-nitrobenzoyl chloride in the presence of a Lewis acid, followed by the reduction of the nitro group, yielding ketone **3**. Due to challenges with ketal protection, the keto group was fully reduced after methylation of the amino group. Subsequently, ring closure, oxidation, and arylation produced the methylated rhodol molecule **9**, which, after amidation and subsequent demethylation, results in carborhodol **12** with an overall yield of 1.6%. However, the requirement for halogen-lithium exchange at two key steps limits the synthetic versatility, and employing butyllithium requires specific protecting groups that can withstand this reagent. The resulting compound **12** was primarily utilized for two-color fluorescence imaging.

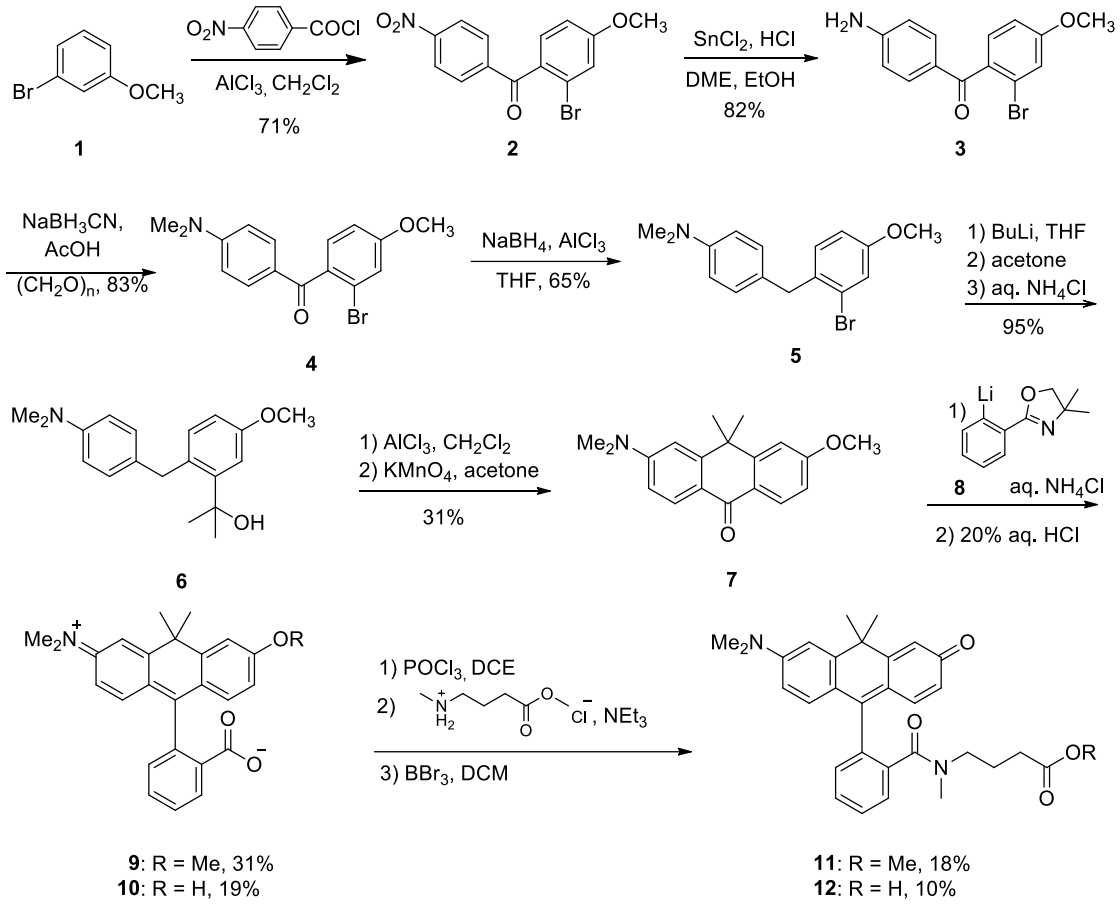

9: R = Me, 31%
10: R = H, 19%

11: R = Me, 18%
12: R = H, 10%

Scheme 3.1. General approach to the synthesis of carborhodols.[40]

Later in 2018, Jia et al. reported an alternative synthetic approach towards the carborhodol skeleton (Scheme 3.2).[41] Copper probes were developed by attaching an arylmetal species with a copper-binding receptor to a carborhodol derivative. These probes show selective turn-on responses upon Cu^{+} binding. In the synthesis process, the Negishi cross-coupling of methyl

2-bromo-5-methoxybenzoate and 4-methoxybenzylzinc chloride yielded methyl benzylbenzoate **13**. Subsequently, ring closure and demethylation produced **15**, followed by a DDQ-mediated oxidation reaction to give dihydroxy-carboxanthone **16**. The conversion of the latter to the corresponding ditriflate **17** with $NPhTf_2$ and a subsequent nucleophilic aromatic substitution with morpholine resulted in the monoamino-substituted carboxanthone **18**. Hydrolysis of the triflate group, followed by protection of the hydroxyl group with TBDMSCl, arylation, and deprotection, led to carborhodol **19**.

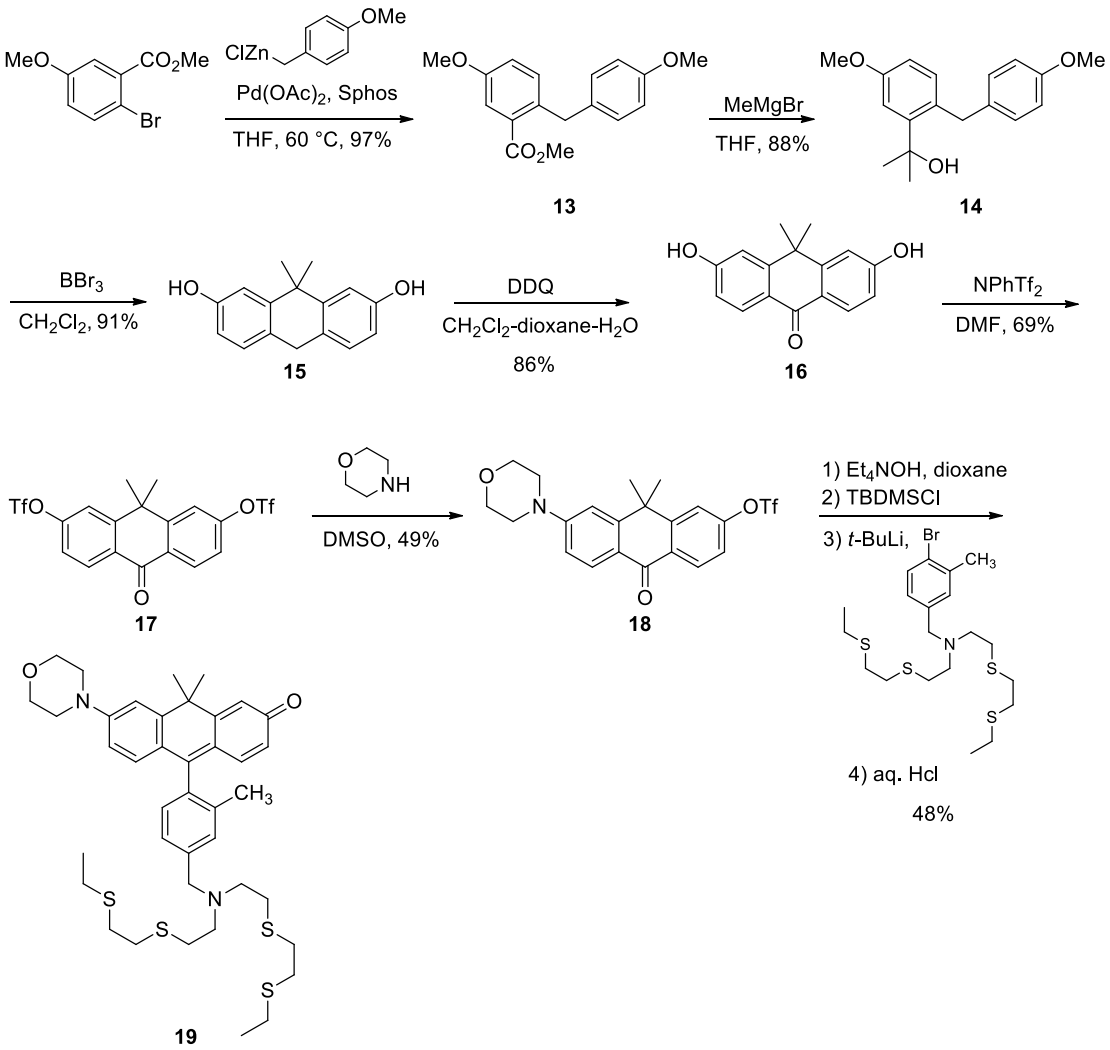

Scheme 3.2. Synthesis of carborhodol-based copper sensors.[41]

Although Sednev et al.[40] discuss the pH equilibrium of carborhodols, which closely resembles that of the well-known rhodols, they do not provide any reference to the application or suitability of these dyes as pH sensors or for ratiometric measurements. For the acidic form, no optical data is available, and the pK_a value is unknown. Knowing that the pK_a of reported rhodols ranges from 4.5 to 7,[38] and assuming that the pK_a of carborhodols should also fall within this range, which is suitable for the detection of wound infections, motivates the

synthesis of various carborhodols with different functionalities. The overall aim is to synthesize photostable carborhodols capable of detecting clinically relevant pH changes. The primary objectives include, firstly, the preparation of halogenated carborhodols, with an aim to improve photostability, as fluorinated analogs of fluorescein (e.g., Oregon Green) are known to exhibit significantly better photostability than the parent fluorophore,[213] and secondly, the introduction of coupling groups for covalently linking the compound to a scaffold. The third goal was to introduce particular quinoline units into the fluorophore to increase rigidity, photostability, and fluorescence quantum yields.[214] Apart from the previously mentioned syntheses, no methods have been reported for synthesizing carborhodol derivatives. Additionally, Sednev et al. could not synthesize fluorinated carborhodol dyes using their approach. Therefore, there is strong motivation to develop shorter and more efficient synthetic routes that enable the preparation of a diverse array of carborhodols with varied functionalities in high yields.

3.2 Results and Discussion

The first synthetic approach developed in this thesis involved the coupling of a methoxy fragment with an amine fragment, introducing both ends of the chromophore at an early stage, followed by ring closure and arylation to produce the corresponding carborhodol. This strategy aimed to reduce the number of synthetic steps and offer flexibility to introduce different heterocyclic amines, such as tetrahydroisoquinoline and julolidine.

Based on this approach, the synthesis proceeded as follows. The reduction of 2-bromo-4-methoxy-benzaldehyde provided the corresponding benzylic alcohol **20**, while the alkylation of 2,2,4-trimethyl-1,2-dihydroquinoline yielded the quinoline fragment **21** (Scheme 3.3). Coupling of **20** with **21** was attempted in the presence of BCl_3. As confirmed by mass spectrometry, the product **22** was formed; however, various column chromatography methods failed to purify the crude product. A second coupling attempt using glacial acetic acid did not lead to any reaction.

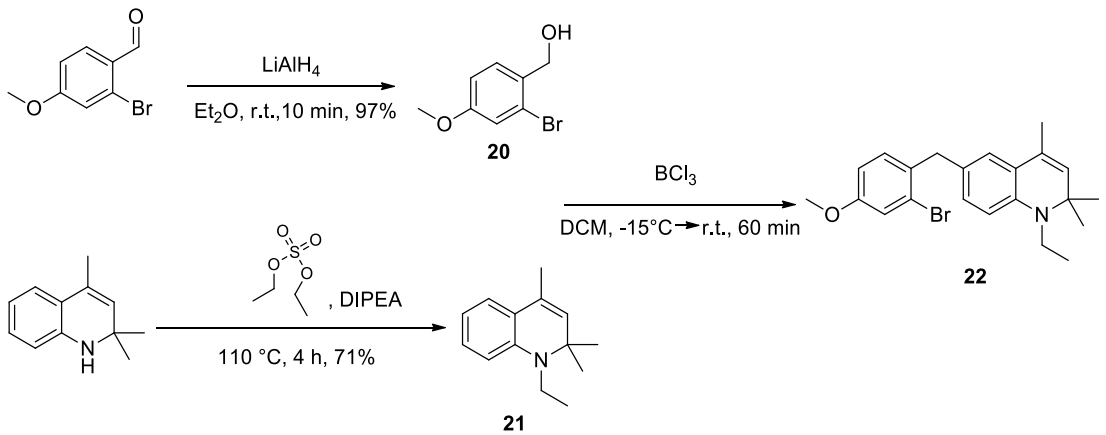

Scheme 3.3. Attempts to prepare the carborhodol precursor **22**.

The alkaline hydrolysis of rhodamines to rhodols has been previously reported; however, this transformation is generally characterized by prolonged reaction times and low yields (<30%), but interestingly, further hydrolysis to fluorescein is not observed.[84,215] Later, Grzybowski et al., reported the synthesis of P=O-bridged rhodols through the hydrolysis of P=O rhodamines in basic aqueous solutions, achieving yields of up to 93%.[216] Moreover, prolonged exposure to aqueous basic conditions generates P=O-bridged fluoresceins. In this context, the alkaline hydrolysis of different carbopyronines to produce carborhodols directly, without further hydrolysis to carboxyfluorescein, was attempted, and the reaction conditions were optimized.

Using this synthetic approach, the preparation of the following nine carborhodols was possible for the first time. Furthermore, the previously reported carborhodol **AS 11**, described by Sednev et al., was also synthesized under the proposed reaction conditions (Figure 3.2).

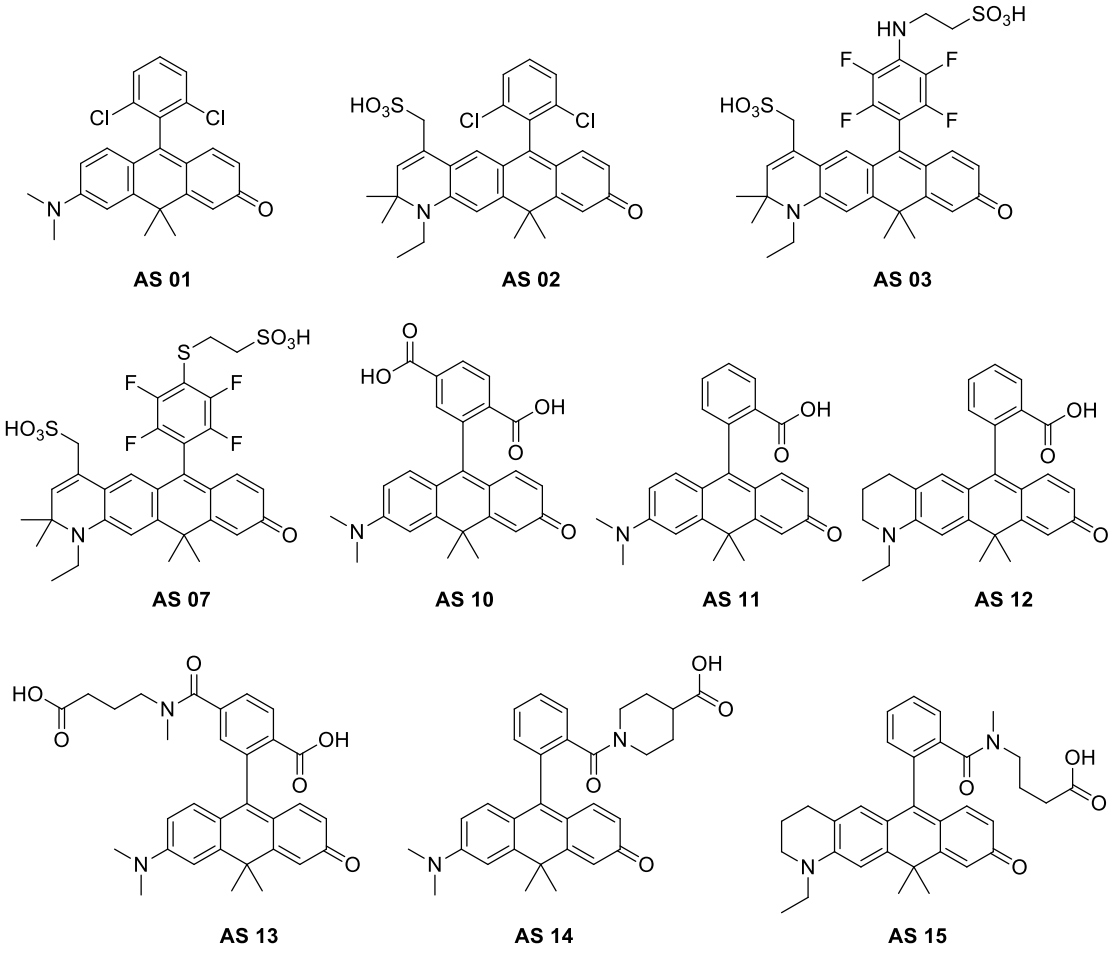

Figure 3.2. Structures of synthesized carborhodol derivatives.

This strategy enabled the efficient synthesis of carborhodol derivatives with aryl head groups (halogenated) and coupling functionalities, with isolated yields reaching up to 70%. Additionally, this synthesis route enabled the simultaneous production of two valuable dyes:

the precursor carbopyronine and the product carborhodol. The only prerequisite for this simple one-step reaction is the presence of a dimethylamino group, at least at one terminal end of the chromophoric system of the parent carbopyronine compound, as shown in the following examples of precursors used for the preparation (Table 3.1).

Table 3.1. Carbopyronine precursor compounds used for the carborhodol synthesis.

Compound	Structure	Precursor of
AZ 229	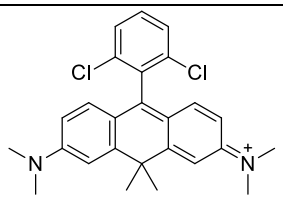	**AS 01**
AZ 234	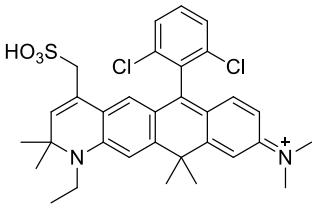	**AS 02**
AZ 233	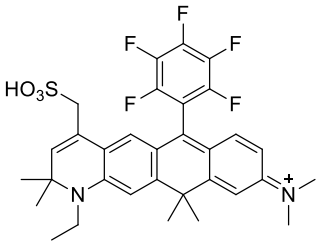	**AS 03 and AS 07** In an intermediate step, the *para*-fluorine is substituted by taurine (**AS 03**) or 2-mercaptoethansulfonic acid (**AS 07**).
AZ 481	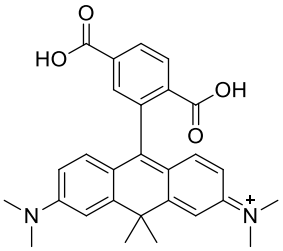	**AS 10**
AZ 43	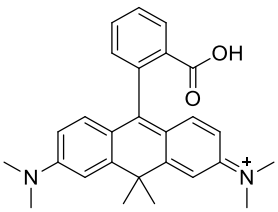	**AS 11**
AZ 129	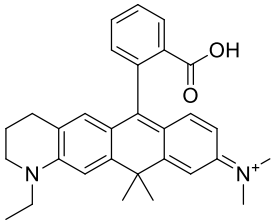	**AS 12**

The ATTO-TEC research group has previously optimized the synthesis of carbopyronines, which can generally be achieved through two different synthetic routes.

Carbopyronine dyes bearing halogenated aryl head groups (e.g., **AZ 229**, **AZ 233**, **and AZ 234**) were synthesized through the coupling of a quinoline derivative (compound **A**) with a halogen-substituted phenol (compound **B**) in glacial acetic acid. The resulting intermediate undergoes sulfonation and partial oxidation upon treatment with concentrated sulfuric acid. Final oxidation and aromatization are accomplished using *p*-chloranil, yielding the fully conjugated carbopyronine chromophore **C** (Scheme 3.4).

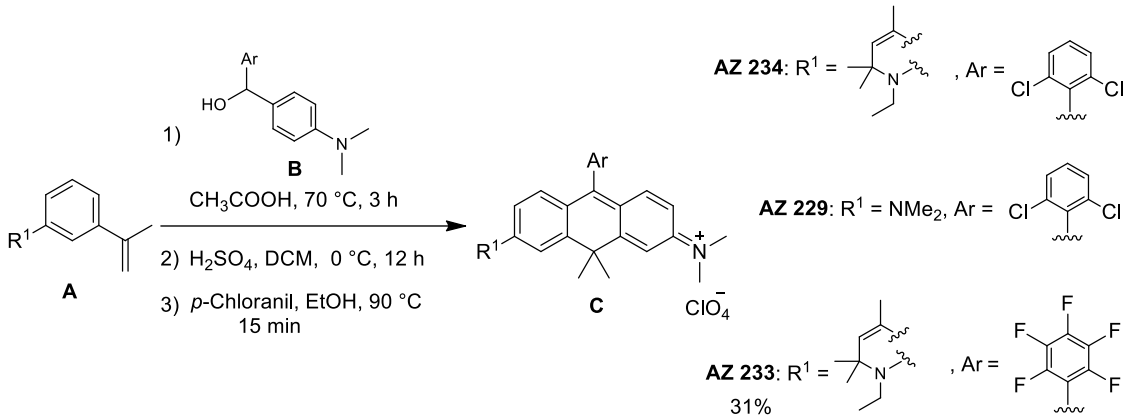

Scheme 3.4. Synthesis of carbopyronine dyes bearing halogenated aryl head groups.

Fragments **A** and **B** were synthesized from readily available commercial starting materials. For the preparation of fragment **A** used in **AZ 233** and **AZ 234**, an iodine-mediated conjugate addition of the 3-bromoaniline to mesityl oxide afforded the dihydroquinoline intermediate **23**. Subsequent ethylation produced compound **24**. Lithiation of **24** with *n*-BuLi in Et_2O, followed by condensation with acetone and acidic work-up, yielded the benzylic alcohol **25**. Finally, dehydration using $KHSO_4$ at elevated temperature produced the precursor **26** in 96% yield (Scheme 3.5).

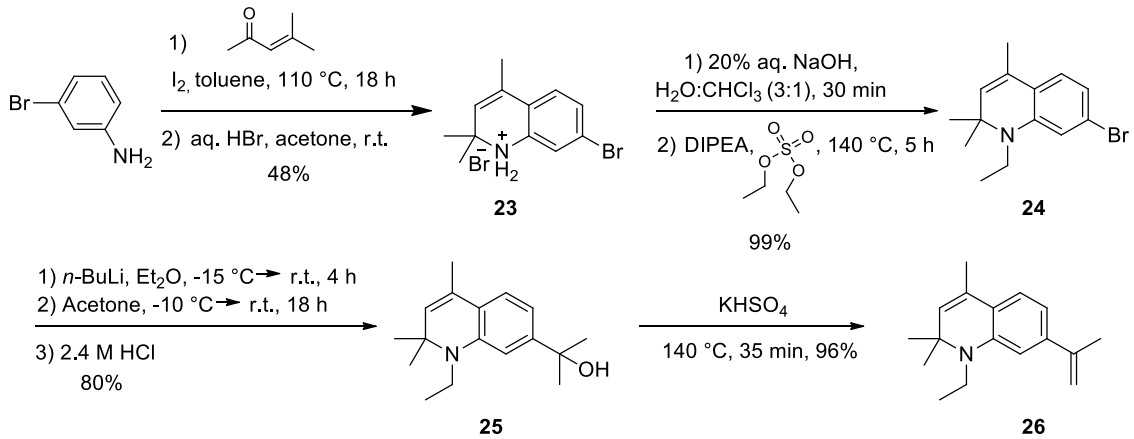

Scheme 3.5. Synthetic route to fragment **A** used in **AZ 233** and **AZ 234** preparation.

Fragment **A** for **AZ 229** was synthesized via a two-step sequence starting from the corresponding methyl ketone derivative. A Grignard reaction yielded secondary alcohol **27,** and subsequent dehydration using $KHSO_4$ afforded 3-isopropenyl-*N*,*N*-dimethylaniline (**28**) in 93% yield (Scheme 3.6).

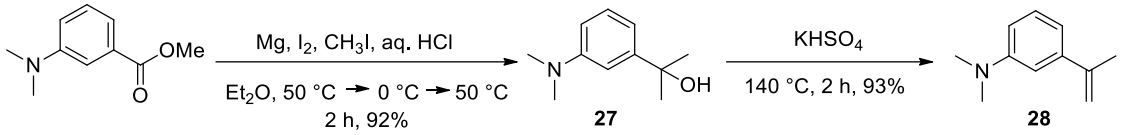

Scheme 3.6. Synthetic route to fragment **A** used in **AZ 229** preparation.

Fragment **B** derivatives were prepared through a Grignard reaction of the N-methylated bromoaniline with the corresponding aryl aldehydes, yielding **29a** and **29b**. The benzylic alcohols **29a**, which bear a dichlorinated aryl moiety, were used in the synthesis of **AZ 229** and **AZ 234**, while **29b**, which contains a perfluorinated aryl group, was specific to **AZ 233** (Scheme 3.7).

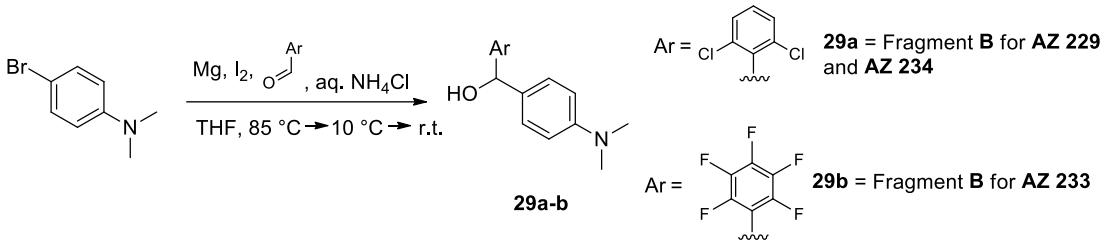

Scheme 3.7. Synthesis of fragment **B** for **AZ 229**, **AZ 233**, and **AZ 234**.

The synthesis of precursors **AZ 43**, **AZ 481**, and **AZ 129** proceeds through an anthrone intermediate (Scheme 3.8). The synthetic route begins with the reduction of a *para*-substituted benzaldehyde, which produces the corresponding benzyl alcohol **30**. This intermediate undergoes a Friedel-Crafts alkylation with 3-isopropenyl-*N*,*N*-dimethylaniline (**28**) in the presence of BCl_3 as a Lewis acid catalyst. The resulting alkylated product subsequently undergoes intramolecular cyclization upon treatment with H_3PO_4, forming the leuco compound **31**. Oxidation of **31** using $KMnO_4$ furnishes the corresponding anthrone derivative **32**. This keto intermediate is then subjected to an arylation reaction with an appropriate oxazolone derivative (either **33a** or **33b**, depending on the target dye) in the presence of *t*-BuLi. The final step involves hydrolysis of the arylated intermediate, affording the fluorescent dyes **AZ 43**, **AZ 481**, or **AZ 129**.

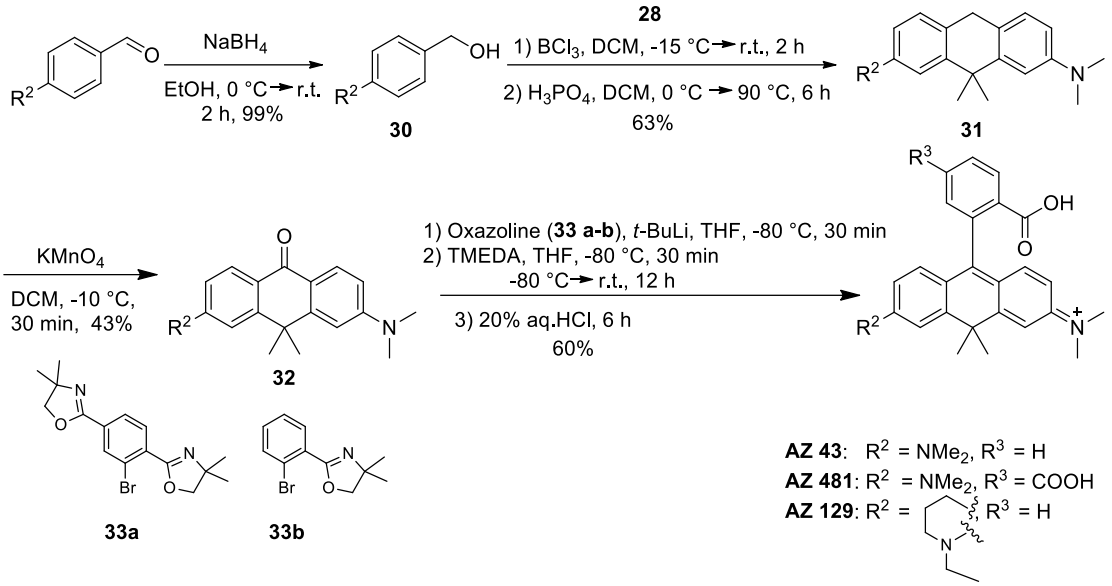

Scheme 3.8. Synthetic route for the preparation of **AZ 43**, **AZ 481**, and **AZ 129**.

Any alkaline or alkaline earth hydroxide, such as lithium, sodium, potassium, cesium, calcium, or barium hydroxide, can be used for the conversion of carbopyronines to carborhodols. Lithium, sodium, and potassium hydroxide are preferred because of their higher reactivity. The direct precursor compound is dissolved in an aqueous hydroxide solution. Organic solvents, such as ethanol, methanol, acetone, or acetonitrile, can be used as co-solvents to enhance the solubility of the reactants. The reaction time depends on the concentration of the reactants (precursor and alkali) and the temperature. The best results were obtained with temperatures between 50 and 90 °C.

For the synthesis of **AS 01** and **AS 02**, the carbopyronine derivatives **AZ 229** and **AZ 234** were each dissolved in a 1:1 mixture of 0.1 M aqueous LiOH and ethanol, and the reaction mixture was stirred at 90 °C. Under these conditions, both precursors were efficiently converted to the corresponding carborhodols (Scheme 3.9a, shows the synthesis of **AS 01**).

However, several side reactions were observed when the same protocol was applied to **AZ 233**. Specifically, nucleophilic substitution at the *para*-fluorine position led to the formation of hydroxylated and ethoxylated byproducts. Additionally, the leaving of the head group generated the corresponding anthrone, alongside the desired carborhodol. The formation of these byproducts was confirmed by mass spectrometric analysis. To overcome these side reactions, **AZ 233** reacted with sodium 2-mercaptoethanesulfonate to produce **AS 06**. A separate reaction with 2-aminoethanesulfonic acid (taurine) afforded **AZ 444**. These modifications prevented undesired nucleophilic substitutions at the fluorine site, allowing for the selective formation of the carborhodol product without significant formation of side products (Scheme 3.9b shows the synthesis of **AS 07**).

Although some anthrone formation persisted, lowering the reaction temperature to 50 °C partially suppressed this pathway. Due to the distinct polarity difference between the anthrone and carborhodols, chromatographic separation was straightforward. Moreover, introducing sulfonic acid moieties improved the overall hydrophilicity of the resulting compounds (Scheme 3.9; one representative example from each synthetic route is shown).

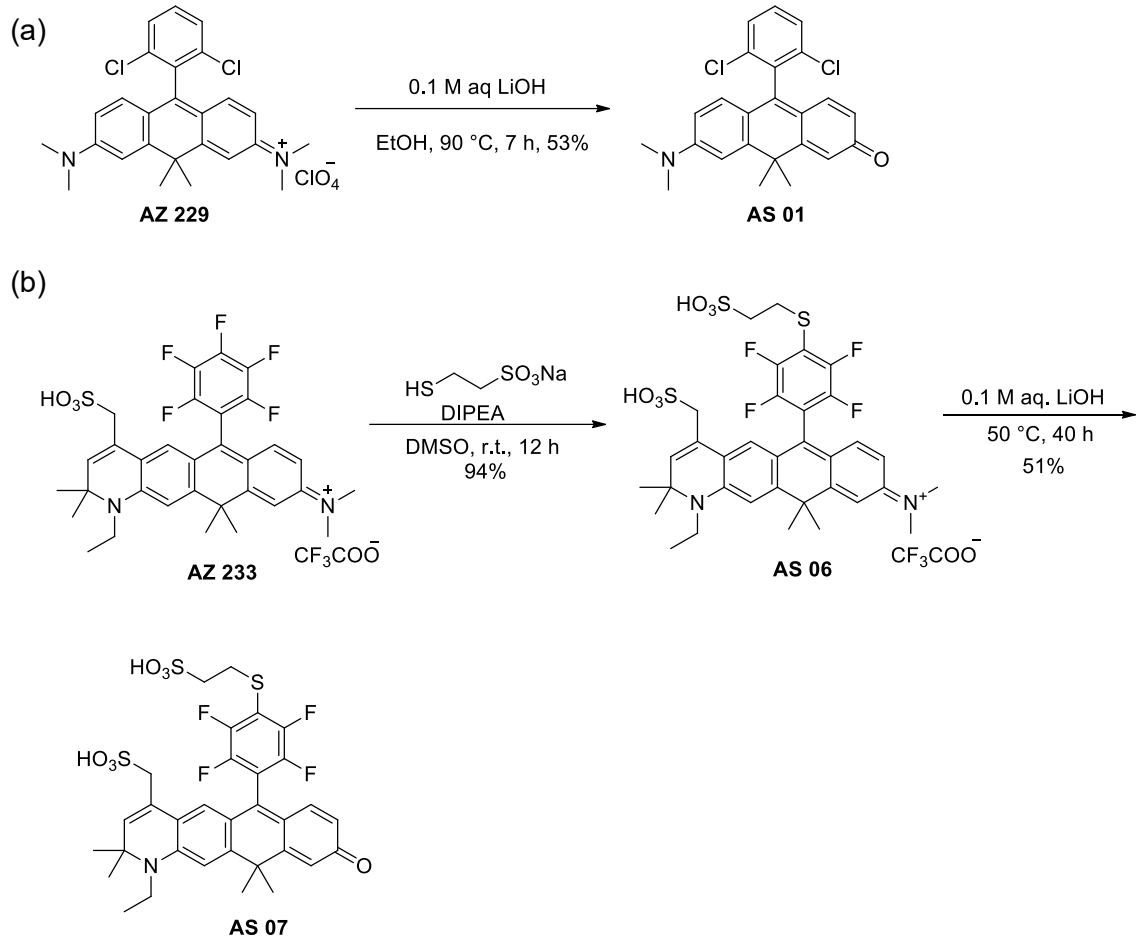

Scheme 3.9. Synthesis of (a) **AS 01** and (b) **AS 07**.

To introduce functional groups suitable for covalent binding to an analyte, carbopyronine derivatives bearing carboxylic acid groups at the aryl substituents (**AZ 43**, **AZ 129**, and **AZ 481**) were selected as precursors. These compounds were treated with a 1:1 mixture of 2.5 M aq. NaOH and ethanol at 85 °C. NaOH, being more reactive than LiOH, facilitated a faster conversion under these conditions. As a result, **AZ 481**, **AZ 43**, and **AZ 129** were successfully converted into the corresponding carborhodol derivatives **AS 10**, **AS 11**, and **AS 12**, respectively (Schemes 3.10 and 3.11).

To prevent the formation of the colorless spirolactone form, often undesirable for fluorescence applications, the *ortho*-carboxylic acid groups of **AS 11** and **AS 12** were further functionalized. Specifically, **AS 11** was modified using piperidine-4-carboxylic acid to yield

AS 14, while **AS 12** was derivatized with methyl 4-(methylamino)butanoate to give **AS 15**. Multiple attempts to directly generate active esters from **AS 11** and **AS 12** were unsuccessful. Consequently, these elongations were carried out via the corresponding acid chloride intermediates. The resulting elongated compounds **AS 14** and **AS 15** were then converted into their respective active esters for coupling applications (Scheme 3.10).

In contrast, for **AS 10**, the NHS ester formation was feasible at the *meta*-carboxylic acid position. Subsequent elongation of this NHS ester with 4-(methylamino) butyric acid furnished the derivative **AS 13** (Scheme 3.11).

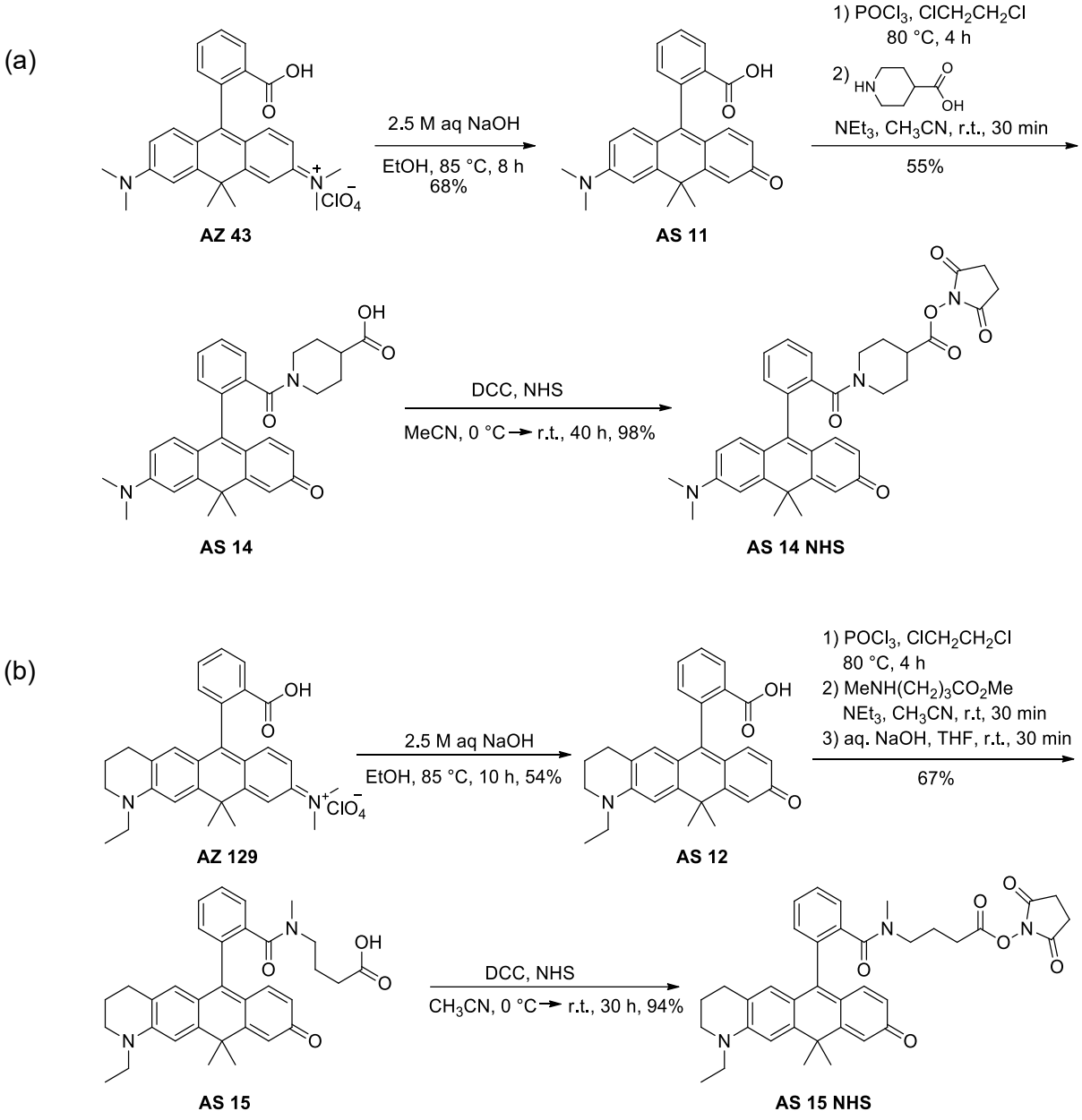

Scheme 3.10. Synthesis of the NHS ester derivatives of (a) **AS 14**, (b) **AS 15**.

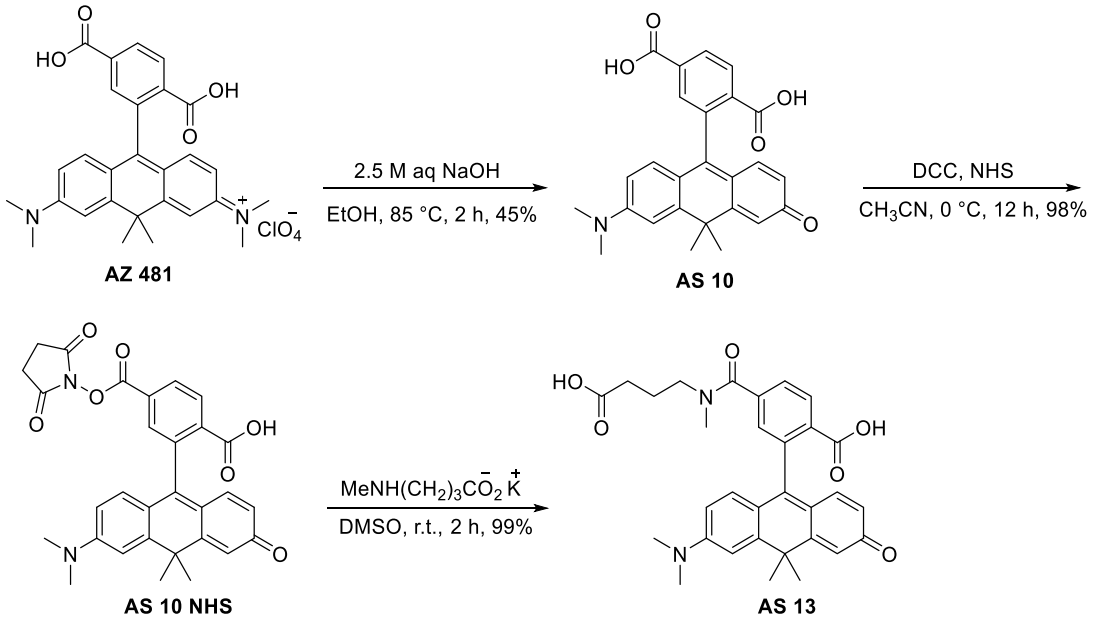

Scheme 3.11. Synthesis of **AS 13**.

3.3 Conclusion and Outlook

In this study, nine novel carborhodols, along with the previously reported carborhodol **AS 11** (as described by Sednev et al.), were successfully synthesized via a straightforward hydrolytic deamination of the corresponding economically produced carbopyronine precursors under basic conditions. The key requirement for this one-step transformation is the presence of a dimethyl amino substituent at at least one terminal position of the carbopyronine chromophoric system. Structural confirmation of the synthesized compounds was achieved through NMR spectroscopic analysis (^{1}H, ^{13}C,^{19}F, COSY, HSQC, HMBC) and mass spectrometry.

This synthetic approach enabled the efficient preparation of halogenated carborhodols, which are promising candidates for dye molecules with improved photostability. Additionally, carborhodols bearing carboxylic acid functionalities were obtained and successfully converted into reactive esters for covalent conjugation to analytes. Quinoline-derived structural elements such as tetrahydroquinoline were incorporated to enhance the photophysical properties, offering increased molecular rigidity and the potential for improved photostability and fluorescence quantum yields. Moreover, *para*-fluorine substitution with sulfonic acid derivatives improved the hydrophilicity of the resulting dyes, which is advantageous for biological applications. The ability to obtain both carborhodol and carbopyronine products in a single process further increases the practicality of this strategy.

These results establish a chemical foundation for subsequent pH sensor application of the resulting carborhodols. Following the evaluation of their pH-responsive behavior (see Chapter 4), further application of these dyes is envisioned through either physical encapsulation or chemical incorporation into polymer-based systems. Hydrophilic derivatives

such as **AS 03** and **AS 07** are well-suited for integration into vesicular carriers like polymersomes (see Chapter 6), while the reactive ester-functionalized compounds **AS 14** and **AS 15** offer potential for covalent attachment within hydrogel networks (see Chapter 7).

3.4 Experimental Section

The carbopyronine precursors **AZ 229**, **AZ 234**, **AZ 43**, **AZ 481**, and **AZ 129** were synthesized by Dr. Alexander Zilles and were directly used for the conversion. The re-synthesis of **AZ 233** was carried out.

3.4.1 Equipment

NMR spectra were recorded with a Jeol ECZ 500 (^{1}H: 500 MHz, ^{13}C: 125 MHz, and ^{19}F: 470 MHz) at 25 °C. Spectra were analyzed with the software Mestre Nova (version: 12.0.3) and referenced to the respective solvents DMSO-d_6 (^{1}H = 2.50, ^{13}C = 39.5), CD_3OD (^{1}H = 3.31, ^{13}C = 49.0), and $CDCl_3$ ($_{1}$H = 7.26, ^{13}C = 77.1). Chemical shifts are given in ppm.

Mass spectra were recorded using an Agilent 1260 Infinity II liquid chromatography system coupled with an Agilent LC/MSD XT mass selective detector. The Electrospray Ionization (ESI) source operated at a capillary voltage of 4 kV, with nitrogen as the working gas. The capillary temperature was set to 300 °C. Chromatographic separation was achieved at a flow rate of 0.5 mL/min, while the column temperature was maintained at 30 °C.

High-performance liquid chromatography (HPLC) analysis was conducted using an Agilent 1260 Infinity system equipped with a quaternary pump (G1311B), a diode array detector (DAD; G1315D), a column compartment with temperature control (25 °C), and an autosampler with an injection valve. Chromatographic separation was achieved on a Poroshell 120 EC-C18 column (3×100 mm, particle size 2.7 µm, pressure limit 1000 bar). The mobile phase consisted of solvent A (acetonitrile) and solvent B (water containing 0.1% trifluoroacetic acid, TFA). The flow rate was set to 0.7 mL/min, and detection was performed via UV absorbance using the DAD module.

Reversed-phase chromatography was carried out using a YMC-DispoPack AT ODS-25 column packed with C18-modified silica (particle size: 25 µm). The separation was performed at a flow rate of 10 mL/min using a gradient elution system composed of acetonitrile and water, containing 0.01% trifluoroacetic acid (TFA). Fractions corresponding to the target compound were collected based on retention time and further analyzed by thin-layer chromatography (TLC) and high-performance liquid chromatography (HPLC) for purity assessment.

The synthesis and characterization of the compounds are described in the synthesis section, and the corresponding NMR spectra are provided in the Appendix associated with this chapter.

3.4.2 Synthesis

(2-Bromo-4-methoxyphenyl)methanol (**20**)

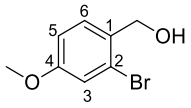

To a suspension of $LiAlH_4$ (2.58 g, 68.0 mmol) in Et_2O (100 mL), a solution of 2-bromo-4-methoxy-benzaldehyde (22.0 g, 97.2 mmol) in Et_2O (400 mL) was added dropwise over 2 hours. Gas evolution was observed at the dropping point. The reaction mixture was stirred at room temperature for 10 minutes before being cooled in an ice/methanol bath. Subsequently, the reaction was quenched by slowly adding an aqueous sodium hydroxide solution (*w* = 5%, 30 mL) over the course of 30 minutes. The precipitate was filtered and washed with Et_2O (3 × 40 mL). The combined organic layers were dried over anhydrous Na_2SO_4, filtered, and concentrated under reduced pressure. The product **20** was obtained as a yellowish oil (20.5 g, 94.4 mmol, 97%)

^{1}H-NMR (500 MHz, $CDCl_3$): δ = 2.29 (t, ^3J = 7 Hz, 1 H, 1-CH_2O<u>H</u>), 3.78 (s, 3 H, 4-OCH_3), 4.65 (d, ^3J = 7 Hz, 2 H, 1-CH_2), 6.84 (dd, ^3J = 8 Hz, ^4J = 2 Hz, 1 H, 5-H), 7.09 (d, ^4J = 2 Hz, 1 H,3- H), 7.33 (d, ^3J = 8 Hz, 1 H, 6-H).

7-Bromo-2,2,4-trimethyl-1,2-dihydroquinoline hydrobromide (**23**)

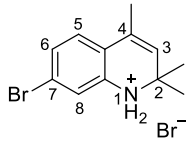

Iodine (17.5 g, 69.0 mmol) was added to a reaction mixture of 3-bromoaniline (95.0 mL, 872 mmol) and mesityl oxide (200 mL, 1.74 mol) under a nitrogen atmosphere. Toluene (400 mL) was added dropwise over 1 hour. The resulting brown solution was heated to 110 °C and stirred for 18 hours. Upon completion, the reaction mixture was cooled to room temperature and concentrated under reduced pressure using rotary evaporation. The crude product was purified by flash chromatography. The collected fractions were concentrated and dissolved in acetone (1000 mL). Aqueous HBr (*w* = 48%, 85 mL) was then added dropwise, resulting in precipitation of the product as its hydrobromide salt, yielding compound **23** as a brown solid (140 g, 420 mmol, 48%).

^{1}H-NMR (80 MHz, $CDCl_3$): δ = 1.71 (s, 6 H, 2-$(CH_3)_2$), 2.09 (d, ^4J = 2 Hz, 3 H, 4-CH_3), 5.68 (d, ^4J = 2 Hz, 1 H, 3-H), 7.24 (d, ^3J = 8 Hz, 1 H, 5-H), 7.59 (dd, ^3J = 8 Hz, ^4J = 2 Hz, 1 H, 6-H), 8.17 (d, ^4J = 2 Hz, 1 H, 8-H).

(9-(Dimethylamino)-1-ethyl-2,2,11,11-tetramethyl-6-(perfluorophenyl)-1,2,11,12a tetrahydronaphtho[2,3-*g*] quinolin-4-yl)methanesulfonic acid (**AZ 233**)

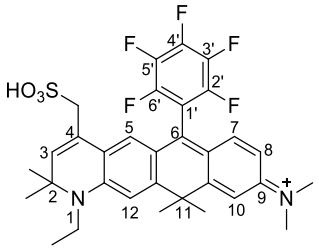

Glacial acetic acid (12 mL) was added to a reaction mixture containing 1-ethyl-2,2,4-trimethyl-7-isopropenyl-1,2-dihydronaphthalene (**A)** (760 mg, 3.15 mmol) and [4-(dimethylamino)phenyl](perfluorophenyl)methanol (**B**) (1.00 g, 3.15 mmol). The brown reaction mixture was stirred for 3 h at 70 °C (TLC control). After cooling to 0 °C, aq. NaOH (*c* = 1 M, 10 mL) and dichloromethane (DCM) (20 mL) were added. The aqueous phase was extracted with DCM (3 × 20 mL), dried over anhydrous Na_2SO_4, and concentrated under reduced pressure. The crude product was redissolved in DCM (20 mL) and added dropwise to concentrated H_2SO_4 (*w* = 96%, 7 mL) at 0 °C under vigorous stirring.

After 12 h, the DCM was removed under reduced pressure. For further oxidation, the crude product was dissolved in ethanol (10 mL) and added to a solution of *p*-chloranil (660 mg, 2.68 mmol) in ethanol (40 mL). The reaction mixture was refluxed at 90 °C for 15 minutes, during which it turned green. After cooling, water (50 mL) and DCM (100 mL) were added, and the product was extracted with DCM. The organic layer was dried over anhydrous Na_2SO_4 and concentrated under reduced pressure. The product **AZ 233** was isolated by reverse phase column chromatography (C18 modified SiO_2, 120 g; H_2O/CH_3CN/TFA 7/3/0.001) as a green solid (695 mg, 966 µmol, 31%).

HPLC: CH_3CN/ H_2O + 0.1 v/v% TFA = 30/70 to 95/5 in 30 min, detection at 676 nm, t_R = 7.17 min (>99%).

^{1}H-NMR (500 MHz, $CDCl_3$): δ = 1.41 (t, ^3J = 7 Hz, 3 H, 1-CH_2-C<u>H</u>$_3$),1.54 (s, 6 H, 2-$(CH_3)_2$), 1.74 (s, 6 H, 11-$(CH_3)_2$), 2.00 (br. s, 1 H, 4-CH_2SO_3<u>H</u>), 3.33 (s, 6 H, 9-N$(CH_3)_2$), 3.73 (s, 2 H, 4-CH_2), 3.79 (q, ^3J = 7 Hz, 2 H,1-CH_2), 5.87 (s, 1 H, 3-H), 6.73 (dd, ^3J = 10 Hz, ^4J = 2 Hz, 1 H, 8-H), 6.96 (s, 1 H, 12-H), 7.02 (d, ^3J = 9 Hz, 1 H, 7-H), 7.04 (d, ^4J = 2 Hz,1 H,10-H), 7.50 (s, 1 H, 5-H).

^{13}C-NMR (125 MHz, $CDCl_3$): δ = 14.3 (1-CH_2-<u>C</u>H_3), 29.3 (2-$(CH_3)_2$), 34.3 (11-$(CH_3)_2$), 41.0 (1-CH_2), 41.1 (9-N$(CH_3)_2$), 41.9 (C11), 53.9 (4-CH_2), 61.9 (C2), 109.6 (t, $^2J_{C–F}$ = 20 Hz, C1'), 111.1 (C10), 111.5 (C12), 113.1 (C8), 119.8 (C6a), 121.5 (C5a), 122.7(C4a), 124.2 (C4), 130.1 (C5), 134.7 (C7), 135.3 (C3), 137.1 (C1'), 138.2 (dm, $^1J_{C–F}$ = 256 Hz, C3' & C5'), 142.2 (dm, $^1J_{C–F}$ = 254 Hz, C4'), 144.1 (dm, $^1J_{C–F}$ = 249 Hz, C2' & C6'), 146.2 (C6), 153.7 (C12a), 155.1 (C10a), 155.6 (C9), 158.5 (C11a).

^{19}F-NMR (470 MHz, $CDCl_3$) δ = -138.2 (dd, ^3J = 22 Hz, ^4J = 7 Hz, 2 F, C2'-F & C6'-F), -149.9 (t, ^3J = 22 Hz, 1 F, C4'-F), -159.2 (ddd, ^3J = 21 Hz, ^4J = 7 Hz, 2 F, C3'-F & C5'-F)

LCMS (ESI$^+$): *m*/*z* calcd for $C_{32}H_{32}F_5N_2O_3S$ $[M + H]^+$ 619.2, found 619.4.

Remark: The ^{13}C-NMR spectrum exhibits broad and low-intensity signals for the C1', C2', C3', C4', C5', and C6' carbon atoms. These signals were tentatively assigned based on their chemical shifts.

2-(4-(9-(Dimethylamino)-1-ethyl-2,2,11,11-tetramethyl-4-(sulfomethyl)-1,2,11,12a tetrahydronaphtho[2,3-*g*] quinolin-6-yl)-2,3,5,6 tetrafluorophenyl) amino)ethanesulfonic acid (**AZ 444**)

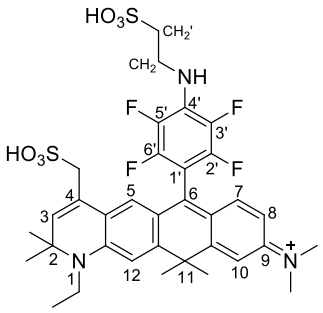

To a solution of **AZ 233** (50 mg, 68 µmol) in DMSO (2 mL), taurine sodium salt (51.0 mg, 341 µmol) was added. The reaction mixture was stirred at 70 °C for 3 h (HPLC control). The product **AZ 444** was isolated by reverse phase column chromatography (C18 modified SiO_2, 40 g; H_2O/ CH_3CN/TFA 8/2/0.001) as a green solid (50.0 mg, 59.8 µmol, 88%).

HPLC: CH_3CN/ H_2O+ 0.1 v/v% TFA = 30/70 to 95/5 in 30 min, detection at 676 nm, t_R = 3.73 min (>99%).

^{1}H-NMR (500 MHz, CD_3OD): δ = 1.41 (t, ^3J = 7 Hz, 3 H, 1-CH_2-CH_3),1.58 (s, 6 H, 2-$(CH_3)_2$), 1.79 (s, 6 H, 11-$(CH_3)_2$), 3.23 (t, ^3J = 7 Hz, 2 H, CH_2'), 3.35 (s, 6 H, 9-N$(CH_3)_2$), 3.74 (s, 2 H, 4-CH_2), 3.89 (q, ^3J = 7 Hz, 2 H,1-CH_2), 3.93 (t, ^3J = 7 Hz, 2 H, CH_2'), 5.81 (s, 1 H, 3-H), 6.92 (dd, ^3J = 9 Hz, ^4J = 2 Hz, 1 H, 8-H), 7.12 (s, 1 H, 12-H), 7.22 (d, ^4J = 2 Hz, 1 H, 10-H), 7.33 (d, ^3J = 10 Hz, 1 H, 7-H), 7.46 (s, 1 H, 5-H).

^{13}C-NMR (125 MHz, CD_3OD): δ = 14.3 (1-CH_2-CH_3), 29.2 (2-$(CH_3)_2$), 34.3 (11-$(CH_3)_2$), 41.4 (1-CH_2), 40.9 (9-N$(CH_3)_2$), 42.4 (CH_2), 42.9 (C11), 52.2 (CH_2'), 54.6 (4-CH_2), 62.5 (C2), 102.0 (C4'), 112.4 (C12), 112.5 (C10), 113.6 (C1'), 114.4 (C8), 121.8 (C6a), 122.3 (C5a), 122.5 (C4a), 124.1 (C4), 131.1 (C5), 137.0 (C3), 137.6 (C7), 139.3 (dm, $^1J_{C-F}$ = 223 Hz, C2' & C6'), 145.4 (dm, $^1J_{C-F}$ = 250 Hz, C3' & C5'), 150.3 (C6), 154.1 (C12a), 157.1 (C10a), 157.6 (C9), 159.5 (C11a).

LCMS (ESI$^+$): *m*/*z* calcd for $C_{34}H_{37}F_4N_3O_6S_2$ $[M + H]^+$ 724.2 found 724.4.

Remark: The ^{13}C-NMR and ^{1}H-NMR signals were tentatively assigned based on their chemical shifts.

2-(4-(9-(Dimethylamino)-1-ethyl-2,211,11-tetramethyl-4-(sulfomethyl)-1,2,11,12a-tetrahydronaphtho[2,3-*g*] quinolin-6-yl)-2,3,5,6-tetrafluorophenyl) thio)ethanesulfonic acid (**AS 06**)

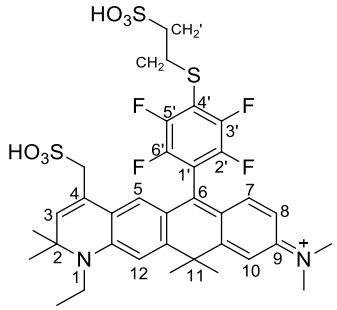

To a solution of **AZ 233** (60.0 mg, 81.9 µmol) in DMSO (3 mL), sodium 2-mercaptoethane sulfonate (68 mg, 0.41 mmol) and *N,N*-Diisopropylethylamine (21.0 µL, 123 µmol) were added. The reaction mixture was stirred at room temperature for 12 h (HPLC control). The product was isolated by reverse phase column chromatography (C18 modified SiO_2, 40 g; H_2O/CH_3CN/TFA 8/2/0.001) as a green solid (66.0 mg, 77.2 µmol, 94%).

HPLC: CH_3CN/ H_2O+ 0.1 v/v% TFA = 30/70 to 95/5 in 30 min, detection at 676 nm, t_R = 3.86 min (99%).

^{1}H-NMR (500 MHz, DMSO-d_6): δ = 1.30 (t, ^{3}J = 7 Hz, 3 H, 1-CH_2-CH_3),1.49 (s, 6 H, 2-$(CH_3)_2$), 1.78 (s, 6 H, 11-$(CH_3)_2$), 2.54 (br. s, 1 H, 4'-S-CH_2-CH_2'SO_3H), 2.80–2.83 (m, 2 H, CH_2'), 3.28–3.30 (m, 2 H, CH_2), 3.32 (s, 6 H, 9-N$(CH_3)_2$), 3.38 (s, 2 H, 4-CH_2), 3.93 (q, ^{3}J = 7 Hz, 2 H,1-CH_2), 5.67 (s, 1 H, 3-H), 6.88 (dd, ^{3}J = 9 Hz, ^{4}J = 2 Hz, 1 H, 8-H), 7.16 (s, 1 H, 12-H), 7.27 (d, ^{4}J = 2 Hz, 1 H, 10-H), 7.32 (d, ^{3}J = 9 Hz,1 H, 7-H), 7.46 (s, 1 H, 5-H).

^{13}C-NMR (125 MHz, DMSO-d_6): δ = 14.0 (1-CH_2-CH_3), 28.7 (2-$(CH_3)_2$), 30.4 (CH_2), 33.6 (11-$(CH_3)_2$), 39.9 (1-CH_2), 40.6 (9-N$(CH_3)_2$), 41.4 (C11), 51.6 (CH_2'), 54.7 (4-CH_2), 61.3 (C2), 111.8 (C12), 111.8 (C10), 113.6 (C8), 114.3 (t, $^{2}J_{C-F}$ = 21 Hz, C1'), 115.6 (C4'), 118.9 (C6a), 119.6 (C5a), 121.4 (C4a), 124.0 (C4), 129.5 (C5), 134.9 (C3), 134.9 (C7), 143.3 (dm, $^{1}J_{C-F}$ = 251 Hz, C2' & C6'), 145.1 (C6), 146.7 (dm, $^{1}J_{C-F}$ = 250 Hz, C3' & C5'), 152.4 (C12a), 154.7 (C10a), 155.5 (C9), 157.2 (C11a).

^{19}F-NMR (470 MHz, DMSO-d_6) δ = -133.2 (dd, ^{3}J = 26 Hz, ^{4}J = 11 Hz, 2 F, C2'-F & C6'-F), -140.4 (dd, ^{3}J = 26 Hz, ^{4}J = 11 Hz, 2 F, C3'-F & C5'-F).

LCMS (ESI^{+}): *m*/*z* calcd for $C_{34}H_{37}F_4N_2O_6S_3$ $[M + H]^+$ 741.1, found 741.4.

2-(4-(1-Ethyl-2,2,11,11-tetramethyl-9-oxo-4-(sulfomethyl)-1,2,9,11 tetrahydronaphtho [2,3-*g*] quinolin-6-yl)-2,3,5,6-tetrafluorophenyl) amino)ethanesulfonic acid (**AS 03**)

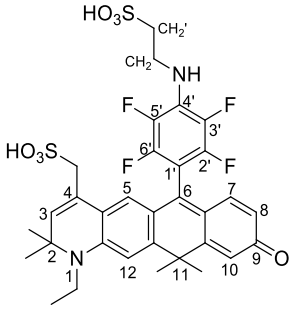

AZ 444 (50.0 mg, 59.7 µmol) was dissolved in a 0.1 M aq. LiOH (10 mL, 1.0 mmol). The solution was stirred at 50 °C for 50 h (HPLC control). The color changed from green to blue after about 8 hours of stirring. After the completion of the reaction, the reaction mixture was acidified to pH 5 using trifluoroacetic acid (TFA). The resulting solution was subjected to reverse phase column chromatography (C18 modified SiO_2, 40 g; H_2O/CH_3CN/TFA 8/2/0.001). The magenta-colored fractions were collected and concentrated, affording **AS 03** as a blue powder (28.0 mg, 34.5 µmol, 58%).

HPLC: CH_3CN/ H_2O + 0.1 v/v% TFA = 15/85 to 95/5 in 30 min, detection at 550 nm, t_R = 7.06 min (>99%).

^{1}H-NMR (500 MHz, CD_3OD): δ = 1.47 (t, ^3J = 7 Hz, 3 H, 1-CH_2-C$\underline{H_3}$), 1.65 (s, 6 H, 2-$(CH_3)_2$), 1.78 (s, 6 H, 11-$(CH_3)_2$), 3.24 (t, ^3J = 7 Hz, 2 H, CH_2'), 3.79 (s, 2 H, 4-CH_2), 3.95 (t, ^3J = 7 Hz, 2 H, CH_2), 4.09 (q, ^3J = 7 Hz, 2 H,1-CH_2), 5.99 (s, 1 H, 3-H), 6.88 (dd, ^3J = 8 Hz, ^4J = 2 Hz, 1 H, 8-H), 7.30 (s, 1 H, 12-H), 7.33 (d, ^4J = 2 Hz, 1 H, 10-H), 7.34 (d, ^3J = 8 Hz, 1 H, 7-H), 7.59 (s, 1 H, 5-H).

^{13}C-NMR (125 MHz, CD_3OD): δ = 14.6 (1-CH_2-C$\underline{H_3}$), 28.7 (2-$(CH_3)_2$), 33.6 (11-$(CH_3)_2$), 42.3 (CH_2), 42.8 (1-CH_2), 42.9 (C11), 52.3 (CH_2'), 54.4 (4-CH_2), 64.3 (C2), 101.5 (C1'), 114.8 (C12), 116.0 (C10), 117.4 (C8), 123.6 (C6a), 123.9 (C4), 124.3 (C4a), 125.4 (C5a), 131.2 (C4'), 132.3 (C5), 136.1 (C7), 139.0 (C3), 139.4 (dm, $^1J_{C-F}$ = 248 Hz, C3' & C5'), 145.6 (dm, $^1J_{C-F}$ = 250 Hz, C2' & C6'), 150.7 (C6), 155.5 (C10a), 156.9 (C12a), 162.3 (C11a), 166.8 (C9).

^{19}F-NMR (470 MHz, CD_3OD) δ = -144.0 (d, ^3J = 17 Hz, 2F, C2'-F & C6'-F), -160.5 (dd, ^3J = 17 Hz, 2F, C3'-F & C5'-F).

LCMS (ESI$^+$): *m*/*z* calcd for $C_{32}H_{32}F_4N_2O_7S_2$ $[M + H]^+$ 697.1, found 697.4.

2-(4-(1-Ethyl-2,2,11,11-tetramethyl-9-oxo-4-(sulfomethyl)-1,2,9,11-tetrahydronaphtho[2,3-*g*] quinolin-6-yl)-2,3,5,6-tetrafluorophenyl) thio)ethanesulfonic acid (**AS 07**)

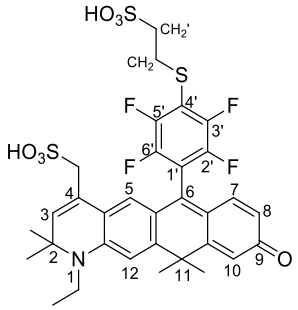

AS 06 (45.0 mg, 52.6 µmol) was dissolved in 0.1 M aq. LiOH (10 mL, 1.0 mmol). The solution was stirred at 50°C for 40 h (HPLC control). The color changed from green to blue after about 9 hours of stirring. After the completion of the reaction, the reaction mixture was acidified to pH 5 using trifluoroacetic acid. The resulting solution was subjected to reverse phase column chromatography (C18 modified SiO_2, 40 g; H_2O/CH_3CN/TFA 8/2/0.001). The magenta-colored fractions were combined and concentrated under reduced pressure yielded **AS 07** as a blue powder (22.0 mg, 26.6 µmol, 51%).

HPLC: CH_3CN /H_2O + 0.1 v/v% TFA = 15/85 to 95/5 in 30 min, detection at 550 nm, t_R = 7.41 min (>99%).

^{1}H-NMR (500 MHz, CD_3OD): δ = 1.48 (t, ^3J = 7 Hz, 3 H, 1-CH_2-C$\underline{H_3}$), 1.65 (s, 6 H, 2-$(CH_3)_2$), 1.80 (s, 6 H, 11-$(CH_3)_2$), 3.22–3.26 (m, 2 H, CH_2'), 3.41–3.44 (m, 2 H, CH_2), 3.82 (s, 2 H, 4-CH_2), 4.12 (q, ^3J = 7 Hz, 2 H, 1-CH_2), 5.98 (s, 1 H, 3-H), 6.87 (dd, ^3J = 8 Hz, ^4J = 2 Hz, 1 H, 8-H), 7.28 (d, ^3J = 9 Hz, 1 H, 7-H), 7.34 (s, 1 H, 12-H), 7.35 (d, ^4J = 2 Hz, 1 H, 10-H), 7.57 (s, 1 H, 5-H).

^{13}C-NMR (125 MHz, CD_3OD): δ = 14.7 (1-CH_2-$\underline{C}H_3$), 28.6 (2-$(CH_3)_2$), 30.5 (CH_2), 33.6 (11-$(CH_3)_2$), 43.0 (1-CH_2), 43.1 (C11), 53.1 (CH_2'), 55.1 (4-CH_2), 64.6 (C2), 115.2 (C12), 116.1 (C1'), 116.3 (C10), 117 (C4'), 117.6 (C8), 122.7 (C6a), 124.2 (C4), 124.6 (C4a), 124.9 (C5a), 132.0 (C5), 135.6 (C7), 139.3 (C3), 145.1 (dm, $^1J_{C–F}$ = 247 Hz, C2' & C6'), 148.3 (C6), 149.1 (dm, $^1J_{C–F}$ = 250 Hz, C3' & C5'), 155.4 (C10a), 157.1 (C12a), 162.2 (C11a), 167.0 (C9)

^{19}F-NMR (470 MHz, CD_3OD) δ = -133.6 (dd, ^3J = 24 Hz, ^4J = 11 Hz, 2 F, C2'-F & C6'-F), - 141.0 (dd, ^3J = 26 Hz, ^4J = 11 Hz, 2 F, C3'-F & C5'-F).

LCMS (ESI$^+$): *m*/*z* calcd for $C_{32}H_{31}F_4NO_7S_3$ $[M + H]^+$ 714.1, found 714.3.

Remark: The ^{13}C-NMR spectrum exhibits broad and low-intensity signals for the C1', C2', C3', C5', and C6' carbon atoms. These signals were tentatively assigned based on their chemical shifts.

10-(2,6-Dichlorophenyl)-7-(dimethylamino)-9,9-dimethylanthracen-2(9*H*)-one (**AS 01**)

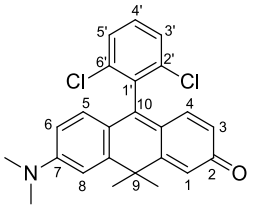

AZ 229 (140 mg, 260 µmol) was dissolved in a 1:1 mixture of ethanol (20 mL) and 0.1 M aq. LiOH (20 mL, 2.0 mmol). The reaction mixture was stirred at 90 °C for 7 h (HPLC control). A color change from greenish blue to blue was observed after 2 h of stirring. Upon completion, the organic layer was separated using DCM, and the aqueous phase was acidified with TFA and extracted with DCM (3 × 30 mL). The combined organic extracts were dried over anhydrous Na_2SO_4 and concentrated under reduced pressure. The crude product was purified by reverse phase column chromatography (C18 modified SiO_2, 40 g; H_2O/ CH_3CN /TFA 7/3/0.001). The red-colored fractions were collected and concentrated under reduced pressure, yielding a sticky residue. This residue was dissolved in MeCN (4 mL) and added dropwise to a stirring solution of water (5 mL), an aqueous $NaClO_4$ solution (10% w/v, 5 mL), and aqueous $HClO_4$ (*w* = 60%, 400 µL). The mixture was stirred for 30 min, leading to the precipitation of the perchlorate salt of the compound. The precipitate was collected by filtration and dried in a desiccator over $CaCl_2$, affording **AS 01** as a red powder (56.0 mg, 136 µmol, 52%).

HPLC: CH_3CN /H_2O + 0.1 v/v% TFA = 30/70 to 95/5 in 30 min, detection at 525 nm, t_R = 6.54 min (>99%).

^{1}H-NMR (500 MHz, DMSO-d_6): δ =1.75 (s, 6 H, 9-(CH_3)$_2$), 3.52 (s, 6 H, N(CH_3)$_2$), 6.87 (dd, ^3J = 9 Hz, ^4J = 2 Hz, 1 H, 3-H), 6.97 (d, ^3J = 8 Hz, 1 H, 4-H), 7.08 (d, ^3J = 10 Hz, 1 H, 5-H), 7.15 (dd, ^3J = 9 Hz, ^4J = 2 Hz, 1 H, 6-H), 7.38 (d, ^4J = 2 Hz, 1 H, 1-H), 7.45 (d, ^4J = 2 Hz, 1 H, 8-H), 7.71 (dd, ^3J = 9 Hz, ^3J = 8 Hz, 1 H, 4'-H), 7.80 (d, ^3J = 8 Hz, 1 H, 3'-H), 7.80 (d, ^3J = 9 Hz, 1 H, 5'-H).

^{13}C-NMR (125 MHz, DMSO-d_6): δ = 32.8 (9-(CH_3)$_2$), 41.6 (C9), 42.0 (N(CH_3)$_2$), 114.2 (C8),115.4 (C1), 116.8 (C3),117.3 (C6), 120.3 (C4a), 121.3 (C10a), 128.8 (C3' & C5'), 132.4 (C4'), 132.6 (C1'), 133.3 (C2' & C6'), 133.9 (C4), 137.1 (C5), 154.6 (C9a), 156.1 (C10), 158.1 (C7), 158.3 (C8a), 165.9 (C2).

LCMS (ESI$^+$): *m*/*z* calcd for $C_{24}H_{21}Cl_2NO$ $[M + H]^+$: 410.1, found 410.2.

(6-(2,6-Dichlorophenyl)-1-ethyl-2,2,11,11-tetramethyl-9-oxo-1,2,9,11-tetrahydronaphtho[2,3-*g*] quinolin-4-yl)methanesulfonic acid (**AS 02**)

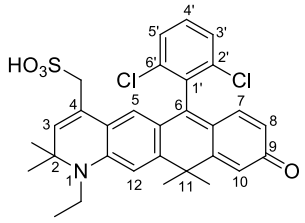

AZ 234 (200 mg, 287 µmol) was dissolved in a 1:1 mixture of ethanol (20 mL) and 0.1 M aq. LiOH (20 mL, 2.0 mmol). The reaction mixture was stirred at 90°C for 7 h (HPLC control). The color of the reaction mixture changed from greenish blue to blue after 2 h of stirring. Upon completion, the organic layer was separated using DCM, and the aqueous phase was acidified with trifluoroacetic acid (TFA) and extracted with DCM (3 × 30 mL). The combined organic extracts were dried over anhydrous Na_2SO_4 and concentrated under reduced pressure. The crude product was purified by reverse phase column chromatography (C18 modified SiO_2, 40 g; H_2O/ CH_3CN /TFA 7/3/0.001). The magenta-colored fractions were collected and concentrated under reduced pressure, yielding **AS 02** as a magenta powder (70.0 mg, 123 µmol, 43%).

HPLC: CH_3CN /H_2O + 0.1 v/v% TFA = 20/80 to 95/5 in 30 min, detection at 550 nm, t_R = 7.79 min (>99%).

^{1}H-NMR (500 MHz, DMSO-d_6): δ = 1.36 (t, ^3J = 7 Hz, 3 H, 1-CH_2-C$\underline{H_3}$), 1.56 (s, 6 H, 2-$(CH_3)_2$), 1.75 (s, 6 H, 11-$(CH_3)_2$), 3.20 (s, 2 H, 4-CH_2), 4.13 (q, ^3J = 7 Hz, 2 H,1-CH_2), 5.93 (s, 1 H, 3-H), 6.85 (dd, ^3J = 9 Hz, ^4J = 2 Hz, 1 H, 8-H), 6.89 (d, ^3J = 9 Hz, 1 H, 7-H), 7.21 (s, 1 H, 5-H), 7.32 (s, 1 H, 12-H), 7.38 (d, ^4J = 2 Hz, 1 H, 10-H), 7.65 (dd, ^3J = 9 Hz, ^3J = 7 Hz, 1 H, 4'-H), 7.72 (d, ^3J = 8 Hz, 2 H, 5'-H, 3'-H).

^{13}C-NMR (125 MHz, DMSO-d_6): δ = 14.2 (1-CH_2-$\underline{C}H_3$), 28.1 (2-$(CH_3)_2$), 32.6 (11-$(CH_3)_2$), 41.3 (1-CH_2), 41.5 (C11), 52.9 (4-CH_2), 62.8 (C2), 113.8 (C12), 115.0 (C10), 116.3 (C8), 120.7 (C6a), 122.1 (C5a), 123.1 (C4a), 123.2 (C12a), 128.6 (C3' & C5'), 129.4 (C5), 132.1 (C4'), 132.4 (C1'), 133.2 (C7), 133.3 (C2' & C6'), 136.2 (C3), 153.6 (C10a), 155.0 (C6), 155.2 (C4), 160.0 (C11a), 164.6 (C9).

LCMS (ESI$^+$): *m*/*z* calcd for $C_{30}H_{29}Cl_2NO_4S$ $[M + H]^+$: 570.1, found 570.3.

2-(6-(Dimethylamino)-10,10-dimethyl-3-oxo-3,10-dihydroanthracen-9-yl)terephthalic acid (**AS 10**)

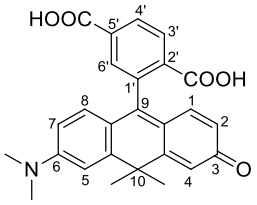

AZ 481 (100 mg, 176 µmol) was dissolved in a 1:1 mixture of ethanol (7 mL) and 2.5 M aq. NaOH (7.0 mL, 17.5 mmol). The reaction mixture was stirred at 85 °C for 2 h (HPLC control). A color change from blue to red was observed within 15 minutes. After the completion of the reaction, the reaction mixture was cooled to 0 °C and acidified to pH 5 using TFA. The resulting solution was subjected to reverse phase column chromatography (C18 modified SiO_2, 40 g; H_2O/MeCN/TFA 8/2/0.001). The red fractions were combined and concentrated under reduced pressure, yielding **AS 10** as a red powder (42.0 mg, 77.3 µmol, 45%).

HPLC: CH_3CN /H_2O + 0.1 v/v% TFA = 15/85 to 95/5 in 15 min, detection at 550 nm, t_R = 5.18 min (>99%).

^{1}H-NMR (500 MHz, DMSO-d_6): δ = 1.68 (s, 3 H, 10-CH_3'), 1.79 (s, 3 H, 10-CH_3), 2.95 (s, 6 H, N(CH_3)$_2$), 6.47 (d, ^3J = 8 Hz, 1 H, 8-H), 6.51 (d, ^3J = 9 Hz, 1 H, 1-H), 6.61 (dd, ^3J = 9 Hz, ^4J = 2 Hz, 1 H, 2-H), 6.62 (dd, ^3J = 9 Hz, ^4J = 2 Hz, 1 H, 7-H), 6.95 (d, ^4J = 2 Hz, 1 H, 5-H), 7.11 (d, ^4J = 2 Hz, 1 H, 4-H), 7.43 (s, 1 H, 6'-H), 8.09 (d, ^3J = 8 Hz, 1 H, 3'-H), 8.16 (dd, ^3J = 8 Hz, ^4J = 2 Hz, 1 H, 4'-H).

^{13}C-NMR (125 MHz, DMSO-d_6): δ = 33.3 (10-CH_3), 34.4 (10-CH_3'), 37.8 (C10), 40.0 (N(CH_3)$_2$), 109.2 (C5),112.1 (C7), 112.7 (C4),114.9 (C2), 117.8 (C8a), 121.1 (C9a), 123.9 (C6') 125.3 (C3'), 128.2 (C1), 128.9 (C8), 129.0 (C9), 130.2 (C4'), 136.9 (C2'), 145.8 (C10a), 147.1 (C4a), 150.6 (C6), 155.3 (C5'), 158.1 (C3),158.0 (C1'), 166.0 (C5'-COOH), 169.0 (C2'- COOH)

LCMS (ESI$^+$): *m*/*z* calcd for $C_{26}H_{23}NO_5$ [M + H]$^+$: 430.16, found 430.2.

4-(3-Carboxypropyl) (methyl)carbamoyl)-2-(6-(dimethylamino)-10,10-dimethyl-3-oxo-3,10-dihydroanthracen-9-yl)benzoic acid (**AS 13**)

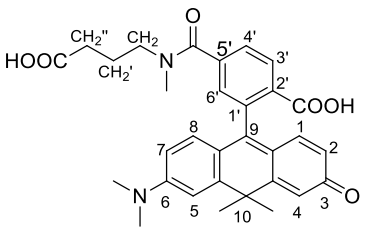

To a stirred solution of **AS 10** (20.0 mg, 36.0 µmol) in anhydrous acetonitrile (10 mL, pre-dried over 3 Å molecular sieves) containing *p*-toluenesulfonic acid (5 g/L) at 0 °C, N-hydroxysuccinimide (5.50 mg, 47.8 µmol and *N,N'*-dicyclohexylcarbodiimide (8.05 mg, 38.6 µmol) were added. A precipitate occurs immediately after the addition of DCC. The dull orange colored reaction mixture was stirred at 0 °C overnight (HPLC control). The reaction mixture was filtered using a 0.2 µm membrane filter to remove the solids. The filtrate was concentrated under reduced pressure, yielding a magenta-colored residue, which was redissolved in CH_3CN (2 mL), and the active ester of **AS 10** was precipitated with diethyl ether as a red powder (19.0 mg, 35.2 µmol, 98%).

HPLC: CH_3CN /H_2O + 0.1 v/v% TFA = 15/85 to 95/5 in 15 min, detection at 550 nm, t_R = 6.64 min (96%).

LCMS (ESI$^+$): *m*/*z* calcd for $C_{30}H_{26}N_2O_7$ $[M + H]^+$: 527.1, found 527.2.

To a solution of **AS 10** active ester (19 mg, 36 µmol) in anhydrous DMSO (3 mL), 4-(methylamino) butyric acid potassium salt (21 mg, 90 µmol) was added. The red-colored reaction mixture was stirred at room temperature for 2 h (HPLC control). The reaction mixture was then added to Milli-Q water (13 mL) while stirring at 0 °C. The product was isolated by reverse-phase column for purification (C18 modified SiO_2, 12 g; H_2O/MeCN/TFA 8/2/0.001), yielding **AS 13** (23.0 mg, 35.8 µmol, 99%) as a red solid.

HPLC: CH_3CN /H_2O + 0.1 v/v% TFA = 15/85 to 95/5 in 30 min, detection at 550 nm, t_R = 4.98 min (99%).

^{1}H-NMR (500 MHz, CD_3OD): δ = 1.74 (s, 3 H, 10-CH_3), 1.77–1.79 & 1.91–1.97 (m, 2 H, CH_2'), 1.85 (s, 3 H, 10-CH_3'), 2.11–2.15 & 2.36–2.41 (m, 2 H, CH_2''), 2.95 & 3.06 (s, 3 H, 5'-CON($C\underline{H_3}$)), 3.28–3.31 & 3.54–3.60 (m, 2 H, CH_2), 3.33 (s, 6 H, 6-N(CH_3)$_2$), 6.70–6.73 (m, 1 H, 2-H), 6.83–6.90 (m, 1 H, 1-H), 6.98 (dd, ^3J = 9.0 Hz, ^4J = 2.0 Hz, 1 H, 7-H), 7.03–7.08 (m, 1 H, 8-H), 7.25–7.28 (m, 2 H, 4-H & 6'-H), 7.37 (s, 1 H, 5-H), 7.71–7.76 (m, 1 H, 4'-H), 8.26 (d, ^3J = 8.0 Hz, 1 H, 3'-H)

^{13}C-NMR (125 MHz, CD_3OD): δ = 23.1 & 24.2 (CH_2'), 31.2 & 32.2 (CH_2''), 32.1 (10-CH_3'), 33.2 & 37.9 (5'-CON($\underline{C}H_3$)), 41.6 (C10), 42.3 (6-N(CH_3)$_2$), 48.2 & 51.7 (CH_2), 113.9 (C5), 114.9 (C4), 116.1 (C7), 116.6 (C2), 123.8 (C9a), 124.3 (C8a), 126.7 (C6'), 129.0 (C2'), 129.1 (C4'), 130.4 (C3'), 134.4 (C1), 136.4 (C8), (142.5 (C1'), 142.7 (C5'), 153.4 (C4a), 156.3 (C10a), 155.9 (C6), 164.1 (C9), 169.1 (2'-COOH), 171.8 (5'-$\underline{C}$ON(CH_3)(CH_2)$_3$COOH), 172.1 (C3), 175.8 (5'-CON(CH_3)(CH_2)$_3\underline{C}$OOH).

LCMS (ESI$^+$): *m*/*z* calcd for $C_{31}H_{32}N_2O_6$ $[M + H]^+$: 529.2, found 529.4.

2-(6-(Dimethylamino)-10,10-dimethyl-3-oxo-3,10-dihydroanthracen-9-yl)benzoic acid (**AS 11**)

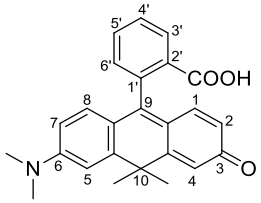

AZ 43 (0.40 g, 0.78 mmol) was dissolved in a 1:1 mixture of ethanol (50 mL) and 2.5 M aq. NaOH (50.0 mL, 125 mmol). The reaction mixture was stirred at 85 °C for 8 h (HPLC control). The color of the solution changed from blue to red within 30 minutes. After the completion of the reaction, the reaction mixture was cooled to 0 °C and acidified to pH 5 using TFA. The organic layer was separated using DCM, and the aqueous phase was extracted with DCM (3 × 30 mL). The combined organic extracts were dried over anhydrous Na_2SO_4 and concentrated under reduced pressure. The crude product was purified by reverse phase column chromatography (C18 modified SiO_2, 120 g; H_2O/MeCN/TFA 7/3/0.001). The red-colored fractions were collected and concentrated under reduced pressure, yielding **AS 11** as red powder (202 mg, 524 µmol, 67%).

HPLC: CH_3CN/H_2O + 0.1 v/v% TFA = 15/85 to 95/5 in 30 min, detection at 550 nm, t_R = 8.48 min (>99%).

^{1}H-NMR (500 MHz, DMSO-d_6): δ = 1.67 (s, 3 H, 10-CH_3), 1.78 (s, 3 H, 10-CH_3'), 2.93 (s, 6 H, 6-N(CH_3)$_2$), 6.44 (d, ^3J = 9 Hz, 1 H, 8-H), 6.47 (d, ^3J = 9 Hz, 1 H, 1-H), 6.59 (dd, ^3J = 9 Hz, ^4J = 2 Hz, 1 H, 7-H), 6.61 (dd, ^3J = 9 Hz, ^4J = 2 Hz, 1 H, 2-H), 6.92 (d, ^4J = 2 Hz, 1 H, 5-H), 7.06 (d, ^3J = 8 Hz, 1 H, 6'-H), 7.09 (d,^4J = 2 Hz, 1 H, 4-H), 7.64 (ddd, ^3J = 7 Hz, ^4J = 2 Hz, 1 H, 4'-H), 7.70 (ddd, ^3J = 7 Hz, ^4J = 2 Hz, 1 H, 5'-H), 7.96 (dd, ^3J = 8 Hz, ^4J = 2 Hz, 1 H, 3'-H), 9.67 (br. s, 1H, 2'-COOH).

^{13}C-NMR (125 MHz, DMSO-d_6): δ = 33.0 (10-CH_3), 34.5 (10-CH_3'), 37.8 (C10), 39.6 (6-N(CH_3)$_2$), 109.0 (C5),111.9 (C7), 112.6 (C4),114.7 (C2), 118.5 (C8a), 121.8 (C9a), 123.6 (C6') 124.5 (C3'), 125.7 (C2'), 128.1 (C8), 128.7 (C1), 128.7 (C9), 129.3 (C4'), 135.2 (C5'), 145.6 (C10a), 147.0 (C4a),150.5 (C6), 155.1 (C1'), 157.9 (C3), 169.8 (2'-COOH).

LCMS (ESI$^+$): *m*/*z* calcd for $C_{25}H_{23}NO_3$ [M + H]$^+$: 386.2, found 386.2.

1-(2-(6-(Dimethylamino)-10,10-dimethyl-3-oxo-3,10-dihydroanthracen-9-yl)benzoyl) piperidine-4-carboxylic acid (**AS 14**)

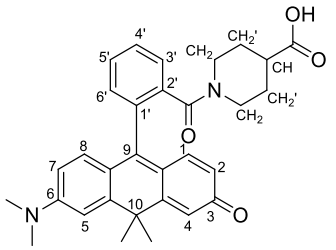

To a solution of **AS 11** (100 mg, 0.2 mmol) in DCM (10 mL), $POCl_3$ (951 µL, 10.2 mmol) was added. After stirring at 80 °C for 4 h, all volatile materials were evaporated *in vacuo*, and the solid residue was dissolved in CH_3CN (5 mL). A solution of piperidine-4-carboxylic acid (129 mg, 1.00 mmol) in CH_3CN (5 mL) was added, followed by the addition of NEt_3 (842 µL, 6.00 mmol). After stirring at room temperature for 30 min, all volatile materials were removed *in vacuo*. The residue was redissolved in DCM (20 mL) and washed with a saturated aq. NH_4Cl solution. The organic layer was separated, dried with anhydrous Na_2SO_4, and the solvent was removed under reduced pressure. Reverse phase column chromatography (C18 modified SiO_2, 40 g; H_2O/CH_3CN/TFA 8/2/0.001) yielded **AS 14** (67 mg, 0.11 mmol, 55%) as a red solid.

HPLC: CH_3CN/H_2O + 0.1 v/v% TFA = 15/85 to 95/5 in 60 min, detection at 550 nm, t_R = 11.97 min (97%).

^{1}H-NMR (500 MHz, CD_3OD): δ = 1.23–1.34 (m, 4 H, CH_2'), 1.67 (s, 3 H, 10-CH_3), 1.84 (s, 3 H, 10-CH_3'), 2.41–2.48 (m, 1 H, CH_2), 2.66–2.71 (m, 1 H, CH_2''), 2.94–3.03 (m, 1 H, CH_2), 3.49 (s, 6 H, 6-N(CH_3)$_2$), 3.56–3.70 (m, 1 H, CH_2), 4.06–4.14 (m, 1 H, CH_2), 6.78 (dd, ^3J = 9 Hz, ^4J = 2 Hz, 1 H, 2-H), 7.01 (dd, ^3J = 9 Hz, ^4J = 2 Hz, 1 H, 7-H), 7.20 (d, ^3J = 9 Hz, 1 H, 1-H), 7.30 (d, ^4J = 2 Hz, 1 H, 4-H), 7.33 (d, ^3J = 7 Hz, 1 H, 8-H), 7.34 (s, 1 H, 5-H), 7.45–7.47 (m, 1 H, 3'-H), 7.56–7.60 (m, 1 H, 6'-H), 7.70–7.74 (m, 2 H, 4'-H & 5'-H).

^{13}C-NMR (125 MHz, CD_3OD): δ = 30.7 (CH_2'), 31.2 (10-CH_3), 31.2 (10-CH_3), 36.1 (10-CH_3'), 41.4 (CH_2), 41.9 (6-N(CH_3)$_2$), 42.1 (CH_2''), 42.9 (C10), 113.8 (C5), 115.8 (C7), 116.3 (C4), 117.1 (C8a), 117.4 (C2), 117.7 (C9a), 123.7 (C9), 128.2 (C6'), 130.5 (C4' & C5'), 130.7 (C1'), 131.6 (C3'), 137.0 (C2'), 138.6 (C1), 140.9 (C8), 157.0 (C4a), 159.9 (C6), 160.6 (C10a), 163.3 (C2'-<u>C</u>ONC$_5$H$_9$COOH), 168.8 (C3), 177.6 (C2'-CONC$_5$H$_9$<u>C</u>OOH).

LCMS (ESI$^+$): *m*/*z* calcd for $C_{31}H_{32}N_2O_4$ $[M + H]^+$: 497.2, found 497.4.

<u>2-(1-Ethyl-11,11-dimethyl-9-oxo-1,2,3,4,9,11-hexahydronaphtho[2,3-*g*]quinolin-6-yl)benzoic acid (**AS 12**)</u>

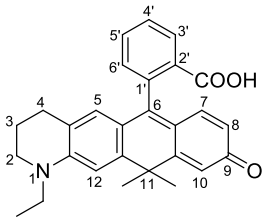

AZ 129 (0.30 g, 0.48 mmol) was dissolved in a 1:1 mixture of ethanol (35 mL) and 2.5 M aq. NaOH (35 mL, 87.5 mmol). The reaction mixture was stirred at 85 °C for 10 h (HPLC control). The color of the solution changed from blue to red after 2 h. After the completion of the reaction, the reaction mixture was cooled to 0 °C and acidified to pH 5.0 using TFA. The organic layer was separated using DCM, and the aqueous phase was extracted with DCM (3 × 30 mL). The combined organic extracts were dried over anhydrous Na_2SO_4 and concentrated under

reduced pressure. The crude product was purified by reverse phase column chromatography (C18 modified SiO_2, 120 g; H_2O/CH_3CN/TFA 8/2/0.001). The red-colored fractions were collected and concentrated under reduced pressure, yielding **AS 12** as a red solid (110 mg, 259 µmol, 54%).

HPLC: CH_3CN/H_2O + 0.1 v/v% TFA = 30/70 to 95/5 in 15 min, detection at 550 nm, t_R = 5.12 min (>99%).

^{1}H-NMR (500 MHz, DMSO-d_6): δ = 1.10 (t, ^3J = 7 Hz, 3 H, 1-CH_2-C$\underline{H_3}$), 1.64 (s, 3 H, 11-CH_3), 1.73 (s, 3 H, 11-CH_3'), 1.75–1.80 (m, 2 H, 3-H), 2.36–2.47 (m, 2 H, 4-H), 3.23 (t, ^3J = 7 Hz, 2 H, 2-H), 3.44 (q, ^3J = 7 Hz, 2 H,1-CH_2), 6.13 (s, 1 H, 5-H), 6.44 (d, ^3J = 9 Hz, 1 H, 7-H), 6.59 (dd, ^3J = 8 Hz, ^4J = 2 Hz, 1 H, 8-H), 6.78 (s, 1 H, 12-H), 7.08 (d, ^3J = 8 Hz, 1 H, 6'-H), 7.09 (d, ^4J = 2 Hz, 1 H,10-H), 7.63 (ddd, ^3J = 7 Hz, ^4J = 2 Hz, 1 H, 4'-H), 7.70 (ddd, ^3J = 7 Hz, ^4J = 2 Hz, 1 H, 5'-H), 7.95 (d, ^3J = 7 Hz, 1 H, 3'-H).

^{13}C-NMR (125 MHz, DMSO-d_6): δ = 10.4 (1-CH_2-$\underline{C}H_3$), 21.4 (C3), 27.1 (C4), 33.1 (11-CH_3'), 34.4 (11-CH_3), 37.7 (C11), 44.9 (1-CH_2), 48.0 (C2), 107.5 (C12), 112.8 (C10), 114.8 (C8), 117.3 (C5a), 121.9 (C4a), 122.1 (C6a), 124.2 (C6'), 125.0 (C3'), 126.2 (C2'), 127.6 (C5), 128.7 (C6), 129.1 (C7), 129.4 (C4'), 135.1 (C5'), 144.7 (C11a), 146.0 (C12a), 147.6 (C10a), 158.2 (C1'), 158.5 (C9), 169.8 (C2'-COOH).

LCMS (ESI$^+$): *m*/*z* calcd for $C_{28}H_{27}NO_3$ $[M + H]^+$: 426.2, found 426.3.

4-(2-(1-Ethyl-11,11-dimethyl-9-oxo-1,2,3,4,9,11-hexahydronaphtho[2,3-*g*] quinolin-6-yl)-*N*-methylbenzamido)butanoic acid (**AS 15**)

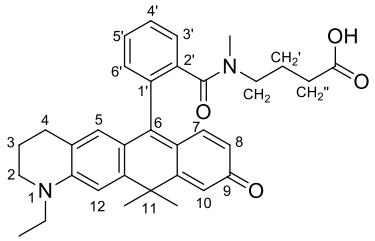

To a solution of **AS 12** (80.0 mg, 148 µmol) in DCM (10 mL), $POCl_3$ (704 µL, 7.50 mmol) was added. After stirring at 80 °C for 4 hours, all volatile materials were evaporated *in vacuo*, and the solid residue was dissolved in CH_3CN (5 mL). A solution of methyl-4-(methylamino) butanoate (97 mg, 0.74 mmol) in CH_3CN (5 mL) was added, followed by the addition of NEt_3 (842 µL, 6.00 mmol). After stirring at room temperature for 30 min, all volatile materials were removed *in vacuo*. The residue was redissolved in DCM (20 mL) and washed with a saturated aq. NH_4Cl. The organic layer was separated, dried with anhydrous Na_2SO_4, and evaporated.

For the hydrolysis of the ester group, the crude product was stirred for 5 h at room temperature in a mixture of H_2O (22 mL), THF (34 mL), and aq. NaOH (*c* = 1 M, 1.4 mL). Acetic acid (23 mL) was added, and the mixture was evaporated to dryness. Purification of the crude

product by reverse phase column chromatography (C18 modified SiO_2, 40 g; H_2O/CH_3CN/TFA 8/2/0.001) yielded **AS 15** (63 mg, 98.6 µmol, 67%) as a red solid.

HPLC: CH_3CN/H_2O + 0.1 v/v% TFA = 15/85 to 95/5 in 15 min, detection at 550 nm, t_R = 6.56 min (>99%).

^{1}H-NMR (500 MHz, CD_3OD): δ = 1.41 (t, ^3J = 7 Hz, 3 H,1-CH_2-C$\underline{H_3}$), 1.43–1.50 (m, 2 H, CH_2'), 1.70 (s, 3 H, 11-CH_3), 1.80 (s, 3 H, 11-CH_3'), 1.83–1.90 (m, 2 H, CH_2''), 1.96–2.05 (m, 2 H, 3-H), 2.65–2.70 (m, 2 H, 4-H), 2.94 (s, 3 H, 2'CON(C$\underline{H_3}$)), 3.17–3.38 (m, 2 H, CH_2), 3.76 (t, ^3J = 6.0 Hz, 2 H, 2-H), 3.83–3.98 (m, 2 H, 1-CH_2), 6.79 (dd, ^3J = 9.0 Hz, ^4J = 2.0 Hz, 1 H, 8-H), 6.97 (s, 1 H, 5-H), 7.13 (d, ^3J = 9.0 Hz, 1 H, 7-H), 7.28 (s, 1 H, 12-H), 7.30 (d, ^4J = 2.0 Hz, 1 H, 10-H), 7.43–7.47 (m, 1 H, 6'-H), 7.62–7.65 (m, 1 H, 3'-H), 7.69–7.73 (m, 2 H, 4'-H & 5'-H).

^{13}C-NMR (125 MHz, CD_3OD): δ = 12.3 (1-CH_2-$\underline{C}H_3$), 21.8 (C3), 23 (CH_2'), 27.6 (C4), 31.7 (CH_2''), 32.1 (11-CH_3'), 35.2 (11-CH_3), 37.9 (2'-CON($\underline{C}H_3$)), 42.5 (C11), 47.5 (CH_2), 49.1 (1-CH_2), 52.2 (C2), 113.4 (C12), 115.7 (C10), 116.5 (C8), 124.0 (C5a), 124.3 (C6a), 127.5 (C4a), 128.4 (C3'), 130.4 (C4' & C5'), 131.7 (C6'), 135.5 (C2'), 137.4 (C7), 137.4 (C1'), 137.4 (C5), 155.8 (C10a), 157.5 (C12a), 160.9 (C11a), 162.9 (C6), 166.3 (C9), 170.6 (C2'-$\underline{C}ONCH_3$), 176.2 (C2'-CON(CH_3)(CH_2)$_3\underline{C}$OOH).

LCMS (ESI$^+$): *m*/*z* calcd for $C_{33}H_{36}N_2O_4$ [M + H]$^+$: 525.2, found 525.4.

2,5-dioxopyrrolidin-1-yl 1-(2-(6-(dimethylamino)-10,10-dimethyl-3-oxo-3,10-dihydroanthracen-9-yl) benzoyl) piperidine-4-carboxylate (**AS 14 NHS**)

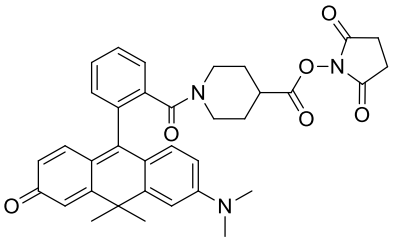

To a stirred solution of **AS 14** (45.0 mg, 73.7 µmol) in MeCN (10 mL), at 0 °C, NHS (17.0 mg, 147 µmol) and DCC (31.0 mg, 0.147 mmol) were added one after the other. A precipitate (dicyclohexylurea) formed immediately after the addition of DCC. The ice bath was removed, and the red-colored reaction mixture was stirred for 40 h (HPLC control). Small amounts of NHS and DCC were successively added to complete the reaction. The reaction mixture was filtered using a 0.2 µm membrane filter to remove the solids. The filtrate was concentrated under reduced pressure, yielding a red-colored residue, which was redissolved in CH_3CN (2 mL). The active ester of **AS 14** was precipitated by the addition to diethyl ether/*n*-hexane (1:1) and obtained as a red powder (43.0 mg, 72.4 µmol, 98%).

HPLC: CH_3CN /H_2O + 0.1 v/v% TFA = 15/85 to 95/5 in 15 min, detection at 550 nm, t_R = 6.5 min (89%).

LCMS (ESI^+): *m*/*z* calcd for $C_{35}H_{35}N_3O_6$ $[M + H]^+$: 594.2, found 594.4.

2,5-Dioxopyrrolidin-1-yl 4-(2-(1-ethyl-11,11-dimethyl-9-oxo-1,2,3,4,9,11-hexahydronaphtho[2,3-*g*] quinolin-6-yl)-*N*-methylbenzamido)butanoate (**AS 15 NHS**)

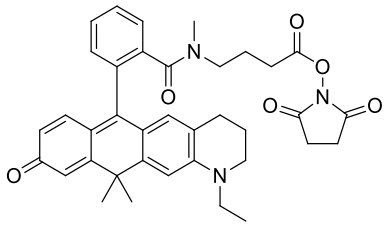

To a stirred solution of **AS 15** (35.0 mg, 54.8 mmol) in MeCN (10 mL), at 0 °C, NHS (13 mg, 0.11 mmol) and DCC (23 mg, 0.11 mmol) were added one after the other. A precipitate (dicyclohexylurea) formed immediately after the addition of DCC. The red-colored reaction mixture was stirred for 30 h at r.t. (HPLC control). Small amounts of NHS and DCC can be successively added to complete the reaction. The reaction mixture was filtered using a 0.2 µm membrane filter to remove the solids. The filtrate was concentrated under reduced pressure, yielding a magenta-colored residue, which was redissolved in CH_3CN (2 mL). The active ester of **AS 15** was precipitated by the addition to diethyl ether/*n*-hexane (1:1) and obtained as a magenta powder (32.0 mg, 51.5 µmol, 94%).

HPLC: CH_3CN /H_2O + 0.1 v/v% TFA = 15/85 to 95/5 in 15 min, detection at 550 nm, t_R = 7.4 min (87%).

LCMS (ESI^+): *m*/*z* calcd for $C_{37}H_{39}N_3O_6$ $[M + H]^+$: 622.2, found 622.4.

A model reaction was conducted using benzylamine as the nucleophilic amine to assess the coupling efficiency of newly synthesized NHS esters. A stock solution of benzylamine (0.1 v/v%) was prepared by diluting 100 µL of benzylamine in 100 mL of anhydrous MeCN. Subsequently, 500 µL of this solution was added to 1 mg of the respective NHS esters (**AS 14** or **AS 15**), and the mixture was allowed to react at room temperature for 30 minutes.

HPLC analysis (CH_3CN /H_2O + 0.1 v/v% TFA = 15/85 to 95/5 in 15 min) showed the appearance of new peaks at retention times of 7.1 min (**AS 14 NHS**) and 7.8 min (**AS 15 NHS**), indicating successful amide bond formation between the NHS esters and benzylamine, which confirms the coupling efficiency of the synthesized esters.

Attempts towards the synthesis of 6-(2-bromo-4-methoxybenzyl)-1-ethyl-2,2,4-trimethyl-1,2-dihydroquinoline (**22**)

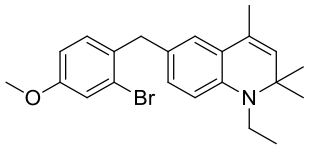

Under a nitrogen atmosphere, a solution of (2-bromo-4-methoxyphenyl)methanol (**20**) (1.00 g, 4.61 mmol) and 1-ethyl-2,2,4-trimethyl-1,2-dihydroquinoline **21** (928 mg, 4.61 mmol) in DCM (30 mL) was cooled to −15 °C using an ice/methanol bath. A solution of BCl_3 in DCM (5.5 mL, 5.53 mmol) was added dropwise over 20 minutes, during which the reaction mixture changed from green to brown. After the addition was complete, the reaction mixture was stirred at room temperature for 60 minutes. Upon complete conversion of **20** (TLC control), the reaction mixture was cooled to 0 °C and quenched by the addition of 10% aq. NaOH, followed by water (50 mL). The organic phase was separated using DCM (3 × 25 mL). The combined organic layers were washed with water (30 mL) and dried over anhydrous Na_2SO_4. After filtration, the solvent was removed under reduced pressure. Mass spectrometry confirmed the presence of the expected product; however, attempts to purify them by column chromatography were unsuccessful.

Second attempt

Glacial acetic acid (5 mL) was added to a mixture of **20** (500 mg, 2.30 mmol) and **21** (463 mg, 2.30 mmol), and the reaction mixture was stirred at room temperature. After 1 hour, TLC analysis indicated no product formation. The temperature was then increased to 60 °C and subsequently to 100 °C; however, no reaction progress was observed.

4 pH-Dependent Photophysical Properties of Carborhodol Dyes

To assess the suitability of the newly synthesized carborhodol dyes, discussed in Chapter 3, for application as pH indicators, their pH-responsive photophysical properties were investigated in aqueous buffer and ethanol. All compounds exhibited notable pH-dependent spectral changes, with increased absorbance and fluorescence intensity under basic conditions. The determined pK_a values (5–7) indicate suitability for sensing applications in physiological environments such as wound dressings. Deprotonation induced a planar, conjugated structure, leading to enhanced absorption, fluorescence quantum yield, and lifetime. Notably, the *N*,*N*-dimethylamino-substituted carborhodol derivative **AS 01**, showed up to 48-fold higher fluorescence in its basic form relative to the acidic form. The dyes also demonstrated superior photostability compared to the standard pH indicator fluorescein and the common NIR fluorescent label Cy 5. These results highlight the potential of carborhodols for use as dual-mode pH sensors, capable of functioning both as colorimetric and fluorogenic probes in bioresponsive materials.

4.1 Introduction and Objective

Rhodols are neutral fluorophores characterized by an asymmetric electron density, with their electronic structure represented by neutral and dipolar forms (Scheme 4.1).[39]

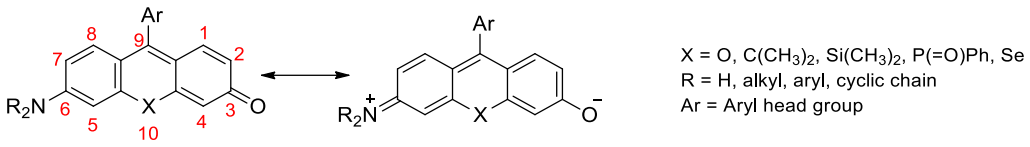

Scheme 4.1. Resonance structure of rhodol showing neutral (left) and dipolar (right) forms. The general position numbering of the rhodol chromophore is illustrated in its neutral form.

Rhodol derivatives can be structurally modified to alter the conjugation pathway, thereby tuning their photophysical properties, which allows one to obtain the desired compound suitable for various applications. Rhodol derivatives with X = O (O-rhodol) containing an unsubstituted amino group demonstrate a strong fluorescence at 516 nm. The introduction of an alkyl (Alk) or aryl (Ar) substituent at the amino group increases the electron-donor strength of the amino group, which results in a bathochromic shift of ~10–15 nm of the absorption and emission maxima.[84] A more pronounced red shift (~25 nm) is observed in rhodols containing fully annulated C-N bonds, such as those incorporating a julolidine moiety, due to the restricted rotation around the amino group.[217]

The aryl group, oriented orthogonally to the xanthene framework, reduces the sensitivity of the fluorophore's π-conjugated system to nucleophilic attack.[218] Additionally, introducing a bulky substituent at the *ortho*-position of the aryl head group enhances fluorescence efficiency by restricting the rotation of the aryl part, thereby minimizing the non-radiative deactivation pathways in the excited state.[219,220] Furthermore, functionalizing amino R groups enables the development of targeted probes.[221] The Dewar-Knott rule states that electron-donating groups (EDG) at the *meso*-position (C9) and the bridging position (C10) cause a hypsochromic shift, while electron-withdrawing groups (EWG) induce a bathochromic shift of the absorption maximum (Figure 4.1).[222]

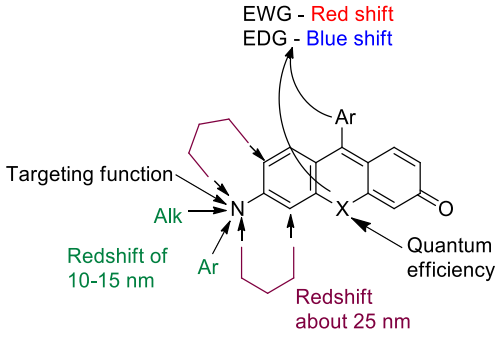

Figure 4.1. The effect of substituents on the optical properties of rhodols.

The presence of an ionizable phenolic hydroxyl group makes the rhodols sensitive to pH. In the case of carborhodols, they exist in their deprotonated dye form under basic conditions, while acidic conditions favor the protonated species (Scheme 4.2). Each of these forms exhibits distinct pH-dependent optical properties, including absorption and emission.

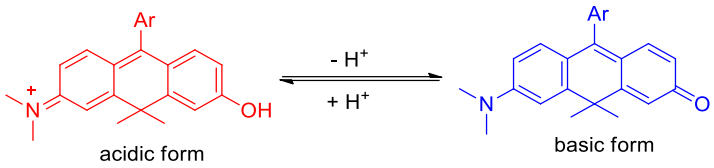

Scheme 4.2. The protonation-deprotonation equilibrium of general carborhodols.

Most of the reported O-rhodol pH-sensors are fluorescence on/off probes; in many cases, structural modifications in the chromophore promote the non-fluorescent spirocyclic (closed) forms, which open under acidic conditions (dye form), thereby restoring fluorescence.[223–225]

The pK_a values of O-rhodol derivatives typically range between 4.5 and 7,[84] and Si-rhodol is reported to have a pK_a of ~6,[226] making them suitable for biological pH monitoring. In contrast, P(=O)-rhodols exhibit lower pK_a values (3.7–4.0),[216] which limits their applicability in physiological contexts such as wound dressings. Previously reported carborhodol derivatives have primarily been explored as fluorescent imaging agents and copper-responsive probes.

However, their potential application as pH sensors or for ratiometric pH measurements has not been investigated, and no pK_a values or optical data for their protonated forms have been reported.

In this chapter, the influence of pH on the photophysical properties, such as absorption, emission, fluorescence quantum yield, and fluorescence lifetime, of newly synthesized carborhodol compounds (see Chapter 3, Figure 3.2) is investigated. Given that rhodol dyes are known to exhibit greater photostability than their parent compound fluorescein, the photostability of both the acidic and basic forms is also assessed, as this property is essential for reliable long-term pH monitoring.

4.2 Results and Discussion

4.2.1 Absorption Properties

The dependence of the absorption properties of carborhodols on pH was determined using photometric acid-base titrations in Britton Robinson buffer at pH levels ranging from 2.0 to 10 (Figure 4.2).

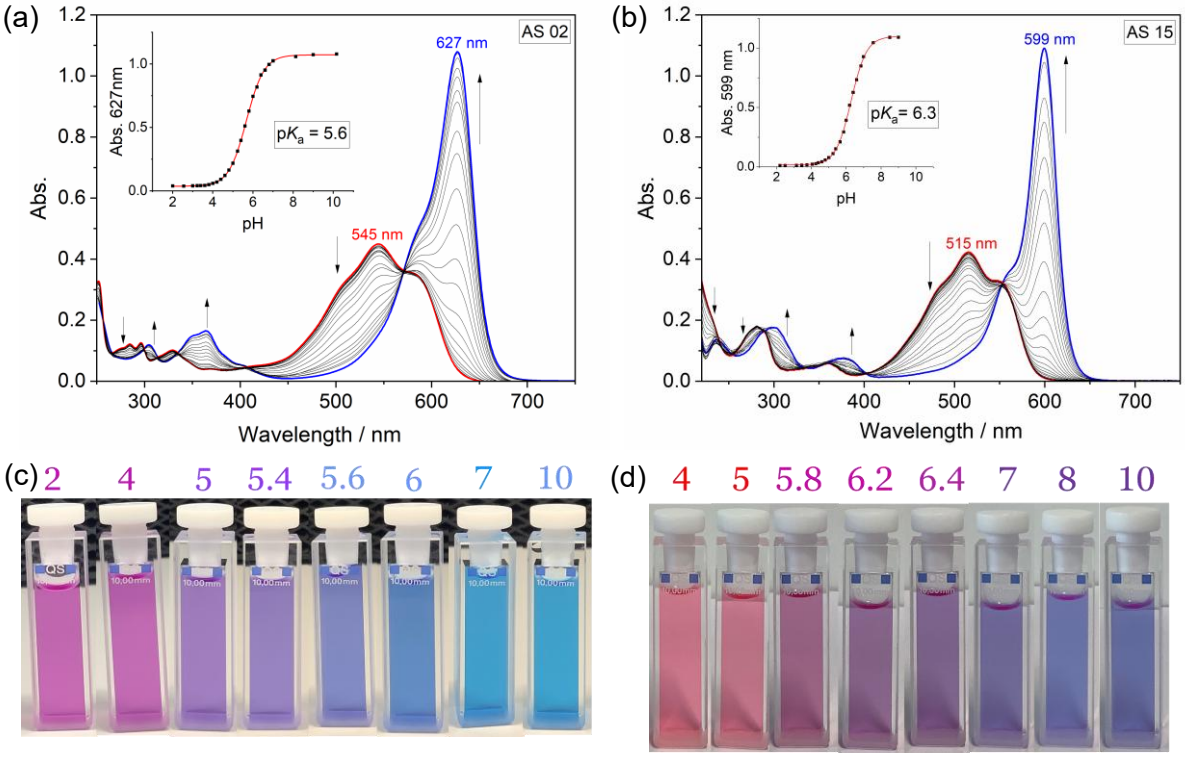

Figure 4.2. pH-dependent absorption spectra of (a) **AS 02** and (b) **AS 15**. Arrows in the spectra indicate the development of absorption bands as the pH increases. The red trace corresponds to the spectrum at pH 2, and the blue trace represents the spectrum at pH 10. Insets show the absorbance at 627 nm (**AS 02**) and 599 nm (**AS 15**) as a function of pH, with the red line denoting the best fit of the experimental data to the theoretical isotherm of a weak acid; the pK_a is determined from this plot. The corresponding visible color changes of (c) **AS 02** and (d) **AS 15** at different pH values.

All the carborhodol dyes exhibit significant spectral changes with increasing pH. Among the ten synthesized carborhodol derivatives, two representative compounds, **AS 02**, which bears

a halogenated aryl head group, and **AS 15**, featuring a coupling functionality, are discussed here.

In the case of **AS 02**, at acidic pH (pH 2), the absorption spectrum displays a broad band centered at 545 nm (red trace), corresponding to the protonated form of the dye. As the pH increases, this band gradually diminishes, while a new, narrow band with a higher absorbance emerges at 627 nm (blue trace), corresponding to the deprotonated form of the dye. The spectral shift is accompanied by a visible color change from magenta to sky blue (Figure 4.2c). The gradual shift in color across the pH range confirms the dye's capability for colorimetric pH sensing and monitoring pH changes in the wound by the naked eye. The measurement of the absorption spectrum at different pH clearly shows a well-defined isosbestic point in the visible region at 571 nm, indicating the conversion between two defined species, i.e., the protonated (acidic) and deprotonated (basic) form (Scheme 4.2). Additionally, less pronounced isosbestic points are also observed in the UV region at 300, 314, 334, and 407 nm. The absorption at λ_{max} = 627 nm was plotted against the pH value of the solution, and the experimental data were analyzed by a fit to the theoretical model for weak acids (Henderson–Hasselbalch)[227], giving a pK_a value of 5.6 (Figure 4.2a, inset).

For **AS 15**, the protonated form exhibits a broad absorption band centered at 515 nm, whereas the deprotonated form displays a narrow band at 599 nm. In addition to the isosbestic point at in the visible region (553 nm), isosbestic points are also observed in the UV region at 289, 338, and 401 nm (Figure 4.2b). The color gradually changes from pink to violet as the pH increases (Figure 4.2d). The pK_a of **AS 15** was determined to be 6.3, based on the sigmoidal fit of the absorbance at 599 nm versus pH (Figure 4.2b, inset). The remaining carborhodols exhibited similar trends. The results are summarized in Table 4.1, and the plot of absorption vs pH is provided in the Appendix associated with this chapter (Figure S1).

The protonated form of the carborhodol derivatives exhibits an absorption spectrum characterized by a broader and less structured band. This spectral feature is indicative of a molecular conformation that is either less rigid or less planar than its deprotonated counterpart. Such structural characteristics enable a more diverse population of vibrational states during the electronic transition, consequently contributing to the broadening of the absorption band.[83] Furthermore, the positive charge at the amine, combined with the presence of the hydroxyl group, restricts the effective delocalization of the π-electron system across the chromophore, which in turn leads to higher energy absorption.[57] Together, these structural and electronic features account for the broader and less intense absorption property of the acidic form.

Upon deprotonation under basic conditions, a redshifted, intense, and narrow absorption band emerges. This bathochromic shift reflects the formation of a phenolate anion, which enhances π-electron delocalization across the chromophore and promotes a more planar, quinoid-like structure. The time-dependent density functional theory (TD-DFT) studies of O-

rhodols have demonstrated that they possess a perfectly planar arrangement in their basic form, which facilitates effective p-orbital overlap between the terminal nitrogen and the oxygen.[218] The narrow bandwidth of the absorption band suggests a rigid and well-defined geometry in both the ground and excited states, minimizing vibrational broadening.[228]

The compounds exhibit pK_a values in the range from 5 to 7, indicating that the pK_a is only slightly affected by changes in molecular structure and the introduction of different substituents. This flexibility allows the structure to be adapted to desired optical and chemical properties without significantly altering the critical pK_a. A slight decrease in pK_a is observed for dyes bearing halogenated aryl head groups compared to those with carboxy-substituted aryl groups. This trend can be attributed to the inductive electron-withdrawing effects of the substituents at the 9-aryl position, which although not part of the conjugated chromophore, are electronically coupled through σ-bonds. For example, **AS 01** (with a dichlorophenyl head group) shows a relatively low pK_a of 5.2, whereas **AS 10**, **AS 11,** and **AS 13** (with carboxyphenyl head groups) exhibit pK_a values of 6.1– 6.2, even though all of them possess the same chromophoric system (Table 4.1). The chlorine atoms exert a stronger inductive effect than the carboxylate (-COO^-) group through σ-bonding, effectively withdrawing electron density from the xanthene core and stabilizing the phenoxide anion, thus lowering the pK_a.

Table 4.1. Absorption maxima and molar extinction coefficients of ten carborhodol derivatives, measured in acidic (pH 3) and basic (pH 10) aqueous buffer solutions, along with their pK_a values determined using Britton-Robinson buffer (pH range 2–10). For the acidic form, $\lambda_{\text{(higher abs.)}}/\lambda_{\text{(lower abs.)}}$ is given.

Dye	pK_a	Acidic form (pH 3 buffer)		Basic form (pH 10 buffer)	
		λ_{abs}, (nm)	ε ($M^{-1}cm^{-1}$)	λ_{abs}, (nm)	ε ($M^{-1}cm^{-1}$)
AS 01	5.2	518/551	35000	594	73000
AS 02	5.6	545/581	31000	627	83600
AS 03	5.6	548/591	16000	632	36000
AS 07	5.6	547/590	15000	635	33000
AS 10	6.2	511/545	14000	575	56000
AS 11	6.1	510/545	13000	573	75000
AS 12	6.6	511/545	17000	587	35000
AS 13	6.2	512/547	15000	578	72000
AS 14	5.7	516/549	22000	586	50000
AS 15	6.3	515/551	20000	599	50000

AS 01 exhibits a bathochromic shift of 20 nm in its basic form relative to analogues **AS 10** and **AS 11**, and 16 nm compared to **AS 13**. This red shift is likely due to the enhanced

stabilization of the polarized excited state by the electron-withdrawing chlorine atom in the phenyl head group of **AS 01**. The incorporation of a fused cyclohexane ring, as seen in analogues **AS 02**, **AS 03**, and **AS 07**, resulted in a more pronounced bathochromic shift compared to **AS 01**. Specifically, the acidic forms of these dyes, along with the basic form of **AS 02**, exhibited shifts of approximately 30 nm. For the basic forms of **AS 03** and **AS 07**, an even larger shift of about 40 nm was noted. These bathochromic shifts are primarily attributed to the restricted rotation of the amino group enforced by the fused ring, which significantly increases the planarity and rigidity of the chromophore, thereby promoting more efficient π-electron conjugation. In **AS 03** and **AS 07**, the combination of the fused ring with strong electron-withdrawing substituents, four fluorine atoms as opposed to two chlorine atoms, further amplifies this effect, resulting in greater red shifts. Additionally, the fused-ring system in **AS 12** induces a bathochromic shift 13 nm in its basic form when compared to **AS 11**. In the acidic form of all dyes, protonation of the amino group reduces its electron-donating ability, thereby disrupting conjugation. This could be the reason for the minimal changes in the absorption maximum upon varying substitutions compared to the basic form. Consistently across the series, as exemplified by **AS 02** and **AS 15**, the basic forms of all dyes exhibit higher molar extinction coefficients (ε) than their corresponding acidic forms (Table 4.1).

4.2.2 Fluorescence Properties

The pH-dependent fluorescence properties of the synthesized carborhodol dye, including fluorescence turn-on ratio, quantum yield, and fluorescence lifetime, were investigated in aqueous buffer solutions at pH 3 and pH 10, corresponding to their protonated (acidic) and deprotonated (basic) forms, respectively. In addition, these photophysical parameters were measured in ethanol under both acidic (EtOH with 0.1% v/v TFA) and basic (EtOH with 0.2% v/v DIPEA) conditions.

Fluorescence Turn-On Ratio

For all dyes, the basic form is strongly fluorescent in comparison to its acidic form, both in aqueous buffer and in ethanol. To quantify this difference, fluorescence turn-on ratios were calculated using the relative quantum yield method, as described in Chapter 2.5.3. In this approach, the basic form of each dye was used as the reference standard, with its quantum yield arbitrarily set to 100. The quantum yield of the corresponding acidic form was then determined relative to this reference. The resulting ratio represents the fluorescence enhancement of the basic form and is referred to as the fluorescence turn-on ratio. Each form was excited at its respective absorption maximum, ensuring matched absorbance at the excitation wavelength. The fluorescence turn-on ratios, emission maxima of both acidic (a) and

basic (b) forms, and Stokes shifts in aqueous buffer and in EtOH of all compounds are summarized in Table 4.2.

Table 4.2. The turn-on ratio, emission maximum of acidic (a) and basic (b) forms (T = 23 °C, Abs. = 0.04–0.05 in a 1 cm cuvette, $\lambda_{exc} = \lambda_{abs}$ (Table 4.1) for each dye, λ_{abs} in EtOH is given in Chapter 5 (Tables 5.1 to 5.5); and Stokes shifts ($\lambda_{em}-\lambda_{abs}$) in aqueous buffer and EtOH.

Dye	Buffer			EtOH		
	Turn on ratio	λ_{em} (nm) a / b	Stokes Shift (nm) a / b	Turn on ratio	λ_{em} (nm) a / b	Stokes shift (nm) a / b
AS 01	48	619 (b) 590 (a)	24 (b) 72 (a)	62	618 (b) 603 (a)	45 (b) 32 (a)
AS 02	4.0	659 (b) 660 (a)	32 (b) 115 (a)	8.0	661 (b) 674 (a)	48 (b) 113 (a)
AS 03	36	662 (b) 649 (a)	30 (b) 101 (a)	36	663 (b) 648 (a)	48 (b) 82 (a)
AS 07	3.6	669 (b) 653 (a)	34 (b) 106 (a)	8.0	674 (b) 655 (a)	59 (b) 90 (a)
AS 10	38	605 (b) 586 (a)	30 (b) 76 (a)	49	593 (b) 592 (a)	38 (b) 34 (a)
AS 11	17	602 (b) 586 (a)	28 (b) 76 (a)	36	595 (b) 587 (a)	40 (b) 32 (a)
AS 12	1.9	615 (b) 599 (a)	27 (b) 88 (a)	1.5	607 (b) 594 (a)	35 (b) 34 (a)
AS 13	27	605 (b) 586 (a)	27 (b) 74 (a)	48	599 (b) 588 (a)	41 (b) 31 (a)
AS 14	29	614 (b) 597 (a)	28 (b) 81 (a)	44	614 (b) 596 (a)	48 (b) 34 (a)
AS 15	1.7	624 (b) 625 (a)	25 (b) 110 (a)	1.5	628 (b) 600 (a)	40 (b) 35 (a)

Among the ten synthesized carborhodol derivatives, two representative compounds were selected for detailed photophysical analysis. The *N*,*N*-dimethylamino-substituted derivative **AS 01** exhibited the highest fluorescence turn-on ratio. In contrast, **AS 02**, which contains a fused-ring system at the amino position, exhibited a comparatively lower turn-on ratio, thereby allowing for a more distinct observation of its emission band in the acidic form (Figure 4.3).

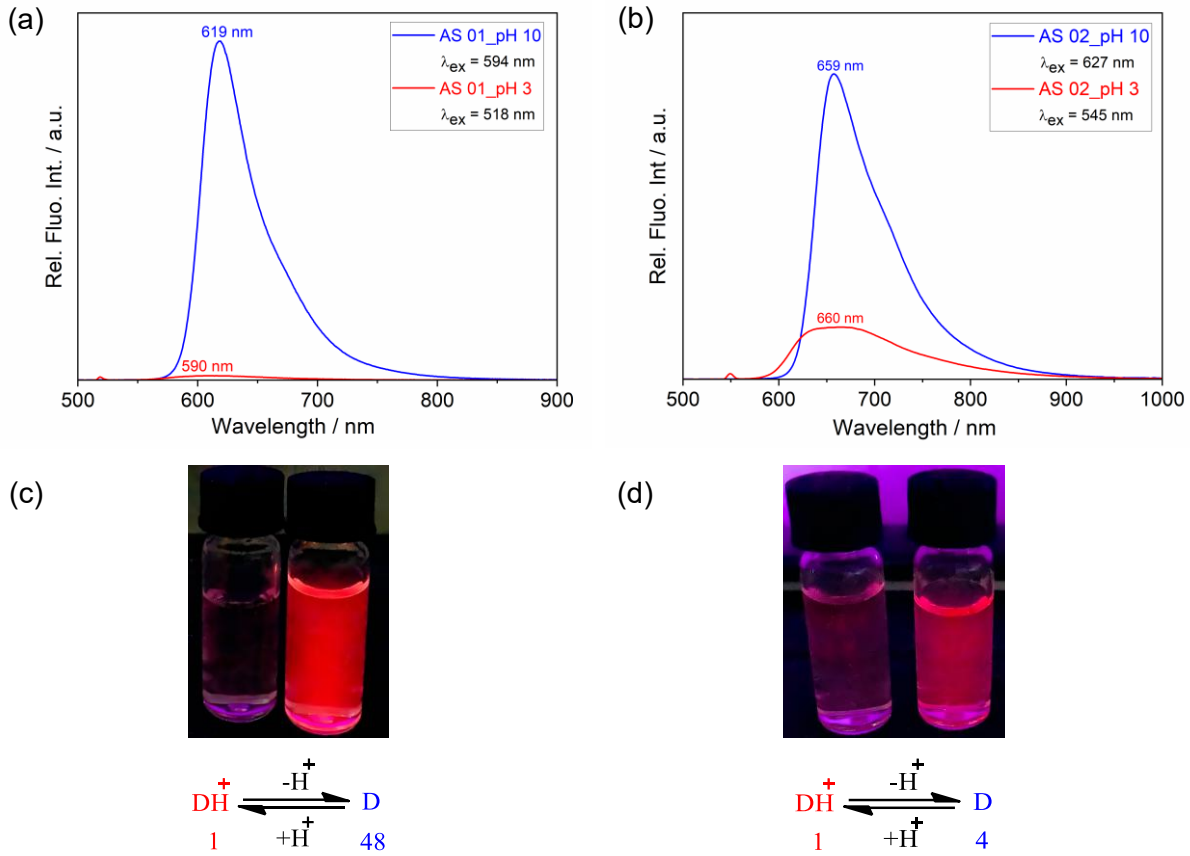

Figure 4.3. Fluorescence spectra of carborhodol dyes recorded in aqueous buffer at pH 10 (blue trace) and pH 3 (red trace). Emission spectra of (a) **AS 01**, excited at their respective absorption maxima: 518 nm (pH 3) and 594 nm (pH 10), and (b) **AS 02**, excited at 545 nm (pH 3) and 627 nm (pH 10). Photographic images of dye solutions in pH 3 (left) and pH 10 (right) buffers under 365 nm UV illumination for (c) **AS 01** and (d) **AS 02,** illustrating the pronounced fluorescence enhancement under basic conditions. These solutions were used to record the emission spectra shown in the figure above. For each pair (acidic and basic forms), the absorbance was adjusted to a constant value in the range of 0.04–0.05 in a 1 cm cuvette, at the excitation wavelength to ensure comparability of fluorescence intensity.

As shown in Figure 4.3a and b, the emission profile of the dye changes significantly with pH. At pH 10 (blue trace), corresponding to the dye's basic form, a strong and narrow fluorescence emission band is observed at 619 nm for **AS 01** and at 659 nm for **AS 02**. Conversely, at pH 3 (red trace), both dyes exhibit significantly reduced fluorescence intensities with broader emission bands, with maxima at 609 nm for **AS 01** and 660 nm for **AS 02**. The basic form of **AS 01** shows a 48-fold higher fluorescence than the acidic form, and the turn-on ratio for **AS 02** is 4. Photographs of the corresponding dye solutions under UV illumination (Figure 4.3c and 4.3d) visually confirm the spectroscopic findings. In both cases, the dye in

basic solution emits brightly, whereas the acidic solution exhibits weak fluorescence for **AS 02** (Figure 4.3d) and practically non-fluorescent to the naked eye for **AS 01** (Figure 4.3c) under UV irradiation.

Figures 4.4 and 4.5 illustrate the fluorescence enhancement of the basic form of all the dyes in aqueous buffer and EtOH, respectively. The emission spectra of the remaining carborhodol derivatives in aqueous buffer and EtOH are provided in the Appendix associated with this chapter (Figure S2 and Figure S3, respectively).

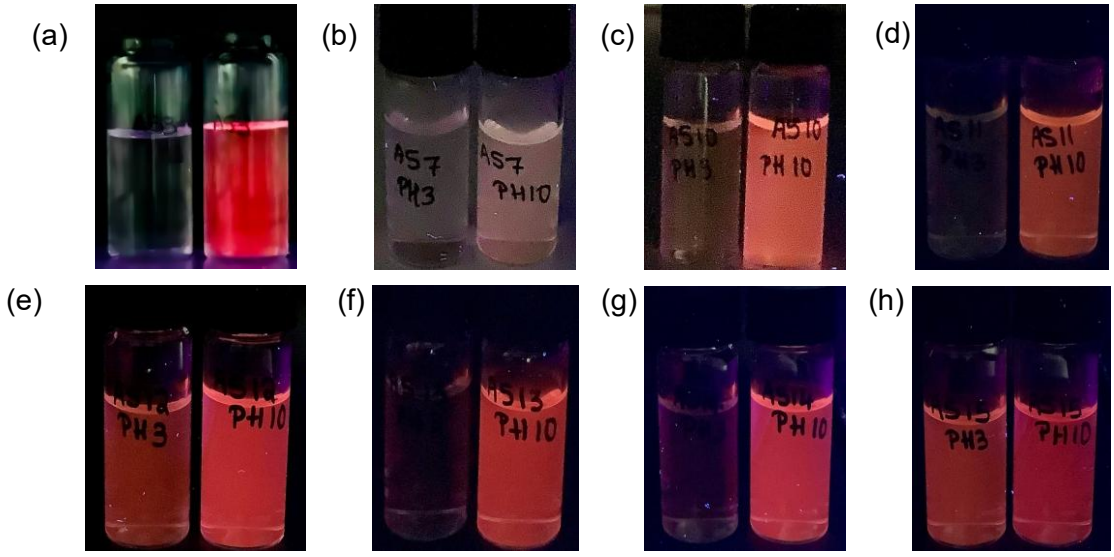

Figure 4.4. Photographic images of dye solutions in pH 3 (left) and pH 10 (right) buffers under 365 nm UV illumination for (a) **AS 03**, (b) **AS 07**, (c) **AS 10**, (d) **AS 11**, (e) **AS 12**, (f) **AS 13**, (g) **AS 14**, and (h) **AS 15**. Each pair has the same absorbance in the range of 0.04–0.05 in a 1 cm cuvette.

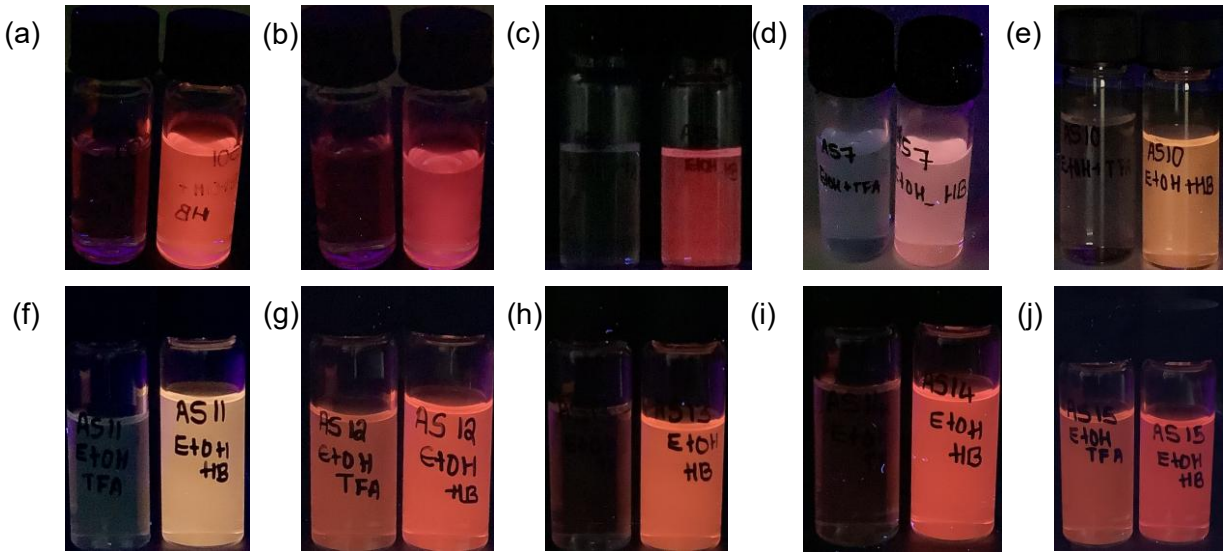

Figure 4.5. Photographic images of dye solutions in acidic EtOH (left) and Basic EtOH (right) under 365 nm UV illumination for (a) **AS 01**, (b) **AS 02**, (c) **AS 03**, (d) **AS 07**, (e) **AS 10**, (f) **AS 11**, (g) **AS 12**, (h) **AS 13**, (i) **AS 14**, and (j) **AS 15**. Each pair has the same absorbance in the range of 0.04–0.05 in a 1 cm cuvette.

The compounds can be effectively used either as ratiometric or as fluorogenic sensors, e.g., to determine the pH of the surrounding medium or environment, or its change during a chemical reaction, a biochemical process, or a metabolic process. The visual difference highlights its utility as a fluorescent turn-on probe in pH-responsive wound dressings. A dressing material with these dyes incorporated would exhibit strong fluorescence (fluorescence turn-on) in chronic wound conditions, and while low or no fluorescence (fluorescence turn-off) would occur in healing wounds.

Carborhodol derivatives bearing fused-ring systems through fully annulated C-N bonds, such as **AS 02**, **AS 07**, **AS 12**, and **AS 15**, generally exhibit lower turn-on ratios compared to those bearing *N,N*-dimethylamino substituents, except **AS 03**. Furthermore, all compounds, except **AS 03**, **AS 12**, and **AS 15**, exhibit enhanced turn-on behavior in ethanol compared to aqueous buffer, while these three analogues display similar turn-on ratios in both media. In line with their absorption properties, the presence of a fused cyclohexane ring, as present in **AS 02**, **AS 03**, and **AS 07**, induces a notable bathochromic shift of approximately 40–50 nm in both solvent environments relative to **AS 01,** which can be attributed to the reduced rotational freedom of the amino substituent and enhanced π-conjugation across the dye scaffold. In particular, the acidic form of **AS 02** in ethanol exhibits a red shift of 71 nm. Similarly, the incorporation of a fused-ring system in **AS 12** results in an approximately 10 nm red shift in both its basic and acidic forms compared to its structural analogue **AS 11** in both solvents.

These compounds exhibit notably large Stokes shifts, typically ranging from 20 to 120 nm. In particular, the protonated (acidic) forms in aqueous buffer display pronounced Stokes shifts between 74 and 115 nm. A large Stokes shift is very beneficial for multiplexing applications, where various dyes are excited simultaneously at one single wavelength and their spectrally separated fluorescence is detected within different emission channels. The spectral separation of excitation light with optical filters is easier for dyes with a larger Stokes shift. This results in a better signal-to-noise ratio and thus a higher detection sensitivity.

An additional advantage of the compounds is their absorption and fluorescence at wavelengths above 550 nm or even above 600 nm in the red region of the visible spectrum. In this spectral region, there is little inherent natural fluorescence in biological samples. Lower absorption and less scattering of light with increasing wavelength enable a greater depth of penetration of the excitation light into samples like blood and tissue.[229] This facilitates a more reasonable and sensitive pH detection in biofilms or infected wounds, respectively.

Fluorescence Quantum Yield and Lifetime

The fluorescence quantum yields (Φ_{fl}), of the carborhodol dyes were determined using established relative methods with well-characterized standards. For measurements in basic conditions (pH 10 buffer), **ATTO 647N** carboxy (Φ_{fl} = 65% in PBS)[230] was used as the

reference. Under acidic conditions (pH 3 buffer), the sample was compared against two standard fluorophores: rhodamine 6G (Φ_{fl} = 95.5% in EtOH)[231] and rhodamine B (Φ_{fl} = 34% in pH 3 buffer, at T = 23 °C, as determined by comparative measurements with rhodamine 6G in EtOH). For measurements in ethanol, **ATTO 647N** carboxy (Φ_{fl} = 88% in acidic EtOH) served as the reference for the basic form, while rhodamine 6G (Φ_{fl} = 95.5% in EtOH) was used for the acidic form. The reference and sample were excited at their respective absorption maxima, with absorbance matched at the excitation wavelengths.

An example of the fluorescence spectral distribution for the sample **AS 12**, along with the reference standards, is presented in Figure 4.6.

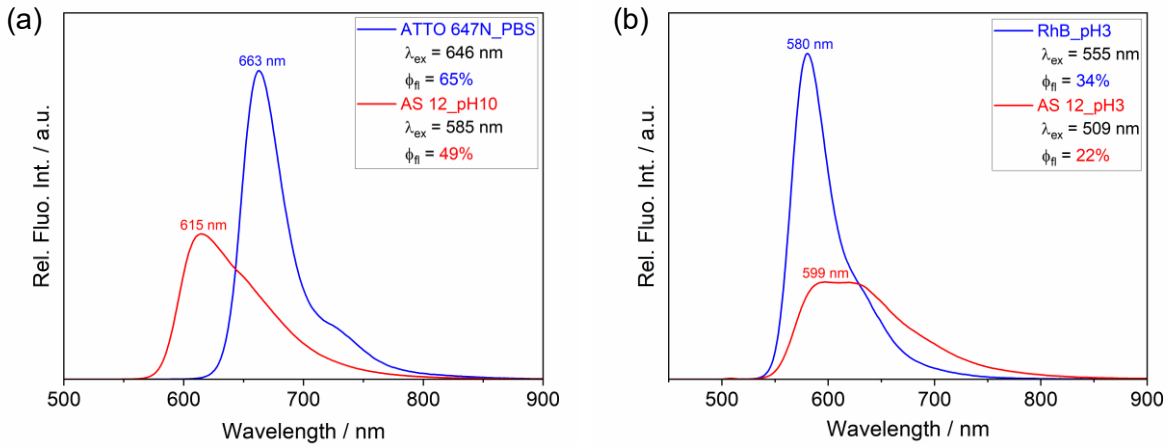

Figure 4.6. Fluorescence spectra of **AS 12** in its (a) basic and (b) acidic forms in buffer for the determination of the fluorescence quantum yield. The red trace corresponds to the emission spectrum of **AS 12**, while the blue trace represents the respective standard. Measurements were conducted at 23°C with absorbance values of 0.04–0.05 in a 1 cm pathlength cuvette.

Consistent with observations for **AS 01** and **AS 02**, the basic form of **AS 12** displayed a relatively sharp emission band centered at 615 nm, whereas the acidic form showed a significantly broader emission profile, spanning from 590 to 630 nm, with a maximum at 599 nm. The Φ_{fl} of remaining carborhodols (both acidic and basic forms) in aqueous buffer and in EtOH is summarized in Table 4.3.

Table 4.3. Fluorescence quantum yield of acidic and basic forms of carborhodols in buffer and EtOH (T = 23 °C, Abs. = 0.04–0.05 in a 1cm cuvette, $\lambda_{exc} = \lambda_{abs}$ (Table 4.1) for each dye, λ_{abs} in EtOH is given in Chapter 5 (Tables 5.1 to 5.5).

Dye	Φ_{fl} (%) Basic form		Φ_{fl} (%) Acidic form	
	Buffer	EtOH	Buffer	EtOH
AS 01	35	66	0.60	1.1
AS 02	15	41	3.2	4.2
AS 03	7.5	26	0.16	0.61
AS 07	5.8	19	1.5	2.2
AS 10	38	89	1.6	1.1
AS 11	40	79	2.0	1.7
AS 12	49	91	22	44
AS 13	43	75	1.3	1.6
AS 14	36	78	1.1	1.8
AS 15	48	72	22	46

Since the fluorescence quantum yield is directly proportional to the fluorescence lifetime (τ), both of which reflect the efficiency of radiative versus non-radiative decay processes,[58] the same trend with the quantum yield values is observed in lifetime measurements as well. The fluorescence lifetimes of both the basic and acidic forms of the dyes in their respective buffer and EtOH conditions were determined using the TCSPC technique, as described in Chapter 2.5.3, and the compilation of the measured fluorescence lifetimes is provided in Table 4.4. From the bi-exponential fit, the lifetime of the dominant species was used to represent the system's decay behavior. The minor component, contributing less than 5%, was considered negligible in this context.

Table 4.4. Fluorescence lifetimes of the acidic and basic forms of carborhodols measured in buffer and ethanol. The quality of fits was assessed using reduced χ^2 values and the distribution of weighted residuals. For the basic form, bi-exponential fits with χ^2 values between 0.900 and 1.200 and an even distribution of the residuals were selected as optimal. For the acidic form with very short lifetime components ($\tau \leq 0.2$ ns), bi-exponential fits with slightly elevated χ^2 values (1.2–1.4) were accepted due to the increased fitting complexity.

Dye	τ, (ns) Basic form		τ, (ns) Acidic form	
	Buffer	EtOH	Buffer	EtOH
AS 01	1.8	3.9	0.20	0.07
AS 02	1.2	3.0	0.50	0.60
AS 03	0.64	2.1	0.30	0.16
AS 07	0.56	1.7	0.23	0.36
AS 10	2.2	4.3	0.16	0.16
AS 11	2.2	4.2	0.10	0.10
AS 12	2.9	4.3	1.5	3.1
AS 13	2.2	4.3	0.16	0.35
AS 14	1.9	4.2	0.21	0.35
AS 15	2.7	4.2	1.6	2.9

In all cases, the basic form of the carborhodol dyes exhibits both higher fluorescence quantum yields and longer fluorescence lifetimes compared to their acidic form. Among the basic forms, **AS 12** showed the highest fluorescence efficiency, with Φ_{fl} values of 49% in aqueous buffer and 91% in ethanol, and corresponding lifetimes of 3.0 ns and 4.4 ns, respectively. In contrast, **AS 07** displayed the lowest Φ_{fl} in the basic form, with values of 5.8% in buffer and 19% in ethanol, and lifetimes of 0.56 ns and 1.7 ns, respectively. The markedly reduced emission of **AS 07** in its basic form is demonstrated in Figure 4.4b, where its brightness is significantly lower than that of the other dyes.

For the acidic form, **AS 12** and **AS 15** exhibited the highest fluorescence quantum yields, with values of 22% for both in buffer, and 44% and 46% in EtOH, and **AS 12** also showed the longest fluorescence lifetime in the acidic form, with 3.2 ns in ethanol and 1.5 ns in buffer, followed closely by **AS 15**, which had a lifetime of 1.6 ns in buffer. In contrast, **AS 03** exhibited

the lowest Φ_{fl} in the acidic form, with values of only 0.64% in buffer and 0.16% in ethanol. The shortest fluorescence lifetimes in the acidic form were observed for **AS 11**, with 0.10 ns in both buffer and ethanol, and **AS 01**, which also showed 0.10 ns in ethanol.

The fluorescence characteristics of the dye can be explained based on the structural differences between its protonated (acidic) and deprotonated (basic) forms, as shown in Scheme 4.2. In the basic form, deprotonation induces a planar, extensively conjugated π-system that facilitates delocalization of excited-state electron density across the molecule.[218] This structural rigidity suppresses nonradiative relaxation pathways, promoting efficient fluorescence and resulting in a high quantum yield and prolonged fluorescence lifetime. The emission spectrum of the basic form strongly overlaps with the absorption spectrum, accompanied by relatively narrow spectral bands (Figure 4.7a), a typical characteristic of symmetric, rigid fluorophores like rhodamines, and indicates minimal geometric reorganization and dipole moment change upon excitation, resulting in a small Stokes shift.[232]

In contrast, the acidic form exhibits significantly reduced fluorescence efficiency. This can be attributed to disrupted conjugation and increased conformational flexibility, particularly around the protonated amino group in non-fused analogues bearing an *N,N*-dimethylamine group, which enhances nonradiative decay processes. The absence of strong mirror-image symmetry between the absorption and emission spectra, with broader bands in the acidic form (Figure 4.7b), and the larger Stokes shift observed for the acidic form, supports the idea that there are more electron distribution changes during excitation, followed by excited-state structural relaxation and nonradiative deactivation.[232]

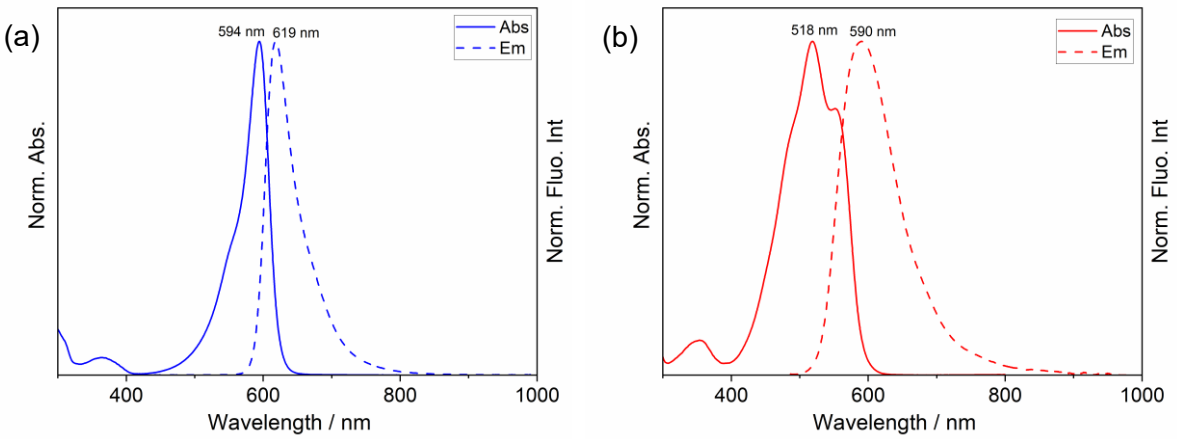

Figure 4.7. Normalized absorption and emission spectra of **AS 01** in (a) its basic form and (b) its acidic form in buffer. (T = 23 °C, Abs. = 0.04–0.05 in a 1 cm cuvette, $\lambda_{exc} = \lambda_{abs}$).

Incorporation of the terminal amino groups into a rigid ring system increases the chromophores structural rigidity, which typically enhances fluorescence quantum yield by suppressing nonradiative decay pathways.[210] This trend is also observed in the current study. However, the effect of rigidification is more pronounced in the acidic form than in the basic

form of the dyes. For instance, **AS 12**, a ring-fused analogue of **AS 11**, exhibits a moderate increase in quantum yield and fluorescence lifetime in the basic form, from 40% to 49%, and from 2.2 ns to 3.0 ns, respectively. In contrast, the acidic form shows a substantial enhancement: the quantum yield increases from 2% (**AS 11**) to 22% (**AS 12**), and the lifetime from 0.1 ns to 1.5 ns. These results support the conclusion that fluorescence quenching in the acidic form is primarily due to the free rotation of the protonated terminal amino group, which facilitates nonradiative decay. Restricting this motion through ring fusion significantly reduces quenching and improves the fluorescence properties of the acidic form. Consequently, the fluorescence turn-on ratios of the ring-fused analogues (**AS 02, AS 07, AS 12**, and **AS 15**), except **AS 03**, are lower compared to their *N,N*-dimethyl analogues (Table 4.2).

AS 02 is the ring-fused analogue of **AS 01**. As discussed earlier, the acidic form of **AS 02** exhibits an increase in both fluorescence quantum yield (from 0.6% to 3%) and lifetime (from 0.2 ns to 0.5 ns), consistent with the suppression of nonradiative decay due to rigidification. In contrast, the basic form of **AS 02** exhibits a decrease in both quantum yield (from 35% to 15%) and lifetime (from 1.8 ns to 1.2 ns), compared to **AS 01**. This unexpected reduction may be attributed to the presence of a double bond within the fused ring system, which has been reported to diminish fluorescence efficiency relative to fused systems lacking such unsaturation.[233] It is possible that the quenching effect introduced by the double bond offsets the fluorescence-enhancing benefit typically conferred by increased rigidity. This interpretation is further supported by **AS 12**, a structurally related ring-fused analogue of **AS 02** that lacks the double bond and demonstrates improved quantum yield (49%) and lifetime (3 ns) in the basic form. Experimentally, this hypothesis could be validated by hydrogenating **AS 02** to remove the double bond and re-evaluating its photophysical properties. Similarly, other fused-ring compounds such as **AS 03** and **AS 07**, which also contain a double bond, display reduced quantum yields and lifetimes in their basic forms, providing additional support to this structure-property relationship.

The acidic form of **AS 03** also exhibits a reduced fluorescence quantum yield, which contributes to the exceptionally higher fluorescence turn-on ratio (36) observed for this ring-fused carborhodol dye. The distinct behavior of **AS 03** compared to its analogue **AS 07** may arise from the presence of a protonated amino group in the taurine moiety. This positively charged site could influence the excited-state dynamics by introducing additional nonradiative decay pathways. In general, the quantum yield and fluorescence lifetime of the dyes increase when moving from aqueous buffer to ethanol, due to reduced hydrogen bonding and lower non-radiative quenching.[231] For example, in **AS 13**, a carborhodol with a terminal *N,N*-dimethyl amino group, the basic form shows a substantial increase in Φ_{fl} (43% to 75%) and lifetime (2.2 ns to 4.3 ns), while the acidic form changes only slightly (Φ_{fl}: 1.3% to 1.6%; lifetime: 0.2 ns to 0.4 ns). This leads to a higher fluorescence turn-on ratio in ethanol. In the ring-fused

analog, for example, **AS 15**, the quantum yield of both the basic and acidic forms significantly increases (basic Φ_{fl}: 48% to 72%; acidic Φ_{fl}: 22% to 46%), reflecting greater solvent sensitivity in both states. As discussed previously, acidic forms of rotation-allowed analogs possess efficient internal non-radiative decay pathways, making them less responsive to solvent changes. For ring-closed analogs, turn-on ratios are generally similar in both solvents, except for **AS 03** and **AS 07**, which exhibit higher turn-on in ethanol. This may be due to additional solvent interactions, and further investigation is needed. Solvent effects are discussed in more detail in Chapter 5.

4.2.3 Photostability Assessment

Compared to the parent fluorescein, rhodols offer greater photostability.[84] High chemical and photochemical stability is essential for future applications. The photostability experiment is designed to measure the photodegradation (decrease in absorbance) of the dye solution as a function of time of irradiation. It was measured under stress conditions by irradiation of both acidic and basic forms in aqueous buffer solutions with a 575 W mercury halide lamp. Fluorescein was used as a pH-sensitive dye standard for the shorter wavelength region, and Cyanine 5 (Cy5), a commonly used NIR fluorescent label, for the long wavelength region, along with the particularly photostable red-emitting dye **ATTO 643**.

Photostability was assessed by monitoring the decrease in absorbance at λ_{max} over time during continuous irradiation. The retained absorbance at each time point was calculated as $(A_t / A_0) \times 100$, where A_0 is the absorbance at $t = 0$. The resulting values were plotted against the irradiation time to assess the rate and extent of photodegradation (Figure 4.8). The photostability profile of both acidic and basic forms in aqueous buffer over 24 hours (1440 minutes) of continuous irradiation is provided in the Appendix associated with this chapter (Figure S4).

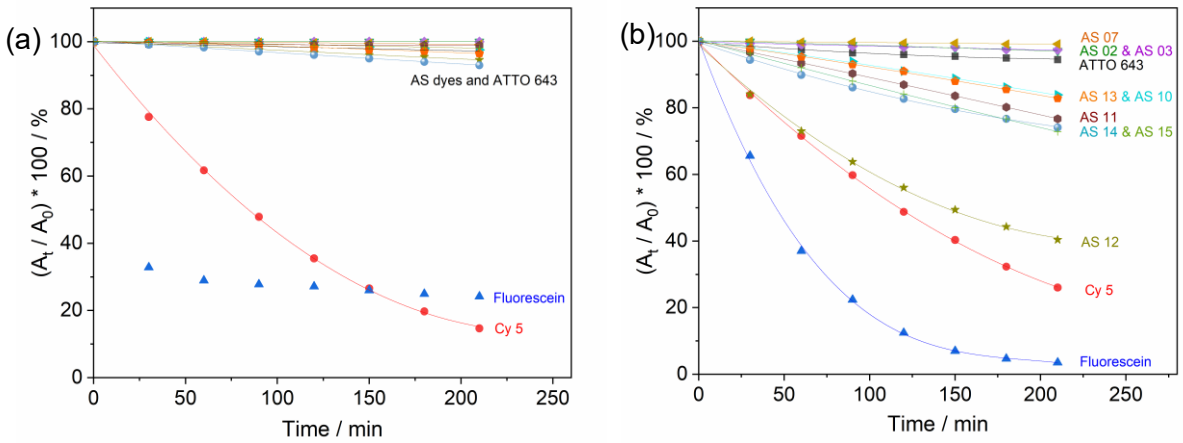

Figure 4.8. Photostability profile of the (a) acidic form and (b) the basic form in pH 3 and pH 10 buffer, respectively, over 3.5 hours of continuous irradiation (575 W mercury halide lamp).

The photostability of the acidic form was comparable to that of the highly photostable, hydrophilic dye **ATTO 643** (Figure 4.8a), and both forms are photostable than that of the commercially available dyes fluorescein and Cy5. As a general trend, the acidic forms of all dyes demonstrated a superior photostability as compared to their corresponding basic forms. Moreover, dyes containing halogenated aryl head groups exhibited greater resistance to photodegradation than those bearing carboxy-substituted aryl groups. For instance, in the case of the fluorinated analog **AS 03**, the basic form displayed only 3% loss in absorbance after 210 minutes of irradiation and 10% after 1440 minutes. In contrast, the acidic form of **AS 03** remained highly stable, showing no observable degradation after 210 minutes and less than 1% degradation after 1440 minutes of continuous exposure (Figure S5). Additionally, no shift of the absorption maximum was detected, indicating structural stability (Figure 4.9).

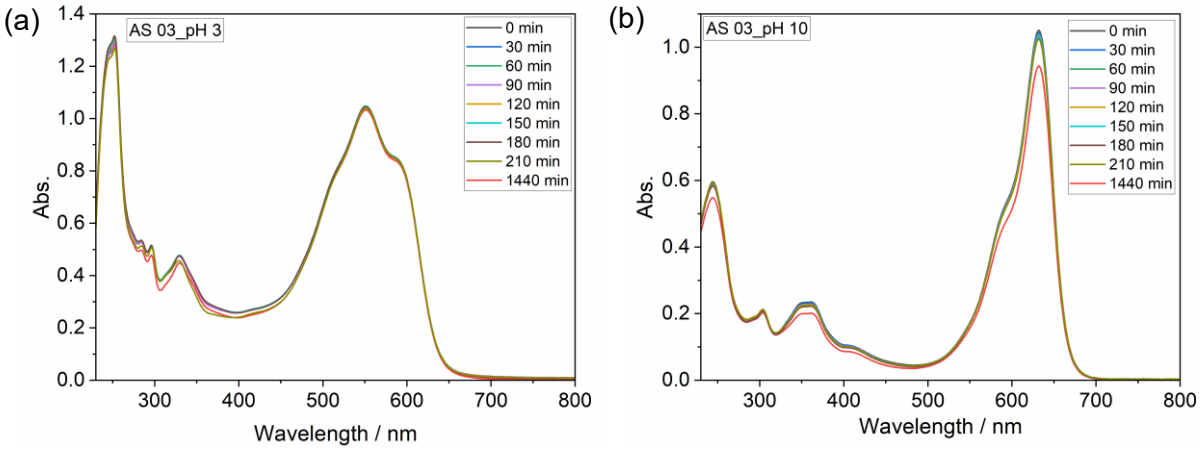

Figure 4.9. Absorption spectra of **AS 03** recorded during the photostability experiment over 24 hours in (a) pH 3 buffer and (b) pH 10 buffer.

According to Sun et al., the enhanced resistance to photobleaching of fluorinated derivatives may be due to the shorter triplet lifetimes, which diminish the likelihood of photochemical processes, or to the generally lower (photo)chemical reactivity of fluorinated compounds, likely due to their ability to stabilize the aromatic system and suppress photochemical degradation pathways in comparison to their non-fluorinated analogs.[213]

In the case of **AS 10**, featuring a carboxylic acid coupling functionality, the basic form of **AS 10** showed 16% and 68% degradation after 210 and 1440 minutes, respectively, whereas the acidic form degraded by only 2% and 30% over the same time periods (Figure S4). After 1440 minutes of irradiation, the acidic forms of **AS 10** and its elongated structural analog **AS 13** exhibited hypsochromic shifts of 13 nm and 15 nm, respectively, in their main absorption bands, and 17 nm and 26 nm, respectively, in their secondary absorption maxima. Additionally, both absorption bands of **AS 10** and **AS 13** had nearly converged in intensity (refer to Figure 4.10a for **AS 10** and to Figure S5 for **AS 13**). This spectral behavior is possibly attributable to the demethylation of the protonated amine functionality under prolonged

irradiation. No shift of the absorption maximum was observed for the basic form of **AS 10** and **AS 13** after 1440 minutes of irradiation (refer to Figure 4.10b for **AS 10** and to Figure S5 for **AS 13**).

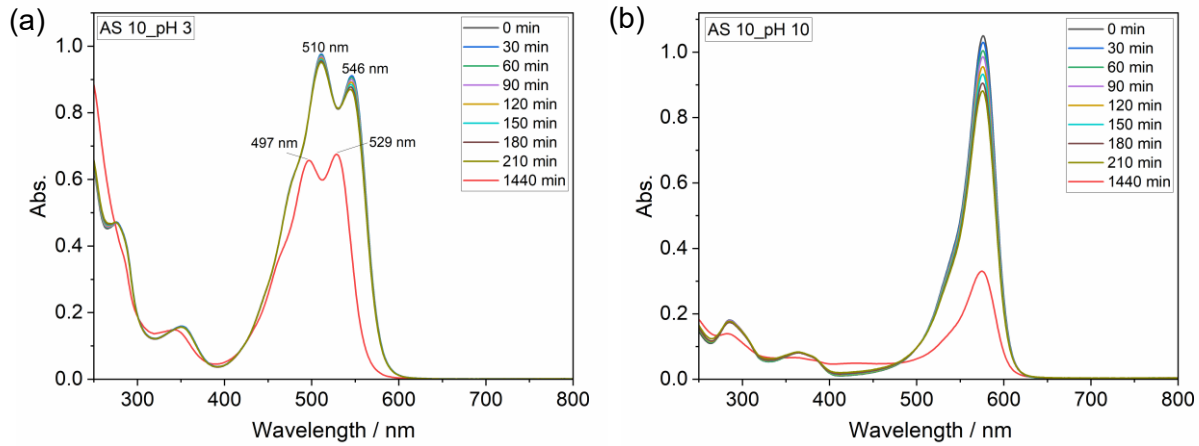

Figure 4.10. Absorption spectra of **AS 03** recorded during the photostability experiment over 24 hours in (a) pH 3 buffer and (b) pH 10 buffer.

Among all dyes, the basic forms of those bearing carboxy-substituted aryl groups exhibited the highest degree of photodegradation, with **AS 12** showing the most pronounced decrease in absorbance. This could be due to the formation of carboxylate anions under basic conditions, which can facilitate reactivity through interactions with solvent molecules or reactive oxygen species. Additionally, the basic forms of **AS 12** and its elongated analog, **AS 15**, displayed about a 20 nm hypsochromic shift after 1440 minutes of continuous irradiation (Figure S5), potentially due to the amine dealkylation.

Due to the hydrophobic nature of dye **AS 01**, it was not possible to dissolve it sufficiently in aqueous buffer to reach an absorbance of 1. As a result, buffer conditions were excluded from the photostability tests. Instead, photostability was evaluated in acidic and basic ethanol solutions along with **AS 02**, **AS 03**, **AS 07**, and **AS 10** (Figure 4.11).

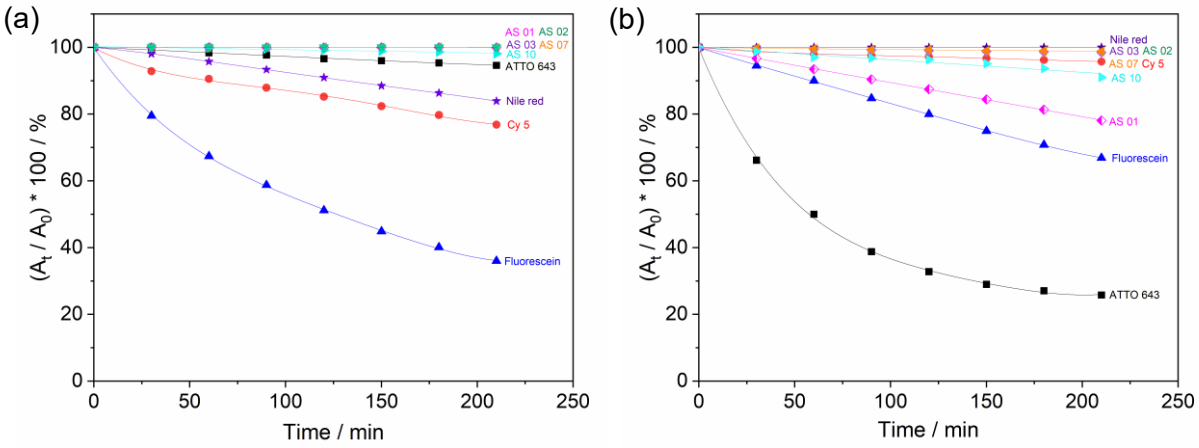

Figure 4.11. Photostability profile of the (a) acidic form and the (b) basic form in EtOH over 3.5 hours of continuous irradiation.

Under Ethanol conditions, **AS 01** exhibited high stability in its acidic form, with no detectable degradation after 210 minutes (Figure 4.11a). In contrast, a 22% decrease in absorbance was observed in the basic form over the same period (Figure 4.11b). **AS 02**, **AS 03**, **AS 07**, and **AS 10** exhibited comparable photostability in ethanol and buffer under both acidic and basic conditions. This suggests that **AS 01** likely follows a similar photostability trend in buffer, and that the overall stability behavior of these dyes remains consistent across different solvent environments.

Figure 4.12 presents photographs of the dye solutions in both acidic and basic forms before and after 1440 minutes of continuous irradiation. Corresponding absorption spectra and degradation profiles over the 24 hours are provided in the Appendix (Figures S5 and S4, respectively).

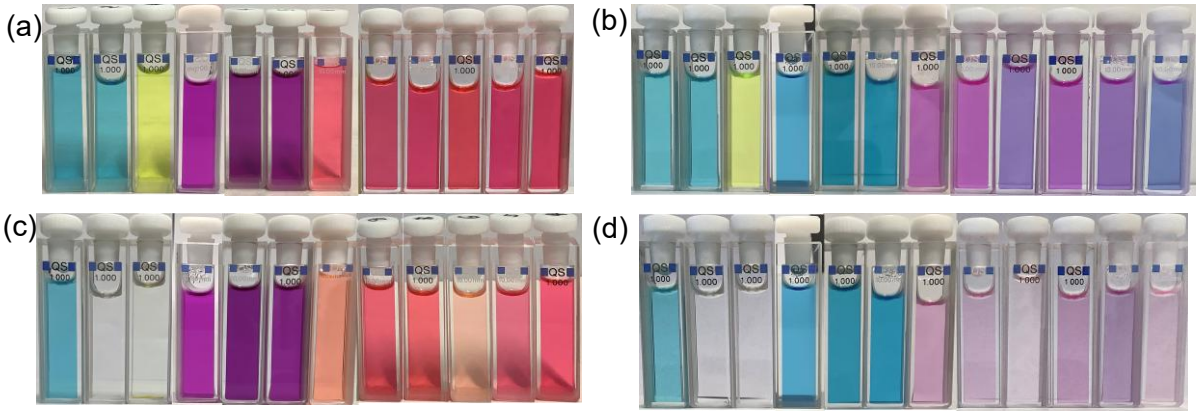

Figure 4.12. Photographs of the dye solutions before and after 24 hours of irradiation. Cuvettes contain dye solutions in buffer, arranged (left to right) as: **ATTO 643**, Cy5, Fluorescein, **AS 02**, **AS 03**, **AS 07**, **AS 10**, **AS 11**, **AS 12**, **AS 13**, **AS 14**, and **AS 15**. Panels show: (a) Dyes in pH 3 buffer at 0 min, (b) dyes in pH 10 buffer at 0 min, (c) dyes in pH 3 buffer after 1440 min of irradiation, and (d) dyes in pH 10 buffer after 1440 min of irradiation.

Under these photochemical stress conditions, both Cy5 and fluorescein exhibited complete bleaching, with no visible color remaining in either pH state after 24 hours. In contrast, all carborhodol dyes demonstrated superior photostability. The acidic form of all carborhodols and the basic form of carborhodols with halogenated aryl head groups retained their color visibly even after prolonged exposure (Figure 4.12c and d). The basic form of the carborhodols with a carboxyphenyl head group analogs maintained weak coloration (Figure 4.12d) but still performed significantly better compared to fluorescein and Cy 5, which exhibited approximately 95% and 80% degradation, respectively, after 3.5 hours of continuous irradiation.

It is important to note that the photostability test was performed under high-intensity irradiation (575 W), representing accelerated degradation conditions far more extreme than those encountered in practical applications such as wound dressings. Higher photostability makes these compounds ideal candidates not only for prolonged usage in wound dressings during the long-term monitoring of wound pH but also for the application in high-resolution

microscopy or nanoscopy, where high laser power for the excitation of fluorescent labels is used.

4.3 Conclusion and outlook

The pH-dependent photophysical properties of the newly synthesized carborhodol derivatives, including absorption, emission, fluorescence quantum yield, and fluorescence lifetime, were investigated in both aqueous buffer and ethanol. All compounds exhibit pronounced spectral shifts in their absorption profiles as a function of pH, with increased absorbance observed under basic conditions. The pK_a values of the dyes fall within a range of 5 to 7, making them well-suited for physiological pH sensing applications, such as in wound dressings for the reliable detection of bacterial infections in chronic wounds.

Upon deprotonation, the dyes adopt a more planar and rigid structure, promoting efficient π-conjugation from the donor (amino group) to the phenolate oxygen. This structural reorganization in the basic form enhances photophysical performance, including stronger absorption, higher fluorescence quantum yields, and longer excited-state lifetimes relative to the acidic form.

Among the studied derivatives, the *N,N*-dimethyl-substituted carborhodol exhibited the most pronounced fluorescence turn-on response upon deprotonation. This is likely due to the presence of nonradiative pathways in the protonated form. Upon deprotonation, the molecule adopts a more planar and conjugated structure, suppressing these pathways and enhancing radiative emission. In contrast, structurally rigid fused analogs inherently limit nonradiative pathways and thus exhibit smaller pH-dependent changes in fluorescence.

In ethanol, the basic forms of the dyes exhibited enhanced quantum yields, longer lifetimes, and a more pronounced fluorescence turn-on ratio, highlighting the solvent effects on excited-state dynamics. Photostability experiments confirmed that these dyes are significantly more stable under prolonged irradiation as compared to the conventional pH indicator fluorescein and the commonly used NIR biological label Cy5.

While the current study is based on experimental data, the structure-property relationships observed could be further rationalized by computational approaches such as density functional theories (DFT) and time-dependent density functional theory (TD-DFT). These methods could provide insights into the electronic structures, transition dipoles, and conformational preferences that govern the observed pH-dependent optical properties.

Given their strong pH sensitivity, high photostability, and tunable fluorescence response, carborhodol derivatives represent promising candidates for fluorogenic and colorimetric pH sensors in biomedical applications. These dyes can be utilized in wound monitoring either as visible pH indicators or as fluorescence turn-on probes, detectable even under UV light (see

Chapter 7). Moreover, the distinct quantum yields and lifetimes between acidic and basic forms introduce ratiometric and time-resolved sensing strategies.

4.4 Experimental Section

4.4.1 Equipment

UV-VIS absorption spectra were recorded using either a PerkinElmer Lambda 750 or a PerkinElmer Lambda 365 UV/VIS spectrophotometer, both equipped with baseline correction. Measurements were conducted in Hellma quartz cuvettes of path lengths 10 mm or 1 mm. For temperature-dependent measurements, the PerkinElmer PTP-1 Peltier temperature controller was used in conjunction with the Lambda 750 spectrometer.

Emission spectra were collected with a Fluorolog 3 spectrofluorometer from HORIBA Jobin Yvon in Hellma quartz fluorescence cells (10 mm) at a controlled temperature of 23 °C. The measurements were carried out in the 90° arrangement with horizontal polarization of emission.

The fluorescence lifetime was determined using the TemPro fluorescence lifetime system from HORIBA Jobin Yvon, employing the time-correlated single photon counting method.

For photostability studies, a Liesegang Trainer Special HR Electronic Overhead Projector was employed as the light source, fitted with a 575 W mercury halide lamp.

4.4.2 Materials and Methods

Spectroscopic measurements in aqueous media were conducted using two representative buffer systems. For acidic conditions, a pH 3 buffer (Carl Roth, Art. No.: T18.1.1), composed of citric acid, NaOH, and NaCl, was used. Basic conditions were established using a pH 10 buffer (Carl Roth, Art. No.: P716.1), containing boric acid, NaOH, and KCl, to obtain the deprotonated form of the analyte. For measurements in ethanol, acidic ethanol was prepared by adding 0.1% v/v TFA, while basic ethanol was obtained by adding 0.2% v/v DIPEA.

Determination of pK_a

pH titrations were carried out in Britton-Robinson (BR) buffer. The BR buffer was prepared by dissolving H_3PO_4, H_3BO_3, and NaOAc (0.04 M each) in water, and then adjusting the pH to 2 by adding 2 M HCl. Working solutions of **AS 02** (c = 20 µM) in BR buffer were prepared by diluting a stock solution in spectral-grade DMSO (c = 9 mM). The initial absorbance at pH 2.0 was recorded using a 1 cm quartz cuvette. After the initial measurement, the cuvette contents were returned to the bulk pH 2.0 solution, which was then titrated with small aliquots of aq. NaOH (6.2 M) to increase the pH. At each titration step, the cuvette was rinsed with the newly adjusted solution before transferring it for measurement. For each pH point, both pH and

absorbance spectra were recorded. The titration was performed in fine increments between pH 2.0 and 7.0 (ΔpH ≈ 0.2), followed by measurements at pH 8.0, 9.0, and 10.0. The total volume of NaOH added during the titration was below 1% of the total solution volume, ensuring negligible dilution and constant dye concentration. The pK_a values were obtained from plots of absorption at fixed wavelength (corresponding to the λ_{max} of the deprotonated species) against the measured pH values and numerical fitting of the experimental data to the Henderson-Hasselbalch equation in the Origin software.[227]

Hydrophobic dyes, such as **AS 01** and **AS 11**, exhibited solubility issues at higher pH levels, leading to precipitation during titration. To address this, approximately 5% (v/v) ethanol was added to the aqueous buffer to enhance solubility. The pK_a values were then determined following the same procedure as described above.

Determination of Fluorescence Quantum Yield and Lifetime

A detailed methodology for determining fluorescence quantum yield and lifetime is provided in Chapters 2.5.2 and 2.5.3. All measurements were carried out by µ-filtering the sample solution (pore size 0.25 µm), and the measuring solutions were freshly prepared. The relative fluorescence quantum yields of all the carborhodols were determined under identical conditions, i.e., the same cuvettes were used, and the measurements were performed at a constant temperature (23 °C) with the same settings on the spectrometer, such as detection wavelength, detector voltage, slit bandwidths, and same absorbance (0.04–0.05 in a 1 cm cuvette) at the excitation wavelength etc.

For the lifetime determination, excitation was performed using 562 or 652 nm laser sources, selected based on the absorption maximum of the compounds. All measurements were carried out at absorbance < 0.1 in a 1 cm quartz cuvette, and to reduce the counting rate, neutral glass filters were inserted into the excitation channel.

Determination of Photostability

For the photostability experiments, solutions of the corresponding dye samples were prepared such that the extinction at the long-wavelength absorption maximum was approximately 1 in a 1 cm quartz cell.

All cuvettes were placed together on an overhead projector with a 575 W mercury halide lamp as the light source, and the lamp was focused on the cell (Figure 4.13). Absorption spectra were recorded at 30-minute intervals for 4 hours and then again after 24 hours. Cuvettes were tightly sealed throughout the experiment.

Figure 4.13. Experimental setup for photostability measurements. The sample solutions were placed vertically in quartz cuvettes on top of the overhead projector.

5 Solvatochromic Behavior of Carborhodol Dyes

While the pH-responsive properties of the new carborhodol dyes have been confirmed in Chapter 4, it is also important to understand how the optical properties of the dyes are influenced by their environment. This chapter presents a comprehensive study on the solvatochromic behavior of the acidic and basic forms of novel carborhodols (see Chapter 3) through absorption, emission, and fluorescence lifetime measurements in solvents of varying polarity. The basic forms exhibit strong positive solvatochromism in absorption ($\Delta\lambda$ = 113 nm for **AS 01**) when the solvent was changed from hexane to water, while the emission maxima show a moderate shift ($\Delta\lambda$ = 44 nm for **AS 01**). These effects are due to the intramolecular charge transfer (ICT) and stabilization of the excited state by polar solvents. Fluorescence lifetimes are longest in polar aprotic solvents and decrease in protic solvents due to hydrogen bond-assisted non-radiative decay. In contrast, acidic forms exhibit weak fluorescence and slight negative solvatochromism in absorption, with no consistent trends in emission or lifetime. The significant positive solvatochromism observed in the absorption spectra of the basic form of carborhodols highlights its potential as a polarity-sensitive probe.

5.1 Introduction and Objective

The hybrid structure of carborhodols includes a keto group and an amino substituent, which possess strong ICT behavior. This makes them highly responsive to changes in their microenvironment, including solvent polarity. These solvent-dependent variations are particularly relevant for understanding the excited-state behavior of carborhodol dyes and for optimizing their performance in applications such as chemical sensing, imaging, and in responsive materials. Scheme 5.1 shows the resonance structures of O-rhodols that include the nonpolar and dipolar limiting forms.[234]

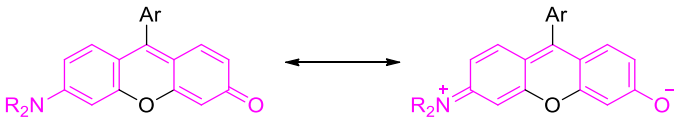

Scheme 5.1. Resonance structures of O-rhodols, showing nonpolar (left) and dipolar (right) limiting forms.

The solvent polarity influences the relative contribution of these two forms, thereby affecting the position of their absorption maxima. When both forms contribute equally, the molecule adopts a nearly ideal conjugated structure with uniform bond lengths and minimal bond alternation.[228] In this situation, the geometry of the excited state remains very similar to the ground-state geometry. As a result, the absorption band becomes sharp and narrow,

displaying little to no vibronic fine structure, which is typical for chromophores with highly delocalized conjugation.[228]

Rhodols that similar to most merocyanine dyes exhibit positive solvatochromism. For example, the O-rhodol (**1**) adopts an electronic structure with low charge separation in nonpolar media and a polarized structure close to the ideally conjugated state in polar media, which is confirmed by Density Functional Theory (DFT) calculations.[216] Nevertheless, all reported O-rhodol derivatives exhibit only a moderate solvatochromic response to changes in solvent polarity.[83,84,234] The P=O-bridged rhodol analogue (**2**) exhibits a pronounced positive solvatochromism, with a red shift of 125 nm in absorption and 70 nm in emission when moving from toluene to water. This significant bathochromic shift is attributed to the enhanced stabilization of the LUMO level in polar protic solvents, primarily through hydrogen bonding interactions involving the P=O and C=O functional groups.[216] The Si- and C-bridged rhodols have only been studied in aqueous solution.[40,226,235] This limited solvent scope highlights the relevance of investigating the solvatochromic behavior of the newly synthesized carborhodol analogues, particularly across a broader range of solvents.

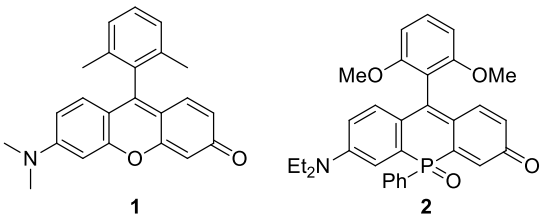

O-rhodol derivatives, typically synthesized via a two-step condensation with phthalic anhydride, feature a carboxyl group at the 2′-position of the meso-aryl ring.[83] This structural arrangement inherently promotes an equilibrium between the colorless spirolactone form **A** and the colored open dye form **B** (Scheme 5.2).

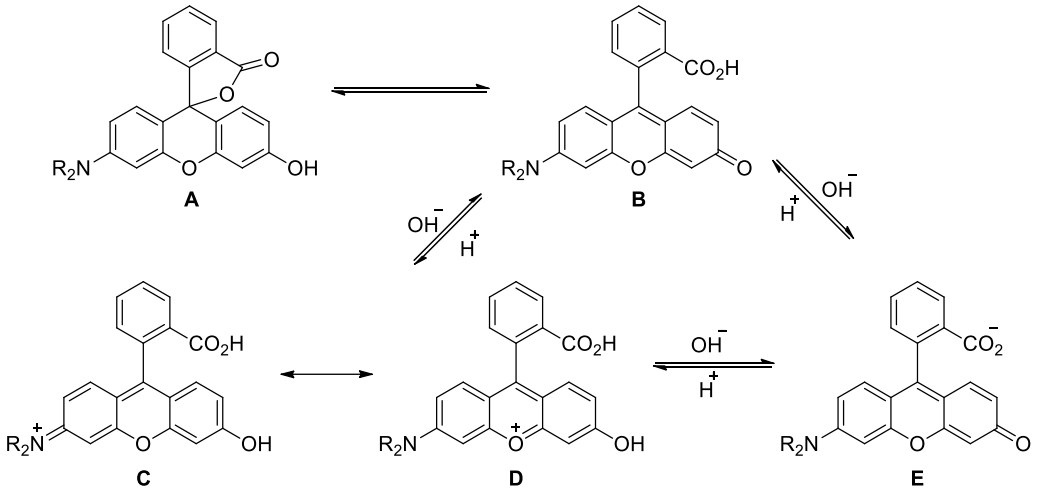

Scheme 5.2. Equilibrium of an O-rhodol derivative between spirolactone **A** and ring-open form **B,** and acid-base equilibrium of the latter.[39]

The equilibrium fraction of the spirolactone form depends on solvent polarity, pH, temperature, and the chemical structure of the dye. For example, in polar aprotic solvents, the rhodamine dye **ATTO 565** mainly exists in the spirolactone form. Consequently, its solutions in acetone appear faintly colored (Figure 5.1c-2) and turn completely colorless under basic conditions (Figure 5.1c-3). Spirolactone formation is also favored in solvents like DMSO and DMF, especially in the presence of bases or nucleophiles. In contrast, in polar protic solvents such as water or ethanol, the equilibrium shifts toward the open, colored dye form (Figure 5.1c-4).[236]

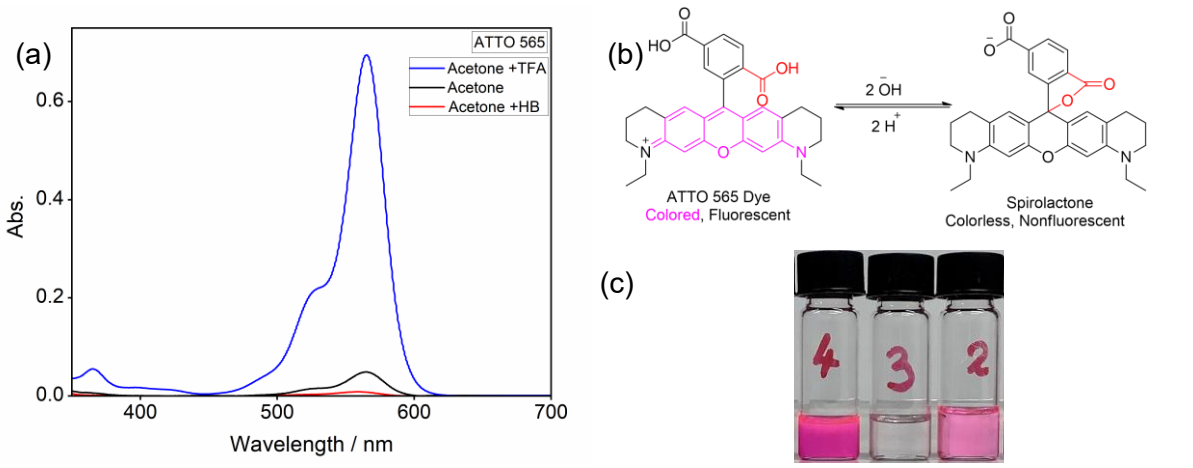

Figure 5.1. (a) Absorption spectra of **ATTO 565** carboxy in pure acetone, acidic acetone (acetone + TFA), and basic acetone (acetone + DIPEA). (b) Dye-spirolactone equilibrium of **ATTO 565**. (c) Photographs of **ATTO 565** solutions in acetone + TFA (4), acetone + DIPEA (3), and pure acetone (2).

Similar to the rhodamine dye **ATTO 565**, O-rhodol dyes bearing an *ortho*-carboxylic acid group predominantly adopt the open, colored dye form (Scheme 5.2E) in polar protic solvents under basic conditions, where protonation of the carboxyl group inhibits spirolactone formation. In contrast, in polar aprotic solvents, the equilibrium favors the formation of the closed spirolactone structure. Under acidic conditions, the equilibrium shifts toward the protonated form (Scheme 5.2C or D), which remains colored across all solvents. The use of the equilibrium between open and closed form as a fluorescence on/off switching mechanism is well documented in the literature and forms the basis of many pH-responsive rhodol-based probes.[223–225,237] Upon protonation in protic solvents or acidic conditions, the spirolactone ring opens, restoring π-conjugation and thereby recovering both color and fluorescence. A comparable spirolactone-dye-equilibrium is anticipated for the carborhodol analogues, and this behavior is also systematically examined in this current chapter.

5.2 Results and Discussion

To evaluate the photophysical behavior of carborhodol dyes in different solvent environments, a range of nonpolar aprotic, polar aprotic, and polar protic solvents was selected. The

absorption spectra, emission spectra, and lifetimes of the dyes were recorded in both their acidic and basic forms in all solvents.

5.2.1 Solvent-Dependent Absorption and Emission of the Basic Form of Carborhodols

Both compounds **AS 01** and **AS 02** exhibit positive solvatochromism, characterized by a bathochromic shift in the absorption maximum with increasing solvent polarity (Figure 5.2ab). For **AS 01**, the absorption maximum in the nonpolar aprotic solvent hexane is observed at 481 nm, shifting to 594 nm in buffer. Similarly, **AS 02** shows a red shift from 543 nm in toluene to 627 nm in buffer. In both cases, the absorption maximum increases with solvent polarity, as indicated by the $E_T(30)$ parameter. A good linear correlation between the absorption maxima and the $E_T(30)$ is observed for **AS 01** (R^2 = 0.94) and **AS 02** (R^2 = 0.87) (Figure 5.2c and d).

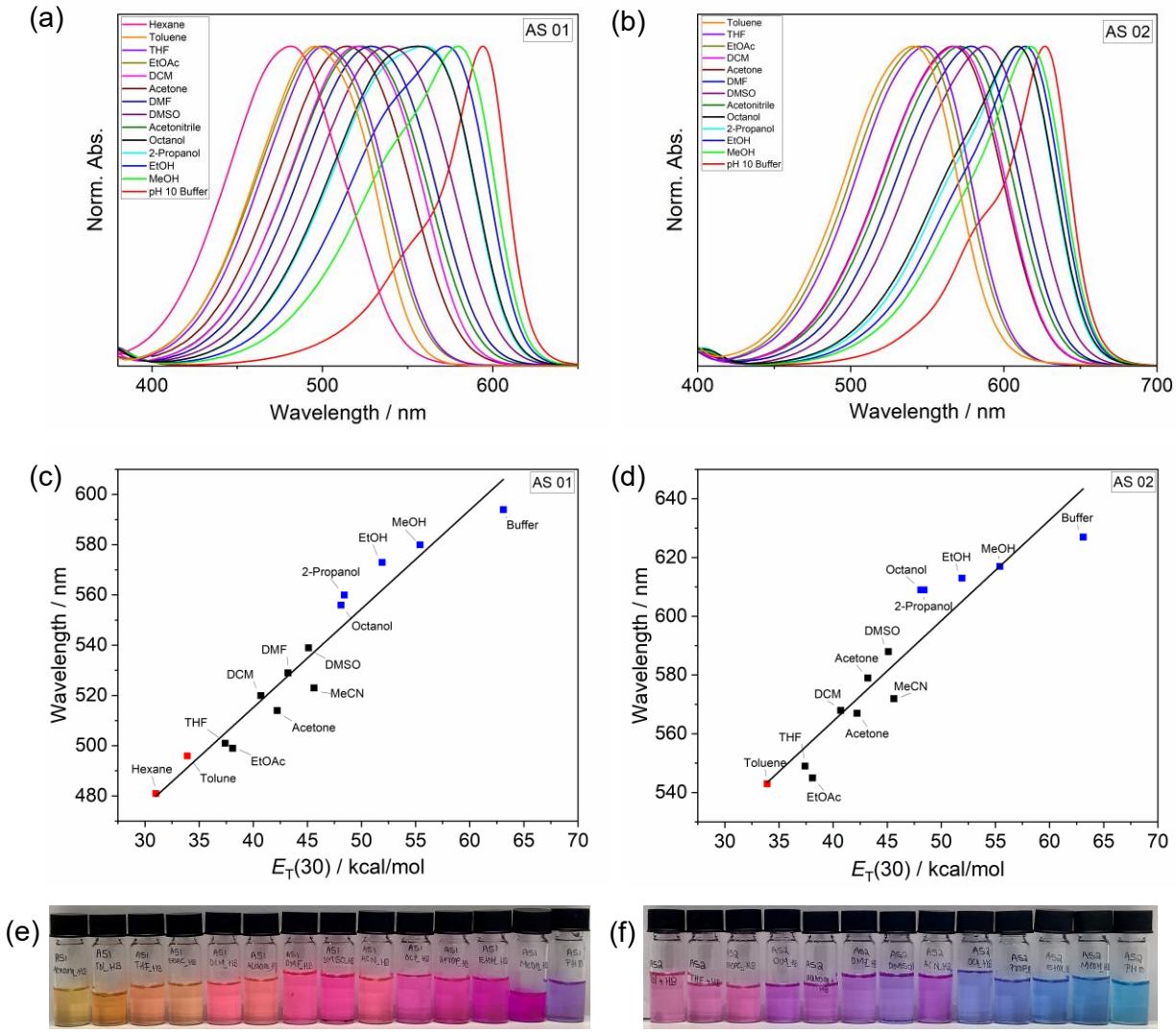

Figure 5.2. Normalized absorption spectra of the basic form of (a) **AS 01** and (b) **AS 02** in various solvents. Absorption maxima of the basic form of (c) **AS 01** and (d) **AS 02** plotted against $E_T(30)$ values of various nonpolar aprotic (red), polar aprotic (black), and polar protic (blue) solvents. Photographs of the solutions of the basic forms of (e) **AS 01** and (f) **AS 02** in various solvents, arranged in order of increasing $E_T(30)$ values, illustrating solvatochromic color changes.

In its basic form, the carborhodol exists in the keto (or dye) form, which supports delocalization of the π-electron system across the chromophore. Previous DFT studies on structurally related O-rhodol derivatives have shown that in HOMO, the major portion of the charge density is localized on the amine part of the chromophore and is transferred to the keto part of the chromophore in LUMO. This orbital distribution indicates a strong ICT effect upon excitation. Additionally, these studies report that the dipole moment in the excited state (S_1) is significantly larger than in the ground state (S_0), i.e., $\mu_e > \mu_g$, confirming the presence of a more polar excited state in rhodol-type chromophores.[218] Based on this, a similar ICT mechanism is proposed for the basic form of carborhodol (Scheme 5.3).

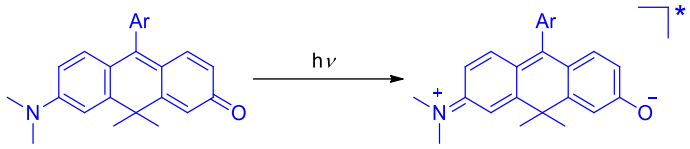

Scheme 5.3. Schematic representation of the ICT in the basic form of carborhodol, illustrating the ground and excited state structures.

Polar solvents preferentially stabilize the more polar excited state over the ground state, resulting in positive solvatochromism. For both **AS 01** and **AS 02**, the spectral shape changes from broad absorption in toluene and hexane to sharp bands in buffer, as indicated by a reduction in full width at half maximum (FWHM) values (Tables 5.1 and 5.2). Thus, the charge-transfer nature of the π-π* transition appears to diminish as the solvent's polarity increases, and then, in the buffer, the distinct π-π* character of the transition becomes evident.[216] In polar protic solvents such as water and alcohol, strong specific hydrogen bonding interactions occur between the C=O group and the solvent molecules, enhancing excited-state stabilization, which induces a substantial bathochromic shift. Additionally, such specific hydrogen bonding interactions may also lead to spectral band narrowing.

In both dyes, the only notable exception was the absorption maximum in acetonitrile (MeCN), which exhibited a hypsochromic shift of 16 nm for **AS 01** and 17 nm for **AS 02**, relative to the absorption maximum in DMSO. This blue shift in MeCN, despite its comparable $E_T(30)$ value to DMSO (45.6 for MeCN vs. 45.1 for DMSO), may arise from differences in solvent-solute interactions, such as weaker hydrogen bonding or lower polarizability of MeCN than DMSO, which influence the stabilization of the excited state.[238,239]

Additionally, among protic solvents, a band broadening is observed with a decrease in hydrogen bond donor strength (decrease in Kamlet-Taft parameter; α), from buffer to 1-octanol.[240] This trend is more pronounced for **AS 01**, which bears a flexible *N,N*-dimethylamine donor group, compared to its rigid fused-ring analogue, **AS 02**. A similar pattern is noted for **AS 13** (Figure S1) and **AS 14** (Figure 5.3a), both of which contain flexible *N,N*-dimethylamine

moieties and display broader absorption bands when going from buffer to 2-propanol relative to the more rigid analogue **AS 15** (Figure 5.3b), along with the positive solvatochromism. The observed broadening could be attributed to the conformational flexibility of the dimethyl amino group, which reduces planarity and delocalization and allows for a broader distribution of solute-solvent microenvironment. In contrast, the structural rigidity and enhanced electron-donating character due to the fused ring in **AS 02** and **AS 15** potentially lead to a more delocalized and defined excited state, as well as relatively narrow bands.

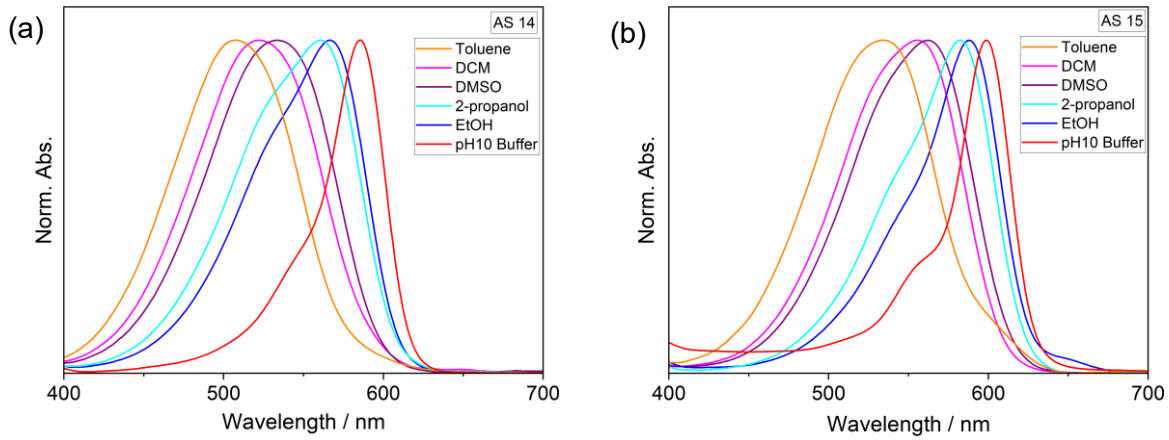

Figure 5.3. Normalized absorption spectra of the basic forms of (a) **AS 14** and (b) **AS 15** in various solvents, showing positive solvatochromism.

For the remaining analogues, representative solvents including toluene, DCM, DMSO, 2-propanol, ethanol, and buffer were selected to evaluate their solvatochromic behavior. In all cases, the basic form exhibits positive solvatochromism in the absorption, characterized by a bathochromic shift of the absorption maximum as solvent polarity increases (Figure S1, Tables 5.3 to 5.5).

Among the carborhodol analogues, those containing *ortho*-carboxylic acid substituents at the aryl head group, specifically **AS 10**, **AS 11**, **AS 12**, and **AS 13**, are colorless in aprotic solvents and become colored when going to protic solvents. This behavior is attributed to the well-known spirolactone (SL) formation mechanism of rhodol dyes, wherein the carboxylate anion undergoes intramolecular nucleophilic attack on the central carbon atom of the xanthene core, resulting in a closed, non-conjugated spirolactone structure (Figure 5.4b). The spirolactone form disrupts conjugation between the xanthene and aryl units, leading to the loss of visible absorption and fluorescence. Instead, a weak absorption band around 280 nm is typically observed, corresponding to localized π–π* transitions within the aromatic parts of the molecule. This spectral feature confirms the closed, non-conjugated nature of the molecule in aprotic media.

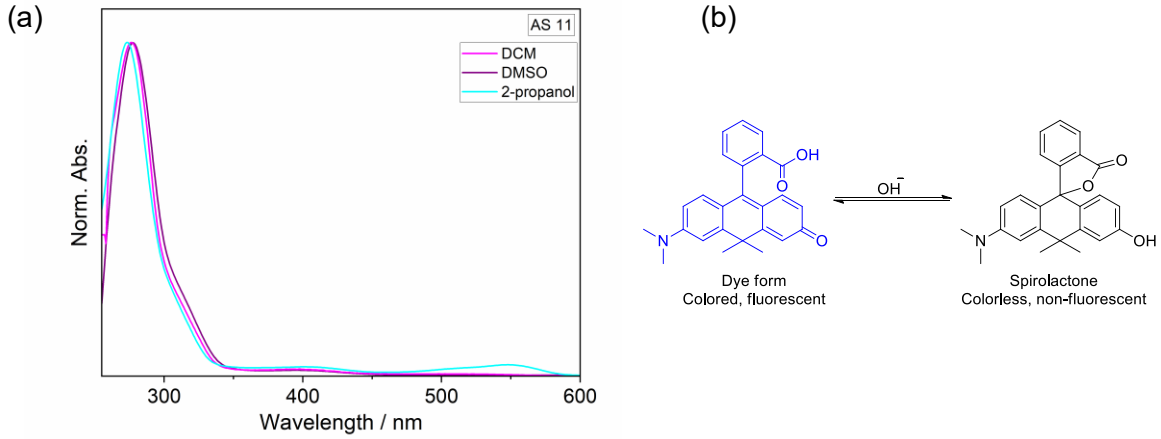

Figure 5.4. (a) Normalized absorption spectra of the basic forms of **AS 11** in DCM, DMSO, and 2-propanol, (b) Dye-Spirolactone-equilibrium of **AS 11**.

The emission behavior of the basic forms of **AS 01** and **AS 02** was also examined across the same solvent series. Figure 5.5a and 5.5b present the normalized emission spectra, while Figure 5.5c and 5.5d display plots of the emission maxima as a function of the solvent $E_T(30)$ values. Both compounds exhibit slight positive solvatochromism, as evidenced by a modest red shift and a change in emission color from orange to deep red with increasing solvent polarity (Figure 5.5e and 5.5f). A moderate linear correlation between the emission maxima and the $E_T(30)$ was observed for **AS 01** (R^2 = 0.71) and **AS 02** (R^2 = 0.57) (Figure 5.5c and d). For **AS 01**, the emission maximum shifts from 574 nm in hexane to 618 nm in aqueous buffer. **AS 02** shows a similar trend, with a shift from 624 nm to 658 nm from toluene to buffer.

Compared to **AS 01**, **AS 02** displays a slightly reduced solvent-dependent shift in emission. For both **AS 01** and **AS 02**, a trend towards positive solvatochromism is observed in the emission spectra, with λ_{em} increasing from hexane to DMSO in correlation with the $E_T(30)$ values of the solvents. However, acetonitrile deviates from this trend, exhibiting a hypsochromic shift of 12 nm and 6 nm relative to DMSO for **AS 01** and **AS 02**, respectively, consistent with the behavior observed in the absorption spectra. From 1-octanol to buffer, the emission maxima show minimal variation and closely match the λ_{em} observed in DMSO, suggesting a saturation effect in excited-state stabilization in highly polar solvents.

The emission bands of both dyes are broader in nonpolar aprotic solvents, such as hexane and toluene, which could be due to the solvent's inability to form strong, structured interactions with the polar excited state. As solvent polarity increases, the bandwidth (FWHM) progressively decreases (Tables 5.1 and 5.2). However, in contrast to the trend observed in absorption, no significant band narrowing is observed in the buffer.

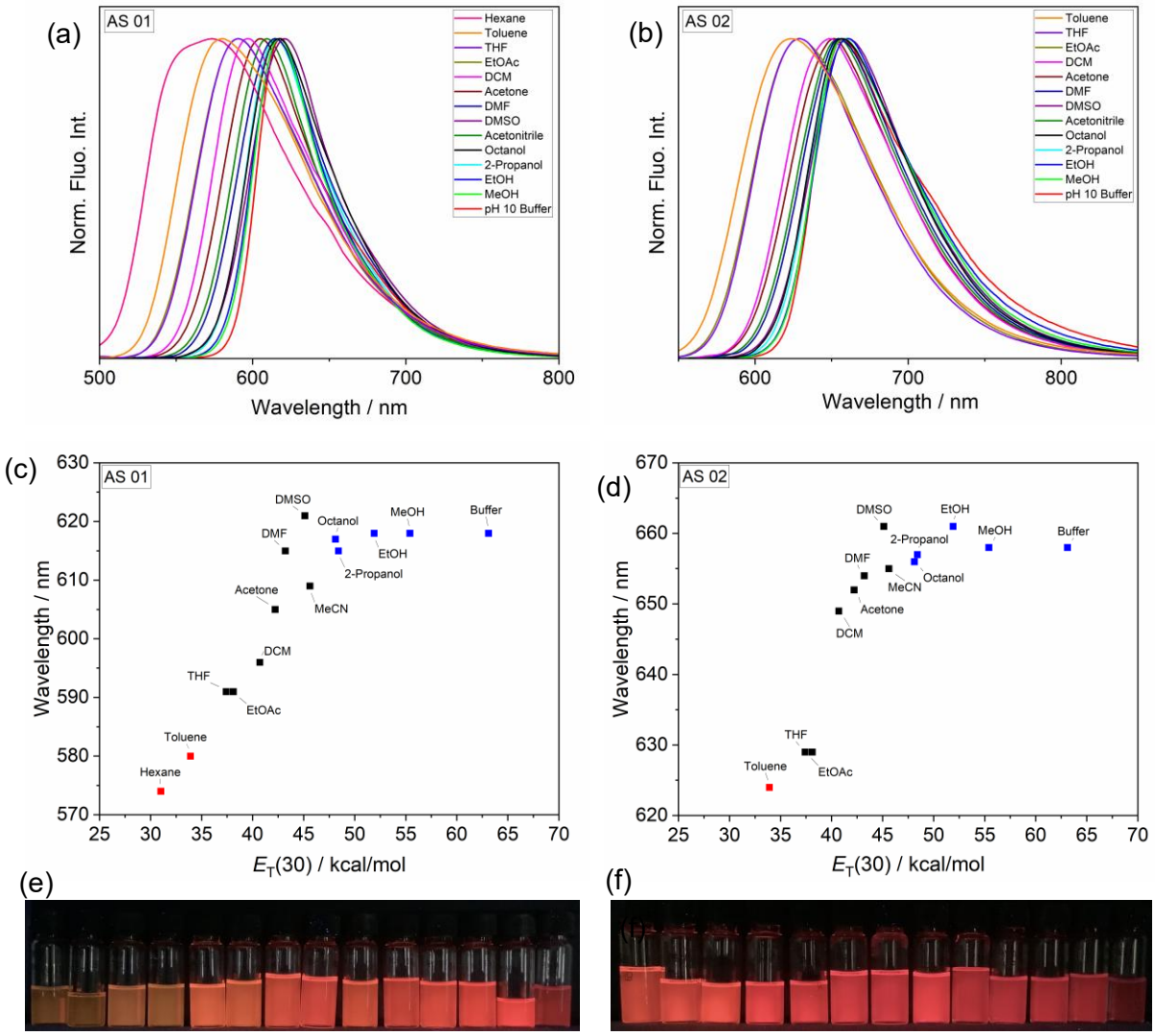

Figure 5.5. Normalized emission spectra of the basic form of (a) **AS 01** and (b) **AS 02** in various solvents. Emission maxima of the basic form of (c) **AS 01** and (d) **AS 02** plotted against $E_T(30)$ values of various nonpolar aprotic (red), polar aprotic (black), and polar protic (blue) solvents. Photographs of the solutions of the basic forms of (e) **AS 01** and (f) **AS 02** in various solvents, arranged in order of increasing $E_T(30)$ values under 365 nm UV light.

The observed fluoro solvatochromism supports the presence of an excited ICT state (Scheme 5.3) that is stabilized in polar environments. However, the relatively small shifts of the emission maxima, when compared to the much larger shifts observed of the absorption, may indicate that the solvent plays a more pronounced role in stabilizing the initial excitation (Franck-Condon region) than in modulating the relaxed excited-state geometry, resulting in only a moderate polarity dependence in emission.

For the remaining analogues, a similar approach to the absorption study was employed, such that only representative solvents were selected to evaluate their solvatochromic behavior. In all cases, the basic form exhibits slight positive fluoro solvatochromism (Figure S3 and Tables 5.3–5.5).

5.2.2 Solvent-Dependent Absorption and Emission of the Acidic Form of Carborhodols

The absorption and emission of the acidic forms of **AS 01** and **AS 02** were examined in the same range of solvents. The normalized absorption spectra and the corresponding plot of absorption maxima (λ_{max}) against $E_T(30)$ are provided in Figure 5.6. Both **AS 01** and **AS 02** exhibit two distinct absorption bands, possibly due to solvent interactions; the longer-wavelength band was selected for evaluation. Across the solvent series, a slight negative solvatochromism is observed. This is evidenced by a hypsochromic shift in λ_{max} with increasing solvent polarity for both compounds.

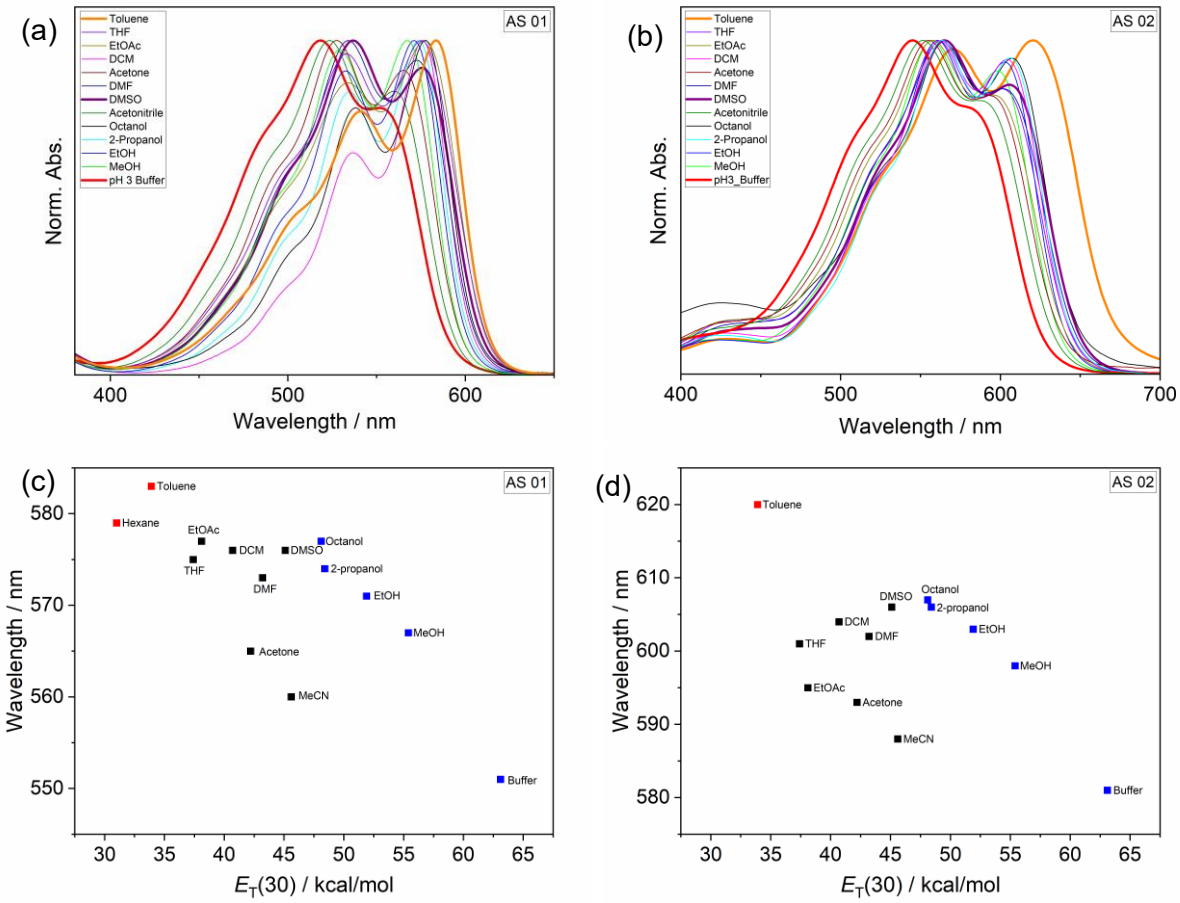

Figure 5.6. Normalized absorption spectra of the acidic forms of (a) **AS 01** and (b) **AS 02** in solvents of varying polarity. Absorption maxima plotted against $E_T(30)$ values for (c) **AS 01** and (d) **AS 02.** Solvent classes are indicated: nonpolar aprotic (red), polar aprotic (black), and polar protic (blue).

The emission maximum of **AS 01** is shifted from 583 nm in toluene to 551 nm in buffer, while the emission maximum of **AS 02** shifts from 620 nm in toluene to 581 nm in buffer, with intermediate solvents falling between these two extremes. The $E_T(30)$ vs. λ_{max} plots further confirm a modest but consistent hypsochromic shift with increasing $E_T(30)$ value, suggesting a polarity-dependent stabilization of the ground state over the excited state.

In the acidic form of the dye with a protonated amino group (which reduces its electron-donating ability) and a hydroxyl group (see Chapter 4, Scheme 4.2), the ICT character is relatively weak due to limited charge separation. Additionally, the phenolic hydroxyl groups participate in hydrogen bonding interactions.[241] As solvent polarity increases, the dipolar interactions and hydrogen bonding with the phenolic group stabilize the ground state more effectively, thereby increasing the energy gap and causing a shift of the absorption to higher energies.

Notably, in polar aprotic solvents, such as acetonitrile and acetone, **AS 01** and **AS 02** exhibit emission maxima at lower wavelengths compared to those in polar protic solvents, such as methanol and ethanol. Except for aqueous buffer, both polar protic and aprotic solvents produce a similar spectral response, with comparable hypsochromic shifts in absorption maxima as polarity increases. This convergence suggests that dipole-dipole interactions and hydrogen bonding contribute to a similar extent to ground-state stabilization in polar solvents, except in the case of the buffer. The overall narrow solvatochromic range further implies limited ground-state dipolar character and minimal conformational reorganization upon excitation.[93]

For the remaining analogues, the same set of representative solvents used for the basic form was employed to investigate their solvatochromic behavior. In all cases, the acidic forms display slight negative solvatochromism in their absorption spectra. Two representative analogues, **AS 14** and **AS 15**, which demonstrate this behavior, are shown in Figure 5.7. In nonpolar toluene, the absorption maxima of **AS 14** and **AS 15** are red-shifted by 23 nm and 33 nm, respectively, compared to the buffer. As the polarity of the solvent increases, the λ_{max} shifts to shorter wavelengths. Although the magnitude of this shift is modest, it is consistent across both compounds, as well as in other carborhodol analogues with a head group (=aryl group) that has a carboxylic acid.

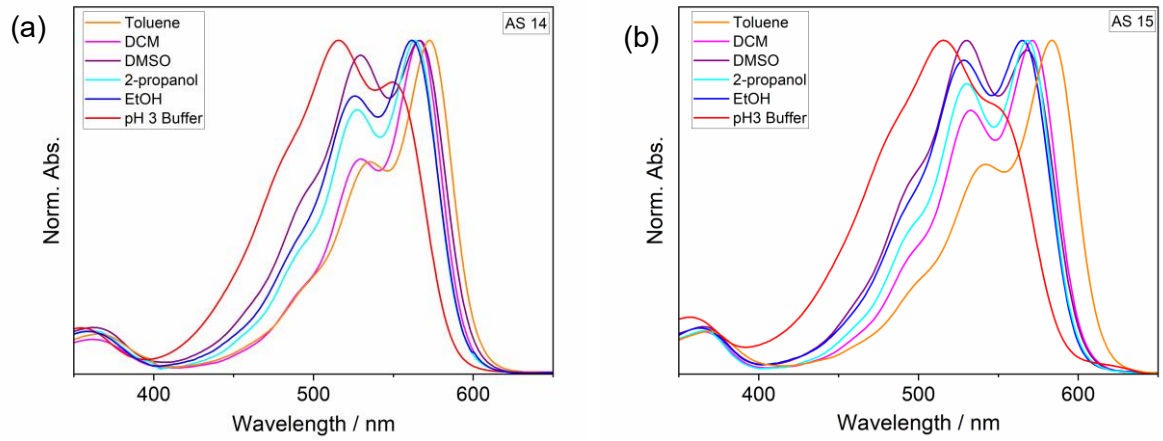

Figure 5.7. Normalized absorption spectra of the acidic forms of (a) **AS 14** and (b) **AS 15** in solvents of varying polarity showing negative solvatochromism.

The absorption spectra of the remaining analogues are provided in the Appendix (Figure S3), and their corresponding absorption maxima are summarized in Tables 5.3–5.5.

The spirolactone formed by carborhodols with *ortho*-carboxylic acid head group (**AS 10**, **AS 11**, **AS 12**, and **AS 13**) in the basic form restored their color in acidic conditions due to the opening of the spirolactone to form the conjugated acidic structure, restoring visible absorption and fluorescence (Figure 5.8).

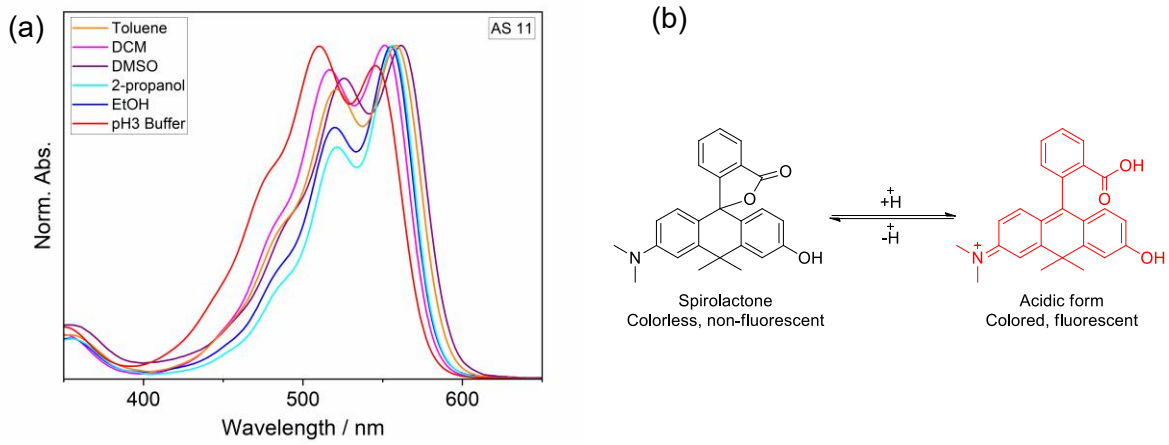

Figure 5.8. (a) Normalized absorption spectra of the acidic form of **AS 11** in solvents of varying polarity. (b) Dye-Spirolactone-equilibrium of **AS 11.**

In contrast, the emission spectra of all carborhodols in their acidic form exhibited negligible solvatochromism, indicating an excited-state geometry with minimal reorganization across different solvent environments. **AS 01** displays minimal solvatochromic response, with its emission band remaining essentially unchanged across all solvents. For **AS 02**, a minor negative solvatochromism was observed, with the emission maximum shifting from 688 nm in toluene to 659 nm in aqueous buffer (Figure 5.9). However, in most solvents, the emission bands of both compounds overlaps, and no clear trend was observed.

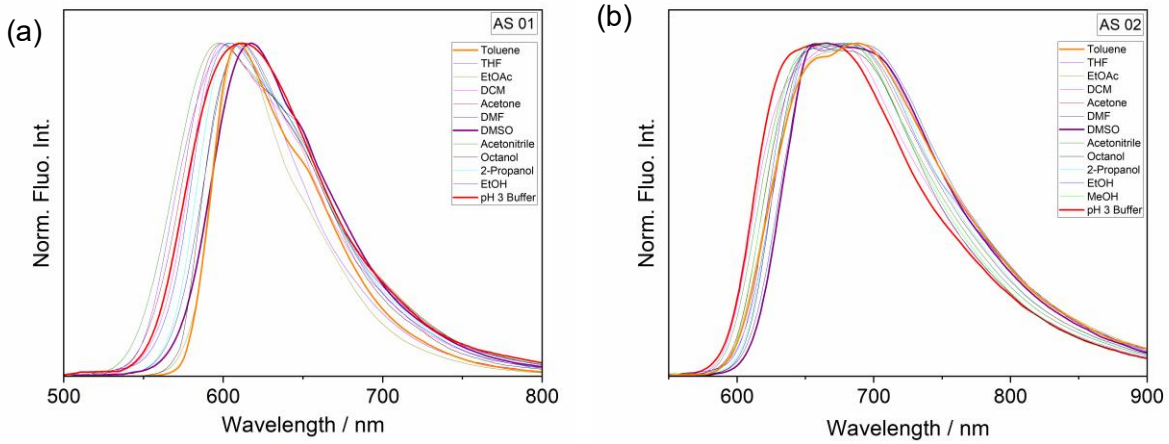

Figure 5.9. Normalized emission spectra of the acidic forms of (a) **AS 01** and (b) **AS 02**.

Given that the acidic forms of carborhodols are weakly emissive, further emission analysis focused on the ring-fused analogues **AS 12** and **AS 15**, whose acidic forms exhibit significantly stronger fluorescence (Figure 5.10). Both **AS 12** and **AS 15** showed slight negative solvatochromism.

For **AS 12**, the emission maximum exhibited a hypsochromic shift from 639 nm in toluene to 621 nm in buffer. Similarly, **AS 15** showed a shift from 650 nm to 625 nm across the same solvent range. As observed in the absorption spectra, the emission bands also displayed shoulders, although these were less pronounced. For consistency, the longer-wavelength emission maxima were used in the solvatochromism analysis.

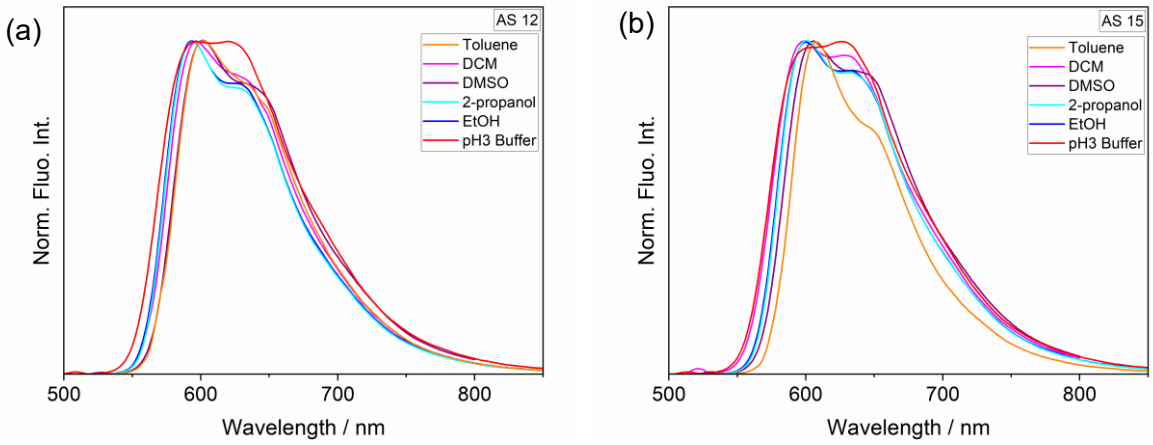

Figure 5.10. Normalized emission spectra of acidic forms of (a) **AS 12** and (b) **AS 15**.

Tables 5.1 and 5.2 summarize λ_{abs}, λ_{em}, and FWHM of the acidic (a) and basic (b) forms of **AS 01** and **AS 02**, respectively, in various solvents. Tables 5.3 to 5.5 present λ_{abs} and λ_{em} for the remaining analogues (**AS 03**–**AS 15**) under both acidic and basic conditions. For the basic forms of **AS 03** to **AS 15**, a clear trend of positive solvatochromism was observed in the absorption spectra. Basic forms of **AS 10**, **AS 11**, and **AS 12** form spirolactone in toluene, DCM, DMSO, and in 2-propanol. **AS 10** and **AS 11** also form SL in the polar protic solvent EtOH as well. For **AS 13**, spirolactone formation occurs in DCM and DMSO. **AS 13** also formed SL in toluene and 2-propanol with an absorption in the long wavelength, but the equilibrium was mainly shifted towards the SL, as indicated by the spectral profile (Appendix Figure S2). The basic forms generally show slight positive solvatochromism, with marginal red shifts. In contrast, the acidic forms exhibit slight negative solvatochromism in their absorption spectra.

Table 5.1. λ_{abs}, λ_{em}, and FWHM of acidic (a) and basic (b) forms of **AS 01** in various solvents. For the acidic form $\lambda_{(higher\ absorbance)}/\lambda_{(lower\ absorbance)}$ is given. Solvents arranged in order of increasing $E_T(30)$ values.

Solvents and $E_T(30)$ in kcal/mol	λ_{abs}, (nm); a / b	FWHM (nm)	λ_{em}, (nm); a / b	FWHM (nm)
Hexane 31	481(b)	80 (b)	574 (b)	108 (b)
	579/539 (a)	101.5 (a)	598 (a)	80.7 (a)
Toluene 33.9	496 (b)	78.8 (b)	580 (b)	95 (b)
	583/541(a)	91 (a)	610 (a)	73.4 (a)
THF 37.4	501(b)	82.6 (b)	591 (b)	85.3 (b)
	575/533 (a)	109.5 (a)	607 (a)	88.3 (a)
Ethylacetate 38.1	499 (b)	82.6 (b)	591 (b)	85.2 (b)
	577/534 (a)	105 (a)	610 (a)	62.1 (a)
DCM 40.7	520 (b)	87.8 (b)	596 (b)	78.4 (b)
	576/537 (a)	68.3 (a)	599 (a)	89.5 (a)
Acetone 42.2	514 (b)	88 (b)	605 (b)	72.8 (b)
	527/565 (a)	99.3 (a)	599 (a)	97.5 (a)
DMF 43.2	529 (b)	90 (b)	615 (b)	67.7 (b)
	534/573 (a)	101.9 (a)	611 (a)	82.7 (a)
DMSO 45.1	539 (b)	92 (b)	621 (b)	63.4 (b)
	537/576 (a)	103.5 (a)	617 (a)	82.4 (a)
Acetonitrile 45.6	523 (b)	90.8 (b)	609 (b)	65.8 (b)
	523/560 (a)	100.6 (a)	597 (a)	101 (a)
Octanol 48.1	556 (b)	95.3 (b)	617 (b)	66 (b)
	577/538 (a)	73.5 (a)	612 (a)	82.7 (a)
2-Propanol 48.4	560 (b)	93.7 (b)	615 (b)	62 (b)
	574/535 (a)	77.6 (a)	606 (a)	87 (a)
Ethanol 51.9	573 (b)	88.8 (b)	618 (b)	55.4 (b)
	571/532 (a)	85.3 (a)	603 (a)	91.2 (a)
Methanol 55.4	580 (b)	81 (b)	618 (b)	53.7 (b)
	567/529 (a)	94 (a)	599 (a)	93.5 (a)
Buffer 63.1	594 (b)	43.5 (b)	618 (b)	51.4 (b)
	518/551 (a)	104 (a)	612 (a)	94.2 (a)

Table 5.2. λ_{abs}, λ_{em} and FWHM of acidic (a) and basic (b) forms of **AS 02** in various solvents. For the acidic form $\lambda_{(higher\ absorbance)}/\lambda_{(lower\ absorbance)}$ is given. **AS 02** was not (fully) soluble in hexane.

Solvents	λ_{abs}, (nm); a / b	FWHM (nm)	λ_{em}, (nm); a / b	FWHM (nm)
Toluene	543 (b)	84 (b)	624 (b)	99 (b)
	620/570 (a)	137.4 (a)	688 (a)	143.7 (a)
THF	549 (b)	85 (b)	629 (b)	89 (b)
	561/601 (a)	116.3 (a)	687 (a)	141 (a)
Ethylacetate	545 (b)	85.4 (b)	629 (b)	91.7 (b)
	558/595 (a)	115.8 (a)	686 (a)	145 (a)
DCM	568 (b)	90.4 (b)	649 (b)	86 (b)
	562/604 (a)	113 (a)	671 (a)	137 (a)
Acetone	567 (b)	89.7 (b)	652 (b)	82.6 (b)
	555/593 (a)	114 (a)	686 (a)	140 (a)
DMF	579 (b)	91 (b)	654 (b)	79.5 (b)
	563/602 (a)	118 (a)	686 (a)	139.5 (a)
DMSO	588 (b)	90.4 (b)	661 (b)	80 (b)
	565/606 (a)	116.6 (a)	666 (a)	134 (a)
Acetonitrile	572 (b)	93.6 (b)	655 (b)	79 (b)
	552/588 (a)	115.5 (a)	680 (a)	140 (a)
Octanol	609 (b)	84 (b)	656 (b)	78 (b)
	565/607 (a)	115 (a)	657 (a)	126 (a)
2-Propanol	609 (b)	81 (b)	657 (b)	78.5 (b)
	564/606 (a)	111.2 (a)	689 (a)	136 (a)
Ethanol	613 (b)	76.8 (b)	661 (b)	77.1 (b)
	561/603 (a)	110.5 (a)	674 (a)	142.4 (a)
Methanol	617 (b)	72 (b)	658 (b)	76.9 (b)
	557/598 (a)	110.7 (a)	650 (a)	133 (a)
Buffer	627 (b)	53.3 (b)	658 (b)	80 (b)
	545/581 (a)	114.3 (a)	659 (a)	132 (a)

Table 5.3. $\lambda_{abs,}$ and λ_{em} of acidic (a) and basic (b) forms of **AS 03**, **AS 07,** and **AS 10** in various solvents. For the acidic form, $\lambda_{(higher\ abs.)}/\lambda_{(lower\ abs.)}$ is given. Solvents arranged in order of increasing $E_T(30)$ values. Spirolactone is represented as SL. [(c)]The SL form was dominant, and the reported λ_{abs} is the long wavelength absorption. **AS 03** and **AS 07** were not fully soluble in toluene.

Solvents	**AS 03**		**AS 07**		**AS 10**	
	λ_{abs}, (nm); a / b	λ_{em}, (nm); a / b	λ_{abs}, (nm); a / b	λ_{em}, (nm); a / b	λ_{abs}, (nm); a / b	λ_{em},(nm); a / b
Toluene	------	------	------	------	SL (b) 566/528 (a)	SL (b)
DCM	570 (b) 570/618 (a)	653 (b)	574 (b) 613/571 (a)	660 (b)	SL (b) 555/519 (a)	SL (b)
DMSO	589 (b) 570/610 (a)	666 (b)	591 (b) 569/609 (a)	674 (b)	SL (b) 564/527 (a)	SL (b)
2-Propanol	606 (b) 567/610 (a)	660 (b)	606 (b) 567/608 (a)	669 (b)	SL (b) 559/523 (a)	SL (b)
Ethanol	615 (b) 566/607 (a)	663 (b)	615 (b) 565/605 (a)	672 (b)	555[c] (b) 558/522 (a)	594 (b)
Buffer	632 (b) 548/591 (a)	661 (b)	635 (b) 547/590 (a)	670 (b)	575 (b) 511/545 (a)	604 (b)

Table 5.4. $\lambda_{abs,}$ and λ_{em} of acidic (a) and basic (b) forms of **AS 11**, **AS 12** and **AS 13** in various solvents. Spirolactone is represented as SL. [(d)]The SL form was dominant, and λ_{abs} is the long-wavelength absorption.

Solvents	**AS 11**		**AS 12**		**AS 13**	
	λ_{abs}, (nm); a / b	λ_{em}, (nm); a / b	λ_{abs}, (nm); a / b	λ_{em}, (nm); a / b	λ_{abs}, (nm); a / b	λ_{em},(nm); a / b
Toluene	SL (b) 558/521 (a)	SL (b)	SL (b) 564/526 (a)	SL (b) 601/639 (a)	575[d] (b) 560/522 (a)	SL (b)
DCM	SL (b) 551/516 (a)	SL (b)	SL (b) 562/525 (a)	SL (b) 596/635 (a)	SL (b) 554/519 (a)	SL (b)
DMSO	SL (b) 561/526 (a)	SL (b)	SL (b) 565/527 (a)	SL (b) 601/640 (a)	SL (b) 564/526 (a)	SL (b)
2-Propanol	SL (b) 556/521 (a)	SL (b)	569[d] (b) 563/525 (a)	SL (b) 594/631 (a)	560[d] (b) 558/523 (a)	599 (b)
Ethanol	555[d] (b) 555/520 (a)	595 (b)	572 (b) 560/523 (a)	607(b) 593/629 (a)	558 (b) 557/522 (a)	600 (b)
Buffer	574 (b) 510/545 (a)	602 (b)	587 (b) 511/545 (a)	614 (b) 621 (a)	578 (b) 512/547 (a)	605 (b)

Table 5.5. $\lambda_{abs,}$ and λ_{em} of acidic (a) and basic (b) forms of **AS 14** and **AS 15** in various solvents.

Solvents	**AS 14**		**AS 15**	
	λ_{abs}, (nm); a / b	λ_{em}, (nm); a / b	λ_{abs}, (nm); a / b	λ_{em}, (nm); a / b
Toluene	507 (b) 572/535 (a)	589 (b)	534 (b) 584/542 (a)	593 (b) 608/650 (a)
DCM	522 (b) 566/530 (a)	600 (b)	556 (b) 571/533 (a)	617 (b) 599/629 (a)
DMSO	533 (b) 566/529 (a)	616 (b)	562 (b) 530/568 (a)	625 (b) 606/642 (a)
2-Propanol	561 (b) 563/527 (a)	611 (b)	582 (b) 568/530 (a)	625 (b) 600/636 (a)
Ethanol	566 (b) 562/526 (a)	614 (b)	588 (b) 565/528 (a)	628 (b) 600/637 (a)
Buffer	586 (b) 516/549 (a)	614 (b)	599 (b) 515/551 (a)	624 (b) 625/600 (a)

5.2.3 Solvent-Dependent Fluorescence Lifetime of the Basic Form of Carborhodols

The fluorescence lifetime (τ) of the basic and acidic forms of **AS 01** and **AS 02** was measured in a series of solvents spanning a broad range of polarity to understand the influence of solvent environment on excited-state deactivation processes. Lifetime was determined using the time-correlated single photon counting (TCSPC) technique, as described in Chapter 2.5.3. From the bi-exponential fit, the lifetime of the dominant species was used to represent the system's decay behavior. The minor component, contributing less than 5%, was considered negligible in this context (Table 5.6).

The basic form of **AS 01** exhibits shorter fluorescence lifetimes (<1 ns) in nonpolar aprotic solvents, consistent with poor stabilization of its polar excited state. In solvents with intermediate polarity, such as THF and ethyl acetate, the lifetime increases moderately to 1.9 ns. The longest lifetimes are observed in polar aprotic solvents, reaching up to 4.3 ns in acetonitrile, indicating effective stabilization of the excited state and suppression of non-radiative decay pathways. However, in solvents with $E_T(30)$ values higher than that of acetonitrile, the excited-state lifetime decreases, reaching 1.8 ns in aqueous buffer. This decline is likely attributed to protic solvents enabling non-radiative decay, potentially through hydrogen bonding interactions.

Table 5.6. Fluorescent lifetimes of the acidic and basic forms of **AS 01** and **AS 02** in various solvents. Bi-exponential fits with χ^2 values between 0.900 and 1.200 and an even distribution of the residuals were selected as optimal. Exception: The acidic forms of **AS 01** and **AS 02** in EtOAc and THF, and the basic form of **AS 01** in hexane and toluene, had χ^2 values of 1.3 for the bi-exponential fits.

Solvents	τ (ns); basic form		τ (ns); acidic form	
	AS 01	**AS 02**	**AS 01**	**AS 02**
Hexane	0.1	-----	0.7	-----
Toluene	0.2	4.2	3.1	0.4
THF	1.8	4.8	1.3	0.6
Ethyl acetate	1.9	5.1	1.2	0.2
DCM	4.0	5.0	0.5	0.6
Acetone	4.2	5.1	0.1	0.5
DMF	4.1	4.7	0.1	0.5
DMSO	3.9	4.7	0.1	0.5
Acetonitrile	4.3	5.3	0.1	0.6
Octanol	4.0	3.4	0.3	0.6
2-Propanol	3.9	3.4	0.5	0.5
Ethanol	3.9	3	0.4	0.5
Methanol	3.6	2.5	0.1	0.5
Buffer	1.8	1.1	0.1	0.4

In contrast, **AS 02** displays longer lifetimes than **AS 01** across non-polar and aprotic solvents, ranging from 4.2 to 5.3 ns from toluene to MeCN. This indicates a more rigid and stable excited state, less prone to non-radiative deactivation. The enhanced rigidity provided by the ring-fused structure of **AS 02** likely contributes to this increased stability. However, in protic solvents, **AS 02** also shows a sharp decline in lifetime, from 3.4 ns in octanol to 1.1 ns in aqueous buffer, suggesting enhanced non-radiative decay via hydrogen bonding interactions with solvent molecules. The plot of fluorescence lifetimes of the basic form of **AS 01** and **AS 02**, versus solvent polarity factor $E_T(30)$, is shown in Figure 5.11.

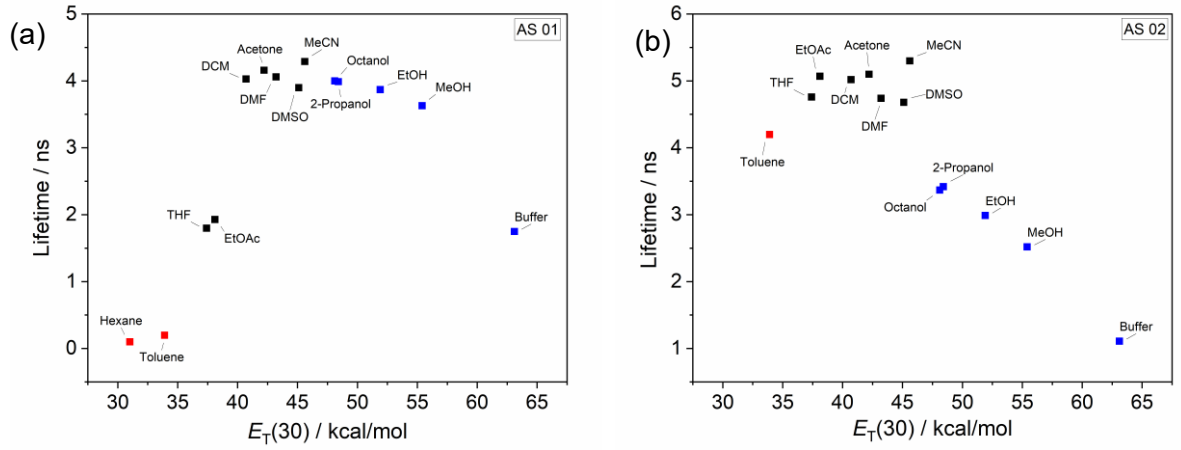

Figure 5.11. Fluorescence lifetimes of the basic forms of (a) **AS 01** and (b) **AS 02** plotted against the $E_T(30)$ polarity parameter. Red: non-polar solvents; black: aprotic polar solvents; blue: protic polar solvents.

As expected, the weakly fluorescent acidic forms generally exhibit low fluorescence lifetimes and do not follow any consistent trend across solvents. The basic forms show longer lifetimes compared to their acidic counterparts. However, an exception was observed for **AS 01** in non-polar solvents (hexane and toluene), where the acidic form exhibits a longer lifetime than the basic form (Table 5.6). To validate this observation, relative fluorescence quantum yields of the acidic and basic forms of **AS 01** were compared in both solvents. In toluene, the acidic form showed 1.6 times higher fluorescence intensity than the basic form, while in hexane, both forms exhibited comparable intensities. These findings confirm that the reversed lifetime behavior in **AS 01** under non-polar conditions represents a notable exception to the general trend.

For the basic forms of the remaining analogues, fluorescence lifetimes were measured in a set of representative solvents, including toluene (non-polar), DCM and DMSO (polar aprotic), and 2-propanol, ethanol, and aqueous buffer (polar protic). **AS 03** and **AS 07**, which are structurally similar to **AS 02**, exhibit comparable photophysical behavior (Table 5.7). Both dyes show high fluorescence lifetimes (~4.5 ns) in polar aprotic solvents such as DCM and DMSO and a steep decline in lifetime in protic solvents. For instance, in **AS 03**, the lifetime drops from 2.9 ns in 2-propanol to 0.6 ns in aqueous buffer. Due to poor solubility in non-polar solvents, toluene measurements were omitted for these analogues.

AS 14 and **AS 15** also show solvent-dependent trends. In toluene, relatively shorter lifetimes were observed (e.g., 3.8 ns for **AS 15** and 3.2 ns for **AS 14**), followed by increased lifetimes (~4.2 ns) in polar aprotic and protic solvents. However, a decrease to approximately 2.0 ns was again noted in buffer, indicating enhanced non-radiative decay under highly polar and protic conditions, possibly via hydrogen bonding (Table 5.7).

Table 5.7. Fluorescent lifetimes of the basic forms of **AS 03**, **AS 07**, **AS 14,** and **AS 15** and the acidic forms of **AS 12** and **AS 15** in various solvents. Bi-exponential fits with χ^2 values between 0.900 and 1.200 and an even distribution of the residuals were selected as optimal.

Solvents	τ (ns); basic form				τ (ns); acidic form	
	AS 03	**AS 07**	**AS 14**	**AS 15**	**AS 12**	**AS 15**
Toluene	-----	-----	3.2	3.8	3.2	3.9
DCM	4.8	4.6	4.4	4.6	3.7	3.6
DMSO	4.5	4.1	4.2	4.4	2.9	2.8
2-Propanol	2.9	2.5	4.2	4.2	3.3	3.1
Ethanol	2.1	1.6	4.2	4.1	3.2	2.9
Buffer	0.6	0.5	2.3	2.7	3.0	1.6

For **AS 10, AS 11, AS 12,** and **AS 13**, spirolactone formation in most solvents limited lifetime measurements to only ethanol and aqueous buffer. In ethanol, these dyes exhibit relatively high fluorescence lifetimes, while in buffer, the lifetimes drop substantially, consistent with trends observed in other analogues (Table 5.8).

Table 5.8. Fluorescent lifetimes of the basic forms of **AS 10 to AS 13** in polar protic solvents. Bi-exponential fits with χ^2 values between 0.900 and 1.200 and an even distribution of the residuals were selected as optimal.

Solvents	τ (ns); Basic form			
	AS 10	**AS 11**	**AS 12**	**AS 13**
2-Propanol	-----	-----	-----	4.2
Ethanol	4.4	4.2	4.4	4.3
Buffer	2.2	2.2	3.0	2.2

Overall, these results conclude that polar aprotic solvents tend to stabilize the emissive excited state of the basic form, while protic solvents, especially aqueous buffer, induce non-radiative deactivation, likely through hydrogen bonding.

In line with emission observations, further lifetime analysis of acidic forms was limited to the strongly fluorescent analogues **AS 12** and **AS 15** (Table 5.7). For **AS 15**, a longer lifetime was recorded in toluene (3.9 ns), while a lower value (1.6 ns) was observed in aqueous buffer. In toluene, the acidic and basic forms of **AS 15** exhibit comparable lifetimes similar to the observation in **AS 01**, whereas in all other solvents, the acidic form shows shorter lifetimes relative to the basic form. For **AS 12**, the highest lifetime was observed in DCM (3.7 ns), with other solvents yielding similar values in the range of 2.9–3.3 ns. In conclusion, the acidic forms, particularly in weakly emissive analogues, do not display a consistent solvent-dependent trend in fluorescence lifetime.

5.3 Conclusion and Outlook

The solvatochromic properties of both acidic and basic forms of a series of carborhodol analogues were investigated using absorption, emission, and fluorescence lifetime measurements across a range of solvents varying in polarity, as quantified by the $E_T(30)$ parameter. The results demonstrate that the solvent environment exerts a significant influence on the photophysical behavior of these dyes.

The basic forms of all analogues exhibited positive solvatochromism in both absorption and emission. A pronounced bathochromic shift was observed in the absorption maxima; for instance, **AS 01** showed a $\Delta\lambda$ of 113 nm when going from hexane to water. Emission maxima exhibit smaller shifts ($\Delta\lambda$ = 44 nm for **AS 01**), consistent with a solvent-stabilized excited state. This behavior can be attributed to an ICT from the amino donor group towards the keto acceptor upon excitation. The LUMO of the basic form possesses CT character, and the excited singlet state (S_1) exhibits a larger dipole moment than the ground state (S_0), leading to greater stabilization in polar solvents. In addition, hydrogen bonding between protic solvents and carbonyl groups further stabilizes the LUMO, collectively contributing to the observed positive solvatochromism.

Fluorescence lifetime measurements further support this interpretation: lifetimes were generally longest in polar aprotic solvents and decreased in protic solvents, suggesting that hydrogen-bond-assisted non-radiative decay is a dominant quenching mechanism in highly polar or hydrogen-bonding environments.

In contrast, the acidic forms showed slight negative solvatochromism in absorption, with hypsochromic shifts of the longest-wavelength absorption maximum as solvent polarity increased. This behavior is attributed to the protonation of the amino group, which restricts ICT, and to hydrogen bonding involving phenolic hydroxyl groups, which stabilizes the ground state more effectively than the excited state in polar solvents. However, the emission maxima and fluorescence lifetimes of the weakly emissive acidic forms did not display consistent trends with solvent polarity.

Overall, the significant solvatochromic shifts observed in the absorption spectra of the basic forms highlight the potential of carborhodol dyes as sensitive probes for investigating solvent-dependent parameters, including polarity, hydrogen-bond donor or acceptor capacity, ionic strength, and dielectric properties. The effect of the local environment on the photophysical properties upon incorporation into a polymer matrix will be examined in greater detail in Chapters 6 and 7.

5.4 Experimental Section

5.4.1 Equipment

UV–VIS absorption spectra were recorded using either a PerkinElmer Lambda 750 or a PerkinElmer Lambda 365 UV/VIS spectrophotometer, with baseline correction. Measurements were conducted in Hellma quartz cuvettes of path lengths 10 mm.

Emission spectra were collected with a Fluorolog 3 spectrofluorometer from HORIBA Jobin Yvon in Hellma quartz fluorescence cells of path length 10 mm, at a controlled temperature of 23 °C. The measurements were carried out in the 90° arrangement with horizontal polarization of emission.

The fluorescence lifetime was determined using the TemPro fluorescence lifetime system from HORIBA Jobin Yvon, employing the time-correlated single photon counting method.

5.4.2 Materials and Methods

Spectroscopic measurements in aqueous media were conducted using two representative buffer systems. For acidic conditions, a pH 3 buffer (Carl Roth, Art. No.: T18.1.1), composed of citric acid, NaOH, and NaCl, was used. Basic conditions were established using a pH 10 buffer (Carl Roth, Art. No.: P716.1), containing boric acid, NaOH, and KCl, to obtain the deprotonated form of the analyte. For non-aqueous acidic and basic conditions, 0.1 vol% TFA or 0.2 vol% DIPEA was added to spectroscopic-grade solvents to generate acidic or basic environments, respectively. Dyes were dissolved in these modified solvents, and all spectroscopic measurements were performed under these conditions.

Stock solutions of **AS 01** (c = 6 mM) and **AS 02** (c = 4.3 mM) were prepared in DMSO and diluted with the appropriate solvents to obtain measuring solutions. For absorption measurements, the solutions were diluted to achieve an absorbance in the range of 0.3–0.40 at the absorption maximum. For fluorescence measurements, these solutions were further diluted to a final absorbance of 0.04–0.05 to avoid reabsorption.

All sample solutions were freshly prepared prior to measurement and filtered through a 0.25 µm pore size syringe filter. Absorption and emission spectra were normalized to their respective maxima to allow for direct comparison of spectral features across different solvents.

A detailed methodology for determining fluorescence lifetime is provided in Chapter 2.5.3. Excitation laser sources were selected to match the absorption maxima of the respective compounds. All lifetime measurements were performed in 10 mm quartz cuvettes, ensuring that absorbance values remained below 0.1. To reduce the counting rate, neutral glass filters were inserted into the excitation channel.

6 Encapsulation of pH-Sensitive Dyes in Poly(ethylene glycol)-*block*-poly(lactic acid) Vesicles for Sensing Applications

The amphiphilic block copolymer PEG_{114}-*b*-PLA_{750} was prepared through ring-opening polymerization in the melt. Using the solvent-shift method, the polymer PEG_{114}-*b*-PLA_{500} self-assembled into nanosized vesicles capable of encapsulating pH-sensitive dyes. The novel carborhodol dyes (see Chapter 3) were classified by their octanol-water partition coefficients (log K_{ow}) as hydrophilic, moderately hydrophilic, or hydrophobic, guiding the selection of encapsulation candidates. The hydrophobic dye **AS 01** precipitated upon vesicle lysis, preventing pH sensing, whereas the hydrophilic dye fluorescein retained strong pH-dependent optical responses, indicating suitability for spectroscopic pH detection. Moderately hydrophilic and hydrophilic carborhodols show limited visible color but display fluorescence enhancement with increasing pH without lysis, including the hydrophobic dye **AS 01**. These novel dye-loaded polymer vesicles show potential for wound dressing applications, where fluorescence-based pH measurements could be performed to determine wound status.[ii]

6.1 Introduction and Objective

Lipid-based vesicles (liposomes) have been extensively investigated as carriers in biosensing applications. One notable strategy, developed by Jenkins and coworkers, involves detecting pathogenic bacteria through their secreted toxins for the early diagnosis of wound infections using dye-loaded liposomes.[242] In 2015, they reported a prototype hydrogel-liposome wound dressing that enables biofilm detection based on a fluorescence turn-on principle. Here, the encapsulated fluorophore, carboxyfluorescein, remains quenched at high concentrations within the liposomes,[243] but upon disruption by bacterial toxins, the dye is released into the aqueous environment, resulting in fluorescence enhancement. While highly effective, this approach requires a high dye concentration (typically around 50 mM) to achieve self-quenching, and the carboxy fluorescein suffers from photobleaching.[35] The use of more photostable dyes that use a different approach for sensing infection with lower concentrations would therefore represent a significant advantage.

Polymeric vesicles (polymersomes) have emerged as a robust alternative to liposomes due to their superior physical and mechanical properties. Amphiphilic BCPs with high molar

[ii] This work was carried out in collaboration with M.Sc. Nicola Cusick (University of Siegen). PEG_{114}-*b*-PLA_{500} synthesis and DLS measurements were performed by Nicola Cusick, FESEM measurements by M.Sc. Aysha Awan (University of Siegen), and confocal fluorescence microscopy with the assistance of Dr. Jan Erik Hoffmann (ATTO-TEC GmbH).

masses, chain interdigitation, and entanglements within the bilayer all contribute to the increased stability of their self-assembled structures, leading to a much thicker membrane than liposomes.[244–246] Typically, the biocompatible polymer poly(ethylene glycol) (PEG) is used as the hydrophilic block, as it is reportedly provides a stealth function, which helps prolong circulation times by resisting protein adsorption.[122,247] Meanwhile, polyester blocks such as poly(ε-caprolactone) (PCL) or poly (lactic acid) (PLA) provide biodegradability and stimuli responsiveness, as their ester bonds are easily hydrolyzed by lipases and proteases in biological environments, making them good candidates as the hydrophobic block.[248,249] This property enables controlled cargo release through enzymatic degradation or, alternatively, by hydrolysis under acidic conditions (pH ~5.5), as demonstrated in polymersome-based drug delivery systems reported by Discher and co-workers.[250]

Therefore, stimuli-responsive polymersomes, therefore, provide a versatile platform for biosensing applications, particularly in pathological environments where enzymatic activity or pH gradients can serve as triggers for dye release. Praveen et al. reported the self-assembly of octadecyl rhodamine-6G with a PDMA-*b*-PMMA-*b*-PDMA block copolymer for pH sensing applications. At low pH (≤ 3.5), opening of the spirolactam ring generated the fluorescent xanthene form, producing a turn-on response. Upon increasing the media pH, the non-fluorescent spirolactam structure dominated. A visible increase in fluorescence and solution color appeared around pH 4.0, while DLS studies at pH 3.0 confirmed vesicle rupture. This system demonstrates the ability of dye-loaded vesicles to act as probes for environmental pH changes through fluorescence on-off signaling.[251]

The different solubility in water or polar solvents, on the one hand, and in nonpolar organic solvents, on the other hand, can be a critical parameter when using vesicles as chemical sensors. Due to the breaking of the vesicle membrane, the dye molecules will be released from their original environment into the external solution. After release, the dyes must remain dissolved in the more hydrophilic medium to effectively perform their sensing function.[252]

Hydrophilicity is typically described by the octanol-water partition coefficient (log K_{ow}), where lower (negative) values indicate hydrophilic compounds and higher (positive) values indicate hydrophobic ones.[253] Several experimental methods exist to determine log K_{ow}, including the shake-flask method,[254] slow-stirring method,[255] generator column method,[256] and HPLC-based techniques.[257] Each has distinct advantages, but the shake-flask method remains a widely applied and reliable approach for organic dye classification. In this study, a combination of the shake-flask and reversed-phase HPLC methods was employed, with retention times providing an additional measure of hydrophobicity.

Following the examination of pH sensitivity (see Chapter 4) and solvent-dependent photophysical properties (see Chapter 5) of the carborhodols, this chapter focuses on their incorporation into PEG-*b*-PLA vesicles, which may subsequently be immobilized on wound

dressing materials for infection detection. Unlike traditional concentration quenching methods, this approach uses low concentrations of photostable dyes, reducing photobleaching while preserving sensitivity. Under alkaline conditions typical of chronic wounds, the vesicles will show a visible color change accompanied by a fluorescence turn-on response. This dual readout offers a simple and long-term platform for diagnostics of wound infection.

6.2 Results and Discussion

6.2.1 Hydrophilicity of Dyes

The hydrophilicity of the dyes was evaluated by determining their octanol-water distribution coefficient (log K_{ow}). In this study, log K_{ow} values for ATTO dyes, reference dyes, and selected carborhodol derivatives were obtained using the widely used shake-flask method (Table 6.1).[258] The concentrations of each dye in the octanol (c_o) and aqueous (c_w) phases were calculated using the Beer-Lambert law (Eq. 2.7), based on their respective absorbance. For each dye, a plot of c_o versus c_w was constructed, and the slope of the linear regression (c_o/c_w) corresponded to the K_{ow} value. For example, the respective plot for **AS 02** exhibits a strong linear correlation (R^2 = 0.999) (Figure 6.1a). From the slope, the K_{ow} of **AS 02** was determined to be 23.7, corresponding to a log K_{ow} of 1.4. Based on the log K_{ow} values, dyes were classified as hydrophilic (log K_{ow}<0), moderately hydrophilic (0≤log K_{ow}<2), and hydrophobic (log K_{ow}≥2).[259]

Table 6.1: log K_{ow} values and hydrophilicity classification of the dyes studied, determined using the shake-flask method.

Hydrophilic log K_{ow}<0		Moderately hydrophilic 0≤ log K_{ow}<2		Hydrophobic log K_{ow}≥2	
Dye	log K_{ow}	Dye	log K_{ow}	Dye	log K_{ow}
ATTO 643	-3.7	Rhodamine 6G	0.1	ATTO 647 N	2.6
ATTO 655	-3.1	Rhodamine 6G BF_4^-	0.5	ATTO 665	2.9
ATTO 680	-3.0	ATTO 633	0.6	**AS 01**	4.0
ATTO 594	-3.0	Rhodamine 6G I^-	0.8	Nile red	5.0
Methylene Blue	-2.3	Rhodamine 630	1.2		
AS 13	-2.2	Rhodamine B Cl^-	1.3		
Fluorescein	-2.1	**AS 02**	1.4		
Methylene Green	-2.1	ATTO Oxa 12	1.6		
AS 03	-0.9				
ATTO 647	-0.8				

The introduction of hydrophilic or hydrophobic groups can modulate the solubility of carborhodols; for example, incorporating additional sulfonic acid groups increases

hydrophilicity and enhances water solubility (see Chapter 3). As the number of sulfonic acid groups increases, log K_{ow} values of **AS 01** (without sulfonic acid group), **AS 02** (with one sulfonic acid group), and **AS 03** (with two sulfonic acid groups) decrease and become more hydrophilic.

In addition to determining the octanol-water partition coefficients, the relative hydrophobicity of the dyes was further validated using high-performance reversed-phase liquid chromatography (HPLC).[260] A gradient method was employed, decreasing the aqueous content from 80% to 5% over a 30-minute period. Since the stationary phase is hydrophobic, retention time is directly correlated with dye hydrophobicity: hydrophilic compounds elute earlier, while more hydrophobic dyes exhibit longer retention times. The dyes are retained in proportion to their log K_{ow} values. Hydrophilic dyes, such as **ATTO 594**, **AS 13**, **AS 03**, **ATTO 643**, and fluorescein, eluted earlier, while more hydrophobic dyes, like **AS 01** and **ATTO 647N**, showed longer retention. This agreement between the partition coefficient and chromatographic behavior confirms the reliability of both methods in assessing dye hydrophobicity (Figure 6.1b).

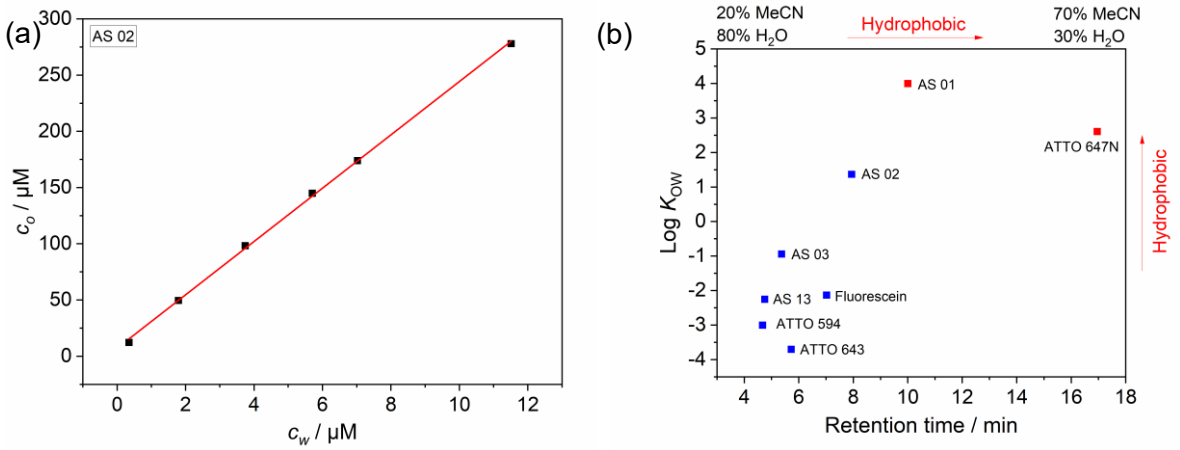

Figure 6.1. (a) Plot of the dye concentration in octanol (c_o) versus that in water (c_w) for **AS 02**. Red line: linear regression curve, R^2 = 0.999. Plots for **AS 01**, **AS 03**, and **AS 13** are shown in Figure S1. (b) Plot of log K_{ow} vs. HPLC retention time for selected dyes using a gradient method, 80 to 30% H_2O. Higher retention time and a more positive log K_{ow} correspond to increased hydrophobicity.

Based on the results, **AS 01** was selected as a hydrophobic candidate, AS 02 as a moderately hydrophilic candidate, and fluorescein, **AS 03**, and **AS 13** were chosen as hydrophilic dyes for encapsulation into polymeric vesicles. Additionally, **AS 07** was included as a hydrophilic candidate due to its structural similarity to **AS 03**.

6.2.2 Synthesis of Amphiphilic PEG-*b*-PLA Block Copolymers

The amphiphilic block copolymer PEG-*b*-PLA was synthesized via ring-opening polymerization of L-lactide, using poly(ethylene glycol)methyl ether (MeO-PEG_{114}-OH) as the macroinitiator and stannous octoate ($Sn(oct)_2$) as the catalyst, under melt conditions (Scheme 6.1). PEG-*b*-

PLA copolymers with varying PLA block lengths were obtained by adjusting the molar ratio of monomer to macroinitiator.

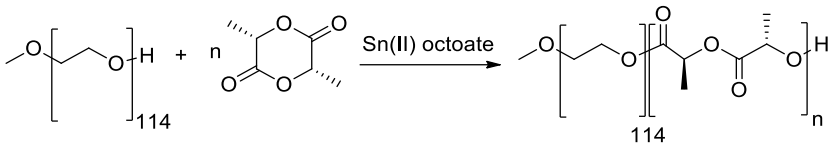

Scheme 6.1. Synthesis of PEG_{114}-*b*-PLA_n via ring-opening polymerization of L-lactide with the macroinitiator $mPEG_{114}$ and Sn (II) octoate as catalyst.

PEG_{114}-*b*-PLA_{750} was synthesized and characterized by ^1H NMR spectroscopy to determine the length of the PLA block. The ^1H NMR spectrum (Figure 6.2) confirms successful polymerization, showing characteristic proton signals for the PEG and PLA blocks observed at 3.64 ppm (PEG), 1.58 ppm (PLA CH_3), and 5.16 ppm (PLA CH).

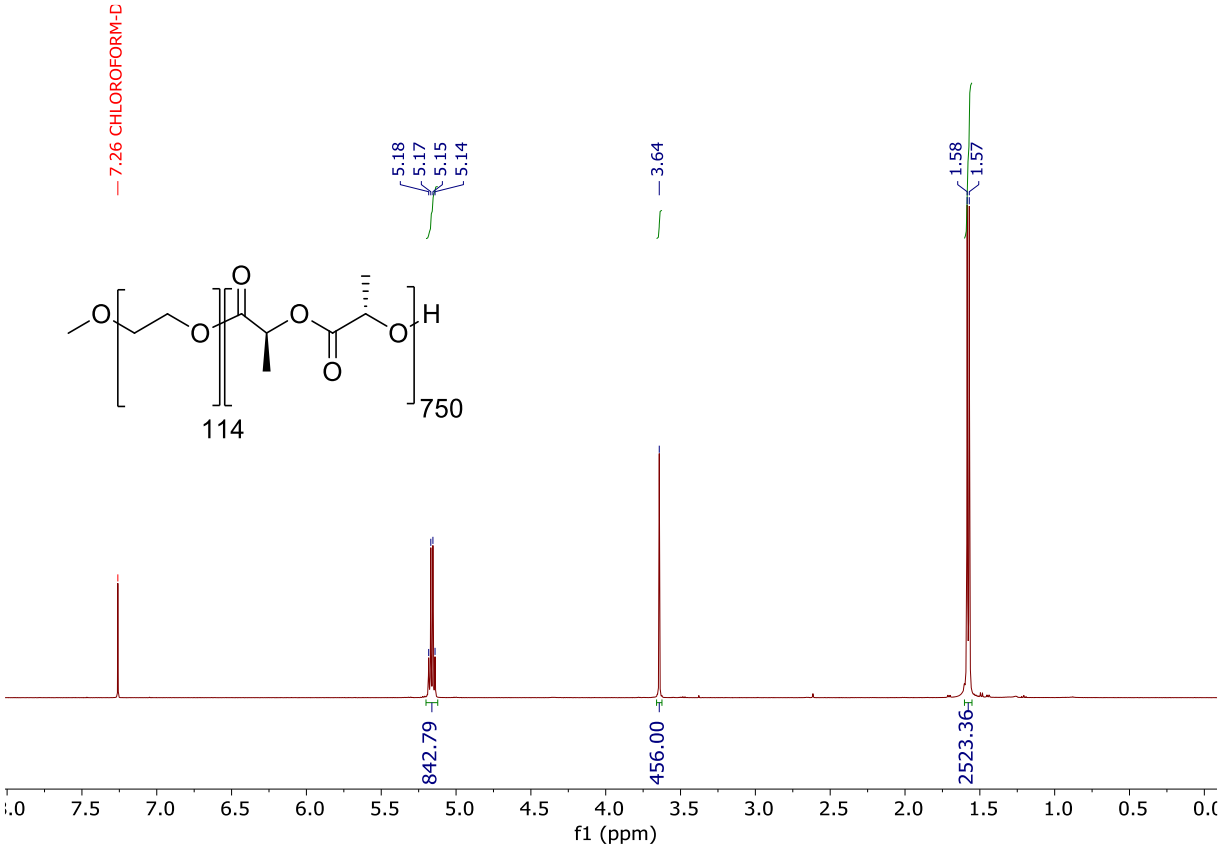

Figure 6.2. ^1H-NMR spectrum of PEG_{114}-*b*-PLA_{750} in $CDCl_3$.

Calculation of PLA chain length via NMR is achieved by comparing the integrated proton signals of the PLA segment to those of the mPEG block. The integral of the mPEG peak at 3.64 ppm was normalized to represent 456 protons, based on an assumed number-average molecular weight (Mn) of 5000 g mol^{-1}. The number of constitutional repeating units (cru) of PLA was then calculated by dividing the integral (I) of the PLA proton signals (corrected by the corresponding number of protons (N)) by the corrected integral of the PEG proton signal, as (Equation 6.1).

$$\frac{cru_{PLA}}{cru_{PEG}} = \frac{I_{PLA}}{I_{PEG}} \frac{N_{PEG}}{N_{PLA}} = \frac{\left(I_{5.2\ ppm} + I_{1.6\ ppm}\right)}{I_{3.64\ ppm}} \frac{4}{4} = \frac{\left(I_{5.2\ ppm} + I_{1.6\ ppm}\right)}{I_{3.64\ ppm}} \quad \text{(Eq. 6.1)}$$

Based on the integral ratios, the PLA chain length was estimated to be 840 repeating units (compared to a nominal 750). This discrepancy may arise from the unexpected termination of some polymer chains, which leaves unreacted free monomers in the melt. These free monomers can subsequently undergo polymerization, leading to longer polymer chains than initially anticipated. As a result, the actual polymer chain length exceeds that predicted by the initial molar ratio of lactide to PEG. As this sample likely had a large dispersity of chain lengths, for the encapsulation studies, which had been previously synthesized with an experimental chain length matching the expected chain length, was chosen.

6.2.3 Encapsulation of Reporter Dyes

The self-assembly of these polymers into micelles and nano-capsules was achieved using the solvent shift method (see Chapter 2). For the encapsulation, PEG_{114}-*b*-PLA_{500} was first dissolved in THF, which dissolves both PEG and PLA blocks. For hydrophilic dyes, the dyes were dissolved in Milli Q water, which was then added gradually to the polymer solution. In the case of hydrophobic dyes, both the dye and polymer were co-dissolved in THF, followed by slow addition of water. This THF-water system acts as a selective solvent, inducing micelle and vesicle formation via solvophobic interactions. Once water was added in sufficient excess to fix the self-assembled structures, the resulting suspensions were purified by dialysis (MWCO = 6–8 kDa), and further purification was achieved by size-exclusion chromatography. Encapsulation was performed for the hydrophilic pH-sensitive dye fluorescein, and several novel pH-responsive dyes, including the hydrophobic dye **AS 01,** moderately hydrophilic dye **AS 02**, and the hydrophilic dyes **AS 03**, **AS 07**, and **AS 13**. The resulting suspensions were characterized by Dynamic Light Scattering (DLS) and Field Emission Scanning Electron Microscopy (FESEM) (Figure 6.3). The number-based distribution of the suspensions showed an average hydrodynamic diameter of 275 ± 1 nm for **AS 01**-loaded PEG_{114}-*b*-PLA_{500} assemblies (Fig. 6.3a). FESEM images revealed spherical features (Fig. 6.3b), characteristics of vesicle formation,[261] with diameters of 193 ± 12 nm, in agreement with the DLS results. The images further indicate that the spherical morphology is largely preserved after drying, demonstrating the structural stability of the assembly.

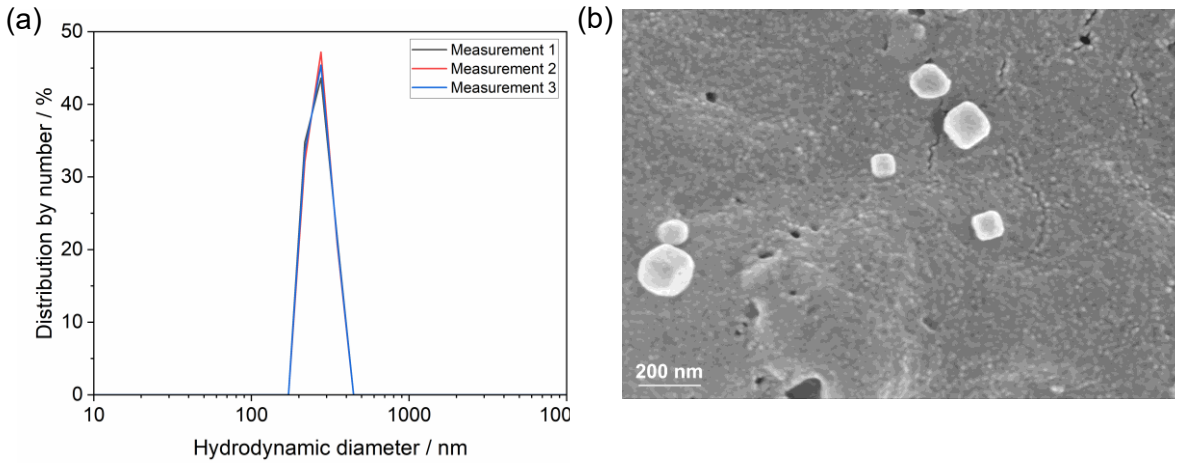

Figure 6.3. (a) DLS particle size distribution by number, (b) FESEM of PEG_{114}-*b*-PLA_{500} vesicles loaded with **AS 01**.

Encapsulation of Fluorescein

The hydrophilic, pH-sensitive dye fluorescein (pK_a = 6.4)[262] was loaded into vesicles which were then incubated with proteinase K (2 mg/mL in PBS, v/v = 1:1) to investigate the enzymatic degradation of the vesicles and the release of fluorescein. Proteinase K serves as a model protease for enzymes secreted by *Pseudomonas aeruginosa*, known to facilitate PLA hydrolysis.[138,139] Degradation of the PLA block leads to destabilization of the vesicle structure, promoting release of the encapsulated dye into the surrounding medium. The release kinetics were monitored over time using absorbance and fluorescence spectroscopy (Figure 6.4). A significant increase in fluorescence intensity at 515 nm was observed with increasing incubation time (Figure 6.4a). The plot of fluorescence intensity at the emission maximum against incubation time demonstrates a rapid initial increase, followed by a slower rise, suggesting a fast initial leakage and slower sustained release over time (Figure 6.4b).

The increase in emission intensity can be attributed to both the enzymatic release of fluorescein from the vesicles and its pH-dependent photophysical behavior. The initial vesicle suspension exhibited a mildly acidic pH (~5.6), under which fluorescein remains predominantly in its weakly fluorescent monoanionic form. Upon enzymatic degradation of the PEG_{114}-*b*-PLA_{500} vesicle membrane by proteinase K, the dye was released into the surrounding phosphate-buffered saline (pH 7.4). At this higher pH, fluorescein is present in its highly fluorescent dianionic form, thereby contributing to the observed increase in fluorescence. At the same time, a gradual dilution of the released dye in the bulk medium resulted in a decrease of absorbance (Figure 6.4c). The final absorption spectrum also exhibited a characteristic band corresponding to the dianion form of fluorescein, further confirming its deprotonation and supporting the fluorescence data. This system shows promise for bacterial enzyme-triggered release of pH-sensitive dyes from PEG-*b*-PLA vesicles. However, fluorescein is known to exhibit low photostability, suggesting that it may not be an ideal candidate for applications such

as wound dressings. Hence, encapsulation of the novel photostable, pH-sensitive carborhodols was investigated.

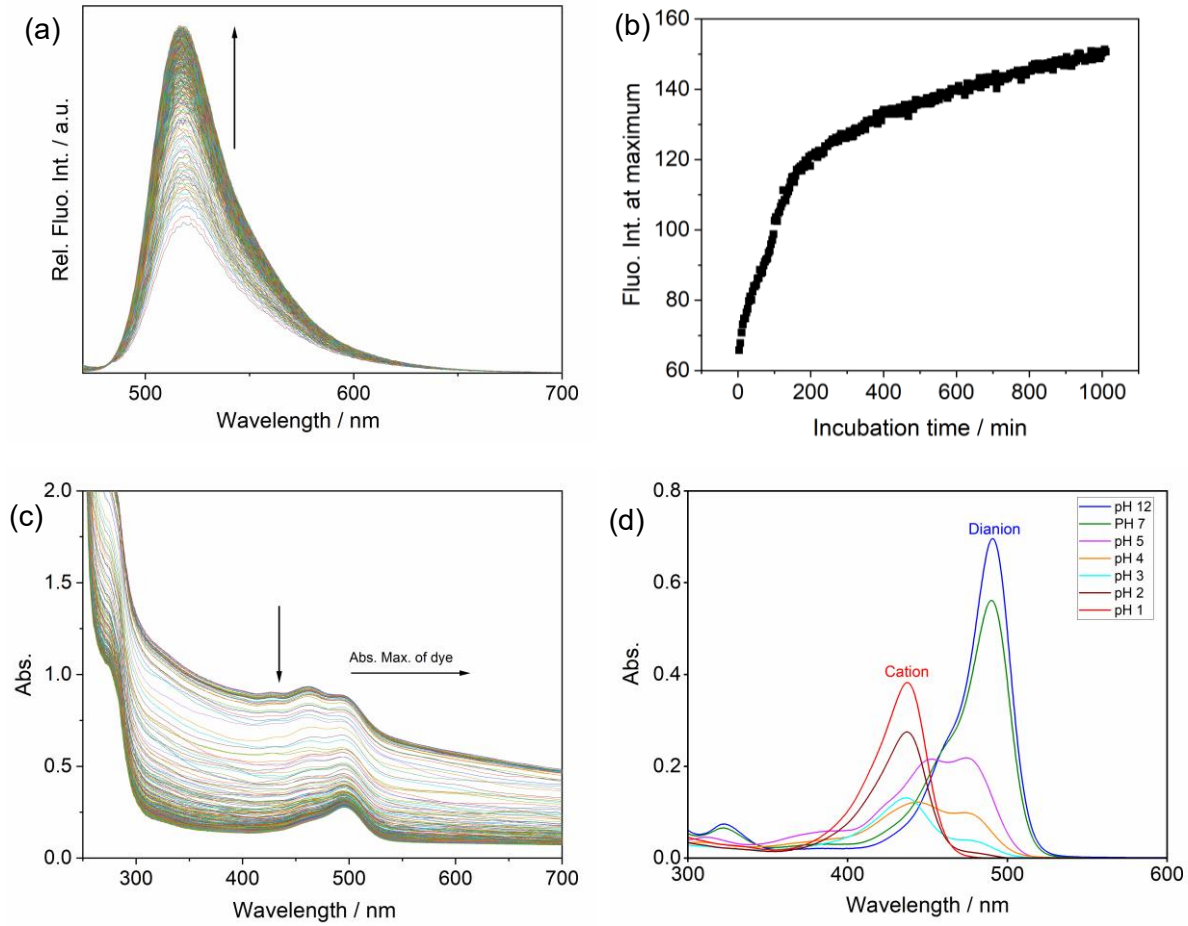

Figure 6.4. Kinetics of fluorescein dye release from PEG_{114}-*b*-PLA_{500} assemblies. (a) Fluorescence spectra recorded over time ($\lambda_{exc.}$ = 460 nm), (b) Fluorescence intensity at the emission maximum as a function of incubation time, (c) corresponding absorption spectra of the system collected over time, (d) Absorption spectrum of free fluorescein dye across a pH range of 1–12.

Encapsulation of Carborhodol Dyes with Varying Hydrophilicity

Hydrophobic Dye

The hydrophobic, photostable, and pH-sensitive dye **AS 01** exhibits a decrease in fluorescence intensity following vesicle lysis by proteinase K (Figure 6.5a and b). Hydrophobic dyes will preferentially associate with the hydrophobic wall of the vesicle.[128] When the vesicle degrades in aqueous medium, the dye's poor water solubility causes it to precipitate out of solution, along with any surrounding (also insoluble) polymer, forming a colored precipitate and a colorless supernatant (Figure 6.5c). This precipitation leads to a decrease in fluorescence intensity because the dye is no longer freely dispersed and available for fluorescence excitation.

The emission maximum of the dye released from the vesicles was observed at 609 nm upon excitation at the isosbestic point of the free dye in solution (555 nm). This emission lies between the characteristic maxima of the acidic (590 nm) and basic (619 nm) forms,

suggesting either the presence of a mixture of protonation states or an environmental influence on the dye's photophysical properties. The latter is plausible given the solvatochromic nature of the dye (see Chapter 5), indicating that the microenvironmental polarity may also contribute to the observed spectral shift under the experimental conditions. In conclusion, **AS 01**-loaded PEG-*b*-PLA vesicles can be utilized as a photostable fluorescent marker via turn-off signaling for the detection of bacterial enzymes capable of hydrolyzing ester bonds. However, this system does not exploit the pH-responsiveness of **AS 01**; hence, the encapsulation and release of the more hydrophilic dyes **AS 02**, **AS 03**, **AS 07**, and **AS 13** were investigated.

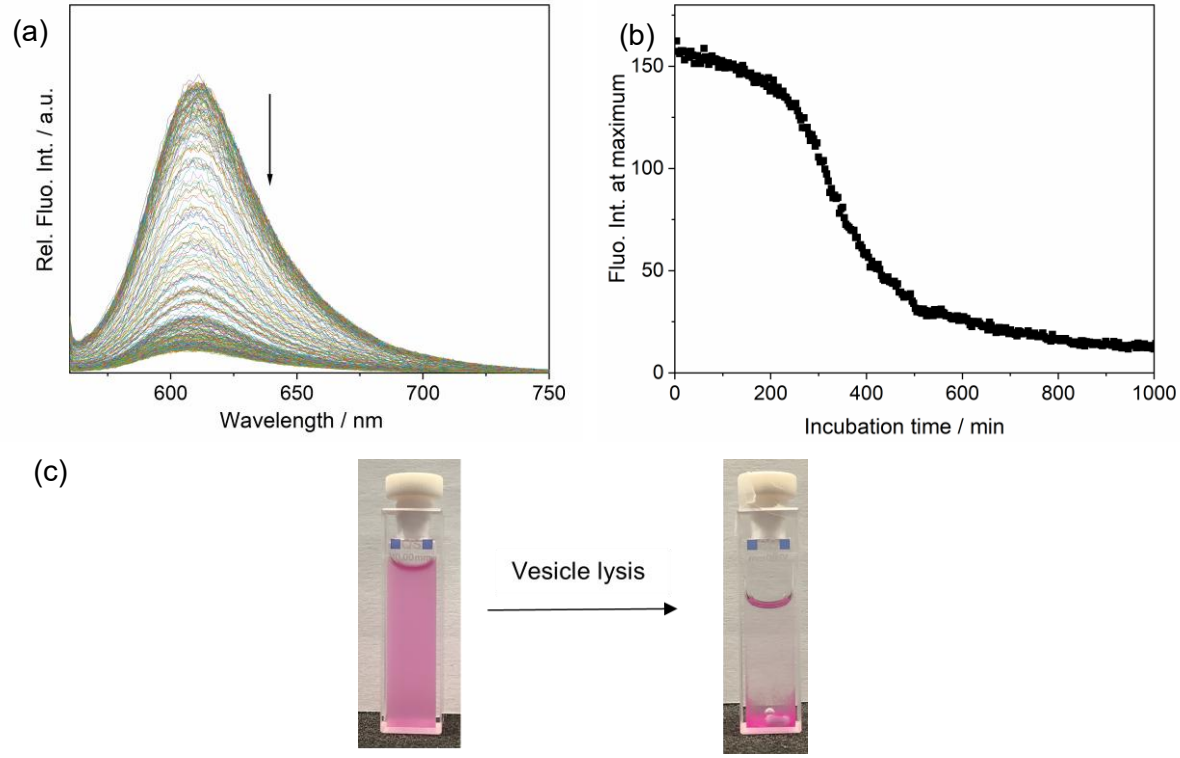

Figure 6.5. Kinetics of **AS 01** dye release from PEG_{114}-*b*-PLA_{500} assemblies upon incubation with proteinase K (2 mg/mL). (a) Fluorescence spectra recorded over time ($\lambda_{exc.}$ = 555 nm, arrow indicates change over time) (b) fluorescence intensity at the emission maximum as a function of incubation time, and (c) photographic image of the vesicle suspension before and after lysis.

Hydrophilic Dyes

Vesicle suspensions loaded with the moderately hydrophilic dye **AS 02** and the hydrophilic dyes **AS 03**, **AS 07**, and **AS 13** became nearly colorless after one week of dialysis, indicating substantial dye loss. Extended dialysis establishes a strong concentration gradient across the vesicle membrane, and for dyes predominantly confined to the aqueous lumen, this gradient gradually drives diffusion out of the vesicles.

In contrast, charged fluorophores such as fluorescein (pH-dependent) and **ATTO 594** (pH-independent), which display comparable overall hydrophilicity to the hydrophilic carborhodols (Table 6.1), retained visible color even after one week. Likewise, the parent charged carbopyronine **AZ 234**, structurally related to **AS 02** (see Chapter 3), remained encapsulated

(Figure S2). These comparisons suggest that leakage primarily affects neutral hydrophilic carborhodol dyes. Such uncharged hydrophiles can slowly diffuse across PEG-*b*-PLA membranes over extended timescales despite the thickness of the polymer bilayer,[244] whereas hydrophobic neutral dyes such as **AS 01** are effectively trapped within the PLA corona through favorable hydrophobic interactions.[263]

To minimize leakage, dialysis was limited to two days, followed by size-exclusion chromatography (SEC) for rapid purification. Nonetheless, the resulting suspensions retained only faint coloration, making them unsuitable for pH sensing based on visible changes (Figure S3). Number-weighted DLS measurements gave mean hydrodynamic diameters of 315 ± 1 nm for **AS 02** (5-day dialysis), and 221 ± 2 nm, 224 ± 3 nm, and 223 ± 3 nm for **AS 03**, **AS 07**, and **AS 13** (after SEC), respectively (Figure S4). The diameter differences between **AS 02**-loaded vesicles and others are most likely due to the different purification procedures used.

Despite the weak visible color, all the encapsulated carborhodol dyes exhibited an increase in fluorescence intensity with increasing pH (Figure 6.6), consistent with the behavior of the free dyes (see Chapter 4).

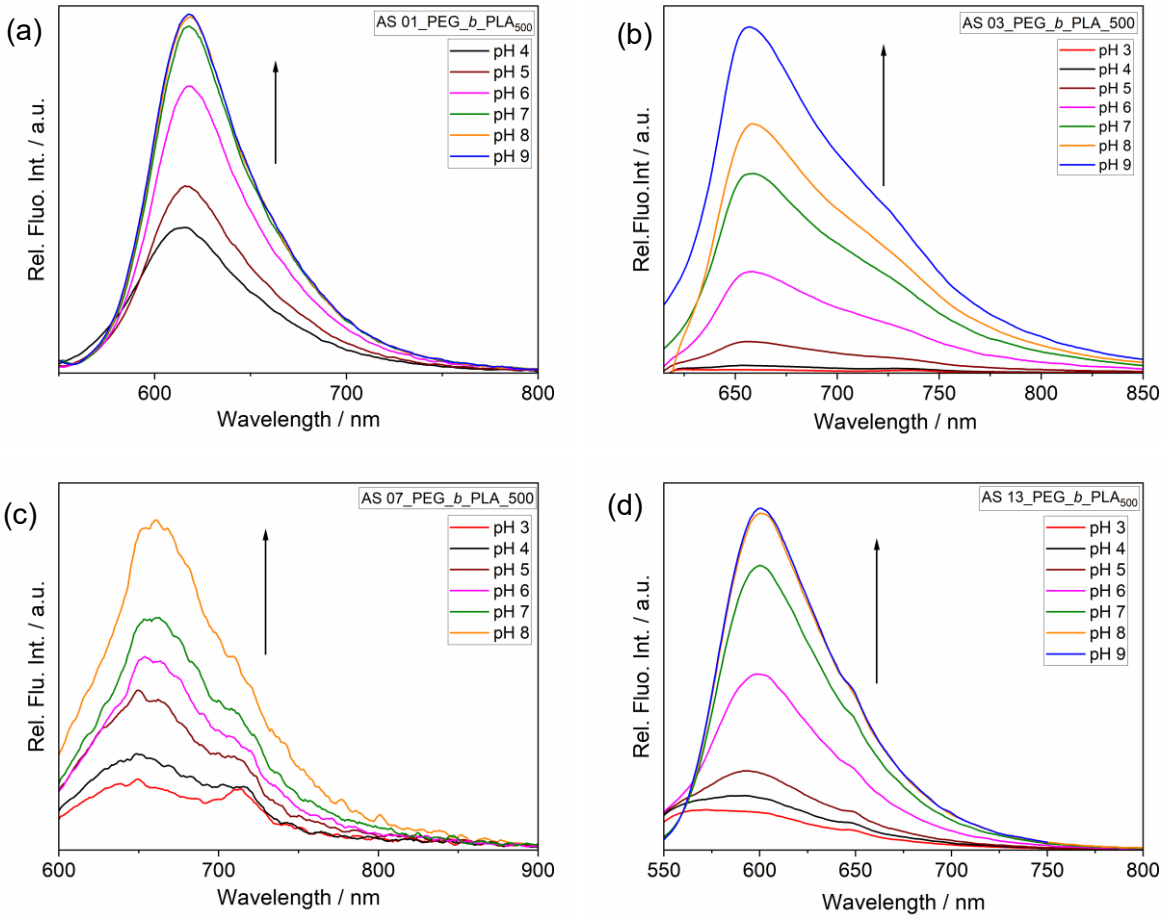

Figure 6.6. Fluorescence spectra of dye-loaded PEG_{114}-*b*-PLA_{500} assemblies at different pH values. (a) **AS 01** (λ_{exc} = 530 nm), (b) **AS 03** (λ_{exc} = 590 nm), (c) **AS 07** (λ_{exc} = 575 nm), and (d) **AS 13** (λ_{exc} = 531 nm),

For **AS 03**, the encapsulated acidic form exhibited an emission maximum (λ_{em}) of 648 nm at pH 3, comparable to that of the free dye in solution. At basic pH, λ_{em} shifted to 657 nm, representing a bathochromic shift of approximately 5 nm relative to the free dye. Both acidic and basic forms were excited at 590 nm (Figure 6.6b).

AS 07 displayed weak fluorescence, consistent with the low fluorescence quantum yield (Φ_{fl}) of the free dye in solution (Chapter 4). The λ_{em} values were 660 nm at pH 8 and 648 nm at pH 3, corresponding to a hypsochromic shift of ~10 nm compared with the respective free dye. Both forms were excited at their isosbestic point (575 nm) (Figure 6.6c).

AS 13 exhibited similar pH-dependent behaviour, with λ_{em} values of 582 nm (pH 3) and 600 nm (pH 9), each showing a bathochromic shift of approximately 5 nm relative to the free dye. Measurements for **AS 13** were also performed with excitation at its isosbestic point (531 nm) (Figure 6.6d).

The hydrophobic dye **AS 01**, which remained fully retained after one week of dialysis, also exhibited enhanced fluorescence intensity with increasing pH of the suspension. The λ_{em} was approximately 617 nm for both acidic and basic forms, closely matching the λ_{em} of the basic free dye (619 nm) and differing from the acidic free dye in a pH 3 buffer (590 nm) (Figure 6.6a). A similar behavior is also expected for **AS 02** due to the structural similarity.

The shifts in λ_{em} of dyes when encapsulated are likely due to the changes in the microenvironment of the dyes upon encapsulation. The solvatochromic behaviour observed for the carborhodol dyes (see Chapter 5) supports this interpretation.

The rapid and reversible fluorescence response of encapsulated dyes to external pH changes indicates that protons can permeate through the PEG-*b*-PLA membrane sufficiently to equilibrate the lumen of the vesicle with the surrounding solution. This effect occurs on a much faster timescale than the pH-triggered release of dyes caused by hydrolytic degradation of the polyester domains at acidic pH (~5), which typically requires hours.[244] Therefore, enzymatic or chemical disruption of the membrane is not required for pH sensing with these formulations. Size-exclusion chromatography (SEC) enriches vesicles in the earliest eluting fraction, whereas free dye elutes later; therefore, collecting only the first fraction minimizes free-dye contamination.

To confirm the purification of dye-loaded vesicles from free dye, confocal microscopy was performed. Images of SEC-purified suspensions show fluorescent vesicles (Figure 6.7). Figure 6.7a shows numerous punctate, vesicle-like structures exhibiting strong localized fluorescence consistent with successful dye encapsulation, confirming that fluorescence was primarily localized to vesicles, with minimal diffuse background. Control images of free dye solutions showed diffuse fluorescence (Figure 6.7b), further supporting vesicle-associated fluorescence as the predominant signal.

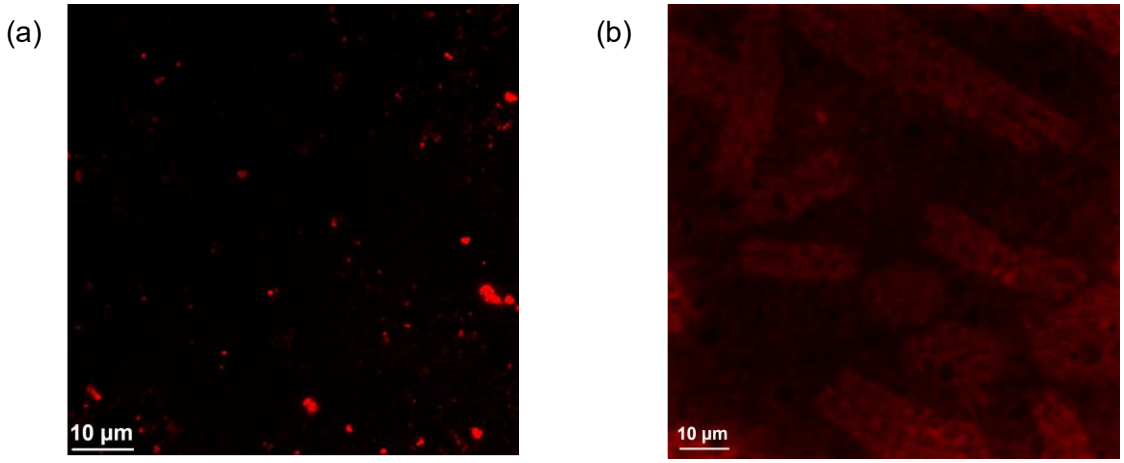

Figure 6.7. Confocal fluorescence microscopy of (a) **AS 13** -loaded PEG-*b*-PLA$_{500}$ vesicles and (b) free **AS 13** dye in solution (1% v/v in PBS, $\lambda_{exc.}$ = 578 nm). The scale bar represents 10 µm.

6.3 Conclusion and Outlook

The amphiphilic block copolymer PEG$_{114}$-*b*-PLA$_{750}$ was synthesized, and PEG$_{114}$-*b*-PLA$_{500}$ was self-assembled into vesicles for the encapsulation of pH-sensitive carborhodol dyes. The octanol-water distribution coefficient (log K_{ow}) was determined for selected carborhodols, ATTO dyes, and reference dyes, allowing for their classification as hydrophilic (log K_{ow}< 0), moderately hydrophilic (0 ≤log K_{ow}< 2), or hydrophobic (log K_{ow} ≥ 2). Based on these values, **AS 01** was selected as a hydrophobic encapsulation candidate, **AS 02** as moderately hydrophilic, and fluorescein, **AS 03**, and **AS 13** as hydrophilic candidates. **AS 07** was included among the hydrophilic dyes due to its structural similarity to **AS 03**.

All dyes were successfully encapsulated and characterized by DLS. The selected vesicles were observed by FESEM and confocal microscopy. Upon enzyme-triggered vesicle lysis, the hydrophobic dye **AS 01** was released and precipitated from solution, along with the surrounding polymer, resulting in fluorescence turn-off and preventing pH sensing capability. In contrast, the hydrophilic dye fluorescein exhibited pronounced pH-dependent absorption and fluorescence responses after lysis, similar to the free dye, indicating its suitability for spectroscopic detection of pH in the surrounding medium.

Moderately hydrophilic and hydrophilic carborhodol dyes exhibited only weak visible coloration after purification, which limits their suitability for direct colorimetric pH sensing. In contrast, their vesicle suspensions showed an increase in fluorescence intensity with rising pH, even in the absence of membrane disruption. These results suggest that incorporating dye-loaded vesicles into a solid support matrix could provide a practical platform for fluorescence-based monitoring of wound pH in smart dressing applications.

6.4 Experimental Section

PEG_{114}-*b*-PLA_{500} synthesis and DLS measurements were performed by M.Sc. Nicola Cusick, FESEM measurements by M.Sc. Aysha Awan, and confocal fluorescence microscopy with the assistance of Dr. Jan Erik Hoffmann.

6.4.1 Equipment

^{1}H-NMR spectra were recorded using a Jeol ECZ 500 (500 MHz) at 25 °C. Spectra were analyzed with the software Mestre Nova (version: 12.0.3) and referenced to $CDCl_3$ (7.26 ppm). Chemical shifts (δ) are given in ppm, and J values are given in Hz.

DLS measurements were performed using a Wyatt Dynapro Plate Reader III (laser wavelength 818.3 nm, detector angle 150°) at 25 °C. For each measurement, five acquisitions of 5 s each were recorded. Samples were diluted with Milli-Q water (10 % v/v), and 30 µL aliquots were measured in triplicate. Number-weighted hydrodynamic diameters were calculated using a Gaussian fit (OriginPro 2021). The mean and standard deviation were determined from three independent measurements (3 samples).

FESEM images were obtained using a field-emission scanning electron microscope (Zeiss Ultra 55cv, Zeiss, Oberkochen, Germany). The samples were prepared by drop-casting a diluted vesicle suspension (1% v/v in Milli-Q water) onto silicon wafers that had been pre-cleaned with chloroform, ethanol, water, and UV-ozone. To create a conductive surface, samples were sputtered with gold for 30 s, resulting in a ~ 5.0 ± 0.5 nm thin gold layer. FESEM measurements were obtained using the Inlens secondary electron detector, with an operation voltage of 5 kV. The images were analyzed using ImageJ software (version 1.54p).

Absorption spectra were recorded using a PerkinElmer Lambda 750 spectrophotometer with baseline correction in Hellma quartz cuvettes (path length: 10 mm or 1 mm). Dye-release absorbance kinetics were measured using a Varian Cary 50 Bio spectrophotometer (Varian, Mulgrave, Victoria, Australia) with baseline correction, using 10 mm acrylic cuvettes (Sarstedt, Germany).

Emission spectra were recorded using either a Fluorolog-3 spectrofluorometer (HORIBA Jobin Yvon, France) to measure emission intensity as a function of surrounding pH, employing Hellma quartz fluorescence cells (path length 10 mm), or a Varian Cary Eclipse spectrometer (Mulgrave, Victoria, Australia) at 25 °C to monitor dye-release fluorescence kinetics, using 10 mm acrylic cuvettes.

Dye-loaded vesicles were imaged using a Stellaris 8 confocal microscope (Leica Microsystems, Wetzlar, Germany) equipped with an 86×/1.20 water-immersion objective. FLIM images were acquired at a resolution of 1024 × 1024 pixels with an excitation wavelength of

578 nm. The samples (both free dye and dye-encapsulated vesicles) were observed by aliquoting them into an 8 Well high-Glass Bottom µ-Slide (Ibidi GmbH, Germany).

6.4.2 Materials and Methods

Poly (ethylene glycol) methyl ether ($mPEG_{114}$, average number average molar mass (Mn = 5000 $gmol^{-1}$)), L-lactide ((3S)-*cis*-3,6 dimethyl-1,4-dioxane-2,5-dione, 98%), and stannous octoate (tin (II) 2-ethylhexanoate, 92.5-100%) were purchased from Sigma-Aldrich (Merck, Germany). Spectra/Por® dialysis membranes (MWCO 6–8 kDa) were obtained from Carl Roth GmbH (Germany). Milli-Q water (resistivity ≥18.2 MΩ cm) was obtained from a Millipore Direct Q8 system (Millipore Advantage A10, Schwalbach) equipped with a Millimark Express 40 L unit (Merck, Germany). All solvents were spectroscopic grade and used as purchased. Zeba Spin Desalting Columns (MWCO 40 KDa, 0.5 mL) were purchased from Thermo Fisher Scientific.

pH 3 buffer (Carl Roth, Art. No.: T18.1.1), composed of citric acid, NaOH, and NaCl, and pH 10 buffer (Carl Roth, Art. No.: P716.1), containing boric acid, NaOH, and KCl, were used. PBS buffer (pH 7.4) was prepared from Milli-Q water and biochemistry-grade chemicals (NaCl, KCl, KH_2PO_4, and $Na_2HPO_4 \cdot 2\ H_2O$).

Octanol/water Partition Coefficient (K_{ow}) Determination

Different concentrations of dye were prepared in centrifuge tubes (15 mL, VWR, Germany) containing PBS buffer (pH 7.4) and octanol in a 1:1 ratio (total volume 8 mL). For example, **AS 02** was tested at 31, 44, 68, 125, 166, and 219 µM. The tubes were shaken for 1 hour using a NeoLab vortex mixer and then allowed to equilibrate. After equilibration, the samples were centrifuged in a Hettich EBA-20 Centrifuge apparatus (2000 rpm, 30 min) to separate the octanol and aqueous layers, which showed clear phase separation (Figure S1d). The layers were carefully separated using a pipette, and dye concentrations in each layer were determined using UV-Vis spectrophotometry. Highly concentrated samples were diluted with the corresponding solvent, and the dilution factor was taken into account when performing the calculations. Concentrations in both layers were calculated using the Beer-Lambert law (Equation 2.7). The partition coefficient (K_{ow}) was obtained from the slope of the plot of octanol concentration (C_o) versus aqueous concentration (C_w), and log K_{ow} was subsequently calculated.

Synthesis of PEG_{114}-*b*-PLA_{750}

Prior to synthesis, all solid reagents were dried overnight in a vacuum oven (5 mbar), and glassware was dried at 60 °C. A dry Schlenk flask equipped with a magnetic stir bar was connected to a Schlenk line and subjected to three cycles of vacuum-argon exchange. Briefly,

the flask was dried under vacuum using a heat gun, then flushed with argon, and the process was repeated three times in total. The synthesis of PEG-*b*-PLA was adapted from Tücking et al.[138]

Molar ratios were adjusted according to the desired PLA chain length. For a PLA chain length of 750, mPEG (100 µmol) was added to stannous octoate (0.1 mL) at 80 °C, and the mixture was stirred under an argon atmosphere. After heating to 130 °C, L-lactide (37.5 mmol) was added, and the reaction mixture was stirred for 30 minutes. Once cooled to room temperature, the resulting white solid was dissolved in approximately 10 mL of DCM and precipitated into ice-cold diethyl ether (in excess, >10x the solvent volume). The precipitate was collected by centrifugation (6000 × g, 10 min), the supernatant was removed, and the solid was redissolved in DCM. This purification cycle was repeated four additional times. The final white solid product was then dried under vacuum at 40 °C overnight (5 mbar).

^{1}H-NMR (500 MHz, $CDCl_3$): δ = 1.58 (d, ^3J = 7 Hz, 2523 H, $C\underline{H}_3CH(C=O)$ O (PLA)), 3.64 (s, 456 H, $OC\underline{H}_2C\underline{H}_2O$ (PEG)), 3.38 (3 H, s, OCH_3 (PEG-OMe)), 5.16 (q, ^3J = 7 Hz, 842 H, $CH_3C\underline{H}(C=O)$ O (PLA)).

Encapsulation of Reporter Dyes

Self-assembly of the block copolymers (BCPs) was performed by the solvent-shift method.

Hydrophilic dye encapsulation: An aqueous solution of the hydrophilic dye (1.0 mL, e.g., **AS 02**, 3.5 mM in Milli-Q water) was added at a rate of 0.5 mL/min using a syringe pump (AL-400, WPI, US) to a stirring polymer solution (1.0 mL, 3 wt% in THF).

Hydrophobic dye encapsulation: Milli-Q water (1.0 mL) was added at the same rate (0.5 mL/min) to a stirring mixture containing the BCP solution (1.0 mL, 3 wt% in THF) and the hydrophobic dye (e.g., **AS 01**, 2.4 mM in THF).

The resulting turbid mixtures were stirred for 16 h at room temperature, after which 10 mL of Milli-Q water was added to each. Suspensions were dialyzed against Milli-Q water (MWCO 6-8 kDa) for 7 days to remove residual polymer, THF, and non-encapsulated dye. The dialysis medium was replaced 3–4 times daily. Dialysis was stopped when the absorbance of the respective dye in the surrounding solution was negligible (A < 0.01).

Purification of Hydrophilic Carborhodol Dyes (AS 03, AS 07, AS 13): After 2 days of dialysis under the above conditions, suspensions were further purified using Zeba spin desalting columns (MWCO 40 kDa; Thermo Fisher Scientific, Germany). Prior to use, columns were centrifuged (1500 rpm, 1 min) to remove the storage solution containing 0.05% sodium azide and they were equilibrated three times with PBS buffer (100 µL each, centrifuged at 1500 rpm for 1 min). Samples (100 µL) were applied to the columns and centrifuged (1500 rpm, 2 min). The first eluate fraction was collected, containing vesicles with or without encapsulated dye.

Fluorescence and Absorbance Monitoring of Enzymatic Degradation

After dialysis, dye-loaded PEG_{114}-*b*-PLA vesicles were treated with proteinase K (2 mg mL^{-1} in PBS buffer) at a vesicle suspension to enzyme solution volume ratio of 1:1. The kinetics of dye release were monitored by recording fluorescence spectra (300 cycles at 2 min intervals) and absorption spectra (204 cycles at 5 min intervals). Excitation wavelengths for each dye were as follows: **AS 01**: 555 nm, and fluorescein: 460 nm.

pH-dependent Emission of Vesicles

Zeba column-purified vesicle fractions (10 µL) were added to 1.0 mL of buffer solutions at pH values ranging from 3 to 8. Fluorescence spectra were recorded using the following excitation wavelengths: **AS 07**: 575 nm, **AS 13**: 531 nm (respective isosbestic points), **AS 03**: 590 nm, and **AS 01**: 530 nm.

7 pH-Responsive Chitosan-Based Hydrogels for Detecting Wound Infections

While the physical encapsulation of carborhodol dyes in polymeric vesicles (see Chapter 6) demonstrated their potential for fluorescence-based pH sensing in wound infection detection, their pH-responsiveness was further investigated by chemical immobilization onto a chitosan (CS) surface. Smart pH-responsive wound dressings were produced by covalently coupling NHS esters of the photostable carborhodol dyes **AS 14** and **AS 15** (see Chapter 3) to chitosan (CS) films. Successful grafting was confirmed by ATR-FTIR, UV-VIS, and fluorescence spectroscopy, while FESEM provided film thickness and surface morphology. The resulting materials exhibited reversible color changes within pH 4–7, with pK_a values of 4.9 (**AS 14-CS**) and 5.3 (**AS 15-CS**). **AS 14-CS** displayed both chromogenic and fluorogenic responses, achieving a fluorescence turn-on ratio of 30 in the basic versus the acidic form, whereas **AS 15-CS** acted primarily as a chromogenic sensor (turn-on ratio 1.2). Both films exhibited pH-dependent fluorescence lifetimes, high photostability, color stability, leaching resistance, and a swelling ratio of ~200%, with fully reversible responses after prolonged irradiation with a 575 W mercury halide lamp. This approach yielded stable, dual-mode (chromogenic-fluorogenic) wound dressings capable of real-time pH monitoring, offering potential for visual and fluorescence-based detection of wound healing and infection status.[iii]

7.1 Introduction and Objective

Monitoring the pH of wounds in real time provides valuable insights into the healing process and can serve as an early indicator of potential bacterial infection.[17] Over the past decade, a wide range of devices for monitoring wound pH have been developed, including flex-circuit inductive transducers,[13] optical sensors based on chemical dyes,[14] pH-sensitive electrodes,[15] and carbon quantum dots.[16] These methods usually depend on advanced technologies, which can raise production costs. In contrast, incorporating pH-sensitive dyes that undergo visible color changes with pH variation into a carrier material presents a simpler and more cost-effective approach for wound pH monitoring.

Hydrogels are promising carrier materials for wound dressings due to their flexibility, biocompatibility, and ability to retain moisture through their crosslinked network structure. They help absorb exudates, maintain a moist environment, and support oxygen diffusion, all

[iii] The swelling ratio and FESEM measurements were performed by M.Sc. Nicola Cusick (University of Siegen), AFM measurements by M.Sc. Joshua Schumacher (University of Siegen), and FLIM measurements were carried out with the assistance of Dr. Jan Erik Hoffmann (ATTO-TEC GmbH).

essential for wound healing.[264,265] Among them, chitosan, a natural polymer obtained by deacetylating chitin, has gained significant interest for its combined biocompatibility, biodegradability, antimicrobial activity, and ability to promote hemostasis and tissue regeneration.[266] It is already used in commercial wound dressings, and its free amine and hydroxyl groups allow easy chemical modification, which makes it an ideal choice.

In recent years, various natural dyes, including anthocyanins,[18–22] anthraquinone,[23] green tea extract,[24] and curcumin,[25,26] have been investigated with regard to their incorporation into polymers to develop pH-sensitive films that have shown promise in applications such as smart food packaging and wound dressings. These natural dyes are non-toxic and biocompatible, but they often have limited stability under high temperatures, intense light, or higher pH. Moreover, variability in the extraction source can lead to inconsistent colors and lower reproducibility.[267] In contrast, synthetic dyes provide more reliable and consistent performance for pH indication.

Chemical grafting of synthetic pH-responsive dyes onto polymer backbones has emerged as a promising approach for developing polymeric dyes that can be modified into functional films. This method offers a significant advantage over direct mixing or adsorption, as the covalent attachment of dye molecules minimizes leaching or migration while preserving pH sensitivity.[268] For example, CS has been chemically modified with dyes such as methyl red and rose bengal through coupling reactions to produce colorimetric nanofibers for biomedical applications.[269] In a similar approach, CS has also been grafted with phenol red and rosolic acid using the Mannich reaction to create colorimetric pH-sensing films, enabling applications such as smart wound dressings and food spoilage sensors.[27] All these dyes exhibit low photostability and function primarily as pH indicators through absorbance changes, rather than enabling more sensitive and accurate fluorescence-based sensing.[28–31]

An example of pH-sensitive fluorescent probes in hydrogel systems is demonstrated by Qiao et al., who developed a smart hybrid hydrogel by the physical crosslinking of polyvinyl alcohol (PVA) and a UV-cleavable linker (1-(5-methoxy-2-nitro-4-prop-2-ynyloxyphenyl)ethyl *N*-succinimidyl carbonate) used to link an antibiotic to a polymeric backbone (gentamicin sulfate-linker-mPEG). Cy3 and Cy5-modified silica nanoparticles (SNP-Cy3/Cy5) were loaded into the hydrogel and acted as a pH-responsive fluorescent probe to detect bacterial infection based on the fluorescence resonance energy transfer (FRET) between Cy3 and Cy5.[270] However, the low photostability of cyanine fluorophores limits their long-term performance.

Therefore, there is a clear need for smart pH-sensitive wound dressings incorporating photostable dyes capable of detecting pH changes through both absorption and fluorescence. In this work, two novel pH-responsive carborhodols, **AS 14** and **AS 15**, exhibiting high photostability and pH-dependent changes in absorption, fluorescence, and fluorescence lifetime within the clinically relevant range (pH 4–7), were covalently coupled to a chitosan-

based hydrogel film. The photophysical properties were investigated, and the resulting film was found to function as a dual-mode chromogenic and fluorogenic sensor with excellent color stability, no dye leaching, and reversible color changes, making it highly suitable for smart wound dressing applications.

7.2 Results and Discussion

7.2.1 Coupling of Carborhodol Dyes to Chitosan Hydrogel

The pH-respons CS-based hydrogel films were prepared by covalently attaching the NHS ester-activated carboxylic groups of the carborhodol dyes, **AS 14** and **AS 15**, to the primary amine groups of the glucosamine units in CS via amide bond formation (Scheme 7.1).

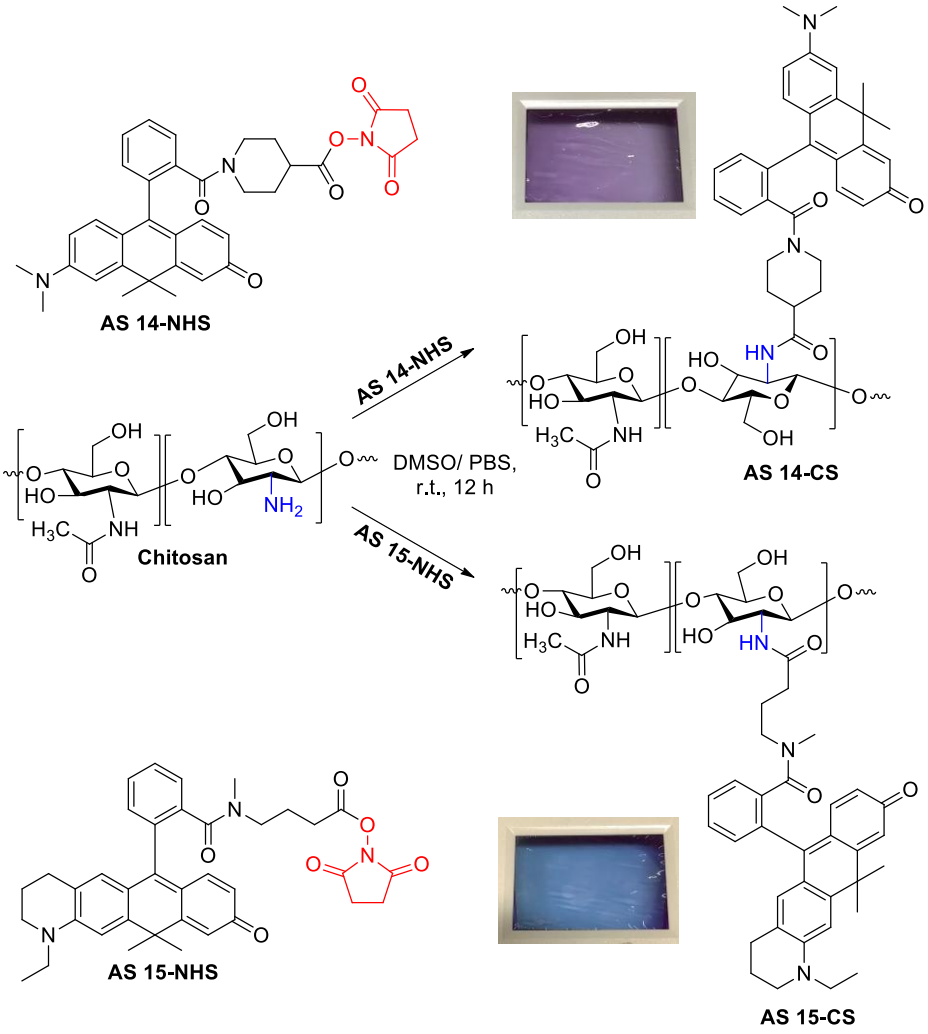

Scheme 7.1. Covalent modification of chitosan films via coupling with NHS esters of pH-sensitive carborhodol dyes, **AS 14** and **AS 15**. The resulting-colored films after washing with PBS are shown. The films depicted here were prepared by drop-casting.

The chitosan films were prepared by solution casting using either spin coating onto glass substrates or drop casting onto polystyrene Petri dishes. Colored and fluorescent films were successfully prepared using both drop-casting and spin-coating techniques. Given the greater

potential of drop-cast films for practical applications in a wound dressing due to a lack of support material, their characterization is presented here, while the photophysical data and photographs of spin-coated films are provided in Appendix (Figures S1 and S2).

The modification was verified by Attenuated Total Reflection Fourier Transform Infrared (ATR-FTIR) spectroscopy (Figure 7.1). In the ATR-FTIR spectra of **AS 14** and **AS 15** immobilized chitosan hydrogels, the disappearance of the band at 1588 cm^{-1}, typically attributed to the primary amine group of the glucosamine unit in chitosan, suggests its involvement in a chemical reaction. The increased intensity of the band at 1650 cm^{-1}, corresponding to amide I (C=O) vibrations, indicates the formation of new amide bonds. Additionally, a band at 1630 cm^{-1} observed in **AS 14-CS**, likely arising from both the dye's inherent tertiary amide and new amide linkages, further supports the generation of amide I. Enhanced intensities near 1570 cm^{-1} for both **AS 14-CS** and **AS 15-CS**, and the appearance of a new band at 1546 cm^{-1} in **AS 15-CS**, characteristic of amide II (N–H), support the conclusion that amino groups participated in covalent bonding through the formation of secondary amide linkages. The assignment of the observed bands is summarized in Table S1.

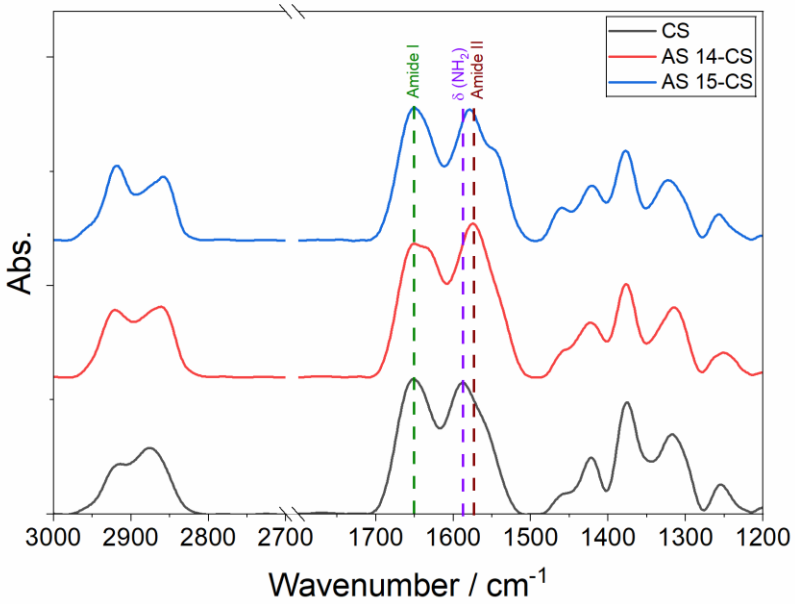

Figure 7.1. ATR-FTIR spectra of non-modified CS, **AS 14-CS,** and **AS 15-CS**.

The dry film thickness of drop-cast chitosan films was analyzed using field emission scanning electron microscopy (FESEM). The non-modified chitosan film exhibited a thickness of 50.7 ± 1.7 µm, whereas covalent modification with NHS ester-functionalized dyes resulted in a significant reduction to 15.5 ± 0.3 µm and 13.8 ± 0.4 µm for **AS 14-CS** and **AS 15-CS** films, respectively, indicating a denser and more compact hydrogel structure (Figure 7.2).

Conversely, the thickness of spin-coated chitosan films, measured by atomic force microscopy (AFM), increased upon dye modification, with the blank film showing a thickness

of 194.5 ± 2.5 nm, while **AS 14-CS** and **AS 15-CS** films exhibited enhanced thicknesses of 239.46 ± 3.5 nm and 252.2 ± 3.6 nm, respectively (Figure S3).

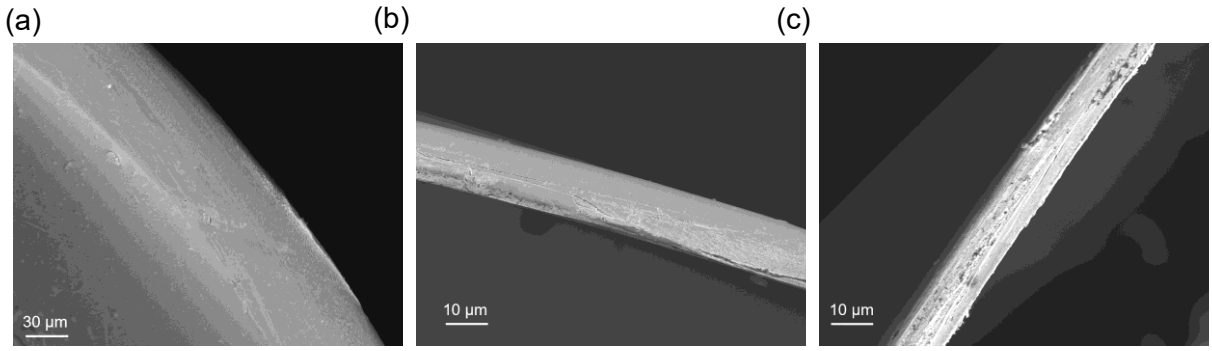

Figure 7.2. FESEM images of (a) non-modified CS, (b) **AS 14-CS**, and (c) **AS 15-CS**.

The gravimetric swelling ratio of the chitosan films was evaluated to assess their water uptake capacity (Figure 7.3). As shown in the swelling profile, all films exhibited the ability to absorb water up to approximately 200% of their dry weight. The maximum swelling was observed within the first hour, after which no significant changes occurred, indicating equilibrium swelling behavior. Notably, both the non-modified chitosan film and the dye-modified films (**AS 14-CS** and **AS 15-CS**) demonstrated similar swelling ratios, suggesting that the modification did not adversely affect the swelling capacity of the polymer. This high swelling ratio is advantageous for wound dressing applications, as it would maintain a moist wound environment, facilitating the wound-healing process.[271]

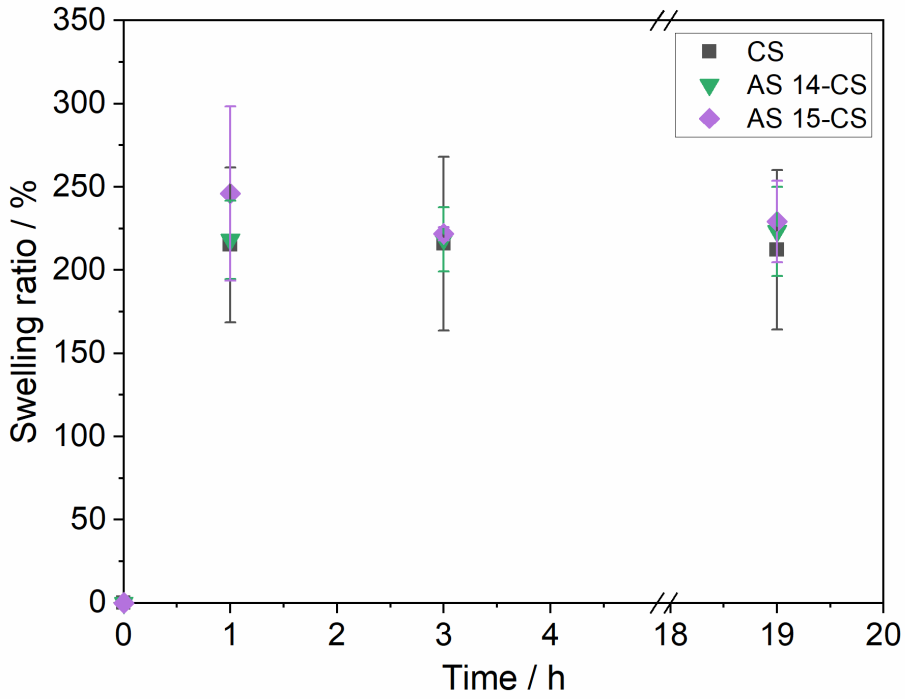

Figure 7.3. Swelling ratios of (a) non-modified CS, (b) **AS 14-CS**, and (c) **AS 15-CS**.

7.2.2 Photophysical Properties of Dye-Coupled Chitosan Films

The color difference between the acidic and basic forms of CS-based films is clearly visible to the naked eye in response to changes in the surrounding media (Figure 7.4). Upon exposure to a pH 4 buffer, both films immediately changed to a pink color and then turned to the characteristic color of the basic form of each dye when washed with pH 8 buffer (purple for **AS 14-CS** and blue for **AS 15-CS**). This reversible color change confirms that both films function as chromogenic (colorimetric) pH indicators, based on their pH-dependent absorption behavior. Under UV illumination at 366 nm, the **AS 14-CS** film exhibited a pronounced fluorescence turn-on response when transitioning from pH 4 to pH 8. This fluorescence enhancement is readily observable by the naked eye, as the film appears significantly brighter at pH 8 as compared to pH 4. This behavior is consistent with the photophysical response of the free **AS 14** dye, which shows a fluorescence turn-on ratio of 29 between acidic and basic conditions. Therefore, **AS 14-CS** can be employed as both a colorimetric and fluorogenic pH sensor. In contrast, the **AS 15-CS** film showed only a minor increase in fluorescence intensity, corresponding to the relatively low turn-on ratio of the free **AS 15** dye (1.7).

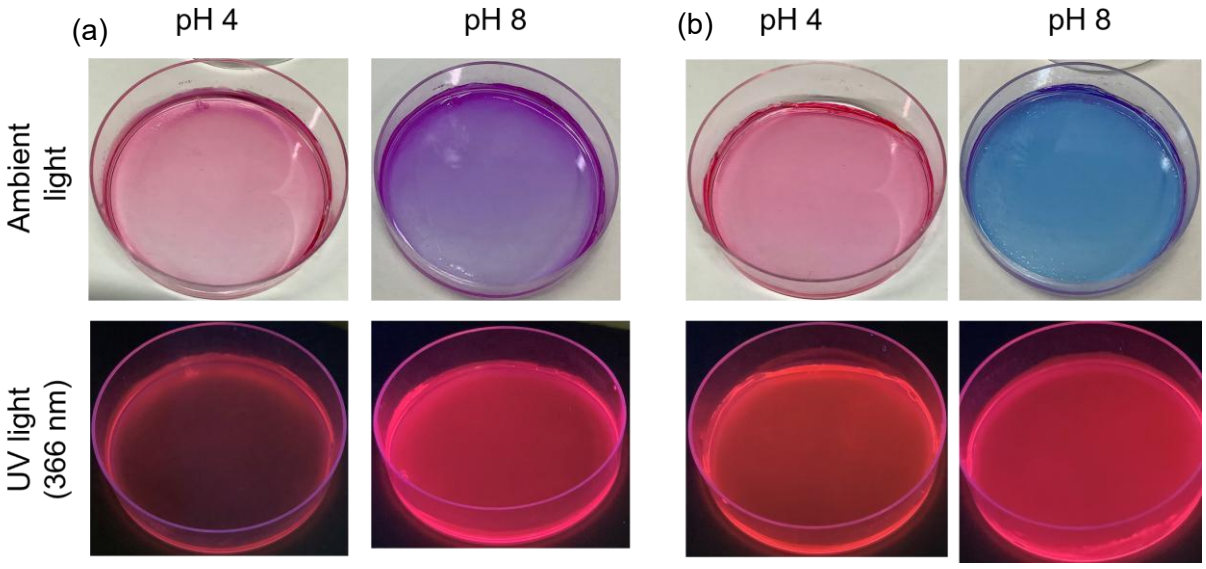

Figure 7.4. Photographs of (a) **AS 14-CS** and (b) **AS 15-CS** films at pH 4 and pH 8, under ambient and UV light (366 nm).

Determination of the pK_a

The pH-dependent absorption behavior of the carborhodol-coupled CS films was investigated by performing photometric acid-base titrations in Britton-Robinson buffer solutions over a pH range of 4.0 to 10.0. For the **AS 14-CS** film, the absorption spectrum at acidic pH (pH 4) shows a broad band centered at 520 nm (red trace), corresponding to the protonated form of the dye (Figure S4). As the pH increases, the intensity of this band gradually decreases, while a narrower band at 590 nm (blue trace), attributed to the deprotonated form of the dye, emerges with higher molar absorptivity. A bathochromic shift of approximately 4 nm is observed for both

the acidic and basic forms compared to the free dye in solution. This spectral shift is accompanied by a visible color change from pink (acidic) to violet (basic) (Figure 7.5e). The spectra exhibit an isosbestic point at approximately 540 nm, indicating a "clean" two-state equilibrium between the protonated and deprotonated species. The absorption at λ_{max} = 590 nm was plotted against the pH value of the solution, and the experimental data were analyzed by a fit to the theoretical model for weak acids (Henderson–Hasselbalch)[227], yielding a pK_a value of 4.9 (Figure 7.5c inset).

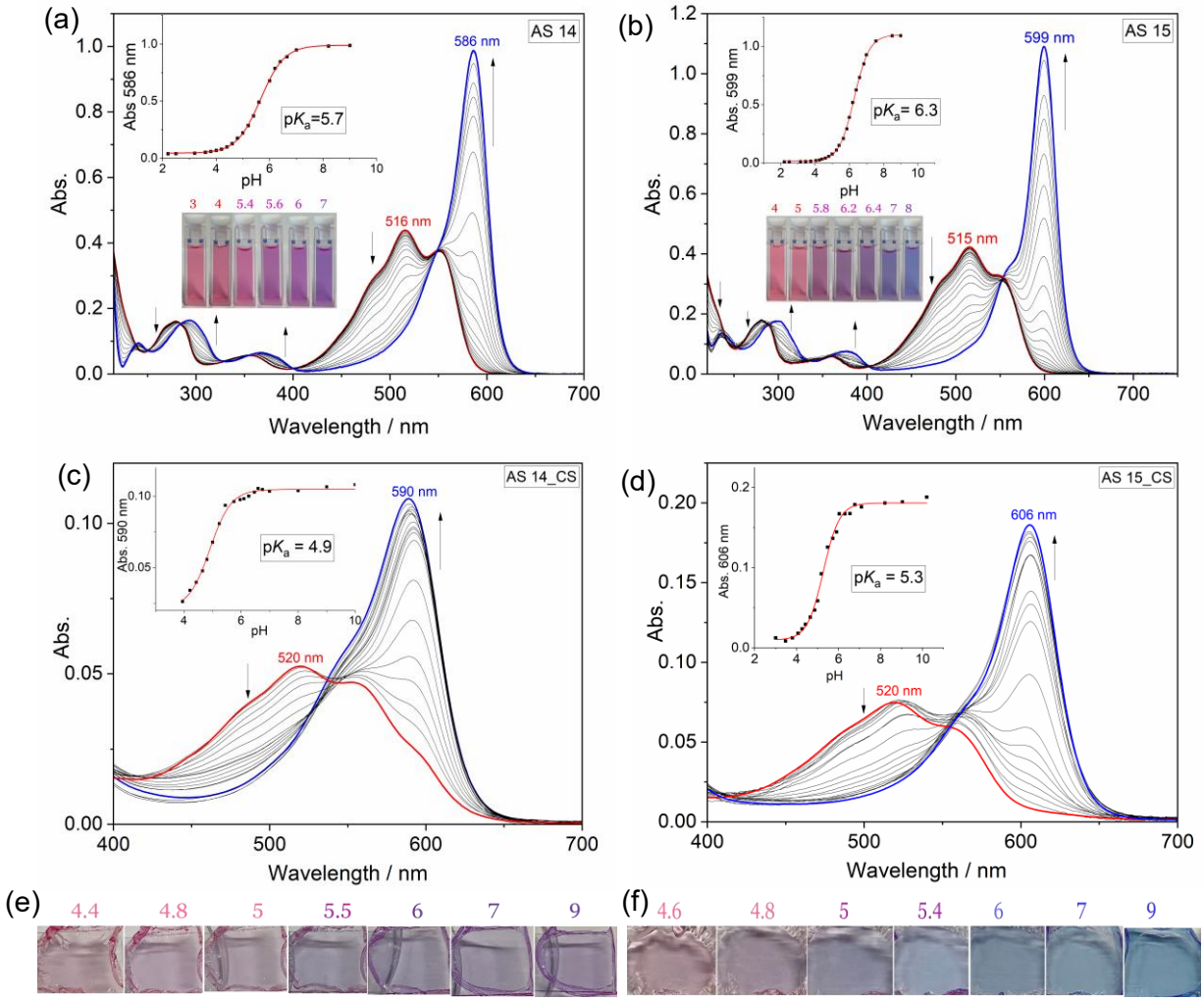

Figure 7.5. pH-dependent absorption spectra of (a) **AS 14**, (b) **AS 15,** (c) **AS 14-CS,** and (d) **AS 15-CS**. Arrows indicate the development of bands with increasing pH value of the solution. Inset: absorbance at long wavelength absorption maxima as a function of pH. The red line denotes the best fit of the experimental data to the theoretical isotherm of a weak acid; pK_a is determined from this plot. Images show color changes of (e) **AS 14-CS** and (f) **AS 15-CS** at various pH.

In the case of **AS 15-CS**, the protonated form exhibits a broad absorption band centered at 520 nm, while the deprotonated form gives rise to a sharper peak at 606 nm. Compared to the free dye, a bathochromic shift of 5 nm (acidic form) and 7 nm (basic form) is observed upon immobilization onto the chitosan hydrogel. The spectra display an isosbestic point ~550 nm. A gradual change from pink to blue is visually observed as the pH increases (Figure 7.5f). The

pK_a value for **AS 15-CS** was determined to be 5.3, based on a sigmoidal fit of the absorbance at 606 nm versus pH (Figure 7.5d inset).

In both cases, the pK_a values of the CS-bound dyes were approximately one pH unit lower than those of the corresponding free dyes in solution. The observed decrease in the pK_a of the dye upon immobilization in the CS film is likely due to several microenvironmental effects, including hydrogen bonding between the CS hydroxyl groups and the deprotonated dye, which stabilizes the conjugate base. Thus, with increased stability of D^-, K_a increases and pK_a decreases (Eq. 2.2).

Fluorescence Turn-On Ratio and Lifetime

As shown in Figure 7.4, the fluorescence intensity of CS films is higher in a basic environment compared to acidic conditions. To quantify this difference, fluorescence turn-on ratios were calculated in the same manner as described for the free dyes in Chapter 4. The basic form of each dye was used as the reference standard, and its quantum yield was arbitrarily set to 100. The quantum yield of the corresponding acidic form was then determined relative to this value. The resulting ratio represents the fluorescence enhancement of the basic form and is referred to as the fluorescence turn-on ratio (Figure 7.6).

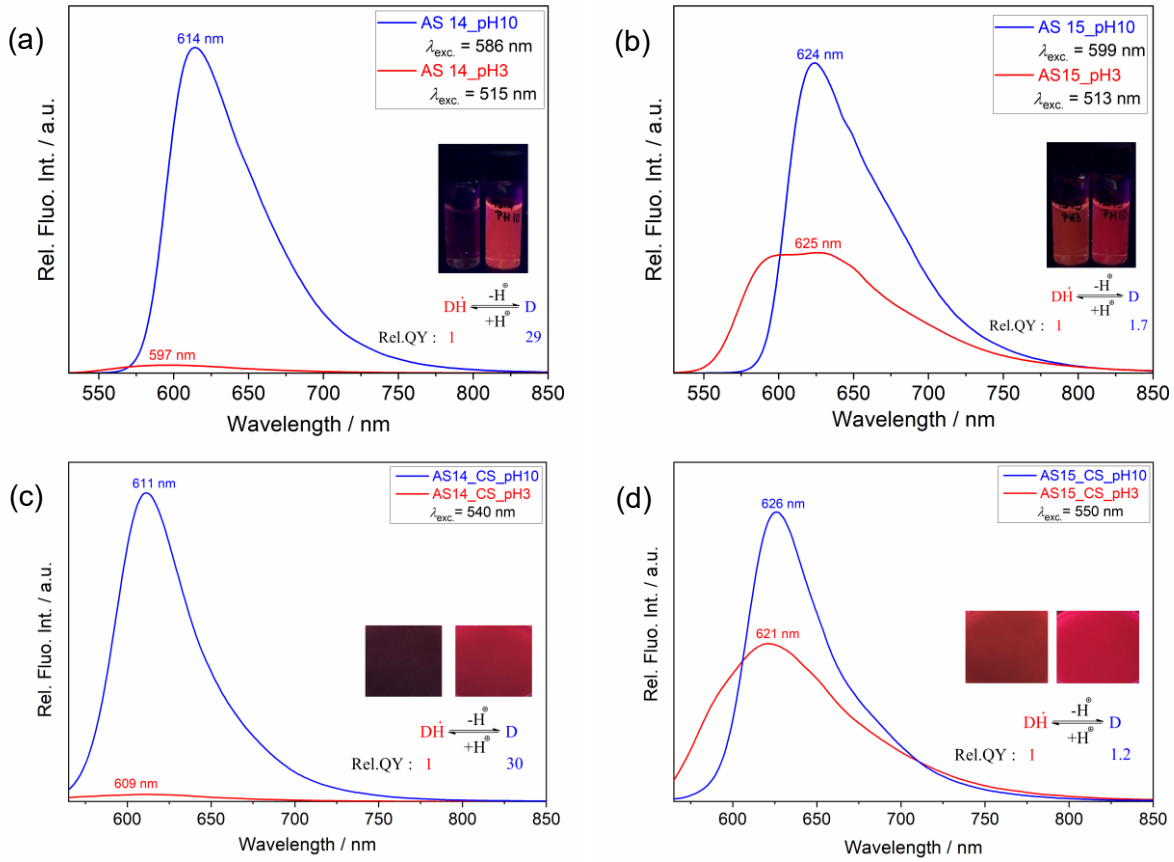

Figure 7.6. Fluorescence spectra of (a) **AS 14**, (b) **AS 15,** (c) **AS 14-CS,** and (d) **AS 15-CS** recorded in aqueous buffer at pH 10 (blue trace) and pH 3 (red trace). $\lambda_{exc.}$ = 540 nm for **AS 14-CS** and 550 nm for **AS 15-CS.** For free dyes in solution, $\lambda_{exc.}$ = absorption maxima. The inset shows photographic images of the corresponding dye solutions and films at pH 3 (left) and pH 10 (right).

Both the acidic and basic forms were excited at their respective isosbestic points, which is the wavelength at which both forms exhibit equal absorbance (i.e., 540 nm for **AS 14-CS** and 550 nm for **AS 15-CS**). The turn-on ratios observed for the CS-bound dyes were comparable to those of the free dyes in solution. **AS 14-CS** exhibited a fluorescence turn-on ratio of 30, closely matching that of the free dye (29), while **AS 15-CS** showed a lower turn-on ratio of 1.2, also comparable to its free dye counterpart (1.7). The modified films exhibited emission wavelength variations of 2–4 nm, except for the **AS 14-CS** acidic film, which showed a 12 nm bathochromic shift compared to the free dye in solution.

The fluorescence lifetime of the dye-coupled films was measured using fluorescence-lifetime imaging microscopy (FLIM), employing time-correlated single-photon counting (TCSPC). The fluorescence decay curves were fitted using a biexponential model (Eq. 2.11). The resulting lifetime components (τ), their relative intensity contributions (f), average lifetime ($\langle\tau\rangle$) and free dye lifetimes in buffer are given in Table 7.1.

Table 7.1. Fluorescence lifetime components (τ), relative intensity contributions (f), average lifetime ($\langle\tau\rangle$), and reference lifetimes of the corresponding free dyes in buffer. (a) and (b) correspond to acidic and basic forms, respectively. The quality of the bi-exponential fit was assessed using reduced χ^2 values and the distribution of weighted residuals (Figure S5).

CS-Film	τ_1, (ns)	f_1 (%)	τ_2, (ns)	f_2 (%)	$\langle\tau\rangle$	Free dye τ (ns) in buffer
AS 15-CS (b)	0.72	2	3.54	98	3.48	2.74
AS 15-CS (a)	1.14	23	2.68	77	2.32	1.58
AS 14-CS (b)	1.11	5	3.29	95	3.18	1.94
AS 14-CS (a)	0.10	46	0.88	54	0.52	0.21

The films were washed with pH 10 and pH 3 buffer solutions to obtain basic and acidic conditions, respectively. In their basic forms, the **AS 15-CS** and **AS 14-CS** films exhibited dominant lifetime components of 3.54 ns (98%) and 3.29 ns (95%), respectively, with the secondary components contributing negligibly to the overall decay. In contrast, in acidic conditions, the secondary lifetime component also contributes to the overall lifetime. In the weakly emissive **AS 14-CS** acidic form, two distinct lifetime components were evident, indicating the presence of multiple emissive states, which is consistent with its lower pK_a (4.9), where small variations in pH can significantly affect the protonation equilibrium and thus modulate the dye's excited-state behavior. For the acidic form of **AS 15-CS**, although a second component was present, the average lifetime remained close to the dominant component, suggesting that the contribution of the secondary species is less pronounced.

Both **AS 14** and **AS 15** exhibited increased fluorescence lifetimes upon incorporation into chitosan films, in both their acidic and basic forms, compared to their free counterparts in aqueous buffer. This enhancement in lifetime is consistent with previous observations in chitosan-based polyelectrolyte complexes doped with xanthene dyes such as eosin Y and

erythrosin B, where changes in the local microenvironment, particularly polarity, influenced the lifetime.[272] As discussed in Chapter 4, both **AS 14** and **AS 15** exhibit solvent-dependent lifetime behavior, with longer lifetimes observed in polar organic solvents compared to an aqueous buffer. When covalently bound to CS, the dye might experience changes in the polarity of its surroundings and show a longer lifetime. Nevertheless, consistent with the behavior observed for the free dyes in solution, the basic form continued to display a longer lifetime than the acidic form in the CS films.

Color and Photostability

The color stability of pH-sensitive films relies on the choice of dyes. Dyes like anthocyanin and alizarin tend to degrade quickly when exposed to heat and light.[18,23] To maintain their color, these films should be stored in refrigeration and protected from light. Moreover, dyes that are incorporated into polymers without covalent bonds may leach out over time.[273,274] Therefore, it is necessary to assess the color and photo stability of pH-sensitive films.

The acidic and basic forms of **AS 14** and **AS 15** exhibited significantly higher photostability compared to the commonly used pH-sensitive dye fluorescein and the NIR fluorescent label Cy5. To evaluate the photostability of the dyes when immobilized, the **AS 14-CS** and **AS 15-CS** films were irradiated under identical conditions using a 575 W mercury halide lamp. Prior to irradiation, the films were washed with pH 4 and pH 10 aqueous buffers to prepare the acidic and basic forms, respectively. The photostability of the dye-coupled films was then assessed by monitoring the decrease in absorbance at λ_{max} over time under continuous illumination (Figure 7.7), following the same procedure used for the free dyes in solution (see Chapter 4). The absorption spectra recorded during the 24-hour photostability experiment for both films are provided in Figure 7.8.

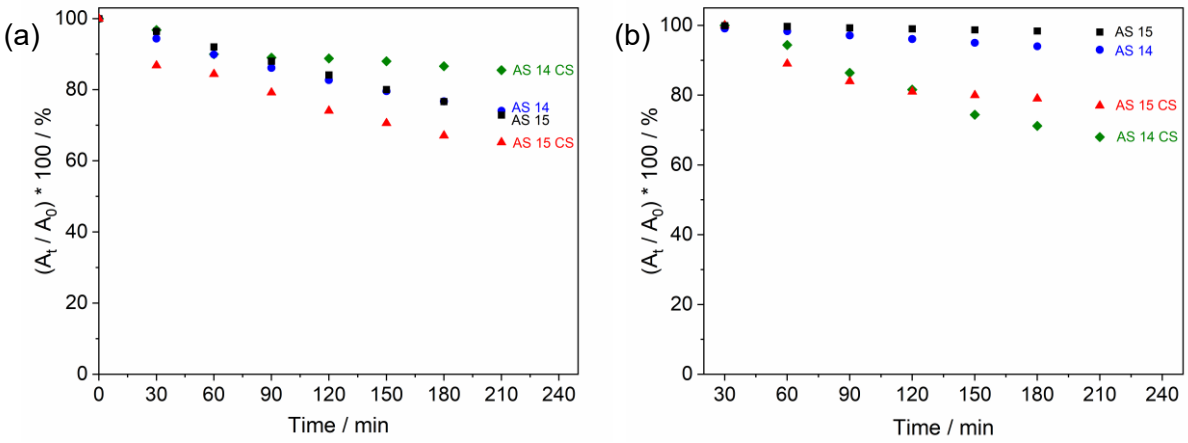

Figure 7.7. Photostability profiles of the (a) basic form and (b) acidic form of the free dyes and chitosan-coupled dyes in pH 4 and pH 10 buffers, respectively, over 3.5 hours of continuous irradiation using a 575 W mercury halide lamp. For the acidic form, the absorbance value recorded after 30 minutes of irradiation was used as the initial reference point.

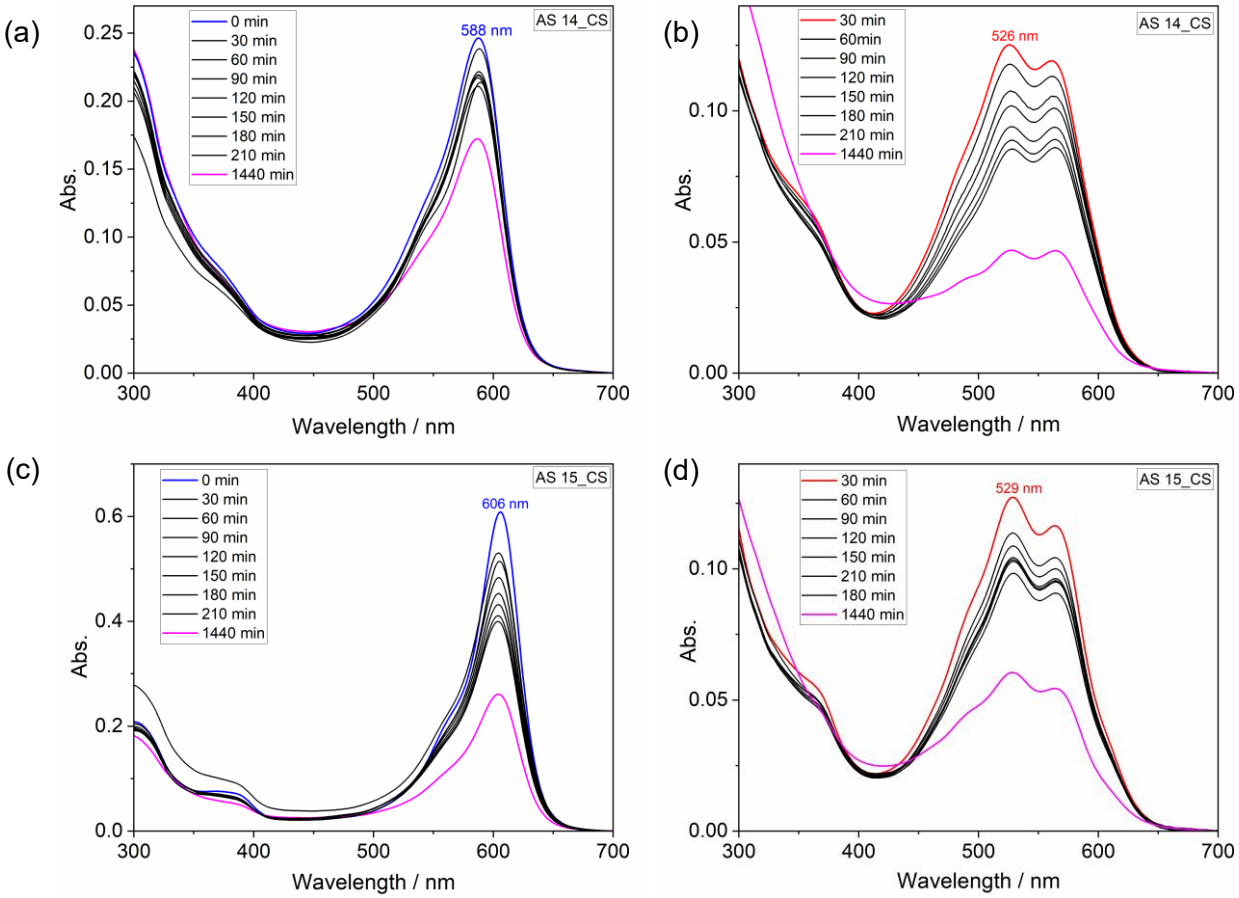

Figure 7.8. Change in absorption spectra over time for **AS 14-CS** (a) basic form, (b) acidic form, and **AS 15-CS** (c) basic form, (d) acidic form.

AS 14 and **AS 15** demonstrated excellent photostability in their acidic forms, with only 7% and 2% degradation, respectively, after 210 minutes of continuous irradiation. When immobilized in chitosan films, **AS 14-CS** and **AS 15-CS** exhibited slightly higher degradation rates under the same conditions, at 32% and 23%, respectively (Figure 7.7b). Under basic conditions, the free dyes showed greater photodegradation, with both **AS 14** and **AS 15** displaying approximately 26% loss in absorbance. In contrast, **AS 14-CS** was the most photostable among all tested systems under basic conditions, exhibiting only 15% degradation, while **AS 15-CS** showed a slightly higher degradation of 35% (Figure 7.7a). All these values still indicate good photostability of the film, considering the harsh experimental conditions compared to the typical wound environment.

Notably, even after 24 hours of continuous light exposure, the films retained their pH responsiveness. When irradiated basic films were immersed in a pH 4 buffer, they exhibited a visible color change to pink, consistent with the protonated (acidic) form of the dye. Conversely, rinsing with pH 10 buffer restored the characteristic color of the deprotonated (basic) form in the acidic films. Subsequent spectral measurements confirmed that these washed films

displayed absorption profiles corresponding to their respective acidic and basic forms (Figure 7.9).

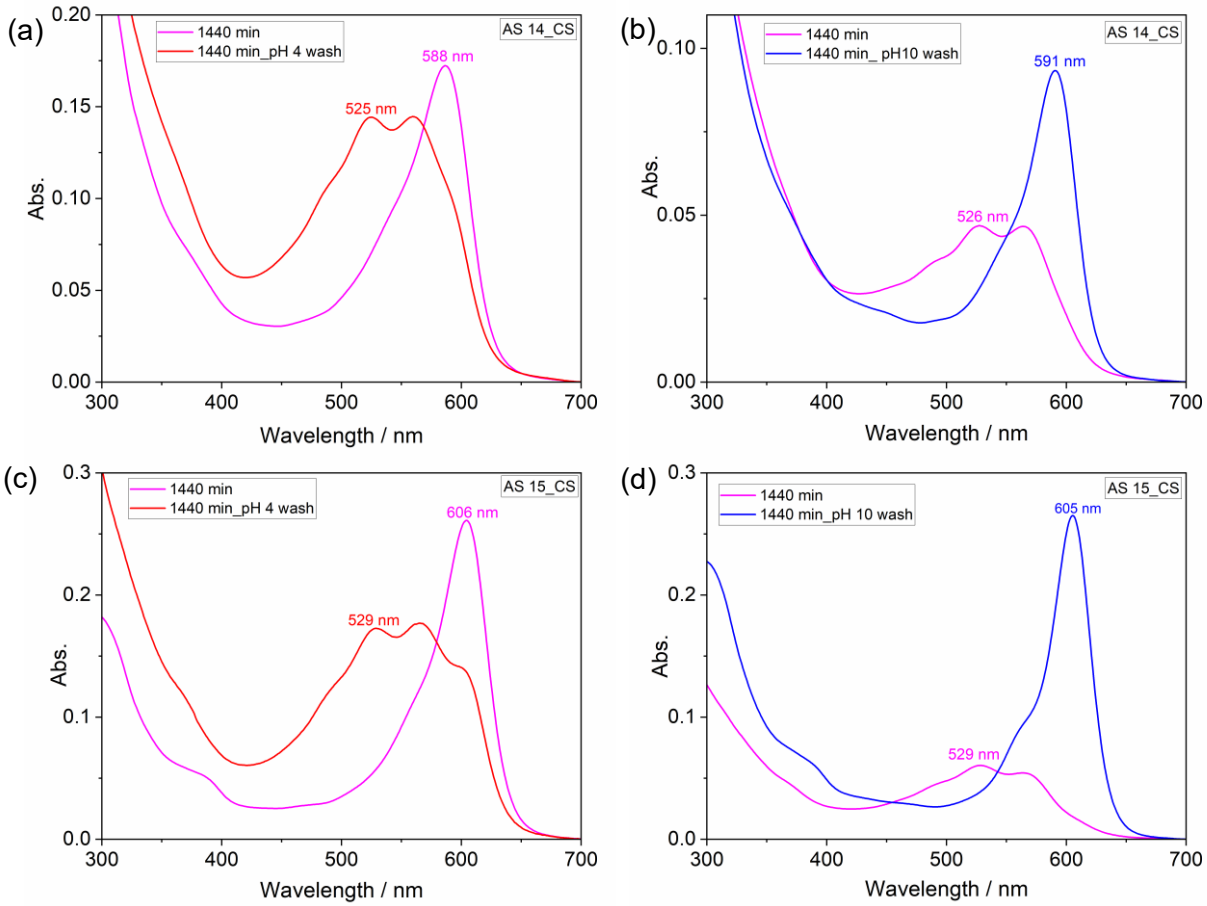

Figure 7.9. Absorption spectra of (a) **AS 14-CS** and (c) **AS 15-CS** basic films after 24 h irradiation and subsequent washing with pH 4 buffer. Absorption spectra of (b) **AS 14-CS** and (d) **AS 15-CS** acidic films after 24 h irradiation and subsequent washing with pH 10 buffer.

As a control, a blank chitosan film without dye was measured under the same irradiation and buffer conditions, and no spectral changes were observed (Figure S6a and b), confirming the stability of the chitosan matrix.

To test the leaching of dyes from the films, the films were immersed in different media (water and EtOH/water 1:1) at room temperature. The films maintained their color in each medium even after three months. In addition, UV-VIS spectra of the solutions used for immersing films were measured after 24 h, and no absorbance corresponding to the leaching dyes were detected, confirming that covalently attaching dyes onto CS completely prevented dye release or degradation of the film color (Figure S7).

Carborhodol dyes covalently bound to CS exhibit strong leaching resistance and retain both optical and chemical stability under prolonged photochemical stress, while maintaining their reversible pH-sensing capability. These results highlight the suitability of these dye-functionalized CS films for potential application in long-term pH monitoring.

7.2.3 Coupling of Rhodamine-Based ATTO Dyes to Chitosan Hydrogels

In addition to the pH-responsive carborhodol dyes, pH-independent rhodamine-based ATTO dyes were covalently immobilized within chitosan hydrogels via NHS-ester chemistry. Specifically, the hydrophobic dye **ATTO Rho13** and the hydrophilic dye **ATTO 594** were incorporated at varying concentrations to investigate how dye concentration affects the film properties. Immobilization was primarily achieved through drop-casting, although additional films containing **ATTO Rho13** were also prepared by spin-coating on glass. The corresponding spectral data for these films is provided in the Appendix (Figure S8).

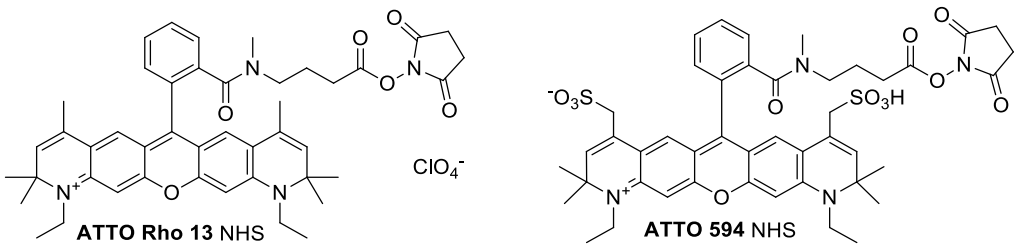

Similar to previously studied **AS 14-CS** and **AS 15-CS** systems, all ATTO-CS conjugates exhibited a consistent bathochromic shift (~6 nm) in their absorption maxima compared to the free dye in solution, indicating an environmental influence from the chitosan matrix after immobilization (Figure 7.10a, b). Additional films containing **ATTO 550** were also prepared, and they demonstrated a 6 nm red shift (Figure S9). For both **ATTO Rho13** and **ATTO 594** dye-CS systems, an increase in absorbance at λ_{max} was observed with increasing dye concentration (Figures 7.10c and d). This trend is also evident in the corresponding film images, where deeper coloration is seen at higher concentrations (Figure 7.10e, f).

At a concentration of 10 mM for **ATTO 594-CS**, the absorbance exceeded 3, surpassing the spectrophotometer's detection range. The normalized absorption spectra of **ATTO 594-CS** films at 1 mM and 5 mM were superimposable (Figure 7.10a). In contrast, the normalized spectra of 1 mM, 2.5 mM, and 5 mM **ATTO Rho13-CS** films exhibited a growing shoulder at ~570 nm on the short-wave flank of the main absorption band, indicating the formation of dimers and dye aggregation, which is common for rhodamine-based hydrophobic dyes at higher concentrations (Figure 7.10b).[275]

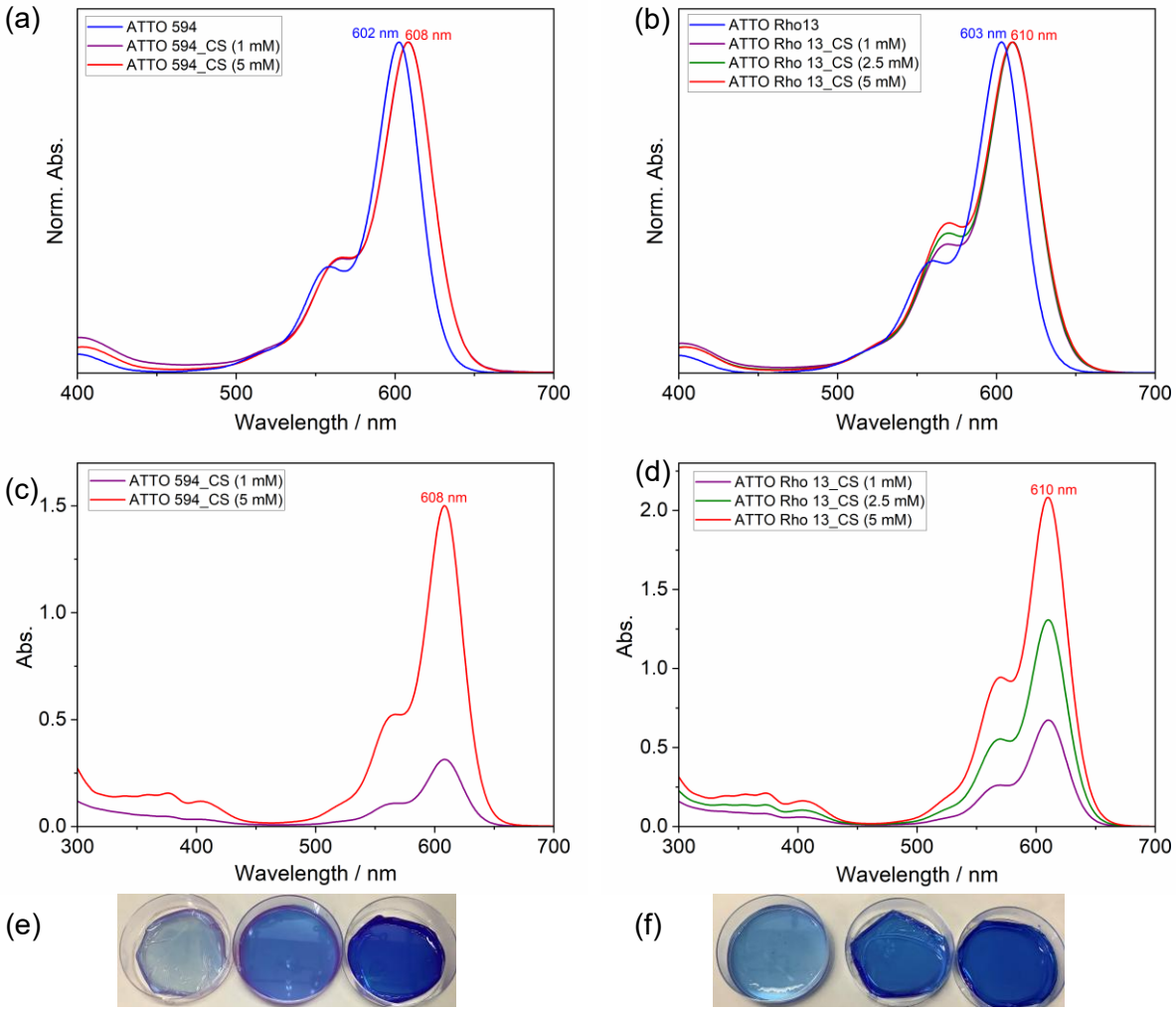

Figure 7.10. Normalized absorption spectra of (a) **ATTO 594** in PBS and **ATTO 594-CS** films and (b) **ATTO Rho13** in PBS and **ATTO Rho13-CS** films at various dye concentrations.
Absorption spectra of (c) **ATTO 594-CS** and (d) **ATTO Rho13-CS** films at different concentrations. Photographic images of (e) **ATTO 594-CS** and (f) **ATTO Rho13-CS** films under ambient light, with concentrations increasing from left to right: 1 mM, 5 mM, and 10 mM for **ATTO 594-CS**; and 1 mM, 2.5 mM, and 5 mM for **ATTO Rho13-CS**.

The dye-coupled films exhibited a bathochromic shift of 5 and 12 nm in emission for **ATTO 594-CS** and **ATTO Rho 13-CS**, respectively, at a dye loading of 1 mM, compared to the free dye in solution (Figure 7.11a, b). For **ATTO 594-CS**, fluorescence intensity increased from 1 mM to 5 mM, consistent with the absence of aggregation; however, a decrease in intensity at 10 mM suggests concentration-dependent dye aggregation and associated quenching.[276] The dye in the film showed an increase in red shift as the concentration of the dye increased (Figure 7.11c). In contrast, **ATTO Rho13-CS** films exhibited a continuous red shift in emission alongside a steady decrease in fluorescence intensity with increasing dye concentration (Figure 7.11d). These trends may indicate dye molecule aggregation, resulting in significant fluorescence quenching. Photographic images of the films under UV illumination further support this conclusion, showing pronounced quenching at higher concentrations (Figures

7.11e, f). Notably, this behavior was consistent in both drop-cast and spin-coated films, as demonstrated by similar spectral shifts and intensity reductions (Figure S8b).

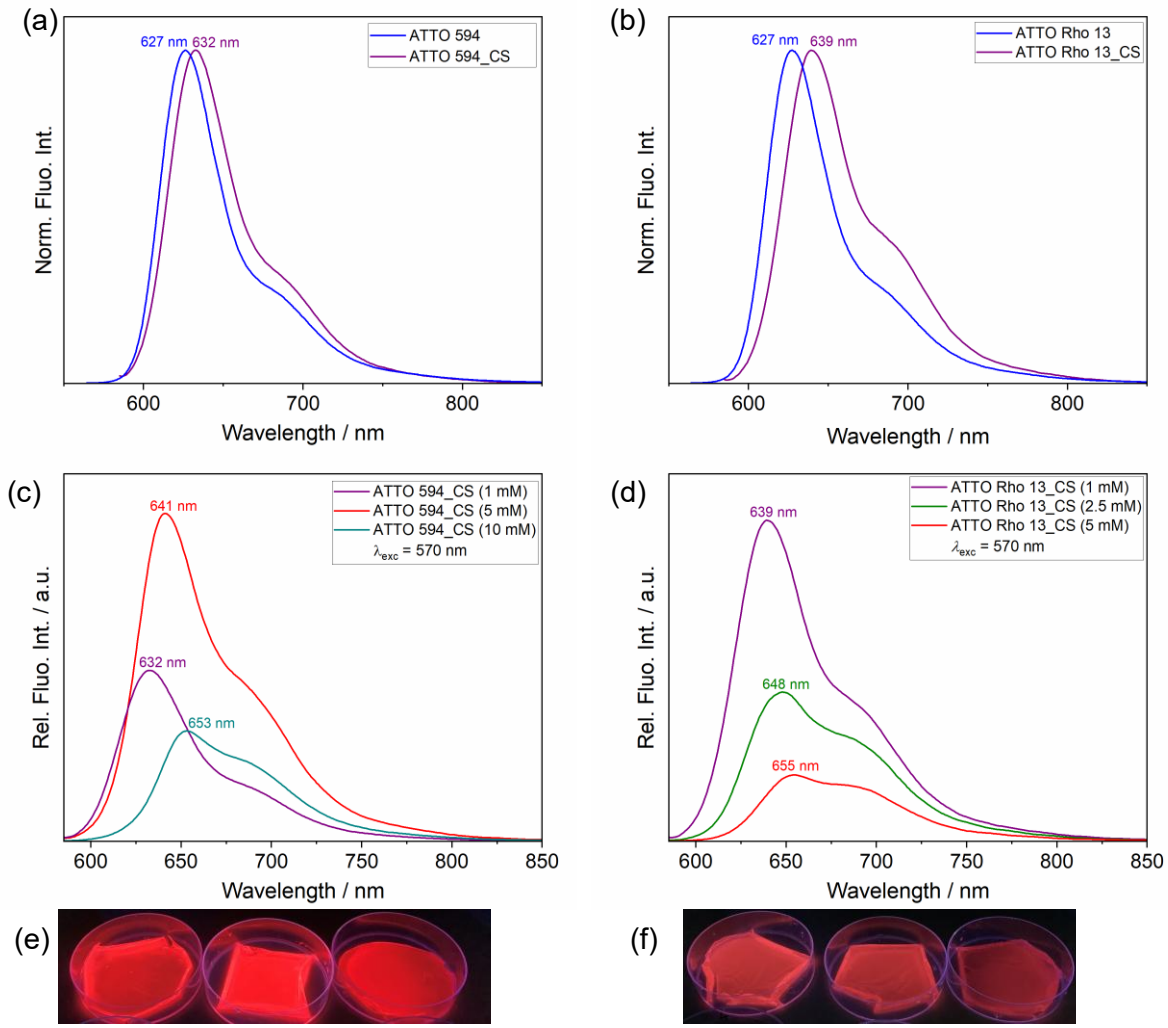

Figure 7.11. Normalized fluorescence spectra of (a) **ATTO 594** in PBS and **ATTO 594-CS** films, and (b) **ATTO Rho13** in PBS and **ATTO Rho13-CS** films at various dye concentrations. Fluorescence spectra of (c) **ATTO 594-CS** and (d) **ATTO Rho13-CS** films at different concentrations. Photographic images of (e) **ATTO 594-CS** and (f) **ATTO Rho13-CS** films under UV light (366 nm), with concentrations increasing from left to right: 1 mM, 5 mM, and 10 mM for **ATTO 594-CS**; and 1 mM, 2.5 mM, and 5 mM for **ATTO Rho13-CS**.

Absorption and fluorescence measurements at varying dye loadings confirm that aggregation becomes more pronounced at higher concentrations, especially for more hydrophobic dyes compared to hydrophilic fluorophores. Films exhibiting absorbance values below 1 did not show any signs of aggregation in either case, indicating that this absorbance threshold represents the optimum condition for film quality. Importantly, the **AS 14-CS** and **AS 15-CS** films used for analysis all exhibited absorbance values below 1.

7.3 Conclusion and Outlook

pH-responsive wound dressings were developed by covalently coupling NHS esters of photostable novel carborhodol dyes, **AS 14** and **AS 15,** to CS films. The coupling was

successfully achieved for CS films prepared via drop-casting on polystyrene and spin-coating on glass, as confirmed by FTIR spectroscopy, UV-VIS absorption, and fluorescence measurements. Film thickness was characterized by FESEM. Both **AS 14-CS** and **AS 15-CS** exhibited distinct and reversible color changes within the clinically relevant pH range of 4–7, with pK_a values of 4.9 and 5.3, respectively. In the basic form, fluorescence intensity was enhanced compared to the acidic form, with turn-on ratios of 30 for **AS 14-CS** and 1.2 for **AS 15-CS**. Consequently, **AS 15-CS** functioned as a chromogenic sensor, whereas **AS 14-CS** exhibited both chromogenic and fluorogenic responses, enabling pH monitoring by the naked eye or under UV illumination.

Based on the observed pH-dependent optical responses, it can be anticipated that in wound environments, alkaline conditions (as in chronic wounds) produce violet coloration for **AS 14-CS** and blue coloration for **AS 15-CS**, whereas acidic conditions (associated with healing wounds) would yield a pink appearance for both films. Furthermore, **AS 14-CS** would be expected to exhibit fluorescence turn-on in chronic wounds and turn-off in healing conditions. Both films would provide clinicians with an easily visible (bare eye or under UV light) indication of the requirement for further intervention, facilitating more appropriate treatment of wounds.

Both films showed pH-dependent fluorescence lifetimes, with longer lifetimes in basic than in acidic states. The materials demonstrated high photostability, color stability, resistance to dye leaching in aqueous and mixed solvent systems, a swelling ratio of approximately 200%. Furthermore, they maintained reversible optical responses after prolonged irradiation. Collectively, these results highlight a novel, simple, and efficient strategy for producing stable, pH-responsive wound dressings capable of real-time visual and fluorescence-based monitoring of wound status. Given that the pH response range of the films (pH 4–7) overlaps with the pH variations associated with food spoilage, these materials may also have potential applications in food freshness monitoring, in addition to their suitability for biomedical use.

7.4 Experimental Section

The swelling ratio and FESEM measurements were performed by M.Sc. Nicola Cusick (University of Siegen), AFM measurements by M.Sc. Joshua Schumacher (University of Siegen), and FLIM measurements were carried out with the assistance of Dr. Jan Erik Hoffmann (ATTO-TEC GmbH).

7.4.1 Equipment

ATR-FTIR spectra of the prepared CS films were recorded using a Tensor 27 Fourier transform infrared spectrometer (Bruker Optik GmbH, Germany) over a wavenumber range of 600-4000 cm^{-1}, with a spectral resolution of 4 cm^{-1}. Air was used to collect the background spectra.

FESEM images were obtained using a field-emission scanning electron microscope (Zeiss Ultra 55cv, Zeiss, Oberkochen, Germany).

Intermittent contact (tapping) mode AFM measurements were performed on an Asylum MFP-3D microscope equipped with a Tap 300 Al-G cantilever from Budget Sensors.

UV-VIS absorption spectra were recorded using a PerkinElmer Lambda 750 spectrophotometer, with baseline correction. Drop-cast films were attached either on microscope slides (Figure S10a) or in a 35 mm slide mount (Figure S10c), dried using air flow, and the spectra were measured. For the spin-coated films, spectra were obtained with a Varian Cary 50 Bio spectrophotometer (Varian, Mulgrave, Victoria, Australia) with baseline correction. The measurements were performed in a quartz cell with 1 mm path length (SUPRASIL, Hellma Analytics, Germany).

Emission spectra were measured using a Fluorolog 3 spectrofluorometer from HORIBA Jobin Yvon. The measurements were carried out in front face arrangement.

Fluorescence lifetime imaging microscopy (FLIM) was carried out using a Stellaris 8 confocal microscope (Leica Microsystems).

For photostability studies, a Liesegang Trainer Special HR Electronic Overhead Projector was employed as the light source, fitted with a 575 W mercury halide lamp.

7.4.2 Materials and Methods

Chitosan (medium molar weight, 190-310 kDa, 75–85% deacetylated) was purchased from Sigma-Aldrich, Germany. pH 3 buffer (Carl Roth, Art. No.: T18.1.1) and pH 4 buffer (Carl Roth, Art. No.: P7128.1), both composed of citric acid, NaOH, and NaCl, and pH 10 buffer (Carl Roth, Germany), containing boric acid, NaOH, and KCl, were used. PBS buffer (pH 7.4) was prepared from Milli-Q water (resistivity 18.2 MΩ cm) and biochemistry-grade chemicals (NaCl, KCl, KH_2PO_4, and $Na_2HPO_4 \cdot 2\ H_2O$, Sigma-Aldrich, Germany). Britton Robinson (BR) buffer was prepared by dissolving H_3PO_4, H_3BO_3, and NaOAc (0.04 M each) in Milli-Q water. Disposable polystyrene petri dishes (55 ×14 mm) were purchased from VWR, Germany. Acetic acid (glacial, Carl ROTH, Germany), chloroform and ethanol (VWR Chemicals, Darmstadt, Germany), glass microscope slides (VWR, 76×26 mm, thickness 1 mm, Lot: 631-1550), 10 mm cover glass (VWR, Germany), and tape (Tesa SE, Hamburg, Germany) were used.

Preparation of Chitosan Films by Drop Casting

A volume of 4 mL of chitosan solution (1.5% w/v in 1% acetic acid, filtered through a 0.45 µm syringe filter) was poured into a polystyrene Petri dish and dried overnight in a laminar flow hood to obtain a thin hydrogel film. The film was then neutralized by shaking for 5 min with 0.1 M NaOH, followed by rinsing with Milli-Q water three times.

Preparation of Chitosan Films by Spin Coating

Glass cover slips (0.9 cm × 1.2 cm) were cut and rinsed in chloroform, then sequentially cleaned three times with ethanol and Milli-Q water. The cleaned cover slips were then dried under a stream of nitrogen and treated with UV-ozone for 30 minutes. Subsequently, 300 µL of chitosan solution was spin-coated onto each cover slip using a home-built spin coater operated at 2000 rpm for 60 s. The resulting films were annealed in a vacuum oven at 40 °C and 5 mbar for 2 hours. After annealing, the films were neutralized by shaking in 0.1 M NaOH for 5 minutes, rinsed three times with Milli-Q water, and dried under a nitrogen stream.

Modification of Chitosan Hydrogel

To each chitosan film (prepared by drop casting) placed in a Petri dish, PBS (pH 7.4) was added, followed by either **AS 14 NHS** (3 mM) or **AS 15 NHS** (4 mM) dissolved in DMSO (PBS: DMSO, 9:1, final volume of 4 mL). The Petri dishes were incubated for 12 h under moderate shaking at room temperature (Thermo Scientific). The modified chitosan films were then washed with PBS (pH 7.4), and the washing solution was replaced every 30 min for a total duration of 3 h, until no absorbance of the AS dyes was detected in the washing solutions. The films were dried under nitrogen flow and subsequently used for spectroscopic analysis.

For spin-coated chitosan films, the same procedure was followed, where each film was placed into a well of a 24-well plate. However, higher dye concentrations (**AS 14 NHS** at 14 mM and **AS 15 NHS** at 20 mM) were used to obtain visibly colored films. The final volume of PBS and DMSO mixture was 300 µL (PBS/DMSO, 9:1).

Film Thickness Determination by FESEM

Drop-casted films were dried overnight in a vacuum oven, sliced with a scalpel, and then attached to a 6-sided metal nut with carbon tape, positioned sideways. To create a conductive surface, samples were sputtered with gold for 30 s, resulting in a $\sim 5.0 \pm 0.5$ nm thin gold layer. FESEM measurements were obtained using the Inlens secondary electron detector, with an operation voltage of 5 kV. The images were analyzed using the ImageJ software (version 1.54p).

Film Thickness Determination via AFM

The measurement was done in intermittent contact mode at the resonance frequency of 295 kHz and measured at 80% of the free amplitude. The film was scratched with a sharp metal scalpel, and the scratched area was measured. From the AFM images, histograms were plotted showing the pixel height distribution to determine the film thickness. The experiments were done under ambient conditions.

Swelling Ratio

The swelling analysis was conducted for hydrogels in PBS (pH 7.4, 25 °C). Hydrogel films were cut into 2×2 cm squares, then dried in a vacuum oven (22 °C, 9 mbar) overnight, and weighed (W_i). The films were then immersed in 20.0 mL PBS (pH 7.4, 25 °C) in glass vials, sealed with lids to prevent evaporation, and placed in an incubator at 25 °C. At 60-minute intervals, the samples were carefully removed from the PBS solution, gently dabbed with filter paper to remove excess surface water, and weighed (W_t). This process was repeated for 3 hours, after which the samples were left in the solution for a total of 19 hours before the final measurement was taken. The swelling ratio was calculated using Equation 7.1.

$$\text{Swelling Ratio } (\%) = \left[\frac{W_t - W_i)}{W_i}\right] \times 100 \qquad \text{(Eq. 7.1)}$$

pK_a Determination of the Modified Films

For the absorbance measurements, the hydrated modified film was placed on a microscope slide with one side of the film taped to the slide, dried using nitrogen flow, and then placed in the sample holder (Figure S10b). The baseline was measured using a blank microscope slide.

To assess measurement reproducibility, a series of control experiments was carried out using an **ATTO 550-CS** film. These involved moving the film along the optical axis, shifting it laterally, and removing and repositioning it in the same location. Small variations in absorbance were observed upon axial movement, whereas repositioning the film precisely at a marked location resulted in consistent absorbance values. Similar reproducibility was achieved after immersing the film in buffer and then drying. Based on these findings, all subsequent measurements were performed by marking the slide position and ensuring identical repositioning after each treatment.

For titration, a BR buffer was initially adjusted to pH 9 using 6.2 M NaOH. The film was immersed in the pH 9 buffer for 5 minutes, dried under nitrogen flow, and its absorption spectrum was recorded. The pH of the buffer was then gradually decreased in steps of approximately 0.2 pH units by adding small aliquots of HCl (2 M), and films were immersed in each pH, and the procedure was repeated. The pK_a values were obtained from plots of absorption at fixed wavelength (corresponding to the λ_{max} of the deprotonated species) against the measured pH values and numerical fitting of the experimental data to the Henderson-Hasselbalch equation.[227]

When the pH reached 3, the films tended to detach from the slide, making further measurements difficult, likely due to partial solubilization of the chitosan matrix under acidic conditions. In contrast, at pH values above 3, the films remained stable and adhered well to the glass surface. However, a single brief washing in pH 3 buffer followed by immediate measurements was still feasible.

Fluorescence Turn-on Ratio Determination

The films were cut into rectangles of 3.0 × 0.9 cm (length × width), and then attached to a quartz cell with a 1 mm path length. After drying using air flow, the spectra were measured (Figure S10f, which shows the setup for the spin-coated films). The same cut film was immersed again in a pH 3 buffer, and the process was repeated. To determine the fluorescence turn-on effect, the quantum yield of the basic form of each dye was determined and arbitrarily set to 100. The quantum yield of the corresponding acidic form was then determined relative to this value. The resulting ratio represents the fluorescence enhancement of the basic form and is referred to as the fluorescence turn-on ratio.

Fluorescence Lifetime Determination via FLIM

Drop-casted films were immersed in the corresponding buffer (pH 10 or pH 3 buffer) and cut into small squares (~0.2 × 0.2 cm). They were then attached to microscope slides and flattened using a 10 mm cover glass slip. FLIM images were acquired with an 86×/1.20 water immersion objective at a resolution of 512 × 512 pixels, with excitation wavelengths selected to match the absorption maxima of the respective dye forms (For the basic form, 590 nm for **AS 14-CS** and 606 nm for **AS 15-CS**, for acidic form, 520 nm for both films). The relative intensity contributions (*f*) of each lifetime component were calculated by dividing the photon count (in kilocounts) of each exponential term by the total counts and multiplying by 100.

Photostability Determination

The drop-casted **AS 14-CS** and **AS 15-CS** films were washed with the corresponding buffer (pH 4 or pH 10), dried using an airflow, attached to a 35 mm slide mount, and placed horizontally on an overhead projector (Figure S10e). Excess film at the edges was trimmed before positioning the samples horizontally on an overhead projector. Absorption spectra were recorded every 30 minutes by placing the films directly on the UV-VIS spectrometer sample holder.

8 Conclusion and Outlook

This thesis has explored the design, synthesis, and characterization of nine novel pH-sensitive carborhodol dyes, along with the previously reported carborhodol **AS 11**, providing a comprehensive investigation from molecular properties to functional material systems. Hydrolytic deamination of the corresponding carbopyronine precursors containing a terminal *N,N*-dimethylamino substituent yielded the novel carborhodols. Structures were verified by NMR spectroscopy and mass spectrometry. The synthetic method tolerates functional structural elements that are critical for application work: halogen substituents (for pK_a and photostability tuning), carboxylic acid groups (for NHS-ester formation and covalent coupling), fused quinoline/tetrahydroquinoline units (to increase molecular rigidity), and the sulphonic acid groups (to enhance aqueous compatibility). The ability to obtain both carborhodol and carbopyronine products from the same precursors further highlights the practicality and cost-effectiveness of this approach.

The photophysical properties are greatly dependent on the pH across the dye series, with pK_a values ranging from 5 to 7, which fall within physiologically relevant ranges. In their deprotonated form, the dyes adopt a more planar conformation with extended donor-acceptor conjugation, resulting in stronger absorption, higher fluorescence quantum yields, and longer excited-state lifetimes compared to their protonated counterparts. Comparative studies with conventional dyes such as fluorescein and Cy5 demonstrated the superior photostability of the novel carborhodols. This combination of pH responsiveness and stability supports their use as both fluorogenic and chromogenic sensors, making them attractive candidates for long-term monitoring applications such as smart wound dressings.

Solvatochromic studies showed that the basic forms of carborhodol dyes exhibit positive solvatochromism in both absorption and emission, with pronounced bathochromic shifts in absorption and moderate red shifts in emission. These results are consistent with an intramolecular charge transfer and stabilization of the excited state in polar solvents, broadening their potential use as polarity-sensitive probes. In contrast, the acidic forms exhibited only slight negative solvatochromism in absorption and negligible solvent-dependent emission. Fluorescence lifetimes were longer in polar aprotic solvents than in protic media, indicating the role of hydrogen-bond-assisted nonradiative decay.

To demonstrate their applicability, the dyes were incorporated into polymer-based systems. **AS 01**, **AS 02**, **AS 03**, **AS 07**, and **AS 13** were successfully encapsulated in PEG-*b*-PLA vesicles, which enabled an assessment of how dye hydrophilicity and neutral character influenced retention. The hydrophobic dye **AS 01** precipitated after vesicle lysis, while hydrophilic dyes tended to leak during prolonged dialysis, limiting their visible colorimetric pH

sensitivity. Nevertheless, the vesicle suspensions exhibited enhanced fluorescence with rising pH, even without lysis. From these results, it became clear that covalent immobilization provides greater reliability than non-covalent encapsulation. Chitosan films proved ideal for this purpose due to their antimicrobial, non-toxic, bioadhesive, and haemostatic properties, as well as their established use in wound dressings. Covalent attachment of NHS-activated **AS 14** and **AS 15** to chitosan produced pH sensors that operated effectively within the physiologically and environmentally relevant range of pH 4–7. Among these, **AS 14-CS** combined chromogenic sensing with a pronounced fluorogenic enhancement (30-fold turn-on), whereas **AS 15-CS** functioned primarily as a colorimetric probe. The films exhibited excellent photostability, resistance to dye leaching, and significant swelling capacity, properties that are highly desirable for real-world applications such as wound monitoring.

Overall, this work demonstrates that molecular design, combined with material integration, can yield functional solid-state pH sensors. The chitosan-based films developed here show strong promise for biomedical and environmental applications, particularly as components of smart wound dressings for the early detection and monitoring of infection. Their brightness, high fluorescence turn-on response, physiological-range pK_a, stability against photobleaching, photodegradation, and leaching establish them as strong candidates for real-time sensing platforms in clinical contexts.

Based on these findings, several directions merit further exploration. Vesicle-based platforms beyond PEG-*b*-PLA could be investigated to determine whether hydrophilic carborhodols can be more effectively retained, enabling a clear colorimetric pH response in encapsulated systems. Another promising direction is the systematic tuning of pK_a values. The observation that chitosan-bound dyes exhibit values about one unit lower than their free counterparts suggests that introducing appropriate substituents to increase the intrinsic pK_a of free dyes could yield immobilized analogues with higher pK_a. Moreover, the pronounced solvatochromism observed for the basic forms highlights the potential for the use in environmental sensing, where changes in polarity or solvent composition can be monitored. Finally, the structure-property relationships identified in this work could be further rationalized by computational methods such as density functional theory (DFT) and time-dependent DFT, which would provide deeper insights into the electronic structures, transition dipoles, and conformational preferences responsible for the observed pH-dependent optical responses. Collectively, these directions will not only strengthen the fundamental understanding of carborhodol dyes but also expand their potential utility across biomedical, environmental, and materials science applications.

References

1 A. M. Sandu, M. C. Chifiriuc, C. O. Vrancianu, R.-E. Cristian, C. F. Alistar, M. Constantin, M. Paun, A. Alistar, L. G. Popa and M. I. Popa, *Infect. Dis. Ther.*, 2025, 1–39.

2 B. Allegranzi, S. B. Nejad and D. Pittet, *Hand hygiene: a handbook for medical professionals*, 2017, 1–7.

3 P. Blatnik and Š. Bojnec, *Cent. Eur. J. Public Health*, 2023, **31**, 90–96.

4 L. M. Asegu, A. Kitschen, M. M. Neuwirth and D. Sauerland, *BMC Infect. Dis.*, 2024, **24**, 1294.

5 F. D. Halstead, G. Pinjuh, G. Antonacci and N. Proudlove*, BMJ Open Qual., 2025,* **14***,* e003153.

6 T. Velnar, T. Bailey and V. Smrkolj, *J. Int. Med. Res*, 2009, **37**, 1528–1542.

7 S. Li, P. Renick, J. Senkowsky, A. Nair and L. Tang, *Adv. Wound Care*, 2021, **10**, 317–327.

8 S. Bhattacharya, *Virulence*, 2013, **4**, 172–184.

9 H. Lambers, S. Piessens, A. Bloem, H. Pronk and P. Finkel, *Int. J. Cosmet. Sci.*, 2006, **28**, 359–370.

10 S. Schreml, R. Szeimies, S. Karrer, J. Heinlin, M. Landthaler and P. Babilas, *J. Eur. Acad. Dermatol. Venereol*, 2010, **24**, 373–378.

11 C. Watters, T. T. Yuan and K. P. Rumbaugh, *Chronic Wound Care Manag. Res.*, 2015, 53–62.

12 S. Jin, M. A. A. Newton, H. Cheng, Q. Zhang, W. Gao, Y. Zheng, Z. Lu, Z. Dai and J. Zhu, *Gels*, 2023, **9**, 694.

13 V. Sridhar and K. Takahata, *Sens. Actuators A: Phys.*, 2009, **155**, 58–65.

14 S. Trupp, M. Alberti, T. Carofiglio, E. Lubian, H. Lehmann, R. Heuermann, E. Yacoub-George, K. Bock and G. J. Mohr, *Sens. Actuators B: Chem.*, 2010, **150**, 206–210.

15 J. Phair, L. Newton, C. McCormac, M. F. Cardosi, R. Leslie and J. Davis, *Analyst*, 2011, **136**, 4692–4695.

16 M. Omidi, A. Yadegari and L. Tayebi, *RSC Adv.*, 2017, **7**, 10638–10649.

17 L. A. Schneider, A. Korber, S. Grabbe and J. Dissemond, *Arch. Dermatol. Res.*, 2007, **298**, 413–420.

18 M. Moradi, H. Tajik, H. Almasi, M. Forough and P. Ezati, *Carbohydr. Polym.*, 2019, **222**, 115030.

19 J. Petkovska, N. Geskovski, D. Marković, V. Dimova, D. Mirakovski, M. Radetić and I. Jordanov, *Carbohydr. Polym. Technol. Appl.,* 2024, **7**, 100438.

20 A. A. Arafa, A. A. Nada, A. Y. Ibrahim, P. Sajkiewicz, M. K. Zahran and O. A. Hakeim, *Int. J. Biol. Macromol.*, 2021, **182**, 1820–1831.

21 X. Zhang, S. Lu and X. Chen, *Sens. Actuators B: Chem.*, 2014, **198**, 268–273.

22 K. Kiti, C. Thanomsilp and O. Suwantong, *Microchem. J.*, 2022, **177**, 107277.

23 P. Ezati, H. Tajik and M. Moradi, *Sens. Actuators B: Chem.*, 2019, **285**, 519–528.

24 H. Wen, Y.-I. Hsu, T.-A. Asoh and H. Uyama, *Polym. Degrad. Stab.*, 2020, **178**, 109215.

25 P. Ezati and J.-W. Rhim, *Carbohydr. Polym.*, 2020, **230**, 115638.

26 N. Pan, J. Qin, P. Feng, Z. Li and B. Song, *J. Mater. Chem. B.*, 2019, **7**, 2626–2633.

27 J. Chalitangkoon and P. Monvisade, *Carbohydr. Polym.*, 2021, **260**, 117836.

28 L. G. Devi, K. S. A. Raju and S. G. Kumar, *J. Environ. Monit.*, 2009, **11**, 1397–1404.

29 L. Ludvíková, P. Friš, D. Heger, P. Šebej, J. Wirz and P. Klán, *Phys. Chem. Chem. Phys.*, 2016, **18**, 16266–16273.

30 N. Almulhem, C. Awada and N. M. Shaalan, *Crystals*, 2022, **12**, 911.

31 A. M. Amat, A. Arques, M. A. Miranda, S. Seguí and R. F. Vercher, *Desalination*, 2007, **212**, 114–122.

32 A. A. M. Saeed, M. S. S. Al-Salimi, M. T. A. Qashqoosh, G. A. A. Al-Dahbali, W. S. A. Yusef, T. H. A. Mohammed, S. M. A. Abdallah, O. M. O. BA-Fadhl, A. Y. A. Saleh and S. H. H. Abdullah, *Electron. J. Univ. Aden Basic Appl. Sci.*, 2024, **5**, 320–330.

33 G. Panzarasa, A. Osypova, C. Toncelli, M. T. Buhmann, M. Rottmar, Q. Ren, K. Maniura-Weber, R. M. Rossi and L. F. Boesel, *Sens. Actuators B: Chem.,* 2017, **249**, 156–160.

34 F. Le Guern, V. Mussard, A. Gaucher, M. Rottman and D. Prim, *Int. J. Mol. Sci.*, 2020, **21**, 9217.

35 L. Song, E. J. Hennink, I. T. Young and H. J. Tanke, *Biophys. J.*, 1995, **68**, 2588–2600.

36 O. Seksek, N. Henry-Toulmé, F. Sureau and J. Bolard, *Anal. Biochem.*, 1991, **193**, 49–54.

37 C. Richter, C. Schneider, M. T. Quick, P. Volz, R. Mahrwald, J. Hughes, B. Dick, U. Alexiev and N. P. Ernsting, *Phys. Chem. Chem. Phys.,* 2015, **17**, 30590–30597.

38 H. J. Lin, H. Szmacinski and J. R. Lakowicz, *Anal. Biochem.*, 1999, **269**, 162–167.

39 Y. M. Poronik, K. V Vygranenko, D. Gryko and D. T. Gryko, *Chem. Soc. Rev.*, 2019, **48**, 5242–5265.

40 M. V. Sednev, C. A. Wurm, V. N. Belov and S. W. Hell, *Bioconjug. Chem.*, 2013, **24**, 690–700.

41 S. Jia, K. M. Ramos-Torres, S. Kolemen, C. M. Ackerman and C. J. Chang, *ACS Chem. Biol.*, 2018, **13**, 1844–1852.

42 R. Alford, H. M. Simpson, J. Duberman, G. C. Hill, M. Ogawa, C. Regino, H. Kobayashi and P. L. Choyke, *Mol. Imaging*, 2009, **8**, 2009–7290.

43 R. P. Buck, S. Rondinini, A. K. Covington, F. G. K. Baucke, C. M. A. Brett, M. F. Camões, M. J. T. Milton, T. Mussini, R. Naumann, K. W. Pratt, P. Spitzer and G. S. Wilson, *Pure Appl. Chem.,* 2003, **74**, 2169–2200.

44 W. Sperber and M. Doyle, *Compendium of the microbiological spoilage of foods and beverages,* New York, NY, USA: Springer, 2009, 235–236.

45 M. H. Schmid-Wendtner and H. C. Korting, *Skin Pharmacol. Physiol.*, 2006, **19**, 296–302.

46 D. Neina, *Appl. Environ. Soil Sci.*, 2019, **2019**, 5794869.

47 W. Aoi and Y. Marunaka, *Biomed. Res. Int.*, 2014, **2014**, 598986.

48 L. He, J. H. Xin and S. Chen, *Sens. Actuators B: Chem.*, 2017, **252**, 277–283.

49 S. Chiappin, G. Antonelli, R. Gatti and E. F. De Palo, *Clin. Chim. Acta.*, 2007, **383**, 30–40.

50 S. L. Percival, S. McCarty, J. A. Hunt and E. J. Woods, *Wound Repair Regen.*, 2014, **22**, 174–186.

51 M. A. Weigelt, H. A. Lev-Tov, M. Tomic-Canic, W. D. Lee, R. Williams, D. Strasfeld, R. S. Kirsner and I. M. Herman, *Adv. Wound Care*, 2022, **11**, 330–359.

52 S. H. Kuo, C. J. Shen, C. F. Shen and C. M. Cheng, *Diagnostics,* 2020, **10**, 107.

53 F. B. Jensen, *Acta. Physiol. Scand.*, 2004, **182**, 215–227.

54 H. H. Leveen, G. Falk, B. Borek, C. Diaz, Y. Lynfield, B. J. Wynkoop, G. A. Mabunda, J. L. Rubricius and G. C. Christoudias, *Ann. Surg.*, 1973, **178**, 745.

55 E. M. Jones, C. A. Cochrane and S. L. Percival, *Adv. Wound Care*, 2015, **4**, 431–439.

56 A. McLister, J. McHugh, J. Cundell and J. Davis, *Adv. Mater.,* 2016, **28**, 5732–5737.

57 B. Valeur and M. N. Berberan-Santos, *Molecular fluorescence: principles and applications*, Wiley-VCH, 2013.

58 J. Lakowicz, *Principles of fluorescence spectroscopy*, Springer US, 2006.

59 G. Gabriel. Stokes, *Philos. Trans. R. Soc. Lond.,*1852, **142**, 463–562.

60 N. J. Turro, V. Ramamurthy and J. C. Scaiano, *Principles of molecular photochemistry: an introduction*, University science books, 2009.

61 P. T. Chou and Y. Chi, *Chem. - A Eur. J.*, 2007, **13**, 380–395.

62 K. L. Wong, J. C. G. Bünzli and P. A. Tanner, *J. Lumin.,* 2020, **224**, 117256.

63 W. Vonau and U. Guth, *J. Solid State Electrochem.,* 2006, **10**, 746–752.

64 S. Radunz, H. R. Tschiche, D. Moldenhauer and U. Resch-Genger, *Sens. Actuators B: Chem.,* 2017, **251**, 490–494.

65 I. V. Hovor, O. S. Kolosova, E. V. Sanin, O. M. Obukhova, A. L. Tatarets, E. A. Terpetschnig and L. D. Patsenker, *Dyes Pigm.,* 2019, **170**, 107567.

66 G. S. Patterson, *J. Chem. Educ.*, 1999, **76**, 395.

67 J. R. Casey, S. Grinstein and J. Orlowski, *Nat. Rev. Mol. Cell Biol.,* 2010, **11**, 50–61.

68 K. C. Gross and P. G. Seybold, *Int. J. Quantum Chem.,* 2000, **80**, 1107–1115.

69 I. Vergne, P. Constant and G. Lanéelle, *Anal. Biochem.*, 1998, **255**, 127–132.

70 K. C. Gross, P. G. Seybold and C. M. Hadad, *Int. J. Quantum Chem.*, 2002, **90**, 445–458.

71 E. Q. Adams, L. Rosenstein, H. Ziegel Brookline Mass, B. Q. Elliot Adams and L. Rosenstbin, *J. Am. Chem. Soc.*, 1914, **36**, 1452–1473.

72 J. Amer, *Chem. Soc.*, 1983, **54**, 1721.

73 S. Qamar, Z. Akhter, S. Yousuf and F. Perveen, *J. Mol. Struct.*, 2020, **1220**, 128667.

74 J. Han and K. Burgess, *Chem. Rev.*, 2010, **110**, 2709–2728.

75 M. M. Martin and L. Lindqvist, *J. Lumin.*, 1975, **10**, 381–390.

76 G. Y. Wiederschain, *Biochem.*, 2011, **76**, 1276–1277.

77 T. I. Rink, R. Y. Tsien and T. Pozzan, *J. Cell Biol.*, 1982, **95**, 189–196.

78 R. M. Effros, L. Olson, W. Lin, S. Audi, G. Hogan, R. Shaker, K. Hoagland and B. Foss, *Am. J. Physiol. Lung Cell. Mol. Physiol.*, 2003, **285**, L476–L483.

79 I. D. Weiner and L. L. Hamm, *Am. J. Physiol. Renal Physiol.,* 1989, **256**, F957–F964.

80 M. L. Graber, D. C. DiLillo, B. L. Friedman and E. Pastoriza-Munoz, *Anal. Biochem.*, 1986, **156**, 202–212.

81 Thermo Fisher Scientific, SNARF® pH Indicators, Molecular Probes, Inc., https://documents.thermofisher.com/TFS-Assets/LSG/manuals/mp01270.pdf, (accessed 25 May 2025).

82 J. Liu, Z. Diwu and W. Y. Leung, *Bioorg. Med. Chem. Lett.*, 2001, **11**, 2903–2905.

83 R. R. Sauers, S. N. Husain, A. P. Piechowski and G. R. Bird, *Dyes and Pigm.*, 1987, **8**, 35–53.

84 J. E. Whitaker, R. P. Haugland, D. Ryan, P. C. Hewitt, R. P. Haugland and F. G. Prendergast, *Anal. Biochem.*, 1992, **207**, 267–279.

85 K. Brinkmann, H. Linnertz, E. Amler, E. Lanz, P. Herman and W. Schoner, *Eur. J. Biochem.*, 1997, **249**, 301–308.

86 S. G. Keller, M. Kamiya and Y. Urano, *Molecules,* 2020, **25**, 5964.

87 L. Yuan, W. Lin and Y. Feng, *Org. Biomol. Chem.*, 2011, **9**, 1723–1726.

88 S. G. Stratton, G. H. Taumoefolau, G. E. Purnell, M. Rasooly, W. L. Czaplyski and E. J. Harbron, *Chemistry*, 2017, **23**, 14064–14072.

89 H. Li, H. Guan, X. Duan, J. Hu, G. Wang and Q. Wang, *Org. Biomol. Chem.*, 2013, **8**, 33.

90 Z. H. Pan, G. G. Luo, J. W. Zhou, J. X. Xia, K. Fang and R. B. Wu, *Dalton Trans.*, 2014, **43**, 8499–8507.

91 A. Hantzsch, *Eur. J. Inorg. Chem.*, 1922, **55**, 953–979.

92 C. Reichardt, *Green Chem.*, 2005, **7**, 339–351.

93 C. Reichardt and T. Welton, *Solvents and solvent effects in organic chemistry*, Wiley-VCH, 2011.

94 C. E. A. de Melo, M. Domínguez, M. C. Rezende and V. G. Machado, *Dyes Pigm.*, 2021, **184**, 108757.

95 M. Homocianu, *Microchem. J.,* 2024, **198**, 110166.

96 C. Reichardt, *Org. Process Res. Dev.*, 2007, **11**, 105–113.

97 S. Nigam and S. Rutan, *Appl. Spectrosc.,* 2001, **55**, 362A–370A.

98 K. Kudo, A. Momotake, Y. Kanna, Y. Nishimura and T. Arai, *Chem. Commun.*, 2011, **47**, 3867–3869.

99 Y. H. Wu, L. Chen, J. Yu, S. L. Tong and Y. Yan, *Dyes Pigm.*, 2013, **97**, 423–428.

100 C. A. Barboza, O. Morawski, J. Olas, P. Gawrys, M. Banasiewicz, K. Suwinska, S. Shova, B. Kozankiewicz and A. L. Sobolewski, *J. Mol. Liq.*, 2021, **343**, 117532.

101 S. Sasaki, Y. Niko, A. S. Klymchenko and G. I. Konishi, *Tetrahedron*, 2014, **70**, 7551–7559.

102 M. A. Kessler and O.-R. S. Wolfbeis, *Spectrochim. Acta., Part A*, 1991, **47**, 187–192.

103 K. Dimroth, C. Reichardt, T. Siepmann and F. Bohlmann, *Justus Liebigs Ann. Chem.*, 1963, **661**, 1–37.

104 C. Reichardt, *Chem. Rev.*, 1994, **94**, 2319–2358.

105 W. E. Waghorne, *J. Solution Chem.*, 2020, **49**, 1360–1372.

106 M. S. Zakerhamidi, A. Ghanadzadeh and M. Moghadam, *Chem. Sci. Trans.*, **2012**, 1–8.

107 M. J. Kamlet, J. L. M. Abboud and R. W. Taft, *Progress in physical organic chemistry,* 1981, 485–630.

108 H. C. Rang, C. H. Mauldin, T. C. W. Slegeir, K. Cann and R. Pettit, *J. Am. Chem. Soc.*, 1977, **99**, 8325–8327.

109 M. J. Kamlet and R. W. Taft, *J. Am. Chem. Soc.*, 1976, **98**, 377–383.

110 M. Homocianu*, J. Adv. Res. Phys.,* 2017, **2**, 1.

111 J. Catalán, *J. Phys. Chem. B.,* 2009, **113**, 5951–5960.

112 J. Catalán and H. Hopf, *Eur. J. Org. Chem.,* **2004**, 4694–4702.

113 U. Mayer, V. Gutmann and W. Gerger, *Monatsh. Chem.,*1975, **106**, 1235–1257.

114 J. Catalán and C. Díaz, *Liebigs Ann.*, 1997, **1997**, 1941–1949.

115 J. Catalán, C. Díaz, V. López, P. Pérez, J. L. G. De Paz and J. G. Rodríguez, *Liebigs Ann.*, 1996, **1996**, 1785–1794.

116 A. Kumar and R. K. Gupta, *Fundamentals of Polymer Engineering*, CRC press, 2018.

117 K. Kataoka, A. Harada and Y. Nagasaki, *Adv. Drug Delivery Rev.*, 2012, **64**, 37–48.

118 D. E. Discher and A. Eisenberg, *Science*, 2002, **297**, 967–973.

119 Y. Mai and A. Eisenberg, *Chem. Soc. Rev.*, 2012, **41**, 5969–5985.

120 L. Zhang and A. Eisenberg, *Science*, 1995, **268**, 1728–1731.

121 J. C. M. Van Hest, D. A. P. Delnoye, M. W. P. L. Baars, M. H. P. Van Genderen and E. W. Meijer, *Science*, 1995, **268**, 1592–1595.

122 A. Blanazs, S. P. Armes and A. J. Ryan, *Macromol. Rapid Commun.*, 2009, **30**, 267–277.

123 G. Battaglia and A. J. Ryan, *J. Phys. Chem. B.,* 2006, **110**, 10272–10279.

124 A. Moscho, O. Orwar, D. T. Chiu, B. P. Modi and R. N. Zare, *Proc. Natl. Acad. Sci. U. S. A.,* 1996, **93**, 11443–11447.

125 K. Kaur, M. Müller, M. Müller and H. Schönherr, *Pharmaceutics*, 2023, **15**, 2683.

126 K. S. Tücking, V. Grützner, R. E. Unger and H. Schönherr, *Macromol. Rapid Commun.*, 2015, **36**, 1248–1254.

127 M. Karayianni and S. Pispas, *J. Polym. Sci.*, 2021, **59**, 1874–1898.

128 K. S. Tücking, PhD Thesis, Universität Siegen, 2017.

129 S. Hocine, D. Cui, M. N. Rager, A. Di Cicco, J. M. Liu, J. Wdzieczak-Bakala, A. Bruîlet and M. H. Li, *Langmuir*, 2013, **29**, 1356–1369.

130 E. Cabane, V. Malinova, S. Menon, C. G. Palivan and W. Meier, *Soft Matter*, 2011, **7**, 9167–9176.

131 W. Zhou, F. Meng, G. H. M. Engbers and J. Feijen, in *9th European Symposium on Controlled Drug Delivery, ESCDD 2006*, 2006.

132 H. Oliveira, E. Pérez-Andrés, J. Thevenot, O. Sandre, E. Berra and S. Lecommandoux, *J. Controlled Release*, 2013, **169**, 165–170.

133 U. Borchert, U. Lipprandt, M. Bilang, A. Kimpfler, A. Rank, R. Peschka-Süss, R. Schubert, P. Lindner and S. Förster, *Langmuir*, 2006, **22**, 5843–5847.

134 C. Sanson, C. Schatz, J. F. Le Meins, A. Brûlet, A. Soum and S. Lecommandoux, *Langmuir*, 2010, **26**, 2751–2760.

135 A. Napoli, M. J. Boerakker, N. Tirelli, R. J. M. Nolte, N. A. J. M. Sommerdijk and J. A. Hubbell, *Langmuir*, 2004, **20**, 3487–3491.

136 J. S. Lee, T. Groothuis, C. Cusan, D. Mink and J. Feijen, *Biomaterials*, 2011, **32**, 9144–9153.

137 F. Meng, W. E. Hennink and Z. Zhong, *Biomaterials*, 2009, **30**, 2180–2198.

138 K. S. Tücking, S. Handschuh-Wang and H. Schönherr, *Aust. J. Chem*, 2014, **67**, 578–584.

139 D. F. Williams, *Eng. Med.*, 1981, **10**, 5–7.

140 I. Aranaz, M. Mengibar, R. Harris, I. Panos, B. Miralles, N. Acosta, G. Galed and A. Heras, *Curr. Chem. Biol.*, 2009, **3**, 203–230.

141 O. C. Agboh and Y. Qin, *Polym. Adv. Technol.*, 1997, **8**, 355–365.

142 M. Rinaudo, *Prog. Polym. Sci.*, 2006, **31**, 603–632.

143 W. L. Teng, E. Khor, T. K. Tan, L. Y. Lim and S. C. Tan, *Carbohydr. Res.*, 2001, **332**, 305–316.

144 N. Acosta, C. Jiménez, V. Borau and A. Heras, *Biomass Bioenergy.*, 1993, **5**, 145–153.

145 F. Croisier and C. Jérôme, *Eur. Polym. J.*, 2013, **49**, 780–792.

146 H. K. No and S. P. Meyers, *J. Aquat. Food Prod. Technol.,* 1995, **4**, 27–52.

147 D. Raafat and H. G. Sahl, *Microb. Biotechnol.*, 2009, **2**, 186–201.

148 E. Khor, *Chitin: fulfilling a biomaterials promise*, Elsevier, 2014.

149 G. Crini and P. M. Badot, *Prog. Polym. Sci.*, 2008, **33**, 399–447.

150 G. Iruoghene, E. Emad, Y. Mohammed and H. Al Mashhadani, *Polym. Bull.*, 2024, **81**, 16457–16507.

151 Y. Z. Du, L. Wang, H. Yuan and F. Q. Hu, *Int. J. Biol. Macromol.*, 2011, **48**, 215–222.

152 G. B. Jiang, D. Quan, K. Liao and H. Wang, *Carbohydr. Polym.*, 2006, **66**, 514–520.

153 Y. Z. Du, P. Lu, J. P. Zhou, H. Yuan and F. Q. Hu, *Int. J. Pharm.*, 2010, **391**, 260–266.

154 Y. Z. Du, L. Wang, H. Yuan, X. H. Wei and F. Q. Hu, *Colloids Surf. B: Biointerfaces*, 2009, **69**, 257–263.

155 M. Elnashar, ed., *Biotechnology of biopolymers*, BoD–Books on Demand, 2011.

156 M. Chen, T. Runge, L. Wang, R. Li, J. Feng, X. L. Shu and Q. S. Shi, *Carbohydr. Polym.*, 2018, **200**, 115–121.

157 C. M. Lehr, J. A. Bouwstra, E. H. Schacht and H. E. Junginger, *Int. J. Pharm.*, 1992, **78**, 43–48.

158 P. He, S. S. Davis and L. Illum, *Int. J. Pharm.*, 1998, **166**, 75–88.

159 M. Nasaj, M. Chehelgerdi, B. Asghari, A. Ahmadieh-Yazdi, M. Asgari, S. Kabiri-Samani, E. Sharifi and M. Arabestani, *Int. J. Biol. Macromol.*, 2024, **277**, 134321.

160 A. Guarnieri, M. Triunfo, C. Scieuzo, D. Ianniciello, E. Tafi, T. Hahn, S. Zibek, R. Salvia, A. De Bonis and P. Falabella, *Sci. Rep.*, 2022, **12**, 1–12.

161 I. Koumentakou, A. Meretoudi, C. Emmanouil and G. Z. Kyzas, *J. Ind. Eng. Chem.,* 2025, **146**, 70–86.

162 Y. Xia, R. Yang, H. Wang, Y. Li and C. Fu, *Front. Mater.*, 2022, **9**, 994265.

163 G. Eric and E. Guibal, *Sep. Purif. Technol.*, 2004, **38**, 43–74.

164 S. Ahmed and S. Ikram, *Achievements Life Sci.,* 2016, **10**, 27–37.

165 Y. Xia, D. Wang, D. Liu, J. Su, Y. Jin, D. Wang, B. Han, Z. Jiang and B. Liu, *Front. Bioeng. Biotechnol.*, 2022, **10**, 894667.

166 P. Feng, Y. Luo, C. Ke, H. Qiu, W. Wang, Y. Zhu, R. Hou, L. Xu and S. Wu, *Front. Bioeng. Biotechnol.*, 2021, **9**, 650598.

167 S. R. B, D. S. R. Rajkumar, K. K and V. Vijayaragavan, *Cureus*, 2024, **16**, e55193.

168 S. M. Mawazi, M. Kumar, N. Ahmad, Y. Ge and S. Mahmood, *Polymers,* 2024, **16**, 1351.

169 J. Varshosaz, *Expert Opin. Drug Deliv.*, 2007, **4**, 263–273.

170 J. H. Park, G. Saravanakumar, K. Kim and I. C. Kwon, *Adv. Drug Deliv. Rev.*, 2010, **62**, 28–41.

171 M. N. V. R. Kumar, R. A. A. Muzzarelli, C. Muzzarelli, H. Sashiwa and A. J. Domb, *Chem. Rev.*, 2004, **104**, 6017–6084.

172 S. V. Madihally and H. W. T. Matthew, *Biomaterials*, 1999, **20**, 1133–1142.

173 I. Y. Kim, S. J. Seo, H. S. Moon, M. K. Yoo, I. Y. Park, B. C. Kim and C. S. Cho, *Biotechnol. Adv.*, 2008, **26**, 1–21.

174 K. Kulka and A. Sionkowska, *Molecules*, 2023, **28**, 1817.

175 W. Zhang, A. Khan, P. Ezati, R. Priyadarshi, M. A. Sani, N. B. Rathod, G. Goksen and J. W. Rhim, *Food Chem.*, 2024, **443**, 138506.

176 D. E. Rockson-Itiveh, F. C. Ozioko and M. Keke, *Int. J. Environ. Pollut. Environ. Model.*, 2024, **7**, 27–36.

177 M. A. M. Rocha, M. A. Coimbra and C. Nunes, *Curr. Opin. Food Sci.*, 2017, **15**, 61–69.

178 L. M. Hemmingsen, N. Škalko-Basnet and M. W. Jøraholmen, *Mar. Drugs, 2021,* **19***,* 697.

179 J. D. Ferry, *Viscoelastic properties of polymers*, John Wiley & Sons, 1980.

180 C. P. Jiménez-Gómez, J. A. Cecilia, M. Guidotti and R. Soengas, *Molecules,* 2020, **25**, 3981.

181 M.-M. S. Ebrahimi, PhD Thesis, Universität Siegen, 2016.

182 R. Riva, H. Ragelle, A. Des Rieux, N. Duhem, C. Jérôme and V. Préat, *Adv. Polym. Sci.,* 2011, **244**, 19–44.

183 S. Ladet, L. David and A. Domard, *Nature*, 2008, **452**, 76–79.

184 M. M. Sadat Ebrahimi, Y. Voss and H. Schönherr, *ACS Appl. Mater. Interfaces.*, 2015, **7**, 20190–20199.

185 A. Pavinatto, A. V. de Almeida Mattos, A. C. G. Malpass, M. H. Okura, D. T. Balogh and R. C. Sanfelice, *Int. J. Biol. Macromol.*, 2020, **151**, 1004–1011.

186 Y. J. Seol, J. Y. Lee, Y. J. Park, Y. M. Lee, Y. -Ku, I. C. Rhyu, S. J. Lee, S. B. Han and C. P. Chung, *Biotechnol. Lett.*, 2004, **26**, 1037–1041.

187 Y. G. Chen, C. X. Li, Y. Zhang, Y. D. Qi, J. Feng and X. Z. Zhang, *Chin. J. Polym. Sci.*, 2022, **40**, 1050–1061.

188 S. C. Shi and Y. W. Chang, *Prog. Org. Coat.*, 2022, **170**, 106981.

189 T. A. Khan, K. K. Peh and H. S. Ch'ng, *J. Pharm. Pharm. Sci.*, 2000, **3**, 303–311.

190 G. Verma and M. Mishra, *World J. Pharm. Res.*, 2018, **7**, 1170–1180.

191 K. Cole and B. S. Levine, *Principles of Forensic Toxicology: Fifth Edition*, 2020, 127–134.

192 D. A. Skoog, F. J. Holler and S. R. Crouch, *Principles of Instrumental Analysis*, Cengage Learning, 2019.

193 D. G. Duff and C. H. Giles, *J. Soc. Dyers Colour.,* 1972, **88**, 181–184.

194 R. F. Kubin and A. N. Fletcher, *J. Lumin.*, 1982, **27**, 455–462.

195 R. Griebel, *Ber. Bunsen-Ges. Phys. Chem.*, 1980, **84**, 84–91.

196 J. Hoche, A. Schulz, L. M. Dietrich, A. Humeniuk, M. Stolte, D. Schmidt, T. Brixner, F. Würthner and R. Mitric, *Chem. Sci.*, 2019, **10**, 11013–11022.

197 E. A. Slyusareva and M. A. Gerasimova, *Russ. Phys. J.,* 2014, **56**, 1370–1377.

198 G. A. Crosby and J. N. Demas, *J. Phys. Chem.*, 1971, **75**, 991–1024.

199 J. H. Brannon and D. Magde, *J. Phys. Chem.*, 1978, **82**, 705–709.

200 J. B. Birks, *J. Res. Natl. Bur. Stand. A: Phys. Chem.,* 1976, **80**, 389.

201 U. Resch-Genger and P. C. DeRose, *Pure Appl. Chem.*, 2010, **82**, 2315–2335.

202 K. Rurack and M. Spieles, *Anal. Chem.*, 2011, **83**, 1232–1242.

203 ATTO-TEC GmbH - Determination of Fluorescence Quantum Yield, https://www.atto-tec.com/fluorescence/determination-of-fluorescence-quantum-yield/, (accessed 25 June 2025).

204 H. Brismar, O. Trepte and B. Ulfhake, *J. Histochem. Cytochem.*,1995, **43**, 699–707.

205 M. Wahl, Time-Correlated Single Photon Counting, Technical Note PicoQuant 2009, https://www.picoquant.com/images/uploads/page/files/7253/technote_tcspc.pdf (accessed 25 June 2025).

206 ATTO-TEC GmbH - Determination of Fluorescence Lifetime, https://www.atto-tec.com/fluorescence/determination-of-fluorescence-lifetime/, (accessed 25 June 2025).

207 M. Adhikari, R. Houhou, J. Hniopek and T. Bocklitz, *J. Exp. Theor. Anal.*, 2023, **1**, 44–63.

208 E. B. Van Munster and T. W. J. Gadella, *Adv. Biochem. Eng. Biotechnol.*, 2005, **95**, 143–175.

209 J. Chen, W. Liu, B. Zhou, G. Niu, H. Zhang, J. Wu, Y. Wang, W. Ju and P. Wang, *J. Org. Chem.*, 2013, **78**, 6121–6130.

210 J. Arden-Jacob, J. Frantzeskos, N. U. Kemnitzer, A. Zilles and K. H. Drexhage, *Spectrochim. Acta A: Mol. Biomol. Spectrosc.,* 2001, **57**, 2271–2283.

211 H. Yutaka and S. K. Rivon, *Theory & Manufacture Dye Chemistry*, Gihodo, KK, Tokyo, 1963.

212 A. Baeyer, *Ber. Dtsch. Chem. Ges.*, 1871, **4**, 555–558.

213 W.-C. Sun, K. R. Gee, D. H. Klaubert and R. P. Haugland, *J. Org. Chem.*, 1997, **62**, 6469–6475.

214 C. Liu and C. N. Scott, *Dyes Pigm.,* 2021, **196**, 109792.

215 J. B. Grimm, B. P. English, J. Chen, J. P. Slaughter, Z. Zhang, A. Revyakin, R. Patel, J. J. Macklin, D. Normanno and R. H. Singer, *Nat. Methods*, 2015, **12**, 244–250.

216 M. Grzybowski, M. Taki and S. Yamaguchi, *Chem. - A Eur. J.,* 2017, **23**, 13028–13032.

217 W. Chen, S. Xu, J. J. Day, D. Wang and M. Xian, *Angew. Chem.,* 2017, **129**, 16838–16842.

218 S. S. Patil, K. G. Thorat, R. Mallah and N. Sekar, *J. Fluoresc.*, 2016, **26**, 2187–2197.

219 Y. Koide, Y. Urano, K. Hanaoka, T. Terai and T. Nagano, *ACS Chem. Biol.*, 2011, **6**, 600–608.

220 J. Liu, Y. Q. Sun, H. Zhang, H. Shi, Y. Shi and W. Guo, *ACS Appl. Mater. Interfaces.*, 2016, **8**, 22953–22962.

221 M. A. Clark, K. Duffy, J. Tibrewala and S. J. Lippard, *Org. Lett.*, 2003, **5**, 2051–2054.

222 M. J. S. Dewar, *J. Am. Chem. Soc.,* 1940, **443**, 770.

223 K. N. More, S. K. Mun, J. Kang, J. J. Kim, S. T. Yee and D. J. Chang, *Dyes Pigm.,* 2021, **184**, 108785.

224 P. M. Engelhardt, M. Veronese, A. A. Eryiğit, A. Das, A. T. Kaczmarek, E. I. Rugarli and H. Schmalz, *Chem. - A Eur. J.*, 2024, **30**, e202400808.

225 S. K. Dwivedi, D. L. Arachchige, T. Vohs, J. Tang, K. Usimaki, A. M. Olowolagba, D. R. Fritz, R. L. Luck, T. Werner and H. Liu, *J. Mater. Chem. B.*, 2023, **11**, 2852–2861.

226 A. Roth, H. Li, C. Anorma and J. Chan, *J. Am. Chem. Soc.,* 2015, **137**, 10890–10893.

227 G. Talsky, *Angew. Chem.,* 1990, **102**, 343–343.

228 H. Mustroph, J. Mistol, B. Senns, D. Keil, M. Findeisen and L. Hennig, *Angew. Chem. Int. Ed.,* 2009, **48**, 8773–8775.

229 Y. W. Jun, H. R. Kim, Y. J. Reo, M. Dai and K. H. Ahn, *Chem. Sci.*, 2017, **8**, 7696–7704.

230 ATTO-TEC GmbH - ATTO 647N, https://www.atto-tec.com/ATTO-647N.html?language=en, (accessed 19 June 2025).

231 D. Magde, R. Wong and P. G. Seybold, *Photochem. Photobiol.*, **2002**, *75*, 327–334.

232 K. H. Drexhage, *J. Res. Natl. Bur. Stand. A: Phys. Chem.,* 1976, **80**, 421.

233 A. Zilles, K. H. Drexhage, N. U. Kemnitzer, J. Arden-Jacob and M. Hamers-Schneider, US Pat., 9,651,490, 2017.

234 Y. M. Poronik, G. Clermont, M. Blanchard-Desce and D. T. Gryko, *J. Org. Chem.,* 2013, **78**, 11721–11732.

235 L. Krishnamoorthy, J. A. Cotruvo Jr, J. Chan, H. Kaluarachchi, A. Muchenditsi, V. S. Pendyala, S. Jia, A. T. Aron, C. M. Ackerman and M. N. Vander Wal, *Nat. Chem. Biol.*, 2016, **12**, 586–592.

236 ATTO-TEC GmbH, *ATTO 565 and ATTO 590 General Information,* https://www.atto-tec.com/fileadmin/user_upload/Katalog_Flyer_Support/ATTO565_ATTO590_DE.pdf, (accessed 25 June 2025).

237 B. F. Dutter, A. Ender, G. A. Sulikowski and C. D. Weaver, *Org. Biomol. Chem.*, 2018, **16**, 5575–5579.

238 Solvent Physical Properties, https://people.chem.umass.edu/xray/solvent.html, (accessed 19 July 2025).

239 J. Kiefer, K. Noack and B. Kirchner, *Curr. Phys. Chem.*, 2012, **1**, 340–351.

240 Kamlet-Taft solvent parameters, https://www.stenutz.eu/chem/solv26.php, (accessed 19 July 2025).

241 T. Koide, S. Iwamori, S. Koga, Y. Suzuki, J. Kawamata and Y. Hisaeda, *Dyes Pigm.,* 2020, **183**, 108667.

242 N. T. Thet, D. R. Alves, J. E. Bean, S. Booth, J. Nzakizwanayo, A. E. R. Young, B. V Jones and A. T. A. Jenkins, *ACS Appl. Mater. Interfaces*, 2016, **8**, 14909–14919.

243 R. F. Chen and J. R. Knutson, *Anal. Biochem.*, 1988, **172**, 61–77.

244 B. M. Discher, Y.-Y. Won, D. S. Ege, J. C. M. Lee, F. S. Bates, D. E. Discher and D. A. Hammer, *Science,* 1999, **284**, 1143–1146.

245 H. Bermudez, A. K. Brannan, D. A. Hammer, F. S. Bates and D. E. Discher, *Macromolecules*, 2002, **35**, 8203–8208.

246 G. Battaglia and A. J. Ryan, *J. Am. Chem. Soc.*, 2005, **127**, 8757–8764.

247 L.-Y. Guo, S.-Z. Yan, X. Tao, Q. Yang, Q. Li, T.-S. Wang, S.-Q. Yu and S.-L. Chen, *Mater. Sci. Eng. C.,* 2020, **106**, 110230.

248 S. Haas, N. Hain, M. Raoufi, S. Handschuh-Wang, T. Wang, X. Jiang and H. Schönherr, *Biomacromolecules*, 2015, **16**, 832–841.

249 F. Kawai, K. Nakadai, E. Nishioka, H. Nakajima, H. Ohara, K. Masaki and H. Iefuji, *Polym. Degrad. Stab.*, 2011, **96**, 1342–1348.

250 F. Ahmed, R. I. Pakunlu, G. Srinivas, A. Brannan, F. Bates, M. L. Klein, T. Minko and D. E. Discher, *Mol. Pharm.*, 2006, **3**, 340–350.

251 L. Praveen, S. Saha, S. K. Jewrajka and A. Das, *J. Mater. Chem. B.*, 2013, **1**, 1150–1155.

252 J. Zhou, D. Yao, Z. Qian, S. Hou, L. Li, A. T. A. Jenkins and Y. Fan, *Biomaterials*, 2018, **161**, 11–23.

253 Y. Oba and S. R. Poulson, *Geochem. J.*, 2012, **46**, 517–520.

254 OECD, *Test No. 107: Partition Coefficient (n-octanol/water): Shake Flask Method, OECD Guidelines for the Testing of Chemicals, Section 1.1*, 1995.

255 J. De Bruijn, F. Busser, W. Seinen and J. Hermens, *Environ. Toxicol. Chem.*, 1989, **8**, 499–512.

256 D. W. Hawker and D. W. Connell, *Environ. Sci. Technol.*, 1988, **22**, 382–387.

257 Y. Yu, W. Yang, Z. Gao, M. H. W. Lam, X. Liu, L. Wang and H. Yu, *Environ. Chem.*, 2008, **5**, 332–339.

258 P.-B. T. Guideline, *The Hershberger*, 2001, **601**, 858.

259 R. Anliker and P. Moser, *Ecotoxicol. Environ. Saf.*, 1987, **13**, 43–52.

260 V. Buschmann, K. D. Weston and M. Sauer, *Bioconjug. Chem.*, 2002, **14**, 195–204.

261 R. Adami, S. Liparoti, L. Izzo, D. Pappalardo and E. Reverchon, *J. Supercrit. Fluids*, 2012, **72**, 15–21.

262 N. Klonis and W. H. Sawyer, *J. Fluoresc.*, 1996, **6**, 147–157.

263 R. Ghosh and J. Dey, *Langmuir*, 2020, **36**, 5829–5838.

264 C. Gong, Q. Wu, Y. Wang, D. Zhang, F. Luo, X. Zhao, Y. Wei and Z. Qian, *Biomaterials*, 2013, **34**, 6377–6387.

265 K. Skórkowska-Telichowska, M. Czemplik, A. Kulma and J. Szopa, *J. Am. Acad. Dermatol.*, 2013, **68**, e117–e126.

266 G. Crini and E. Lichtfouse, eds., *Sustainable Agriculture Reviews 35: Chitin and Chitosan: History, Fundamentals and Innovations*, Springer, **2019**.

267 S. Roy and J.-W. Rhim, *Crit. Rev. Food Sci. Nutr.*, 2021, **61**, 2297–2325.

268 J. Chalitangkoon and P. Monvisade, *Carbohydr. Polym.*, 2019, **223**, 115049.

269 E. Schoolaert, I. Steyaert, G. Vancoillie, J. Geltmeyer, K. Lava, R. Hoogenboom and K. De Clerck, *J. Mater. Chem. B.*, 2016, **4**, 4507–4516.

270 B. Qiao, Q. Pang, P. Yuan, Y. Luo and L. Ma, *Biomater. Sci.*, 2020, **8**, 1649–1657.

271 C. K. Field and M. D. Kerstein, *Am. J. Surg.*, 1994, **167**, S2–S6.

272 E. Slyusareva, M. Gerasimova, V. Slabko, N. Abuzova, A. Plotnikov and A. Eychmüller, *ChemPhysChem*, 2015, **16**, 3997–4003.

273 L. Prietto, T. C. Mirapalhete, V. Z. Pinto, J. F. Hoffmann, N. L. Vanier, L. T. Lim, A. R. Guerra Dias and E. da Rosa Zavareze, *LWT-Food Sci. Technol.*, 2017, **80**, 492–500.

274 M. Moradi, H. Tajik, H. Almasi, M. Forough and P. Ezati, *Carbohydr. Polym.*, 2019, **222**, 115030.

275 J. Hernando, M. Van der Schaaf, E. M. H. P. Van Dijk, M. Sauer, M. F. García-Parajó and N. F. Van Hulst, *J. Phys. Chem. A.*, 2003, **107**, 43–52.

276 V. I. Gavrilenko and M. A. Noginov, *J. Chem. Phys.*, 2006, **124**, 044301.

Appendix

Chapter 3: Synthesis and Characterization of Novel pH-Sensitive Carborhodol Dyes

^{1}H, ^{13}C, and ^{19}F NMR Spectral Data

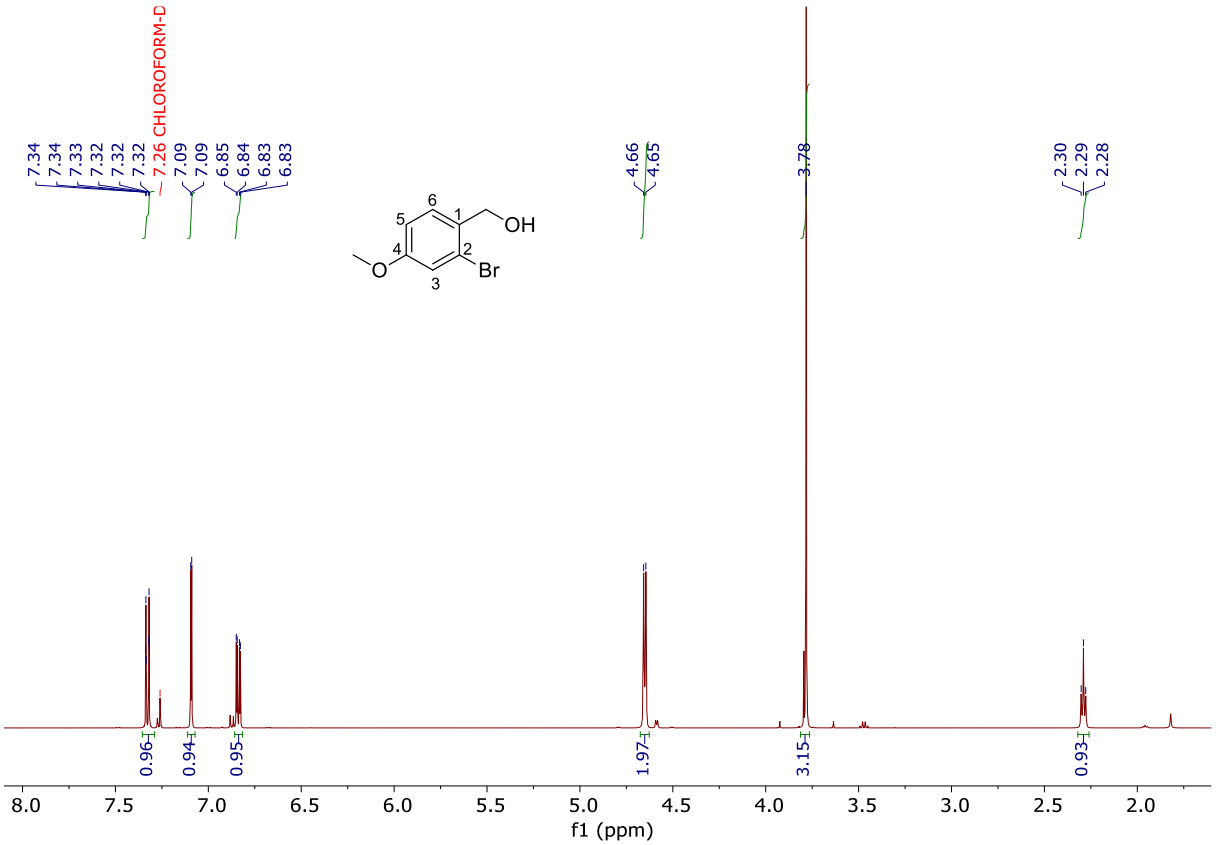

Figure S1. ^{1}H-NMR spectrum (500 MHz) of (2-Bromo-4-methoxyphenyl)methanol (**20**) in $CDCl_3$.

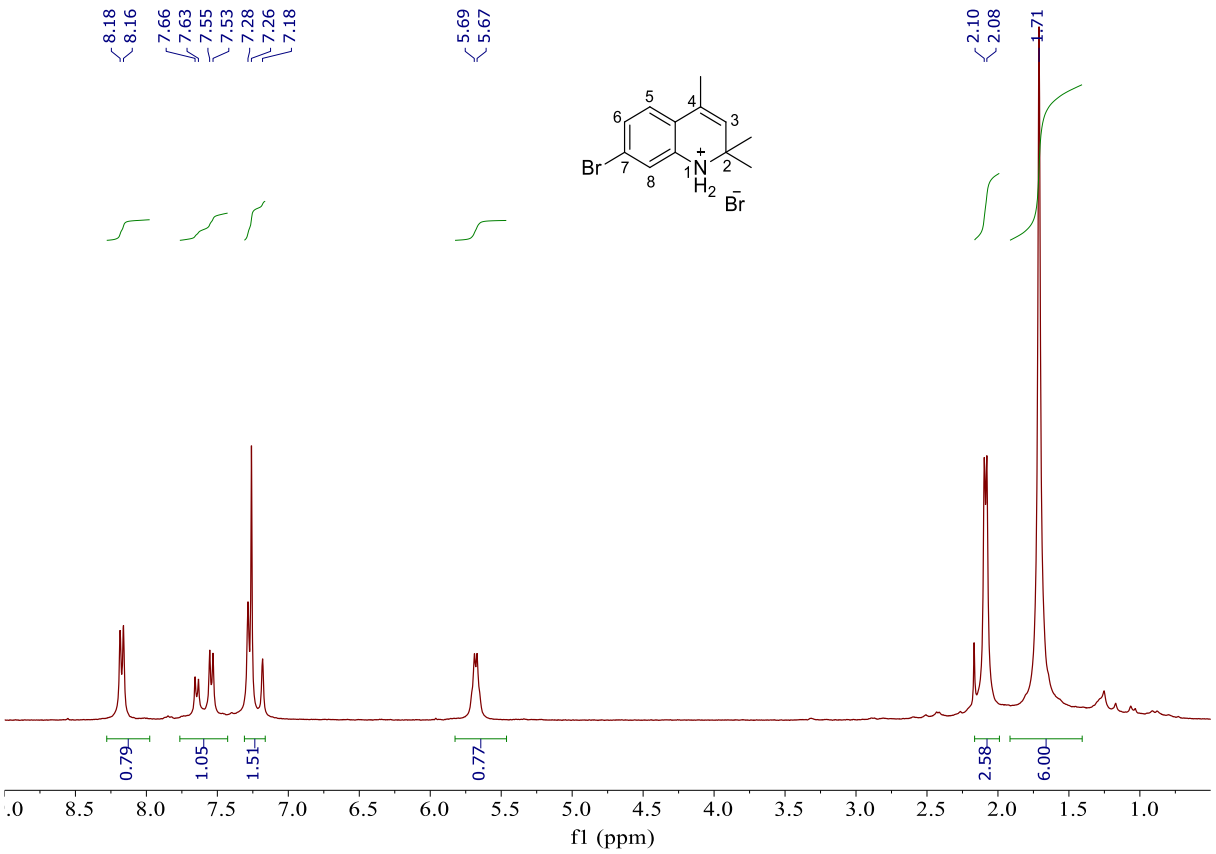

Figure S2. ^{1}H-NMR spectrum (80 MHz) of 7-Bromo-2,2,4-trimethyl-1,2-dihydroquinoline hydrobromide (**23**) in $CDCl_3$.

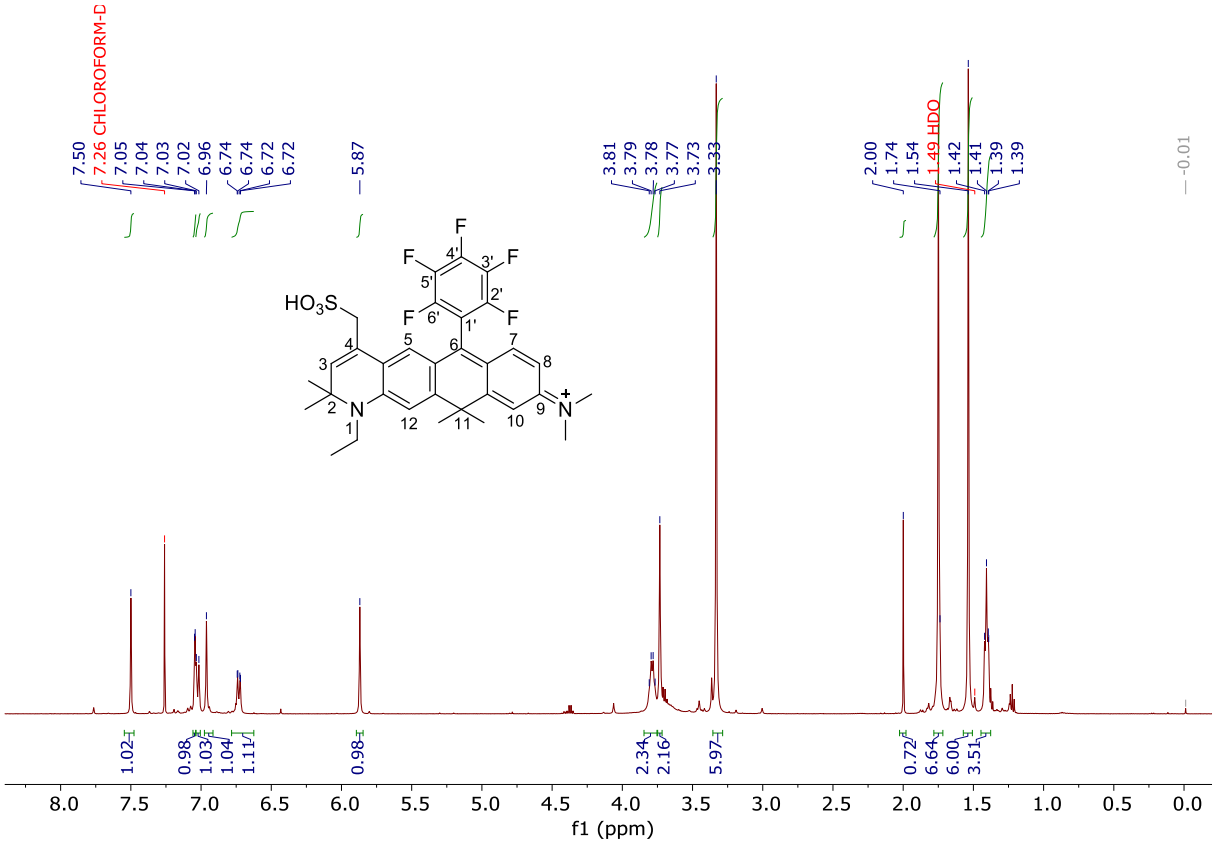

Figure S3. ^{1}H-NMR spectrum (500 MHz) of **AZ 233** in $CDCl_3$.

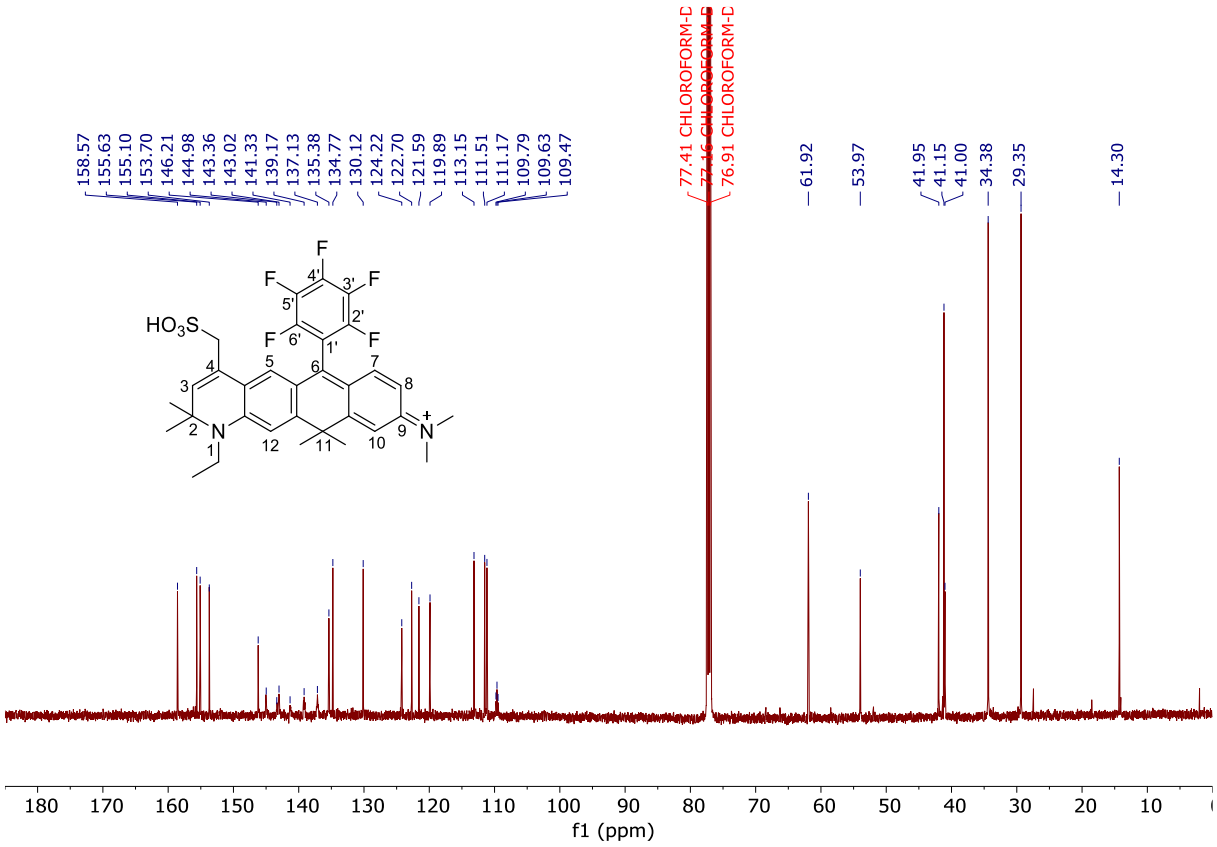

Figure S4. ^{13}C-NMR spectrum (125 MHz) of **AZ 233** in $CDCl_3$.

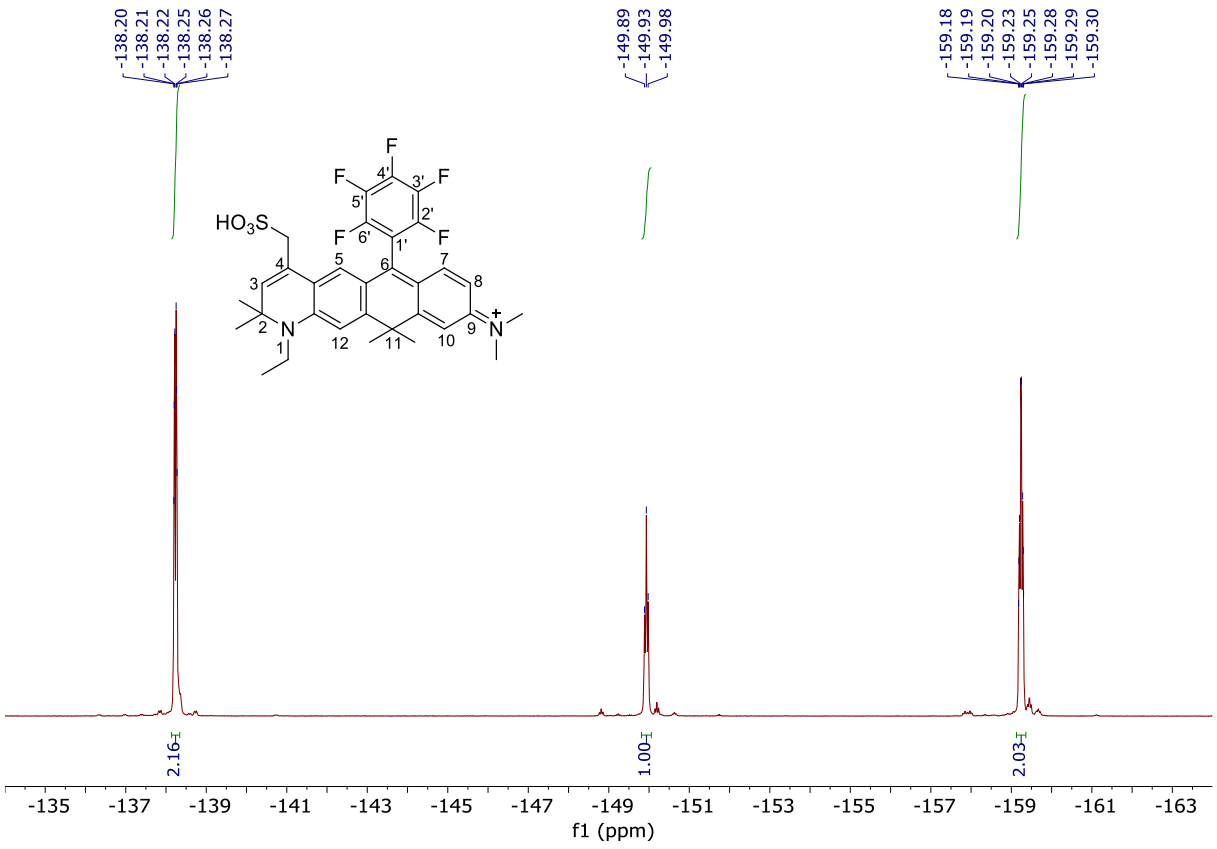

Figure S5. ^{19}F-NMR spectrum (470 MHz) of **AZ 233** in $CDCl_3$.

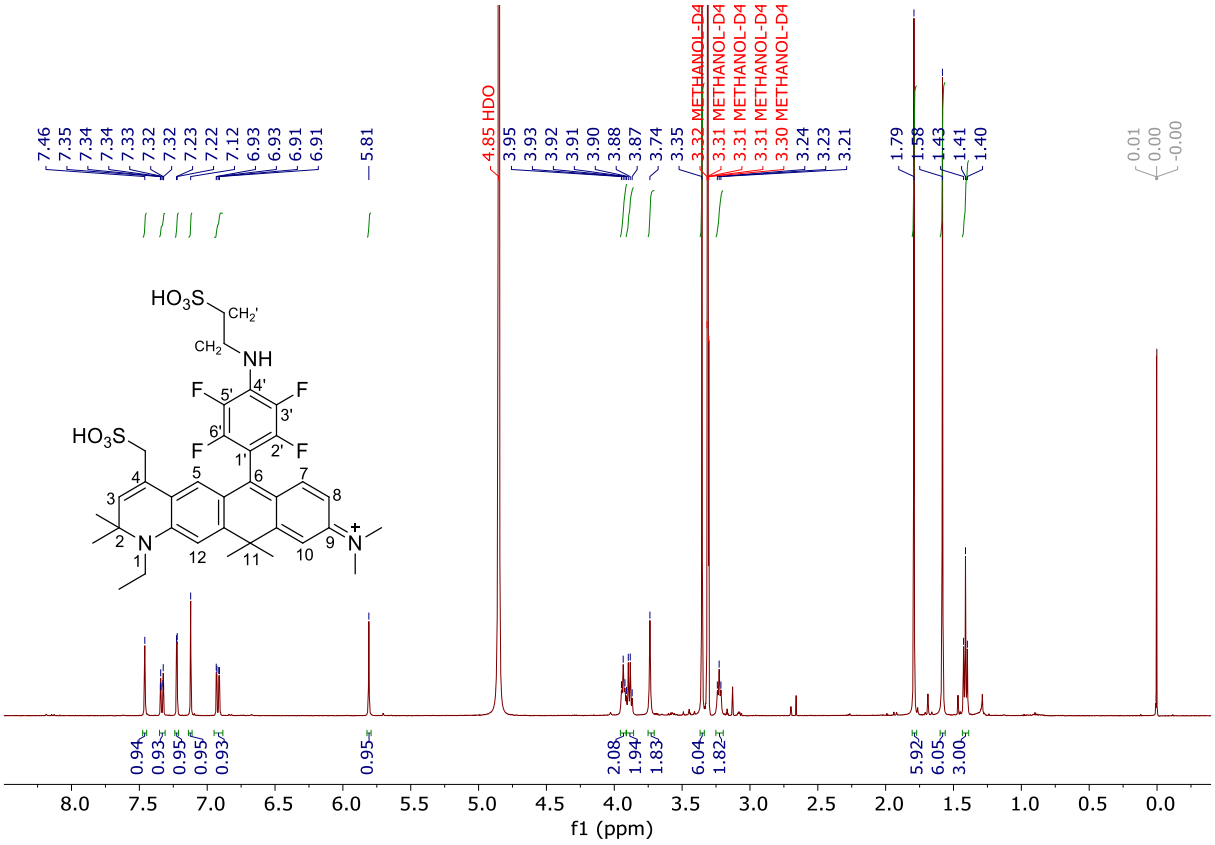

Figure S6. ^{1}H-NMR spectrum (500 MHz) of **AZ 444** in CD_3OD.

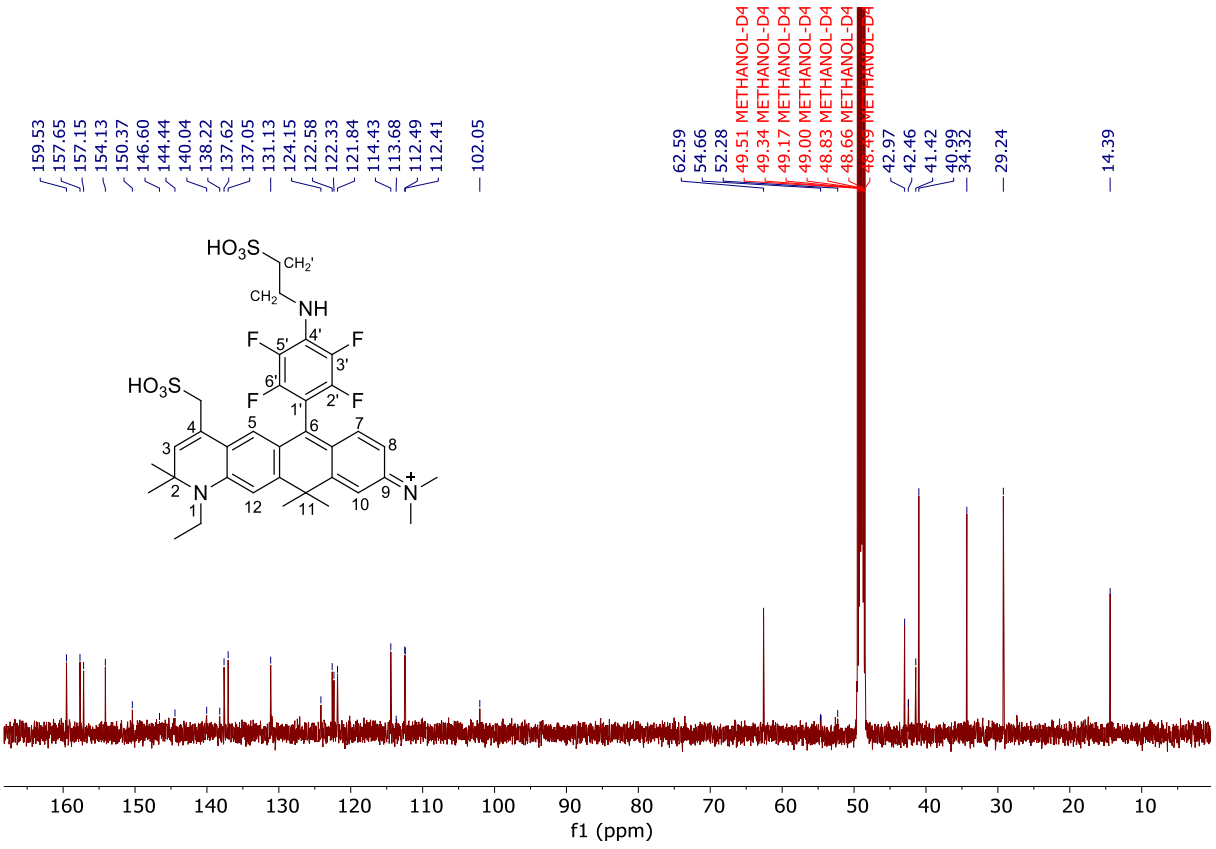

Figure S7. ^{13}C-NMR spectrum (125 MHz) of **AZ 444** in CD_3OD.

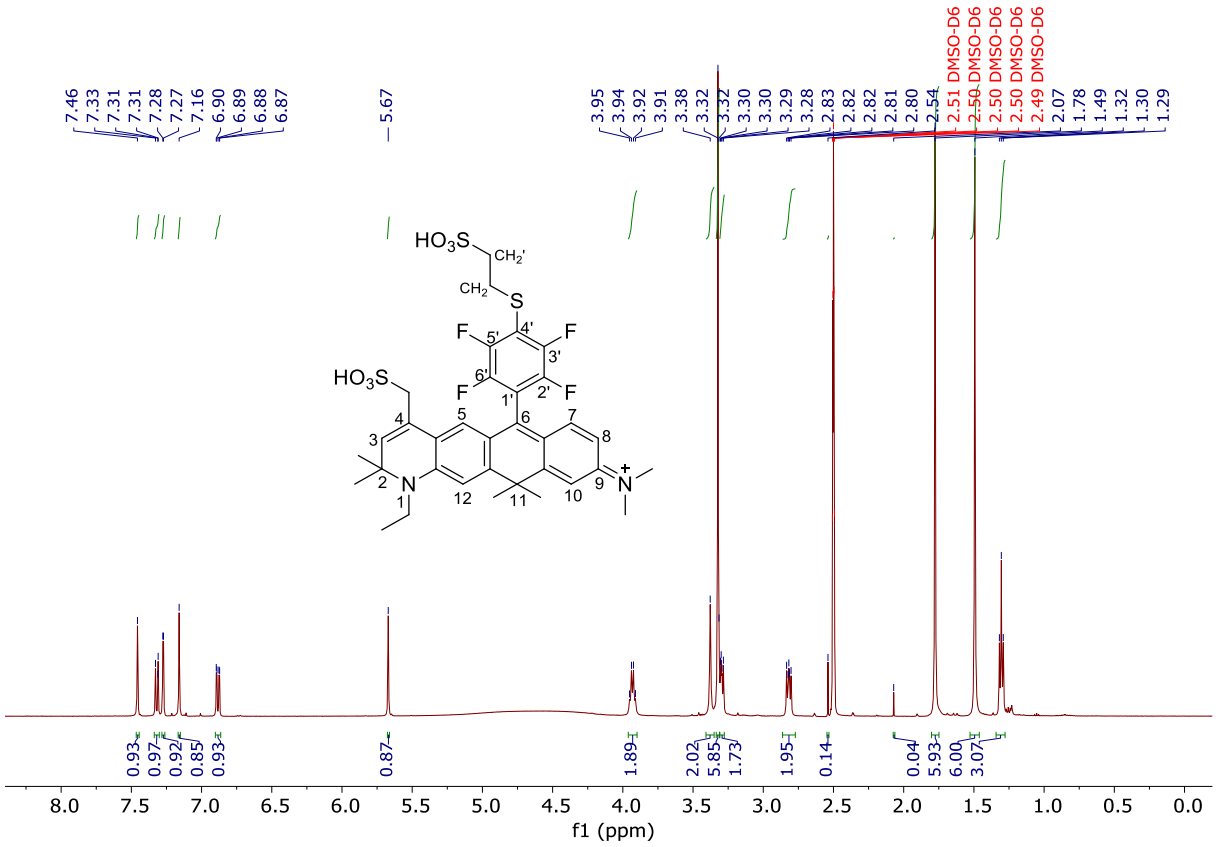

Figure S8. [1]H-NMR spectrum (500 MHz) of **AS 06** in DMSO-d_6.

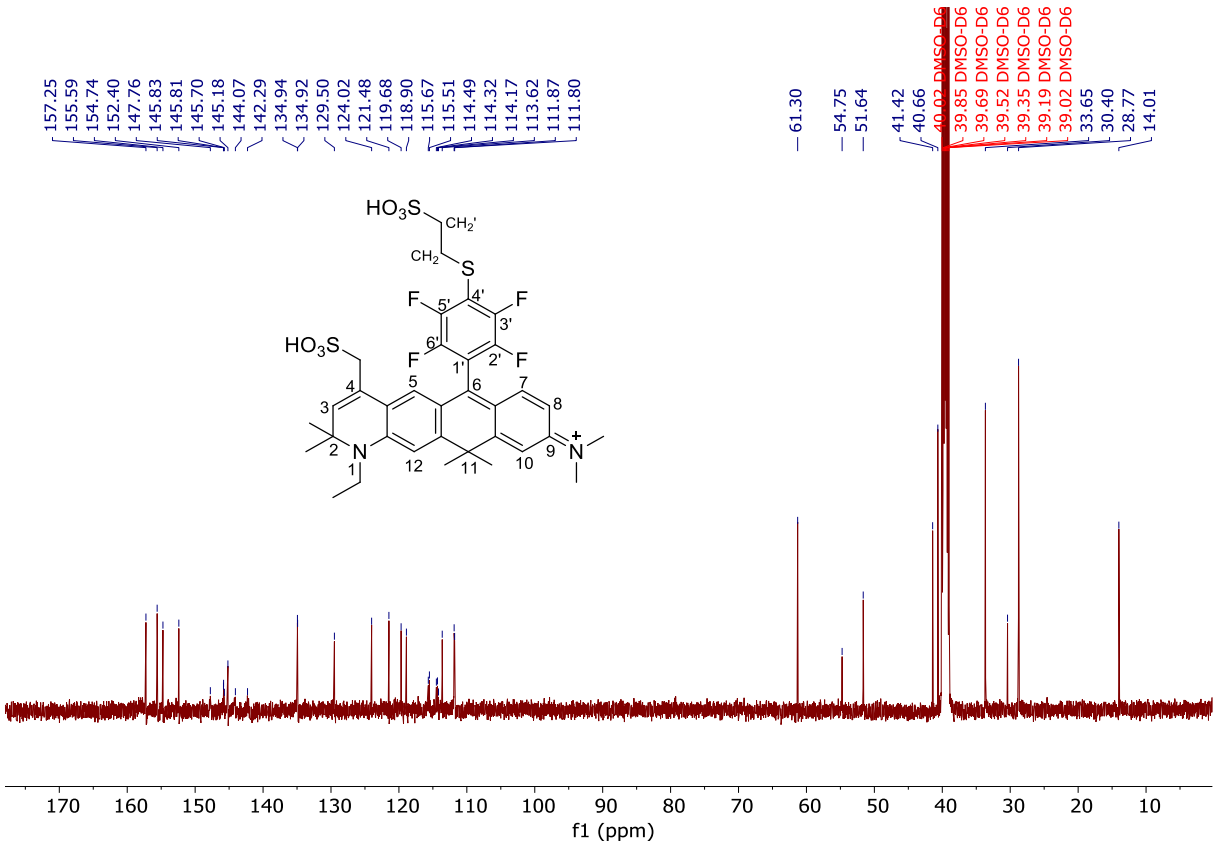

Figure S9. [13]C-NMR spectrum (125 MHz) of **AS 06** in DMSO-d_6.

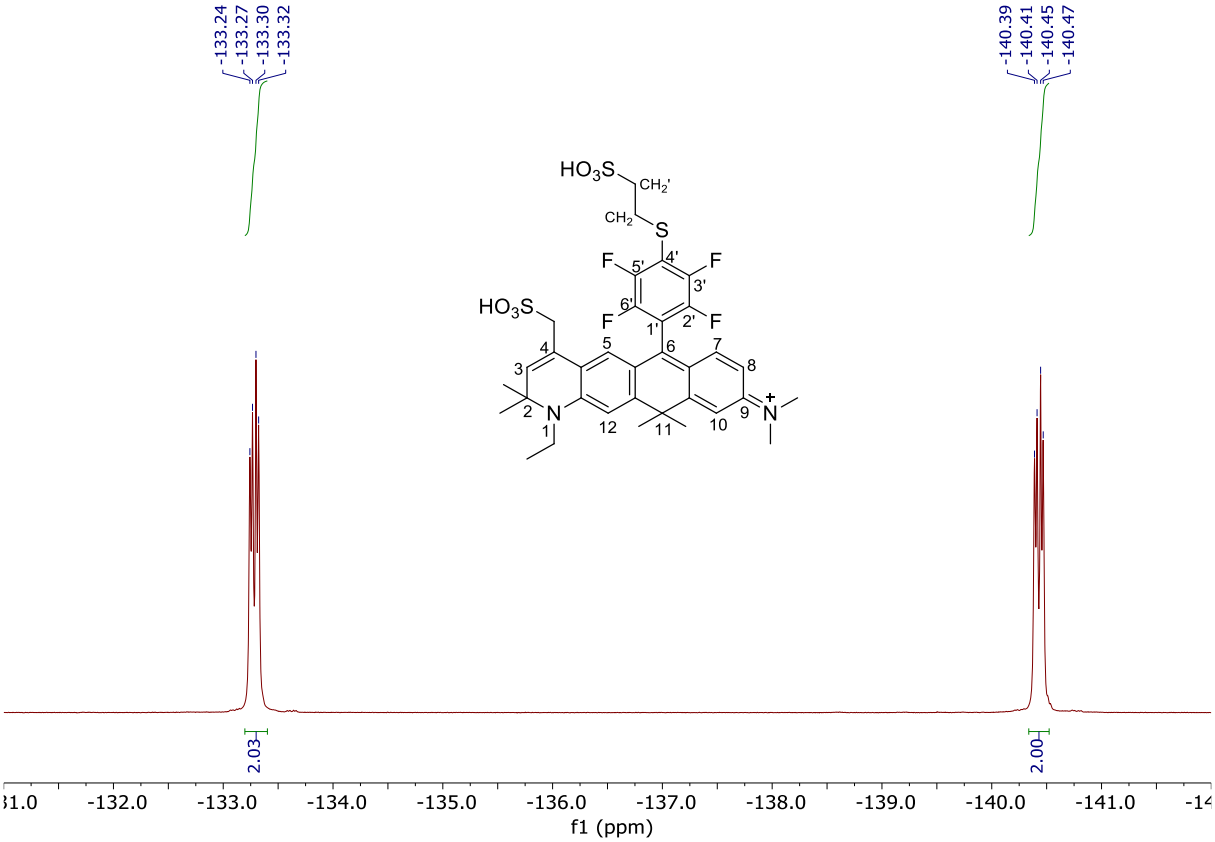

Figure S10. ^{19}F-NMR spectrum (470 MHz) of **AS 06** in DMSO-d_6.

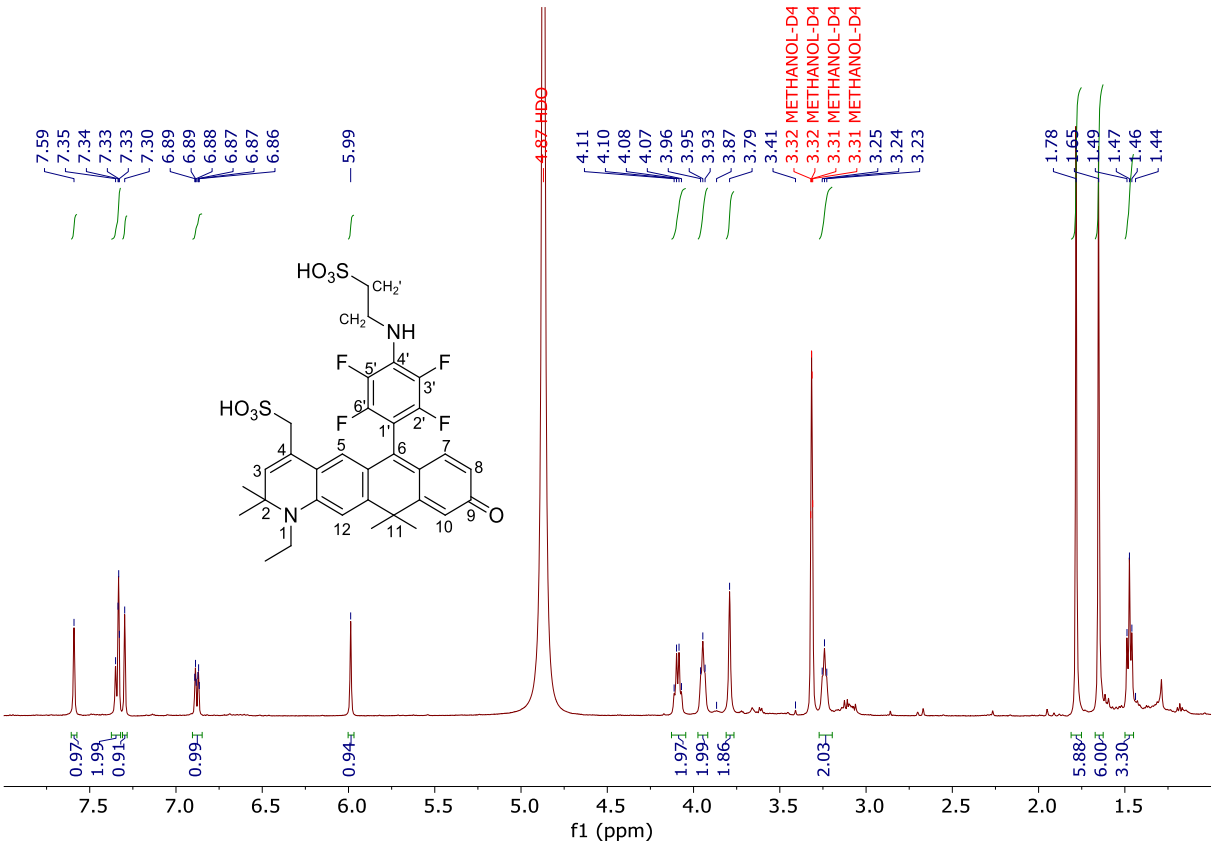

Figure S11. ^{1}H-NMR spectrum (500 MHz) of **AS 03** in CD_3OD.

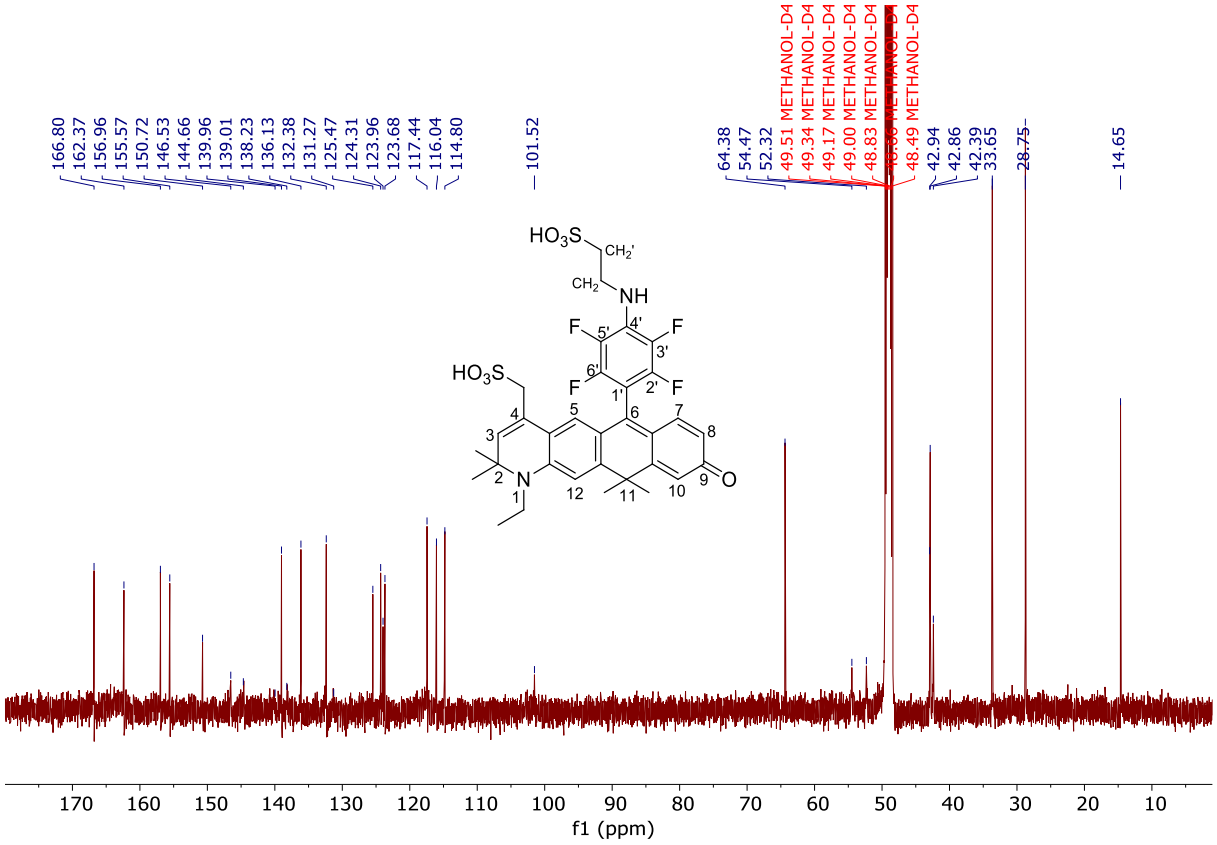

Figure S12. ^{13}C-NMR spectrum (125 MHz) of **AS 03** in CD_3OD.

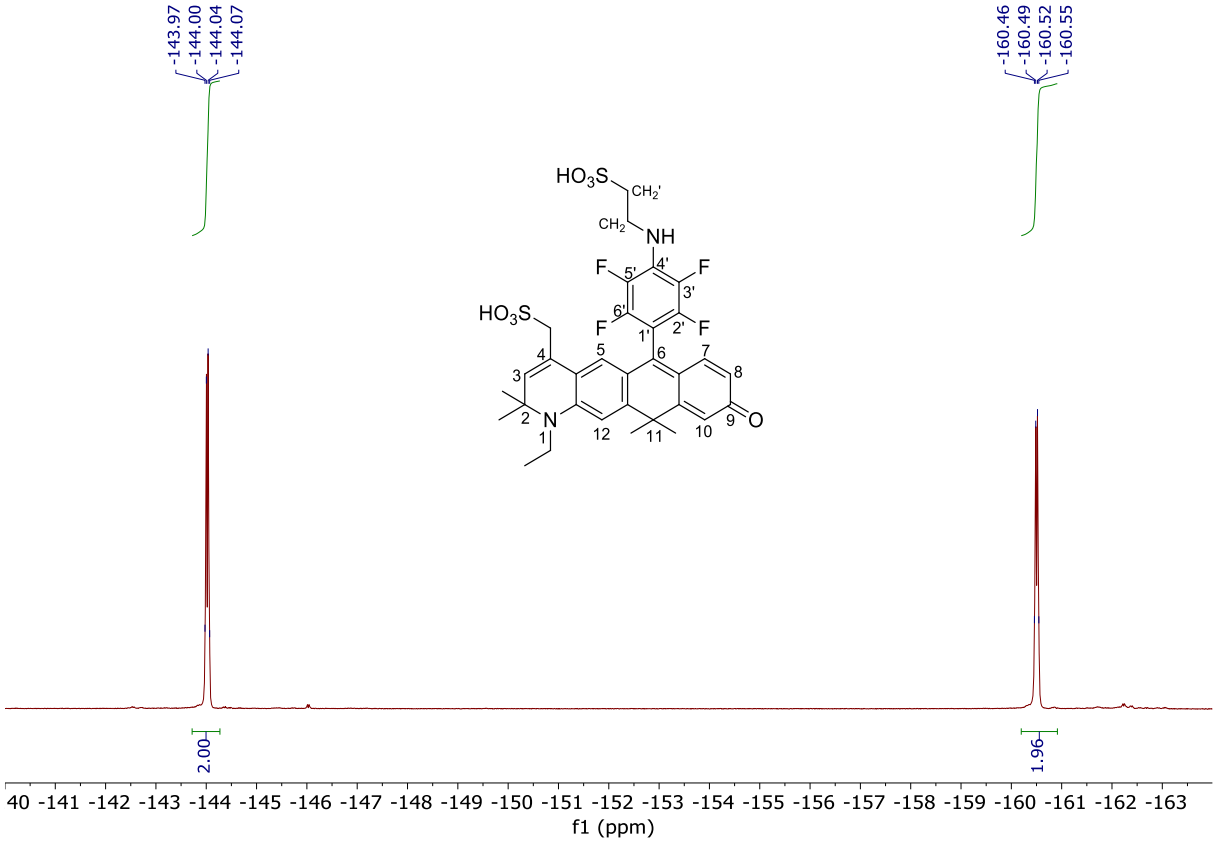

Figure S13. ^{19}F-NMR spectrum (470 MHz) of **AS 03** in CD_3OD.

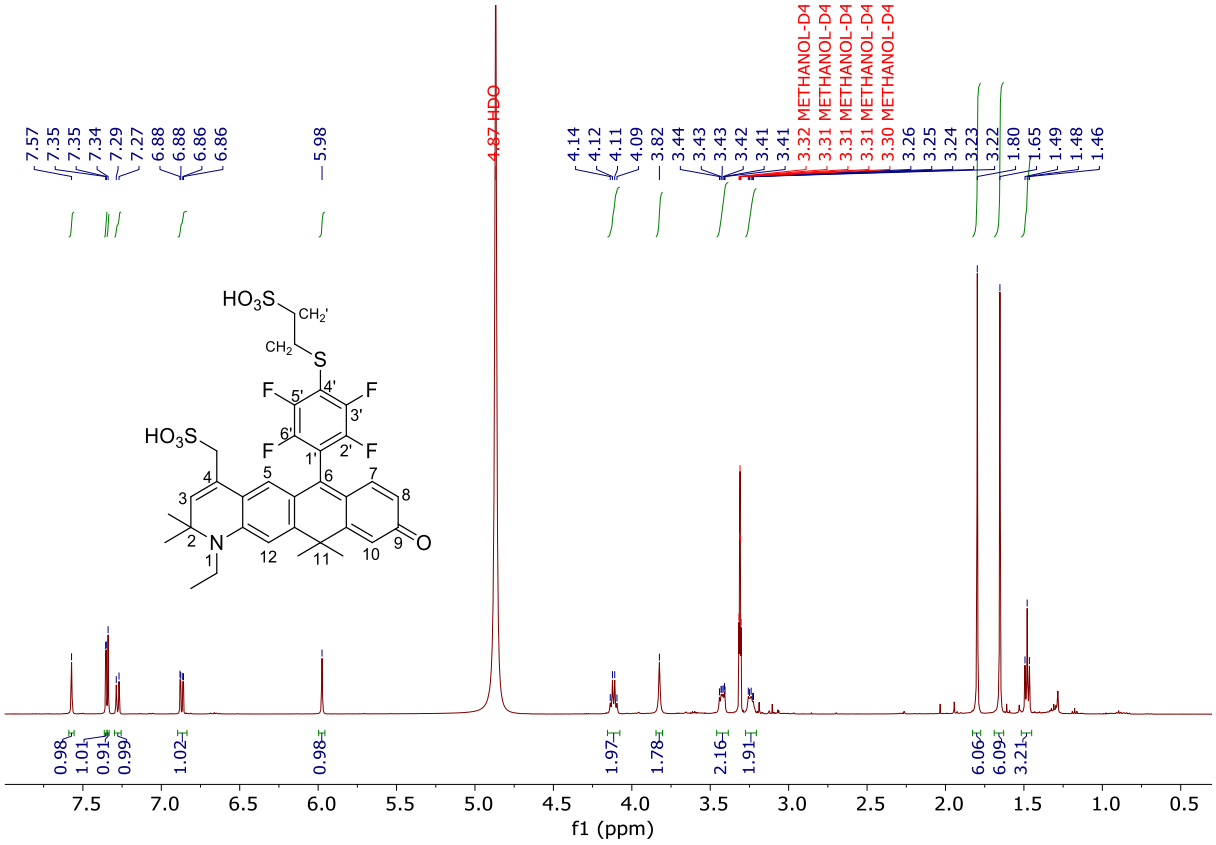

Figure S14. ^{1}H-NMR spectrum (500 MHz) of **AS 07** in CD_3OD.

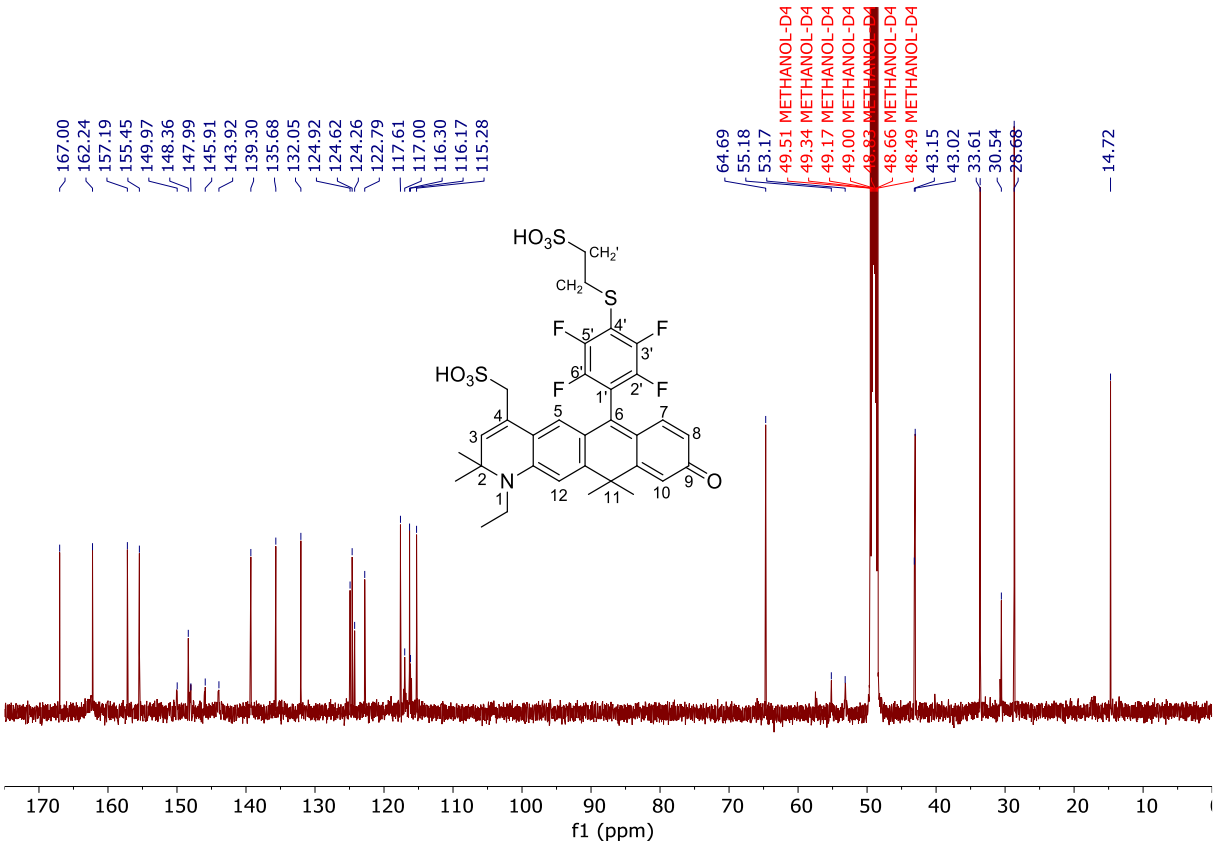

Figure S15. ^{13}C-NMR spectrum (125 MHz) of **AS 07** in CD_3OD.

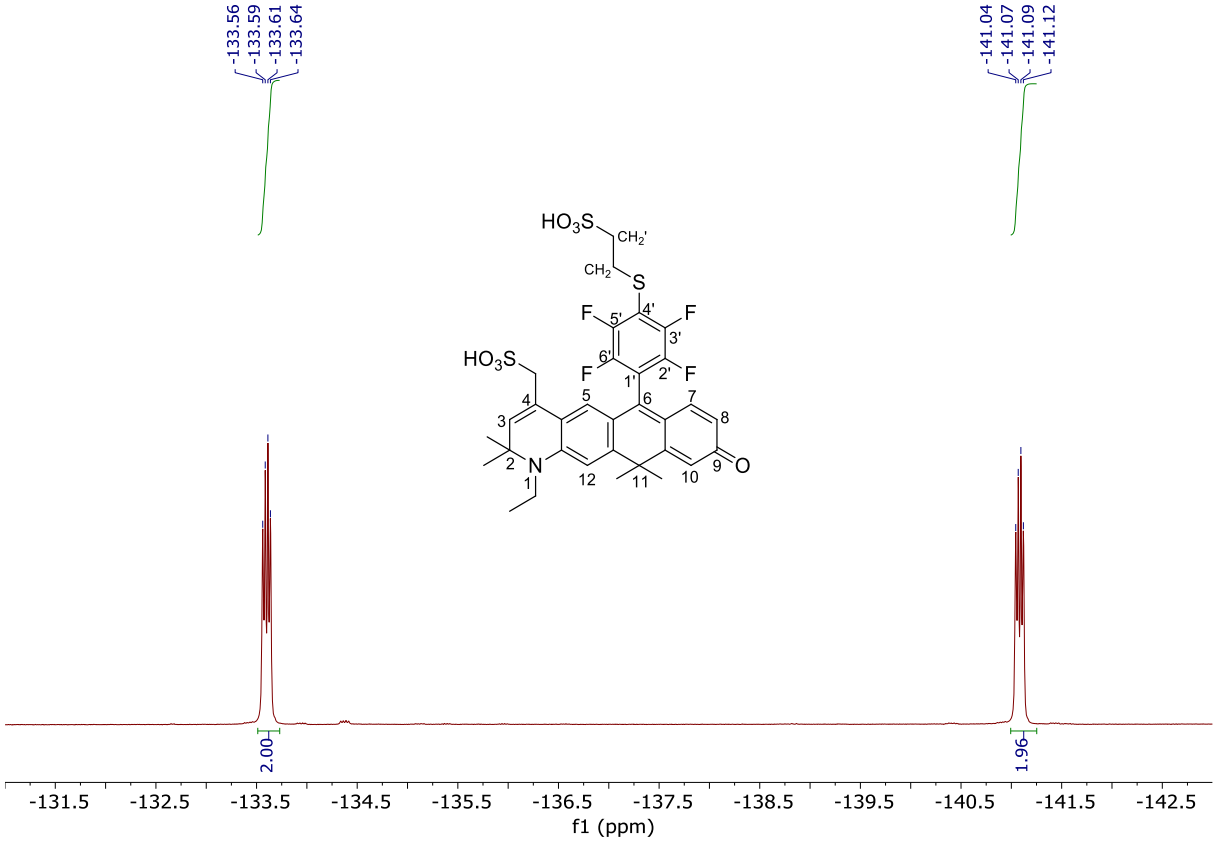

Figure S16. ^{19}F-NMR spectrum (470 MHz) of **AS 07** in CD_3OD.

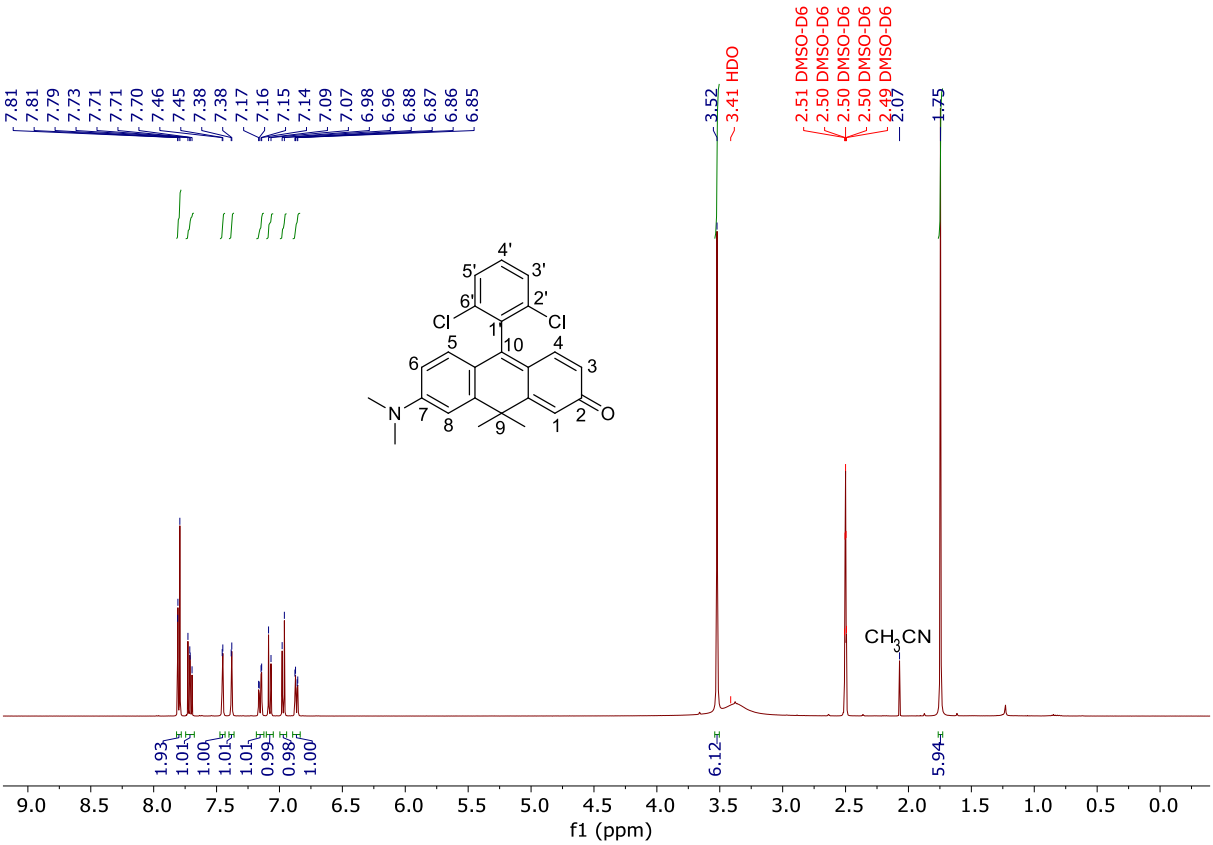

Figure S17. ^{1}H-NMR spectrum (500 MHz) of **AS 01** in DMSO-d_6.

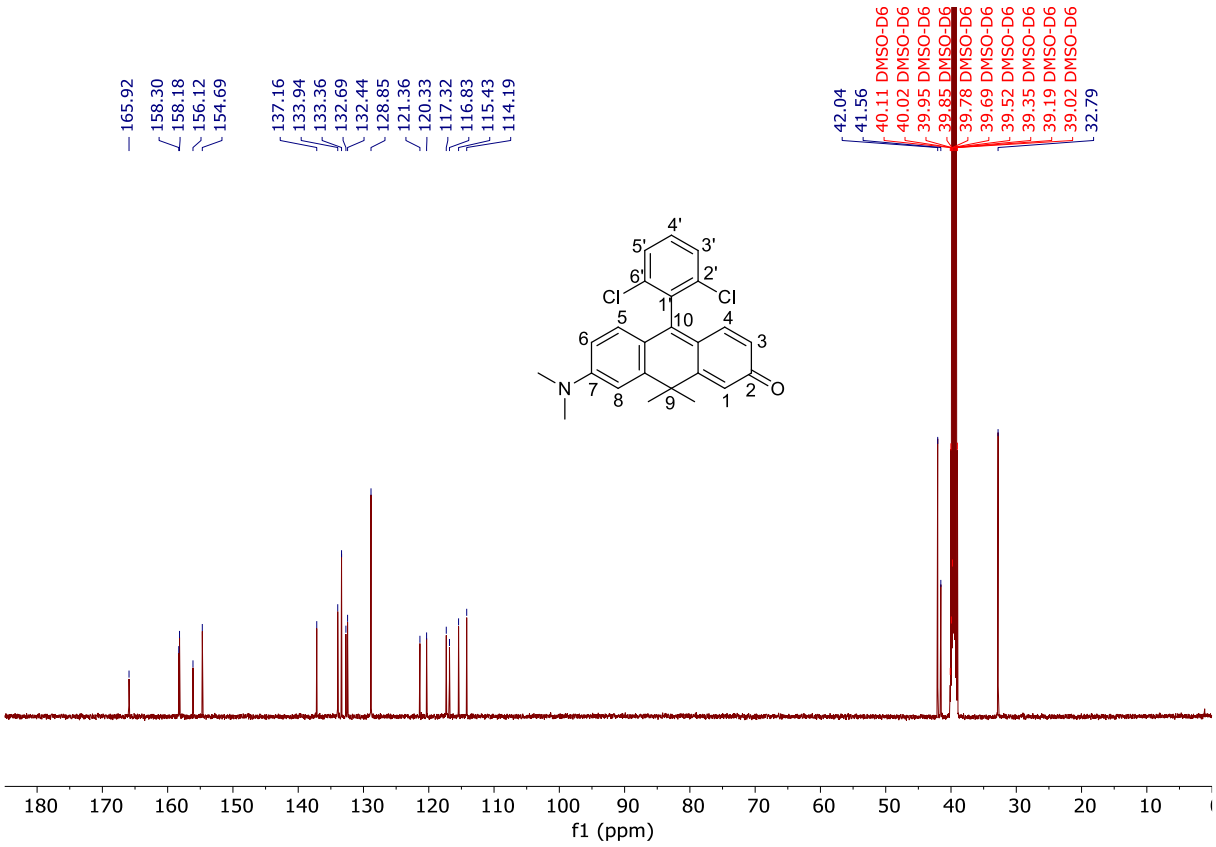

Figure S18. ^{13}C-NMR spectrum (125 MHz) of **AS 01** in DMSO-d_6.

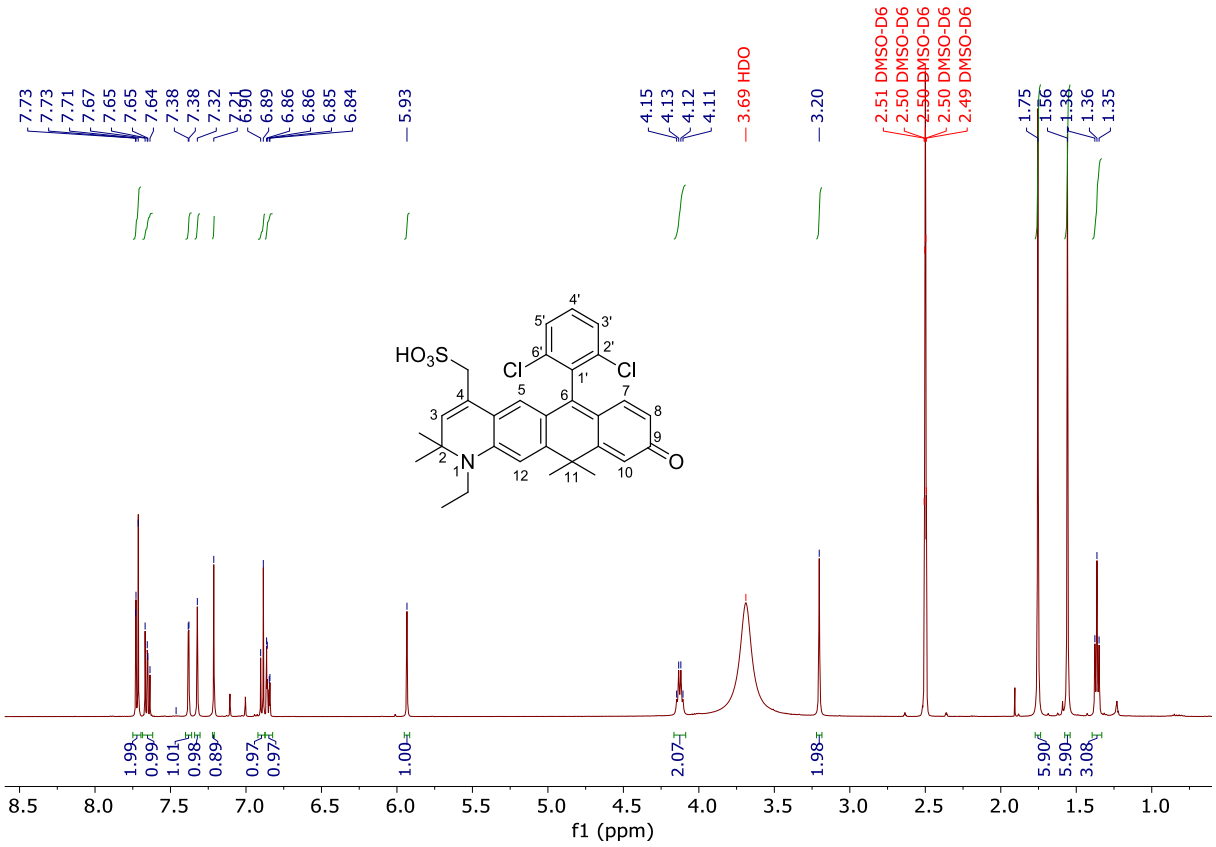

Figure S19. ^{1}H-NMR spectrum (500 MHz) of **AS 02** in DMSO-d_6.

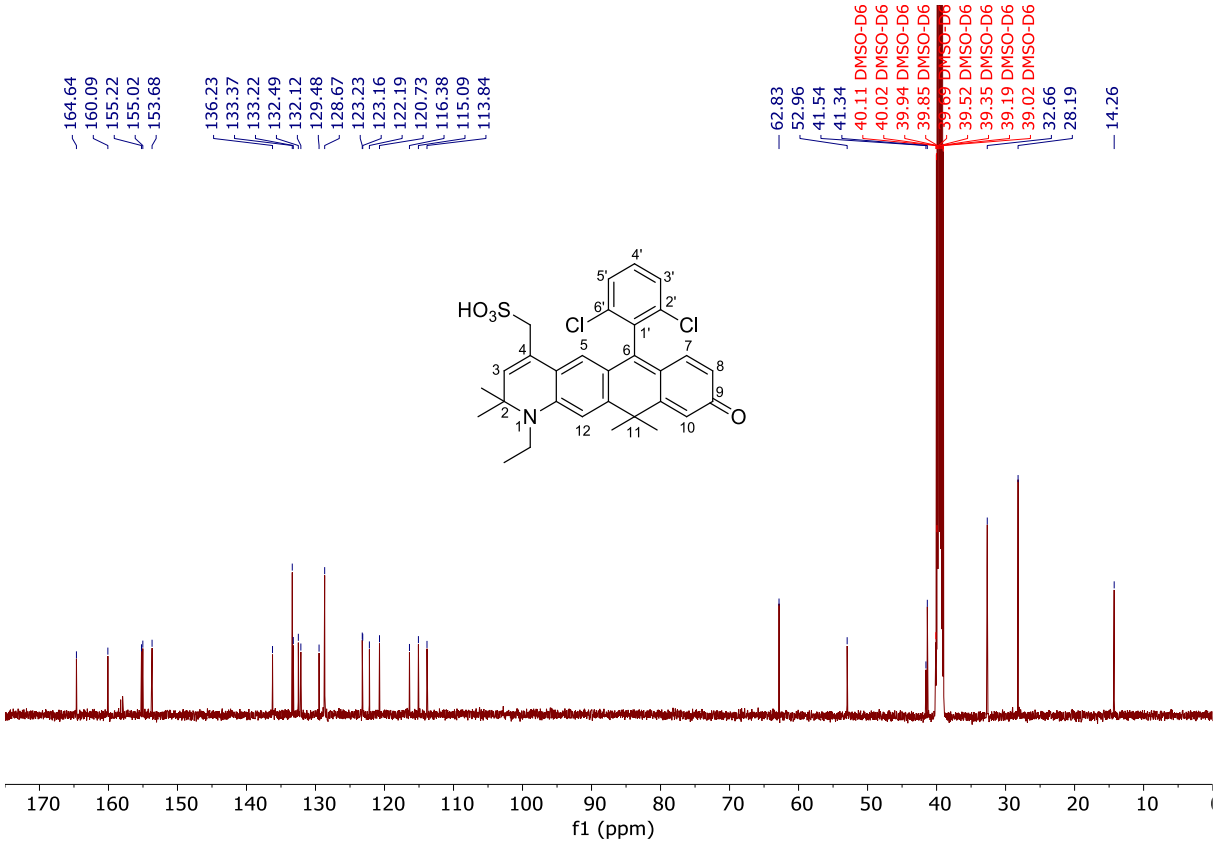

Figure S20. ^{13}C-NMR spectrum (125 MHz) of **AS 02** in DMSO-d_6.

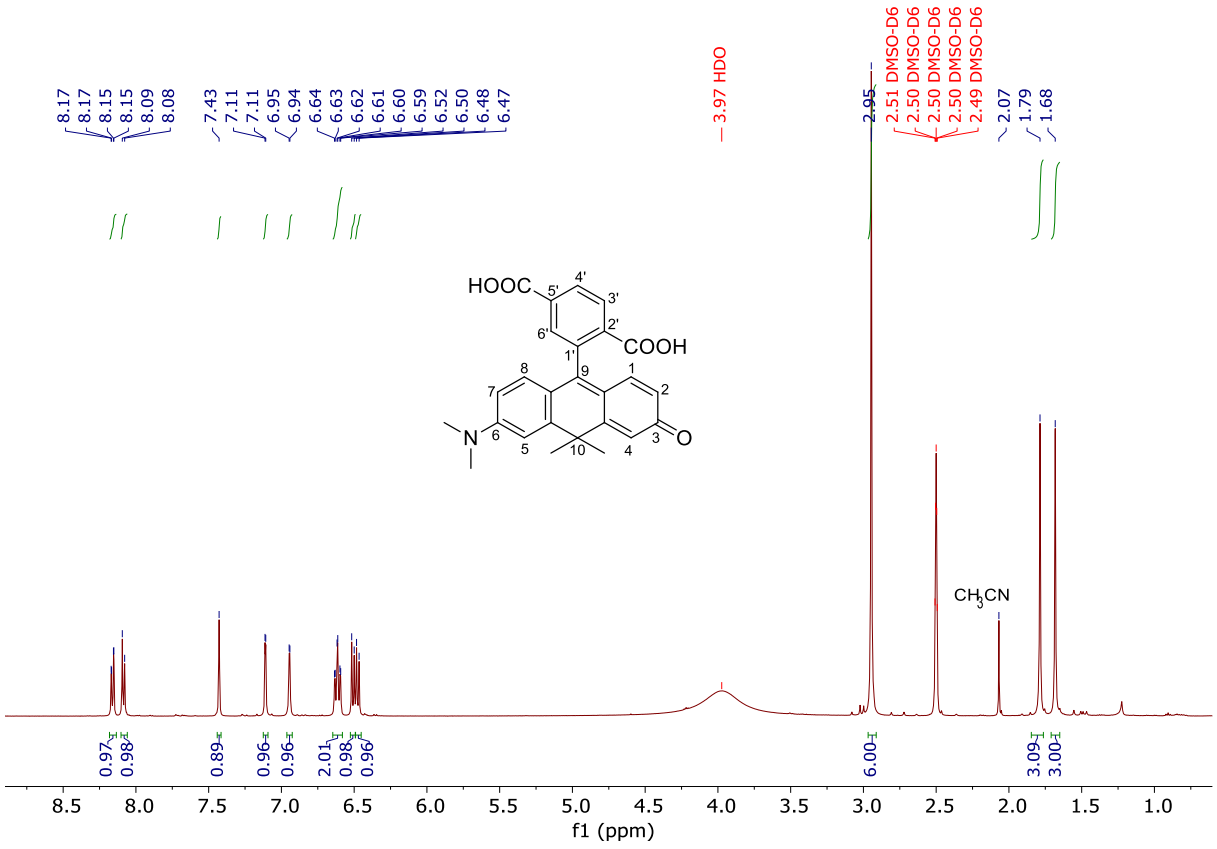

Figure S21. ^{1}H-NMR spectrum (500 MHz) of **AS 10** in DMSO-d_6.

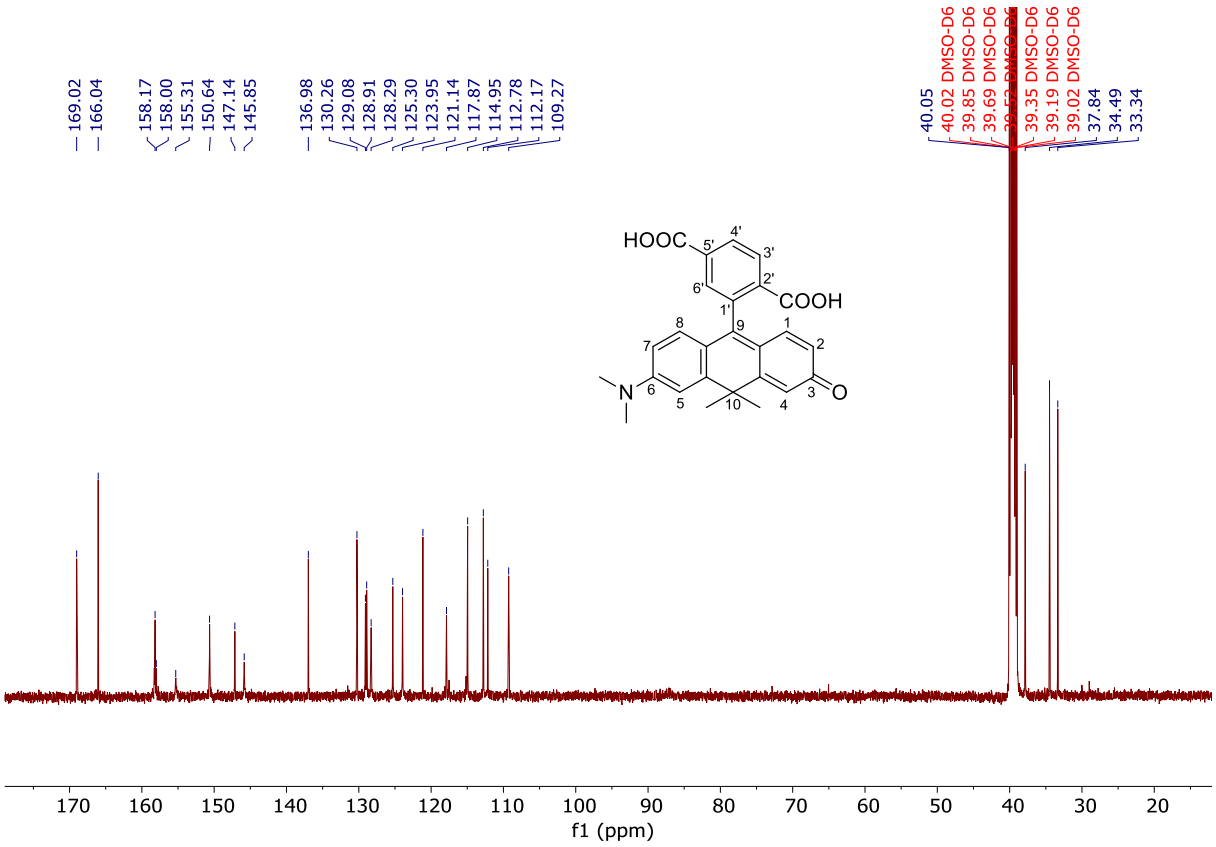

Figure S22. ^{13}C-NMR spectrum (125 MHz) of **AS 10** in DMSO-d_6.

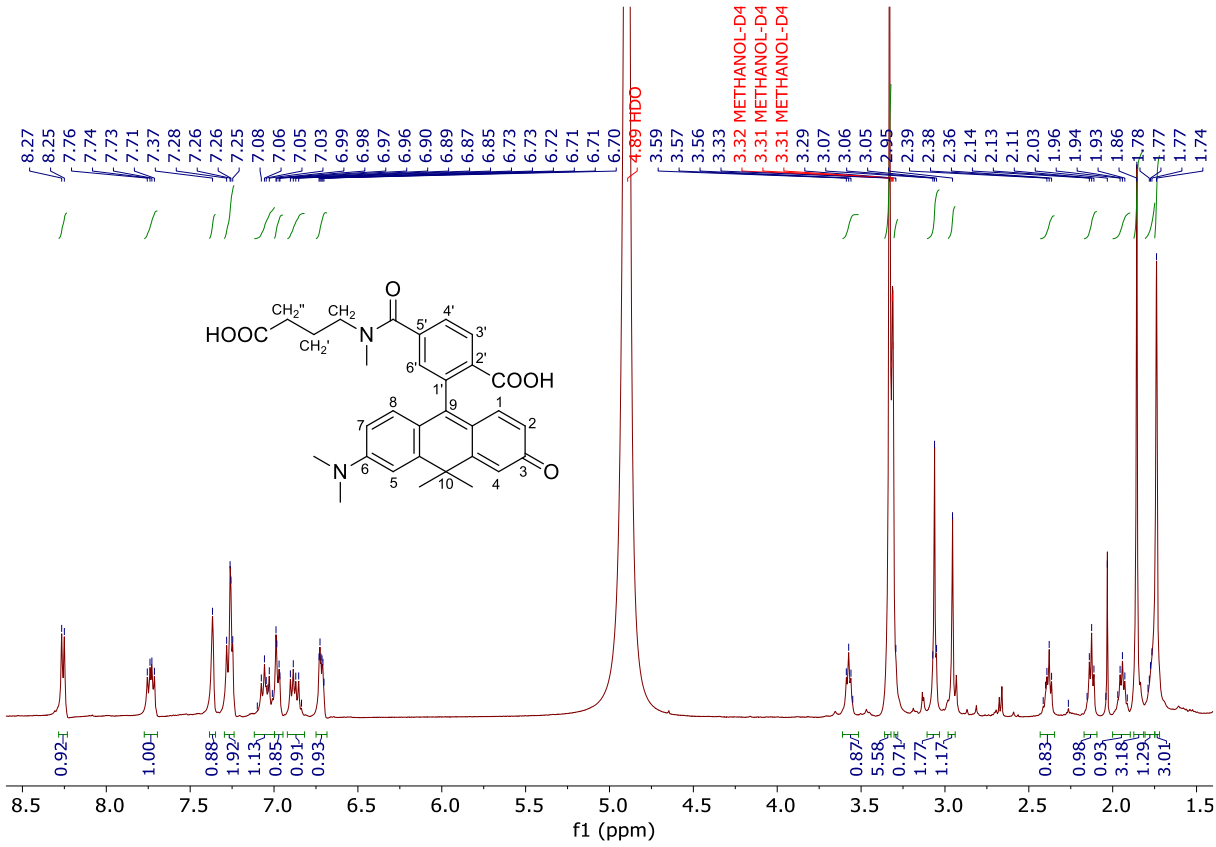

Figure S23. ^{1}H-NMR spectrum (500 MHz) of **AS 13** in CD_3OD.

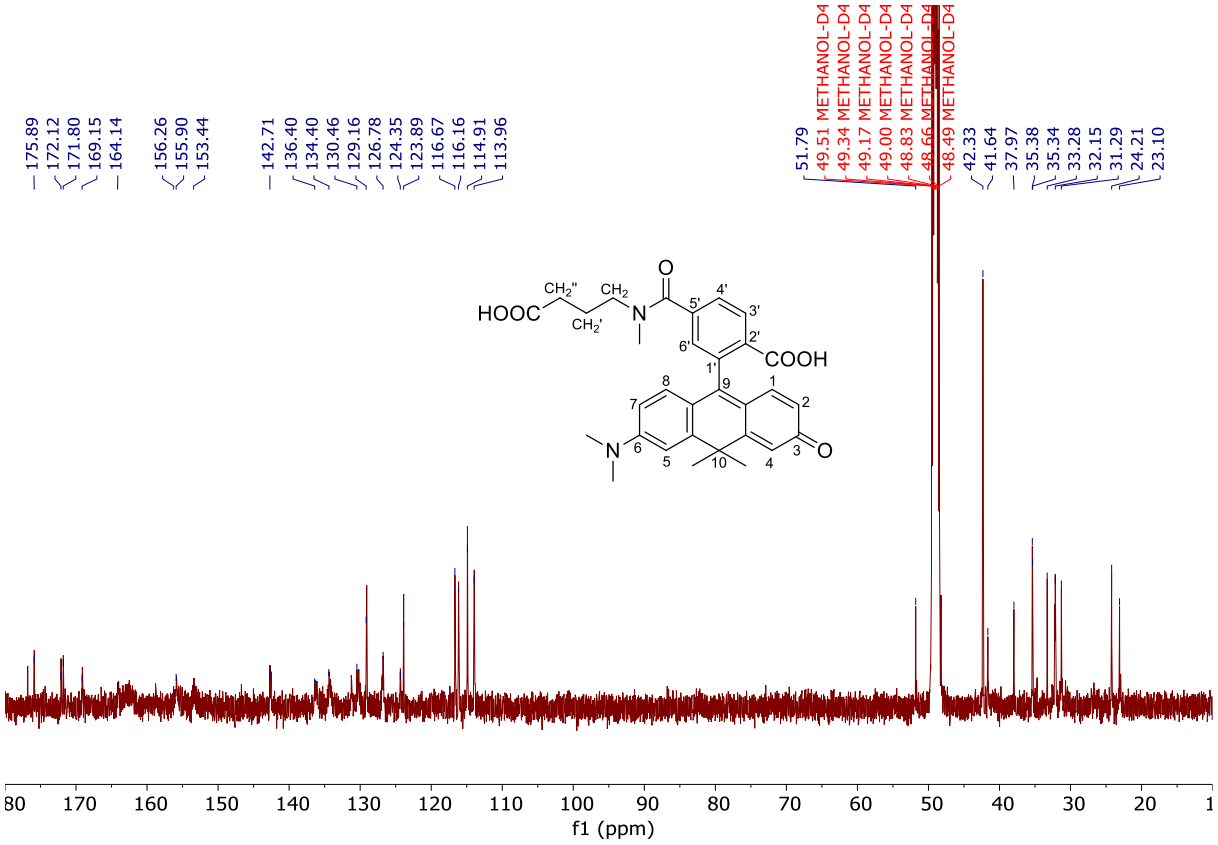

Figure S24. ^{13}C-NMR spectrum (125 MHz) of **AS 13** in CD_3OD.

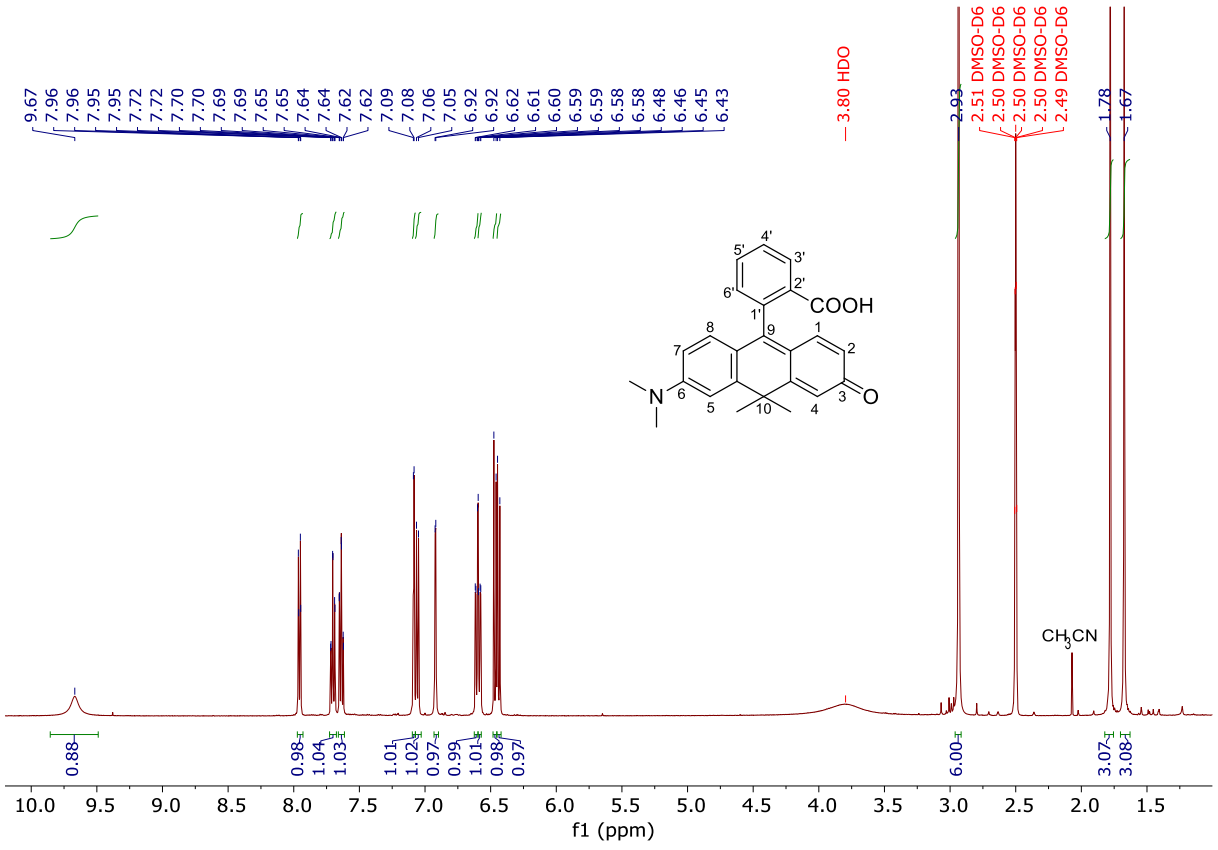

Figure S25. ^{1}H-NMR spectrum (500 MHz) of **AS 11** in DMSO-d_6.

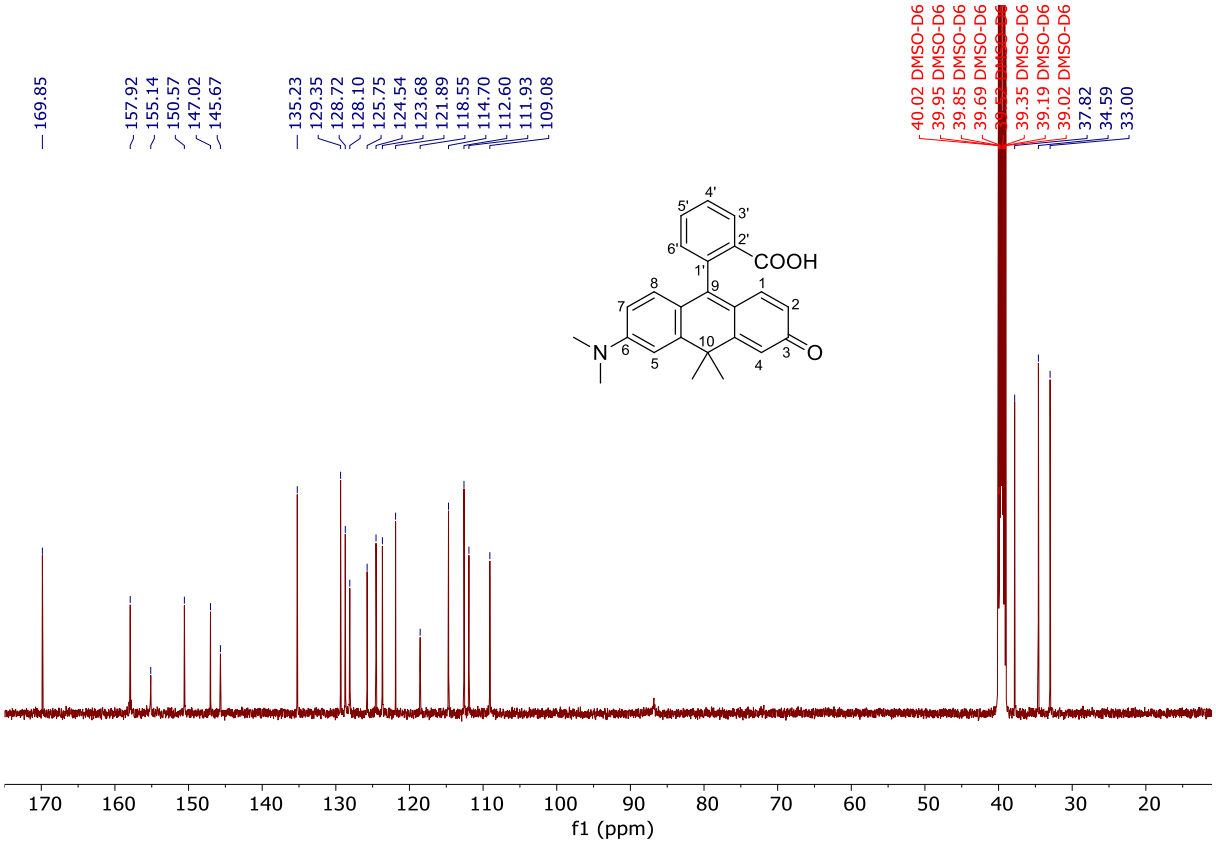

Figure S26. ^{13}C-NMR spectrum (125 MHz) of **AS 11** in DMSO-d_6.

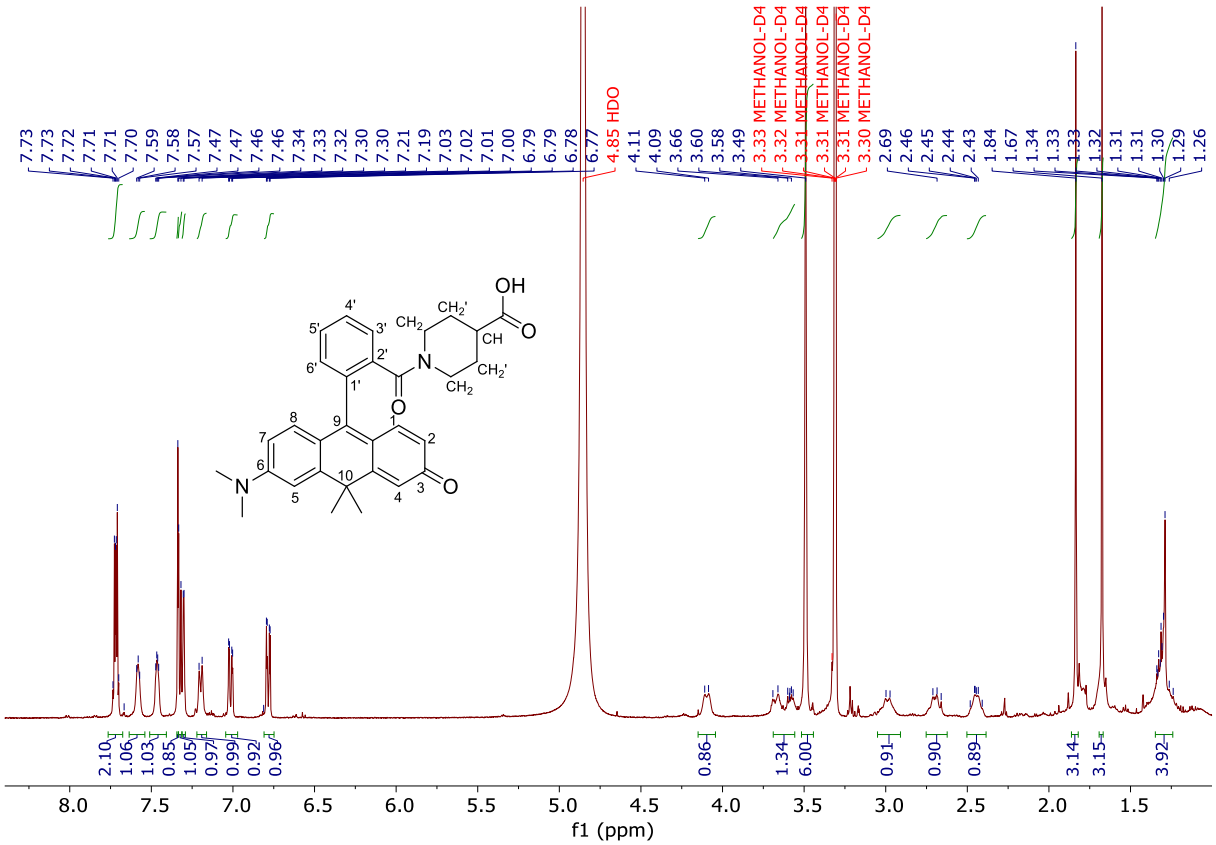

Figure S27. ^{1}H-NMR spectrum (500 MHz) of **AS 14** in CD_3OD.

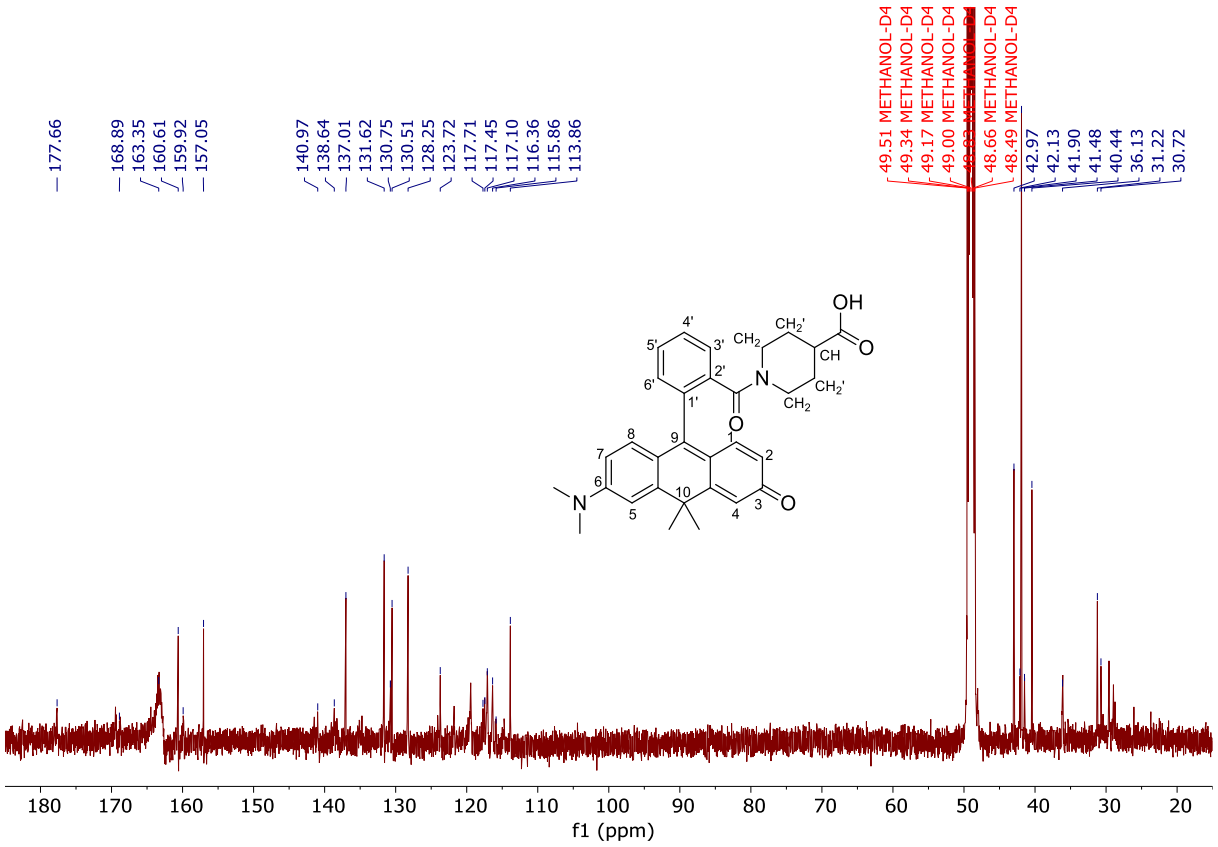

Figure S28. ^{13}C-NMR spectrum (125 MHz) of **AS 14** in CD_3OD.

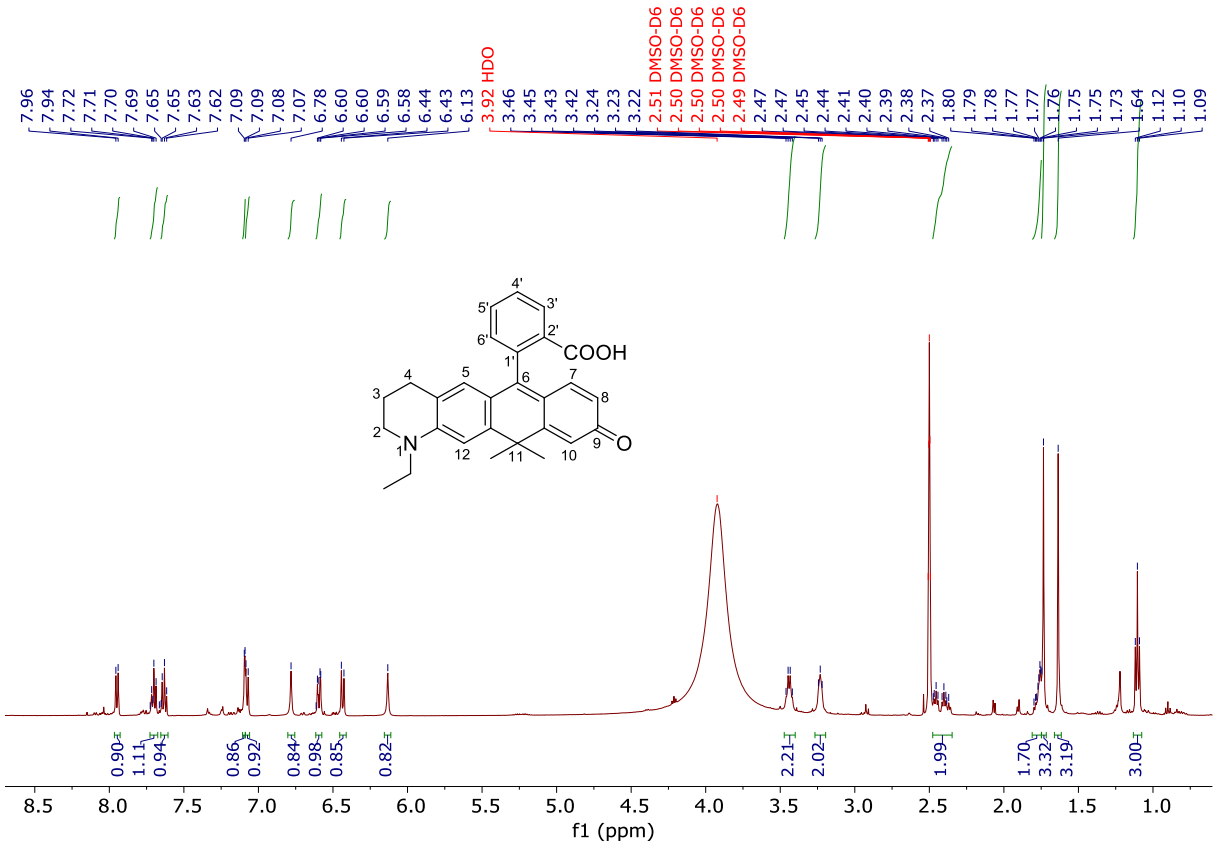

Figure S29. ^{1}H-NMR spectrum (500 MHz) of **AS 12** in DMSO-d_6.

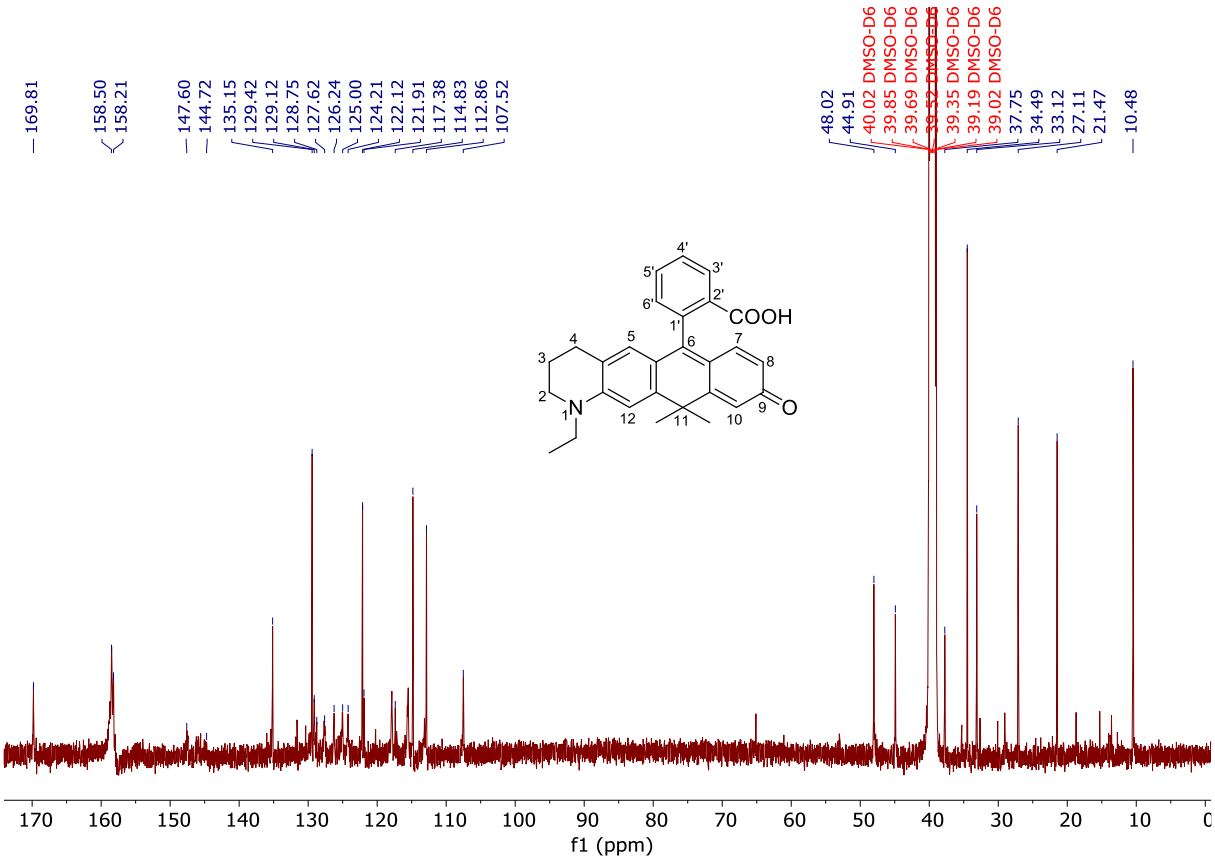

Figure S30. ^{13}C-NMR spectrum (125 MHz) of **AS 12** in DMSO-d_6.

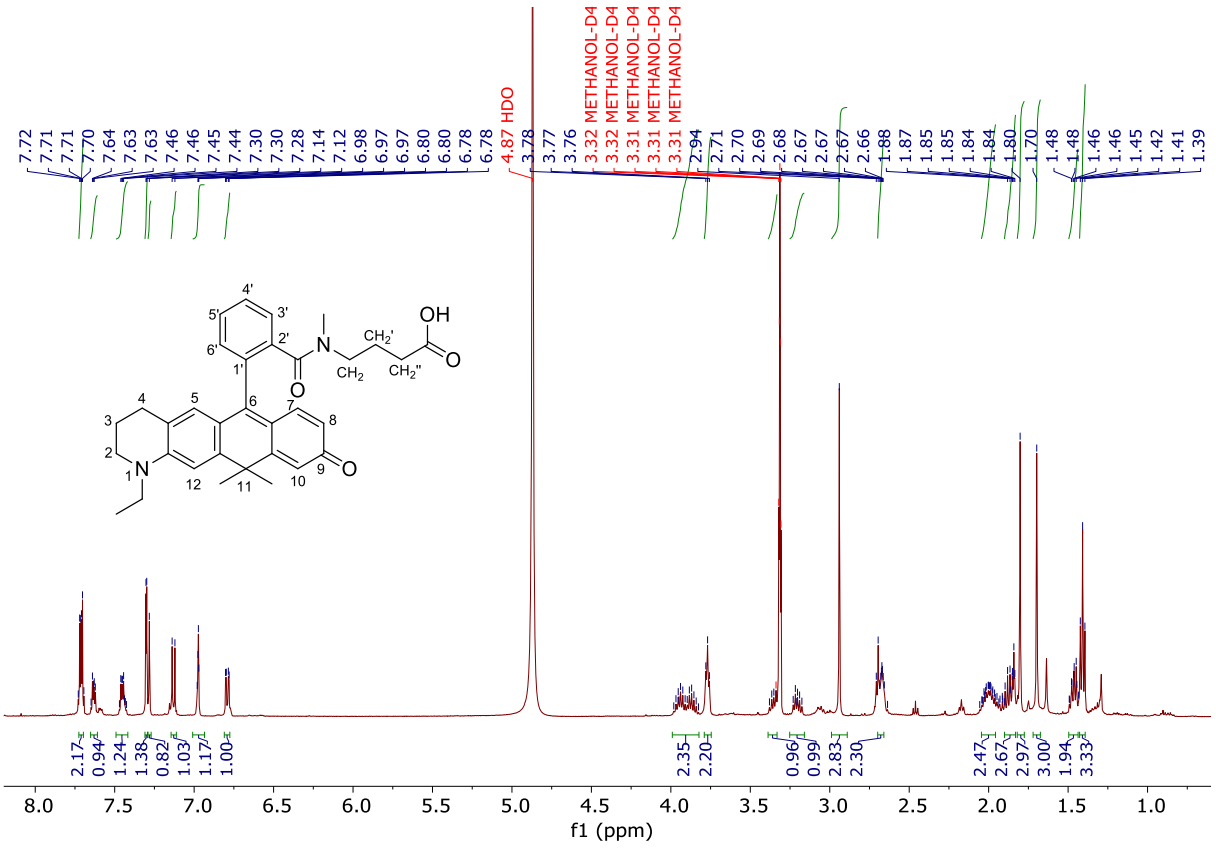

Figure S31. ^{1}H-NMR spectrum (500 MHz) of **AS 15** in CD_3OD.

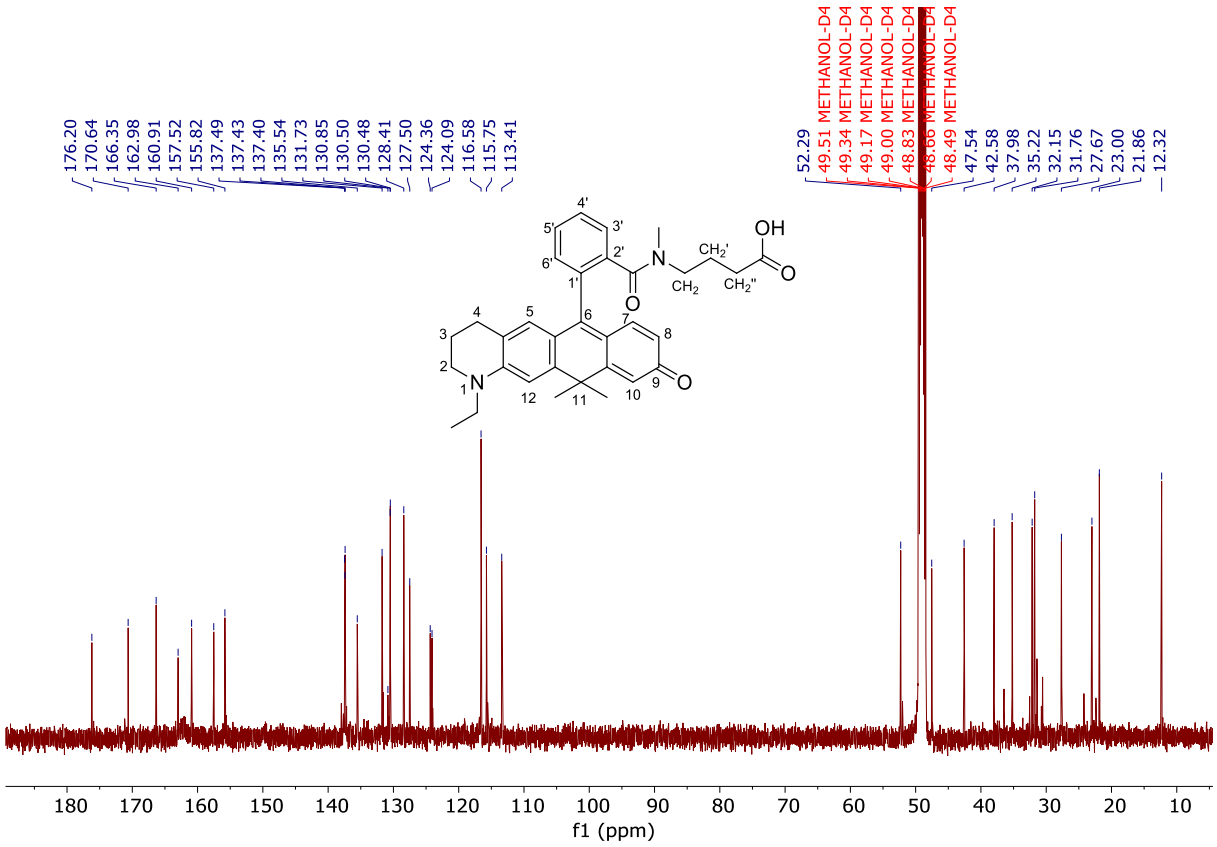

Figure S32. ^{13}C-NMR spectrum (125 MHz) of **AS 15** in CD_3OD.

Chapter 4: pH-Dependent Photophysical Properties of Carborhodol Dyes

pH-dependent Absorption Spectra

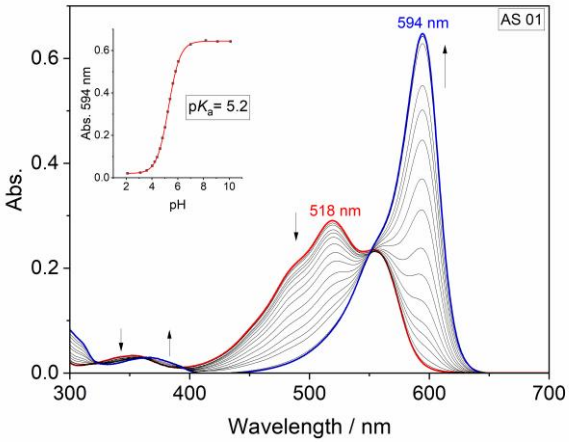

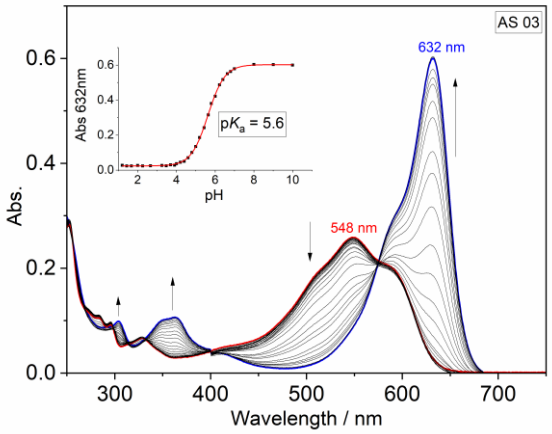

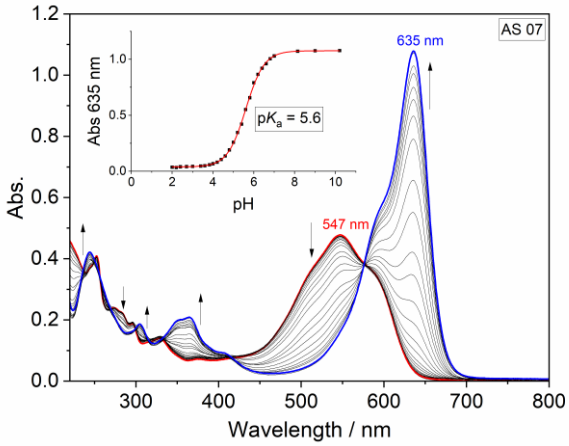

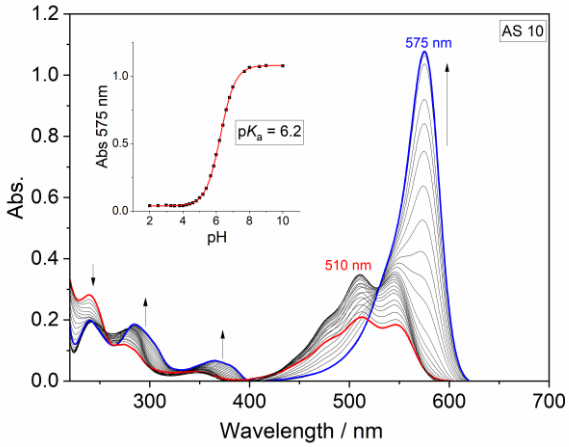

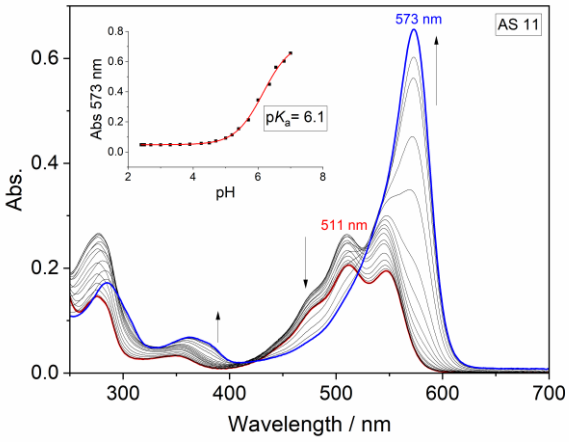

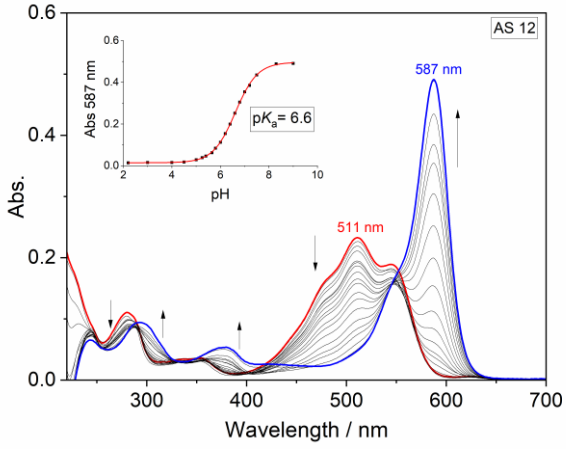

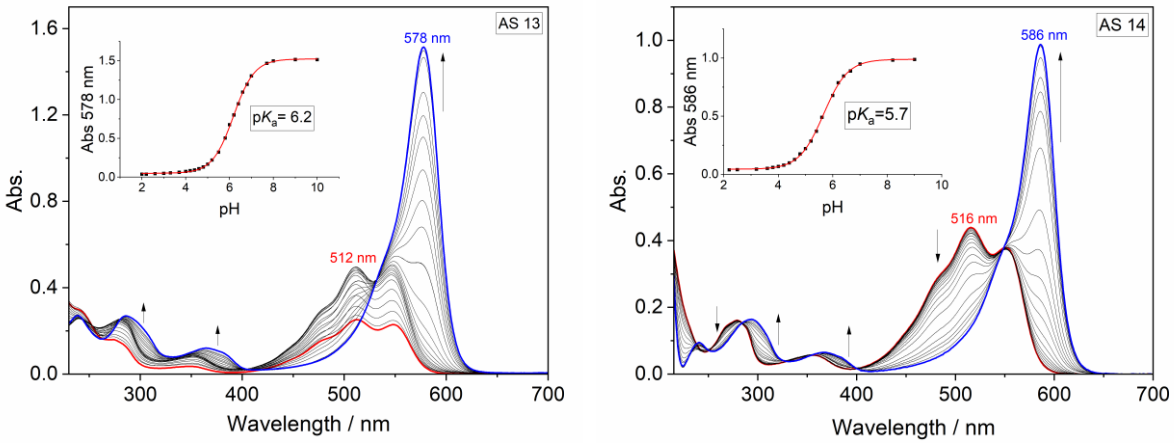

Figure S1. pH-dependent absorption spectra of **AS 01, AS 03, AS 07, AS 10, AS 11, AS 12, AS 13,** and **AS 14**. Arrows indicate the development of bands with increasing pH value of the solution. Inset: Absorbance at long wavelength absorption maxima as a function of pH. The red line denotes the best fit of the experimental data to the theoretical isotherm of a weak acid; pK_a is determined from this plot.

Fluorescence Turn-On Ratio in Buffer

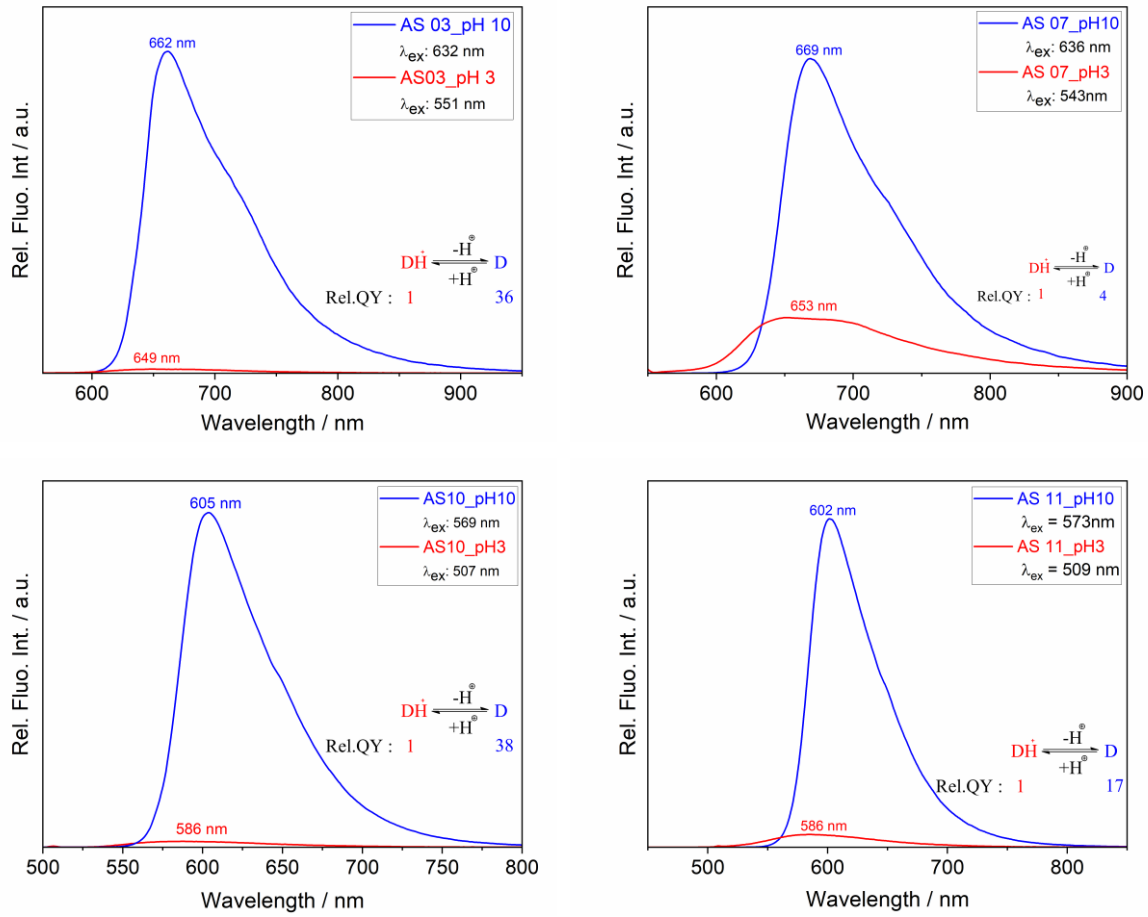

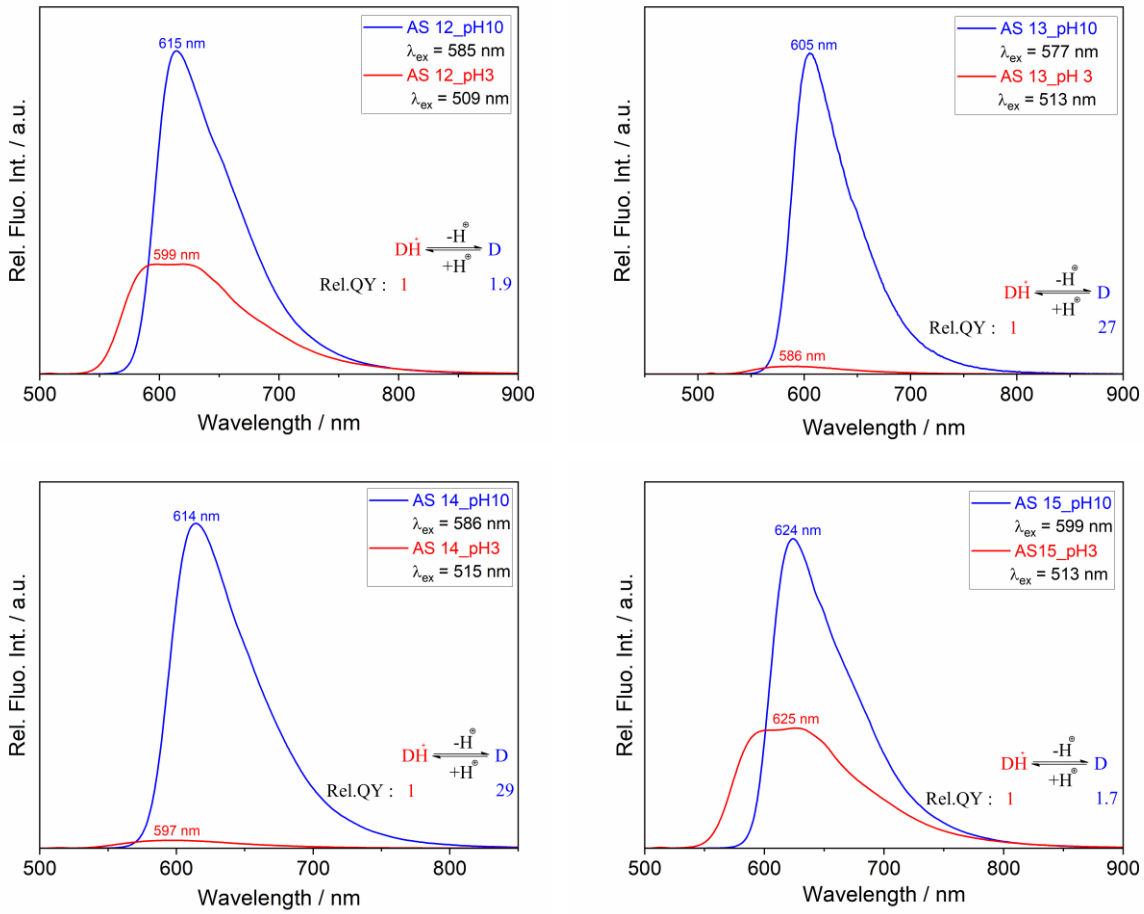

Figure S2. Fluorescence spectra of **AS 03, AS 07, AS 10, AS 11, AS 12, AS 13, AS 14,** and **AS 15** recorded in aqueous buffer at pH 10 (blue trace) and pH 3 (red trace). Both acidic and basic forms are excited at their respective absorption maxima. For each pair (acidic and basic forms), the absorbance was adjusted to a constant value in the range of 0.04-0.05 in a 1 cm cuvette, at the excitation wavelength.

Fluorescence Turn-On Ratio in EtOH

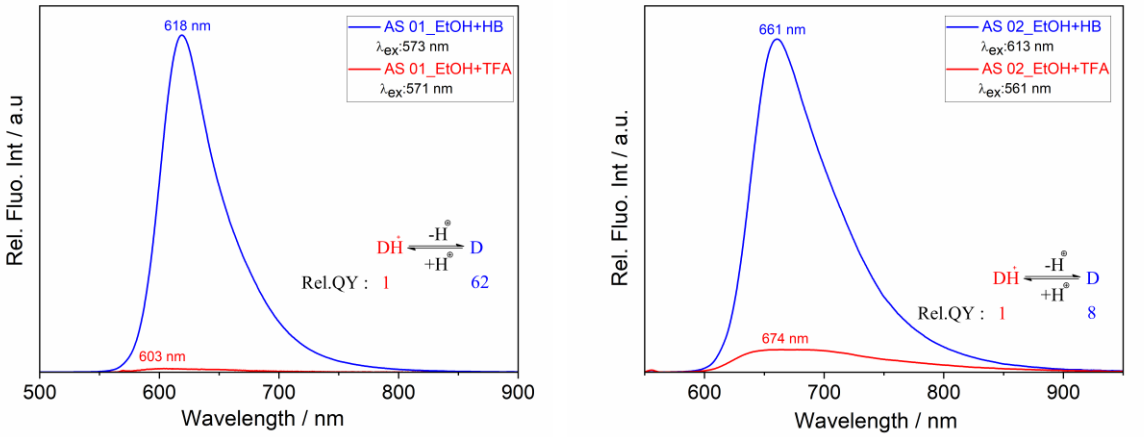

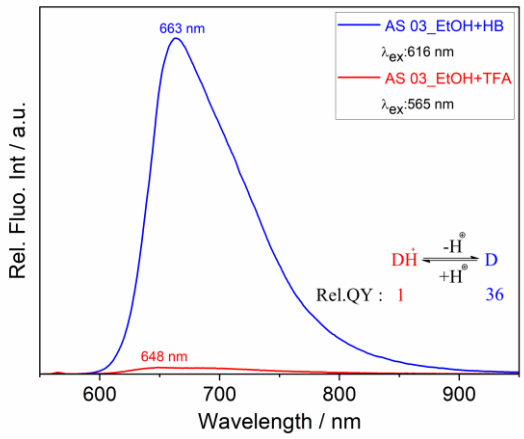
AS 03_EtOH+HB
λex:616 nm
AS 03_EtOH+TFA
λex:565 nm
663 nm
648 nm
DH• -H⊕ D
+H⊕
Rel.QY : 1 36
Rel. Fluo. Int / a.u.
Wavelength / nm

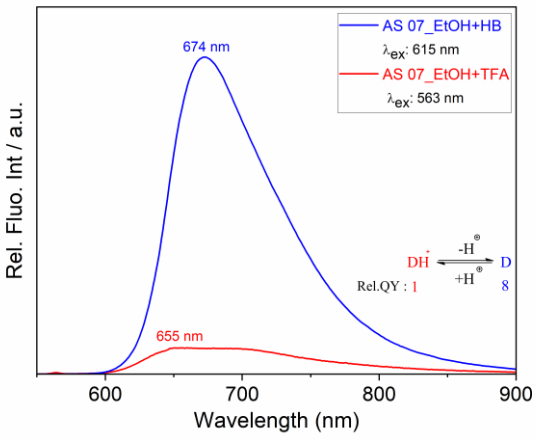
AS 07_EtOH+HB
λex: 615 nm
AS 07_EtOH+TFA
λex: 563 nm
674 nm
655 nm
DH• -H⊕ D
+H⊕
Rel.QY : 1 8
Rel. Fluo. Int / a.u.
Wavelength (nm)

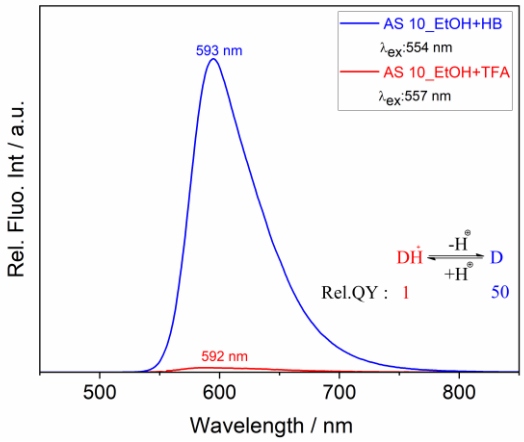
AS 10_EtOH+HB
λex:554 nm
AS 10_EtOH+TFA
λex:557 nm
593 nm
592 nm
DH• -H⊕ D
+H⊕
Rel.QY : 1 50
Rel. Fluo. Int / a.u.
Wavelength / nm

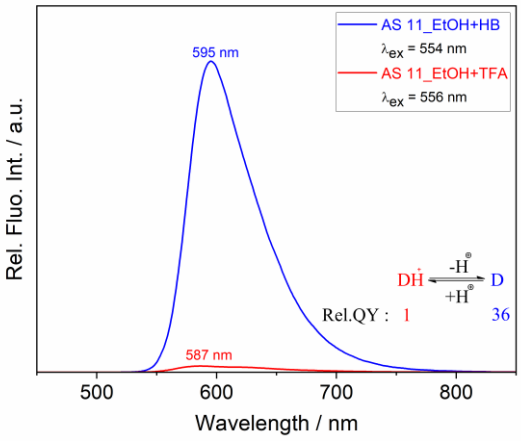
AS 11_EtOH+HB
λex = 554 nm
AS 11_EtOH+TFA
λex = 556 nm
595 nm
587 nm
DH• -H⊕ D
+H⊕
Rel.QY : 1 36
Rel. Fluo. Int. / a.u.
Wavelength / nm

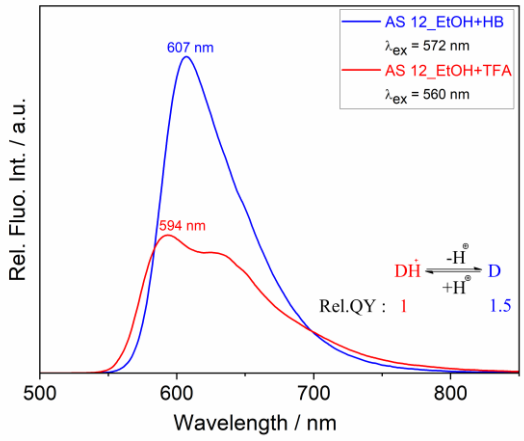
AS 12_EtOH+HB
λex = 572 nm
AS 12_EtOH+TFA
λex = 560 nm
607 nm
594 nm
DH• -H⊕ D
+H⊕
Rel.QY : 1 1.5
Rel. Fluo. Int. / a.u.
Wavelength / nm

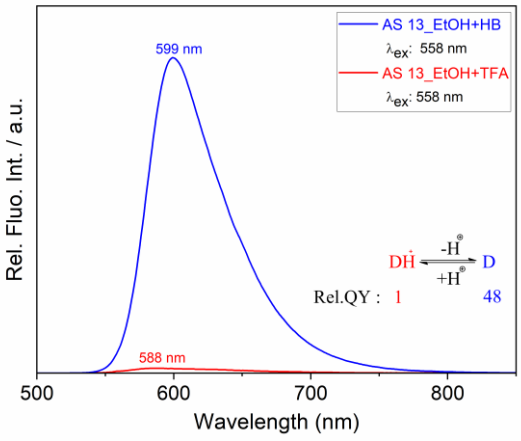
AS 13_EtOH+HB
λex: 558 nm
AS 13_EtOH+TFA
λex: 558 nm
599 nm
588 nm
DH• -H⊕ D
+H⊕
Rel.QY : 1 48
Rel. Fluo. Int. / a.u.
Wavelength (nm)

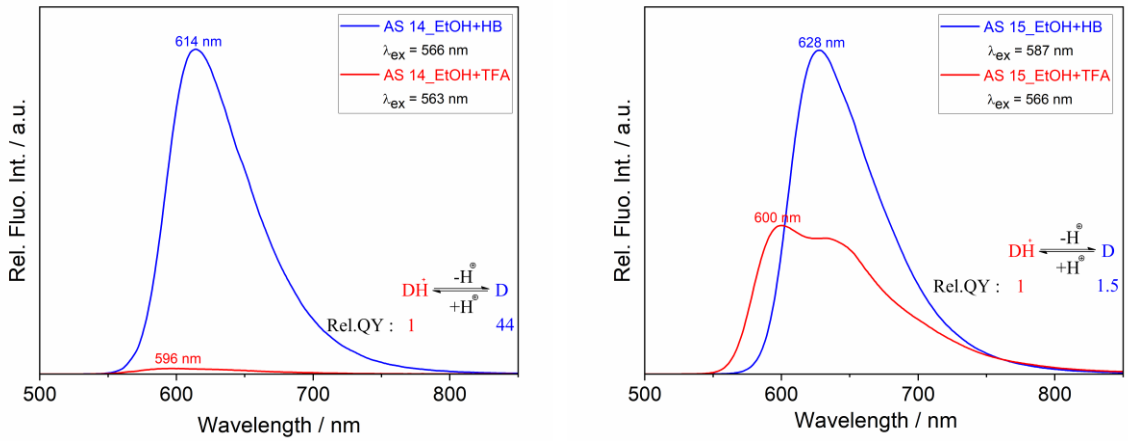

Figure S3. Fluorescence spectra of **AS 01**, **AS 02**, **AS 03, AS 07, AS 10, AS 11, AS 12, AS 13, AS 14,** and **AS 15** recorded in aqueous basic (blue trace) and acidic (red trace) EtOH. Both acidic and basic forms excited at their respective absorption maxima. For each pair (acidic and basic forms), the absorbance was adjusted to a constant value in the range of 0.04-0.05 in a 1 cm cuvette, at the excitation wavelength.

Photostability Assessment in Buffer

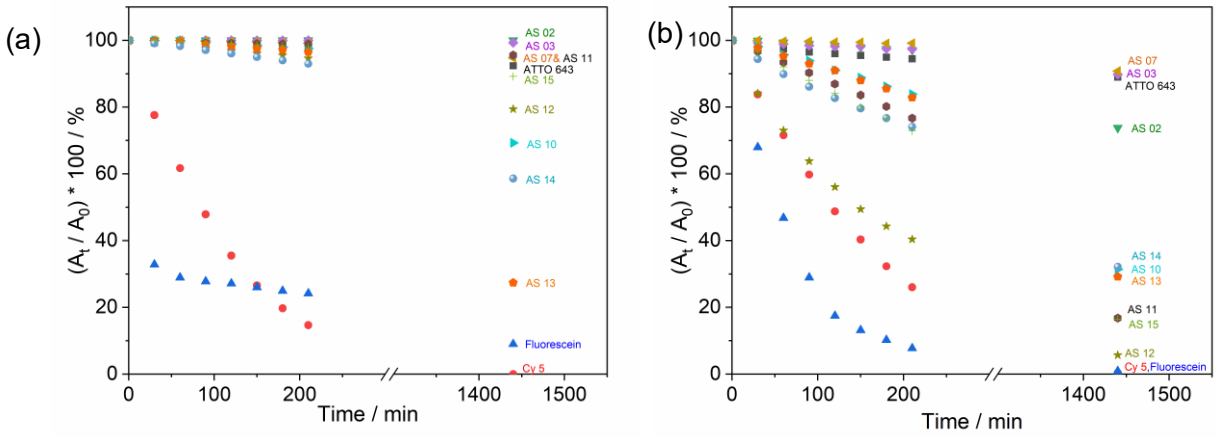

Figure S4. Photostability profile of the acidic form (a) and the basic form (b) in pH 3 and pH 10 buffer, respectively, over 1440 minutes of Irradiation (575 W mercury halide lamp).

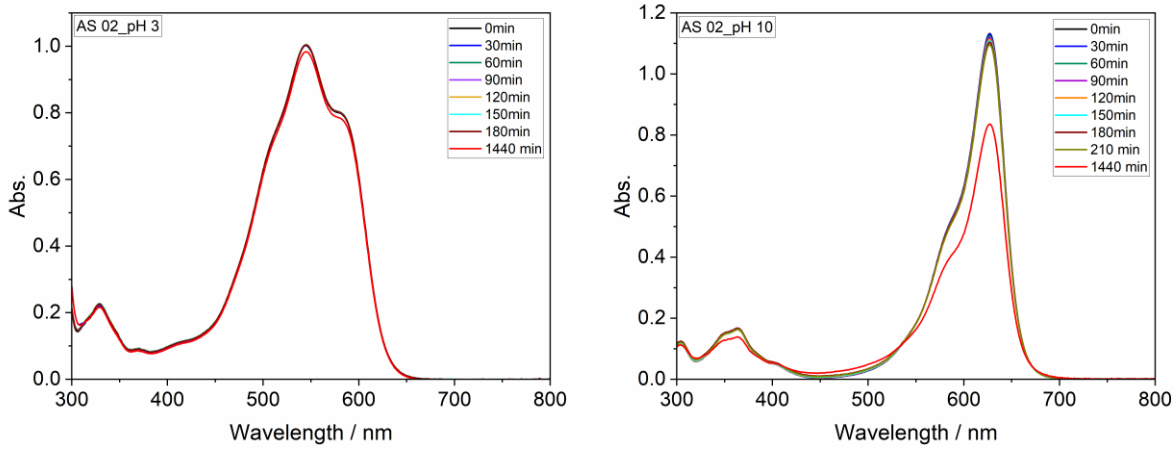

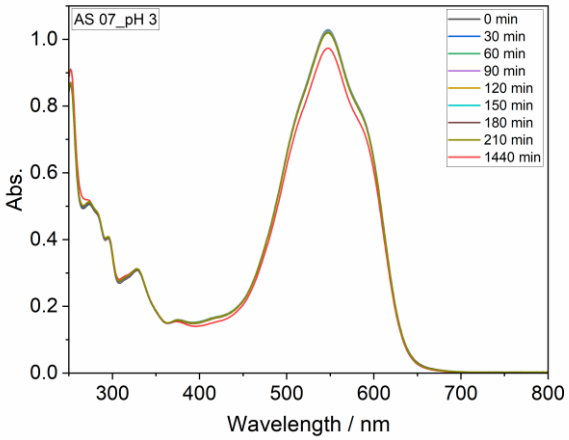
AS 07_pH 3
0 min
30 min
60 min
90 min
120 min
150 min
180 min
210 min
1440 min
Abs.
Wavelength / nm

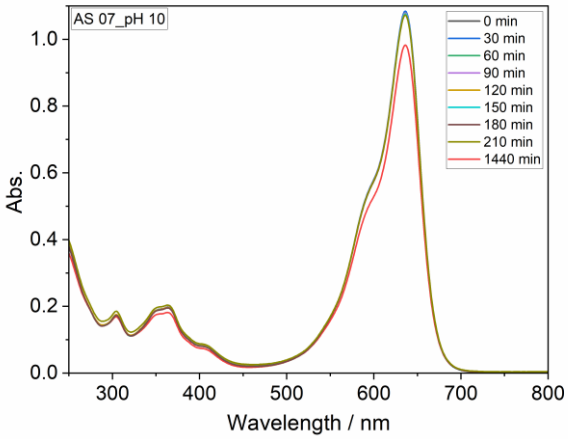
AS 07_pH 10
0 min
30 min
60 min
90 min
120 min
150 min
180 min
210 min
1440 min
Abs.
Wavelength / nm

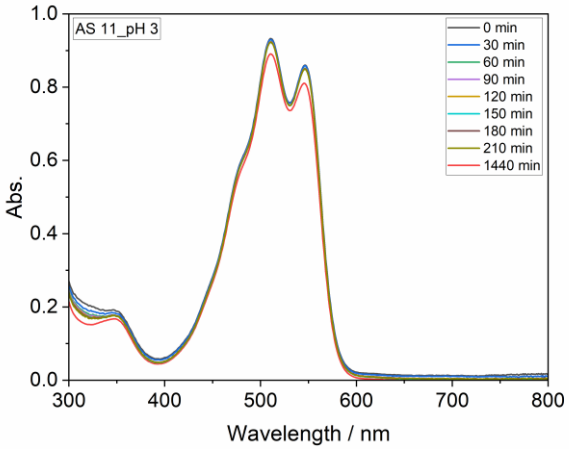
AS 11_pH 3
0 min
30 min
60 min
90 min
120 min
150 min
180 min
210 min
1440 min
Abs.
Wavelength / nm

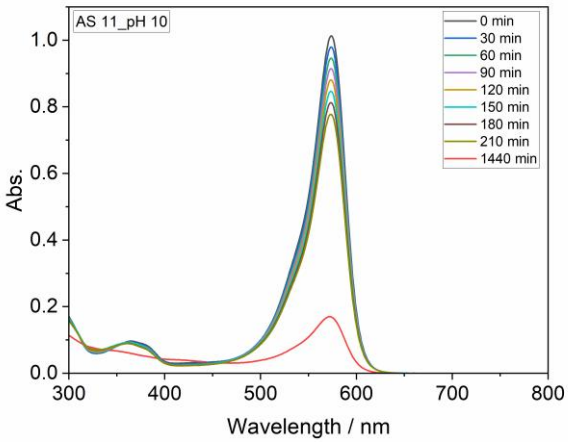
AS 11_pH 10
0 min
30 min
60 min
90 min
120 min
150 min
180 min
210 min
1440 min
Abs.
Wavelength / nm

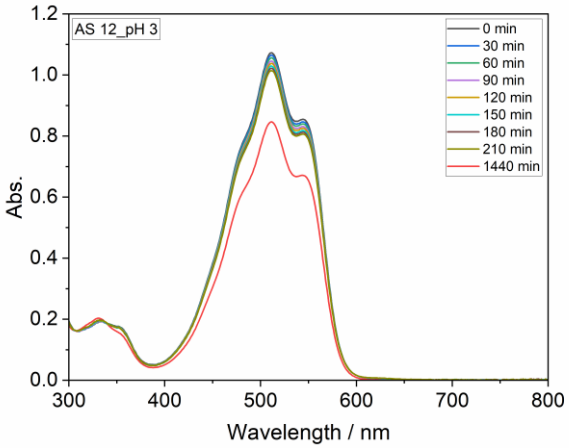
AS 12_pH 3
0 min
30 min
60 min
90 min
120 min
150 min
180 min
210 min
1440 min
Abs.
Wavelength / nm

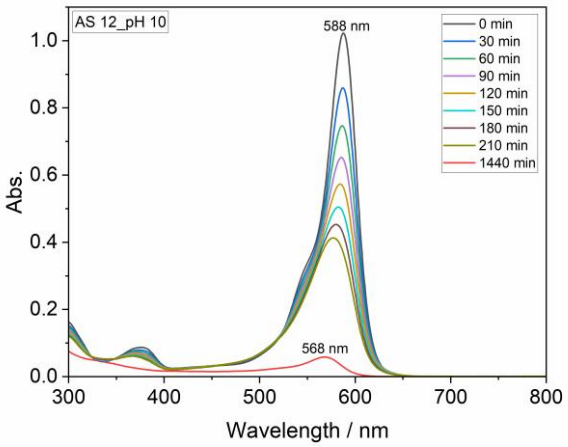
AS 12_pH 10
588 nm
568 nm
0 min
30 min
60 min
90 min
120 min
150 min
180 min
210 min
1440 min
Abs.
Wavelength / nm

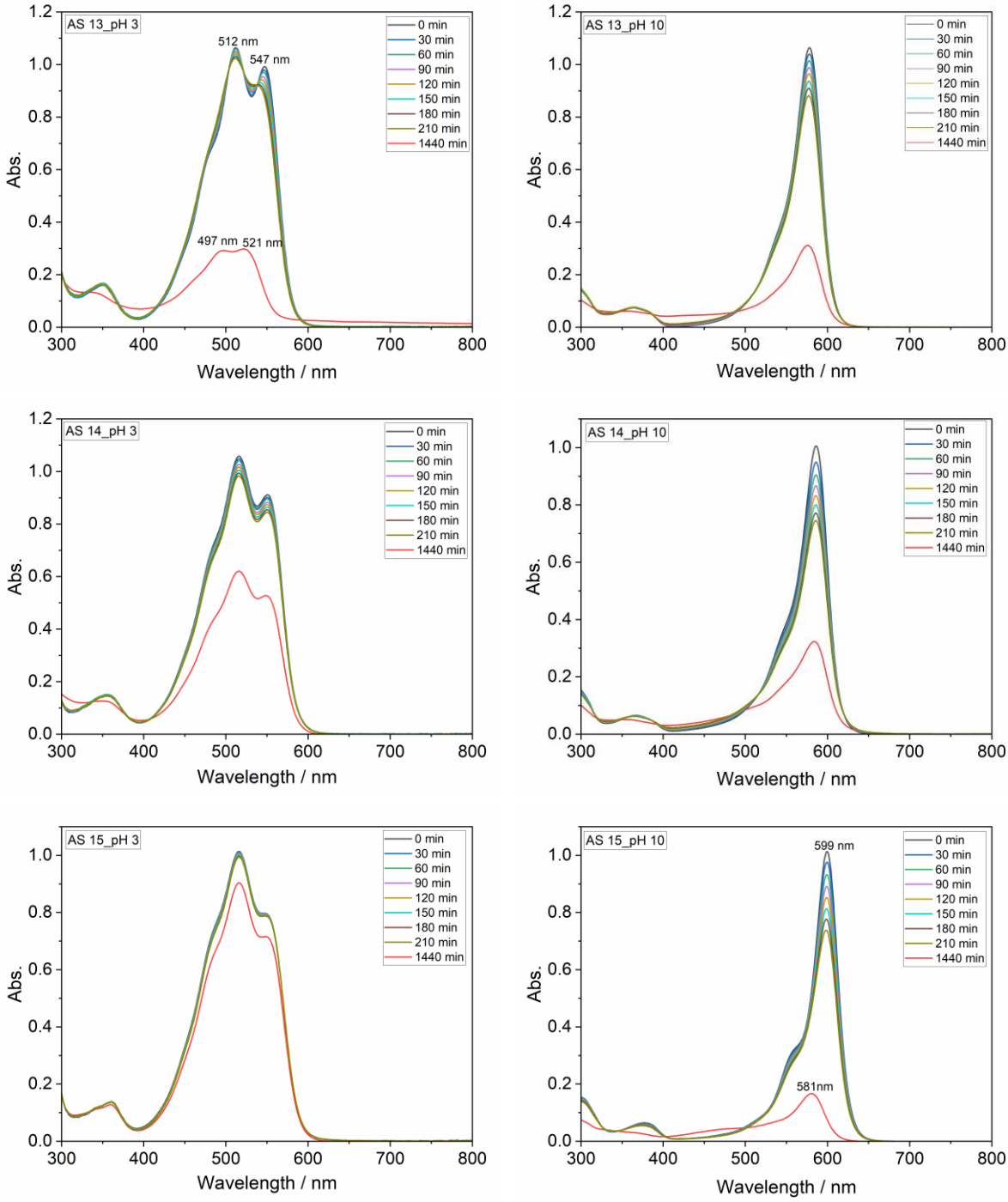

Figure S5. Absorption spectra of carborhodols recorded during the photostability experiment over 24 hours. Spectra were collected in pH 3 buffer (left) and pH 10 buffer (right).

Photostability Assessment in EtOH

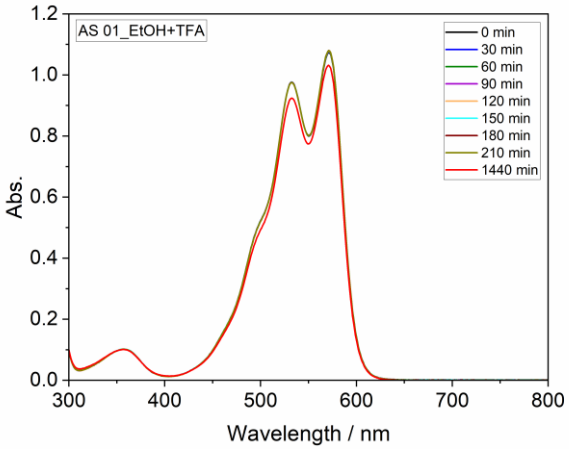

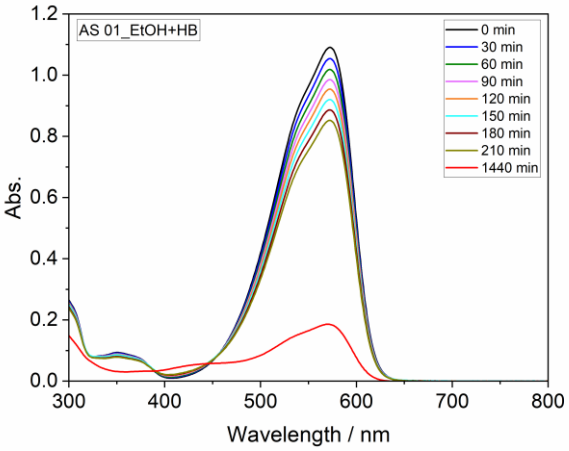

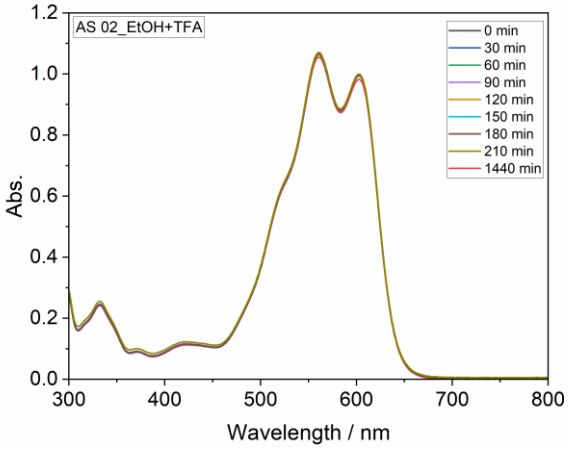

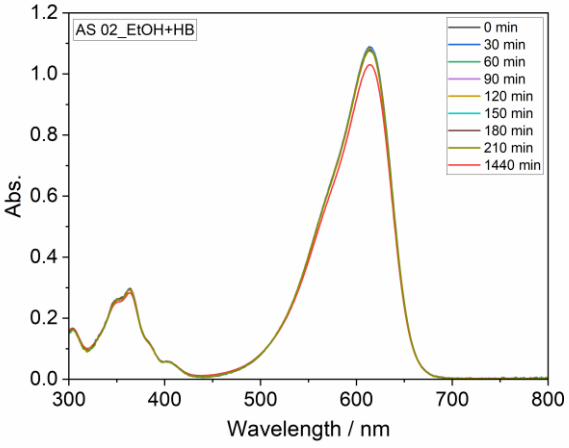

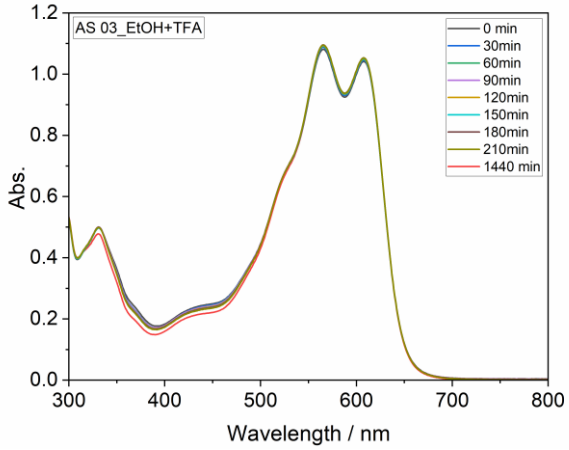

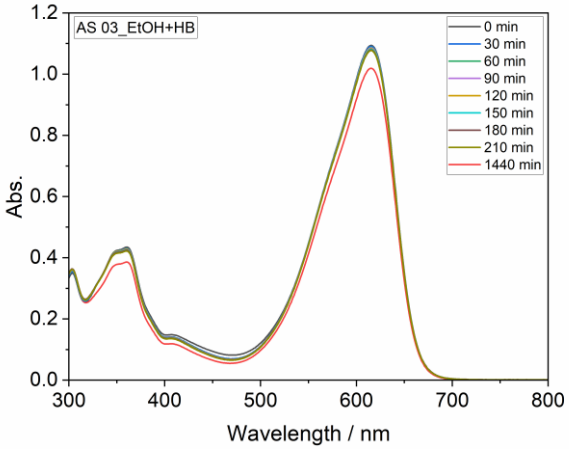

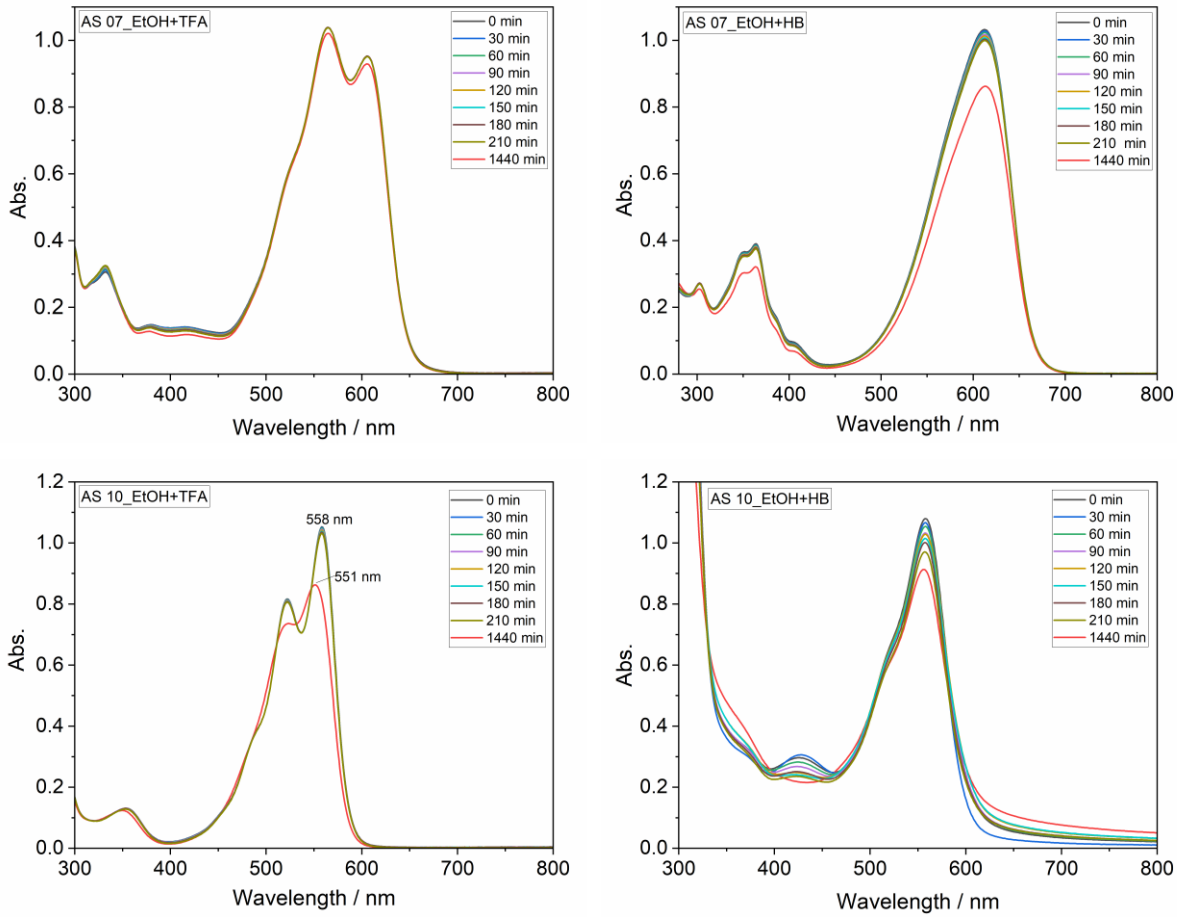

Figure S6. Absorption spectra of carborhodols recorded during the photostability experiment over 24 hours. Spectra were collected in acidic (left) and basic (right) EtOH.

Chapter 5: Solvatochromic Behavior of Carborhodol Dyes

Solvent-Dependent Absorption of the Basic Form of Carborhodols

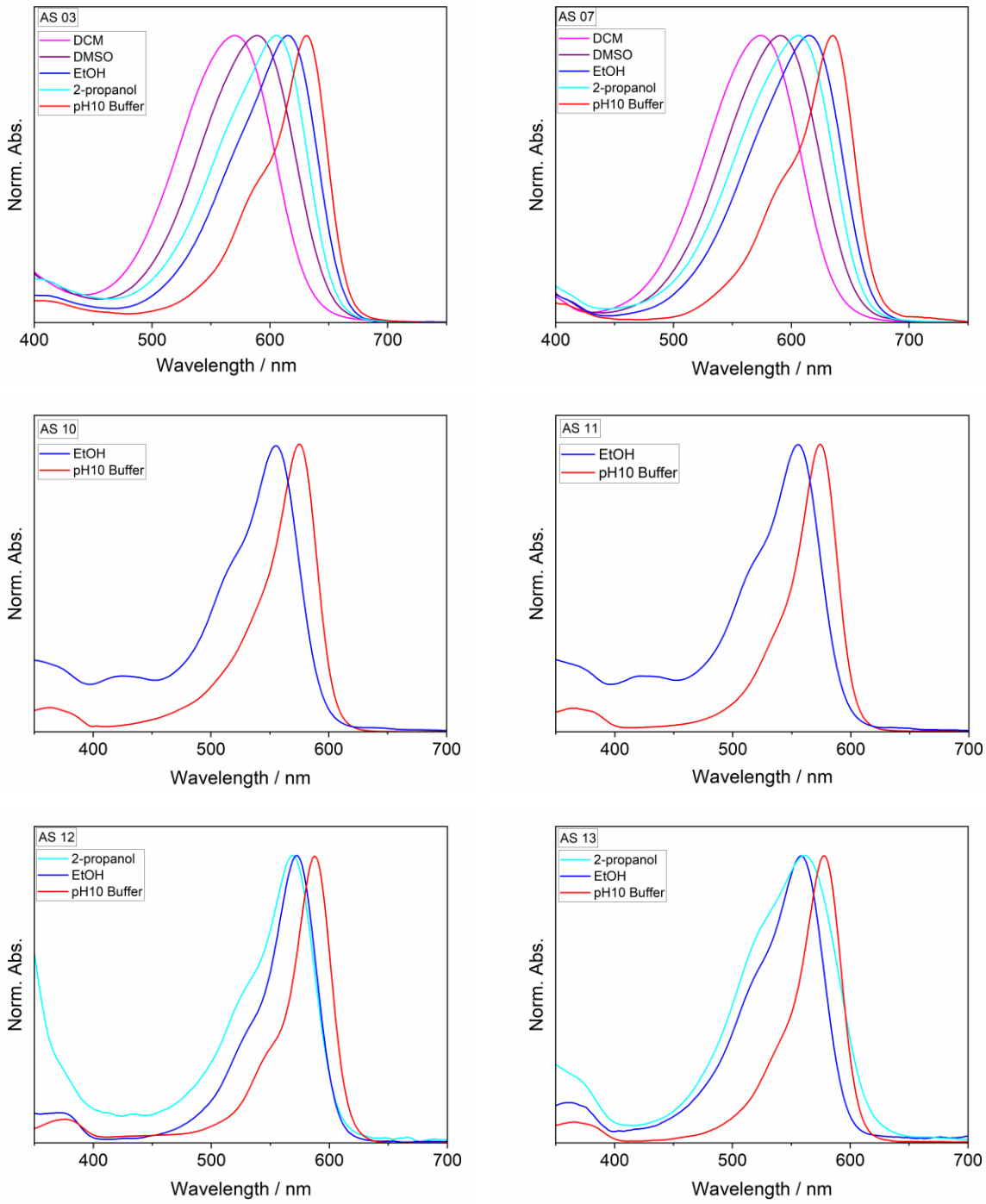

Figure S1. Normalized absorption spectra of the basic form of **AS 03**, **AS 07**, **AS 10**, **AS 11**, **AS 12,** and **AS 13** in various solvents.

Spirolactone Formation of the Basic Form of Carborhodols

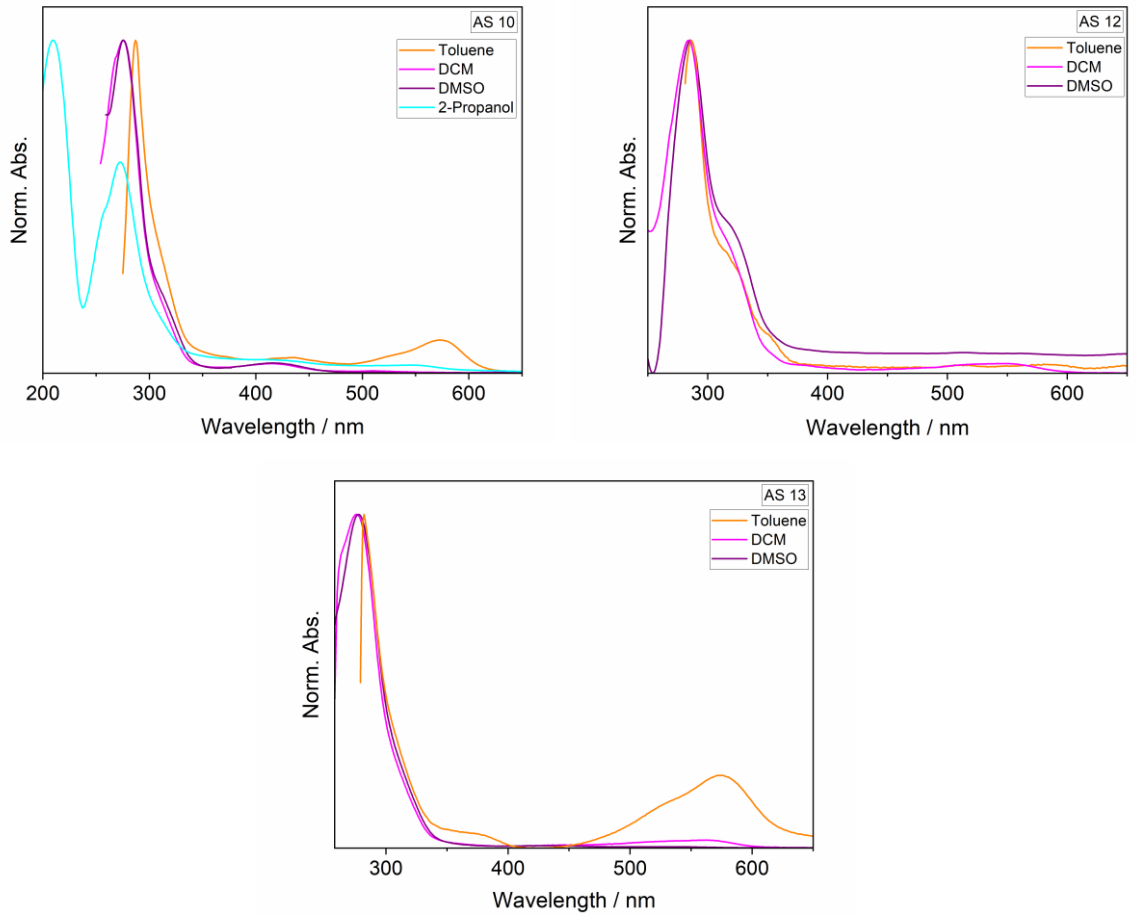

Figure S2. Normalized absorption spectra of the basic forms of **AS 10, AS 12,** and **AS 12** showing spirolactone formation.

Solvent-Dependent Emission of the Basic Form of Carborhodols

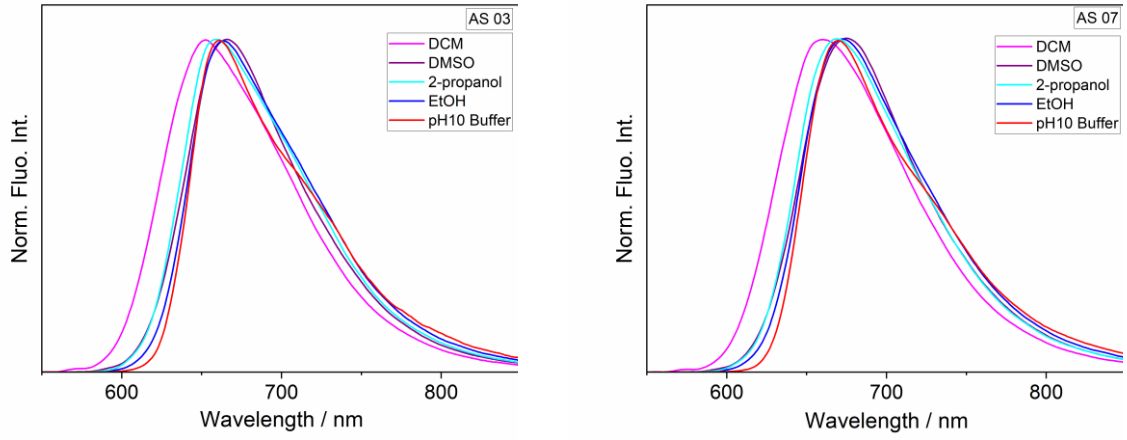

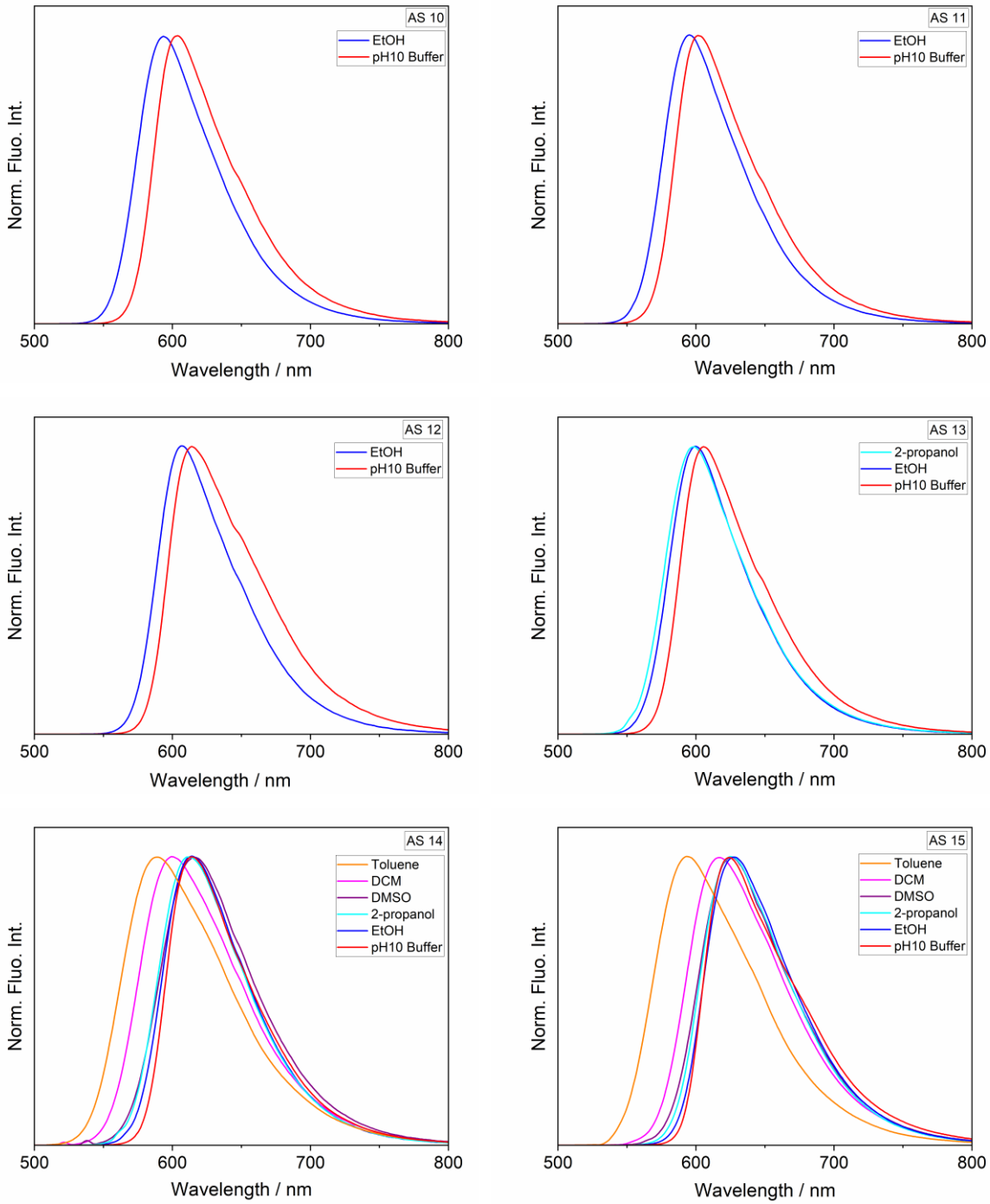

Figure S3. Normalized emission spectra of the basic form of **AS 03**, **AS 07**, **AS 10**, **AS 11**, **AS 12**, **AS 13**, **AS 14,** and **AS 15** in various solvents.

Solvent-Dependent Absorption of the Acidic Form of Carborhodols

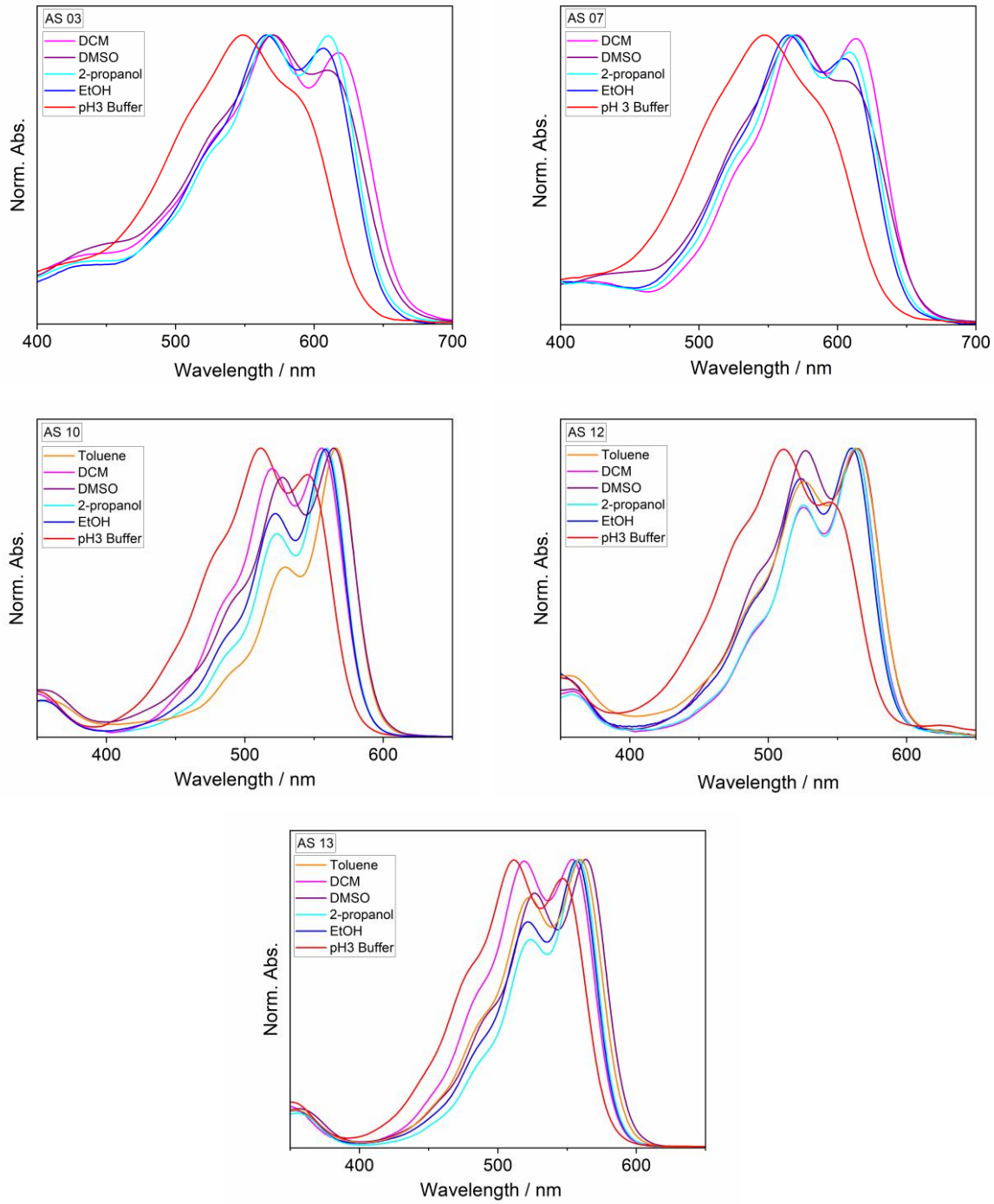

Figure S4. Normalized absorption spectra of the basic form of **AS 03**, **AS 07**, **AS 10**, **AS 12**, and **AS 13** in various solvents.

Chapter 6: Encapsulation of pH-Sensitive Dyes in poly (ethylene glycol)-*block*-poly (lactic acid) Vesicles for Sensing Applications

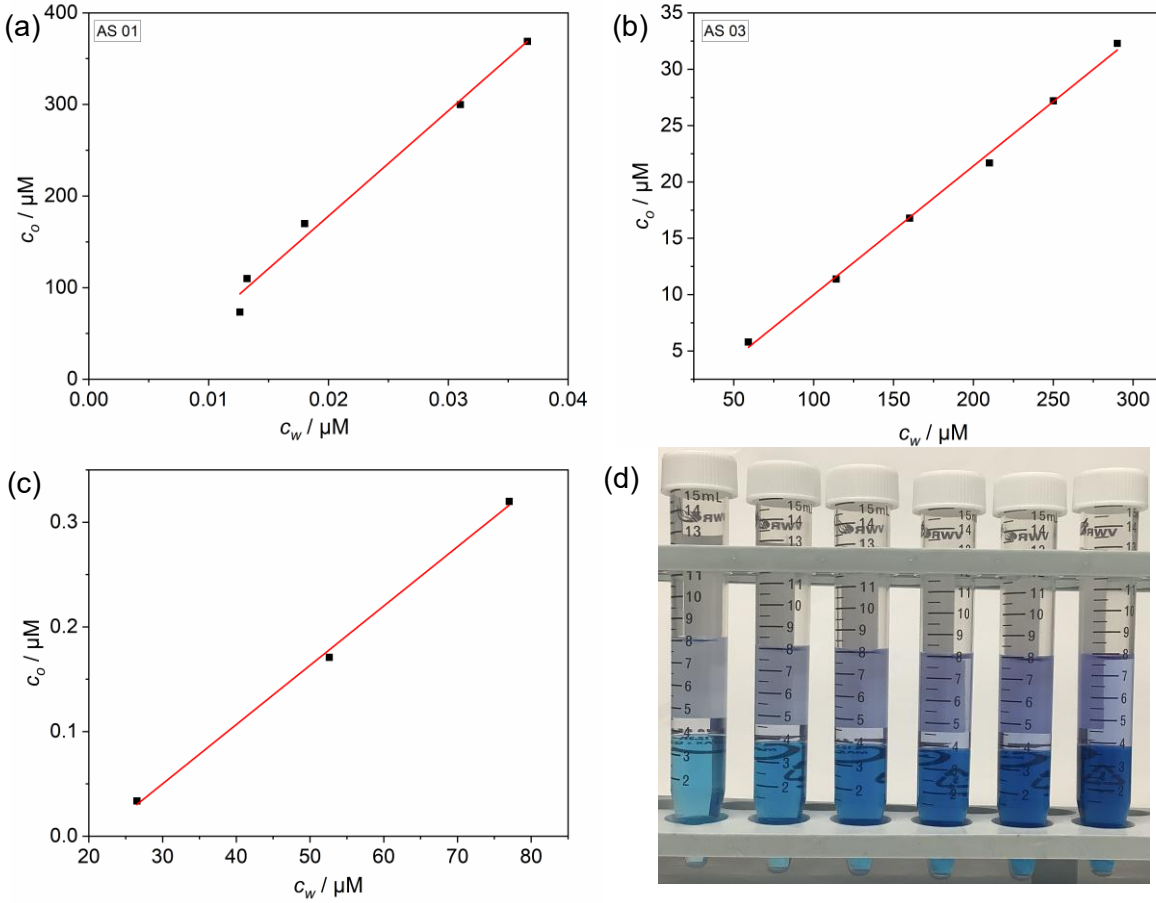

Figure S1. Plot of the dye concentration in octanol (c_o) versus that in water (c_w) for (a) **AS 01,** R^2 = 0.984, (b) **AS 03,** R^2 = 0.997, and (c) **AS 13,** R^2 = 0.996. (d) **AS 02** at different concentrations after centrifugation, illustrating phase separation between the octanol (top) and aqueous (bottom) layers.

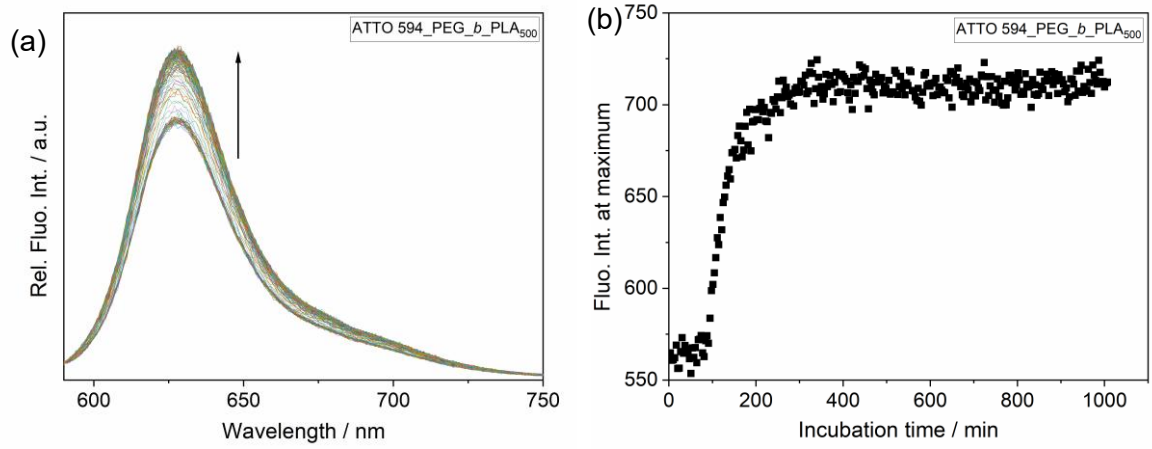

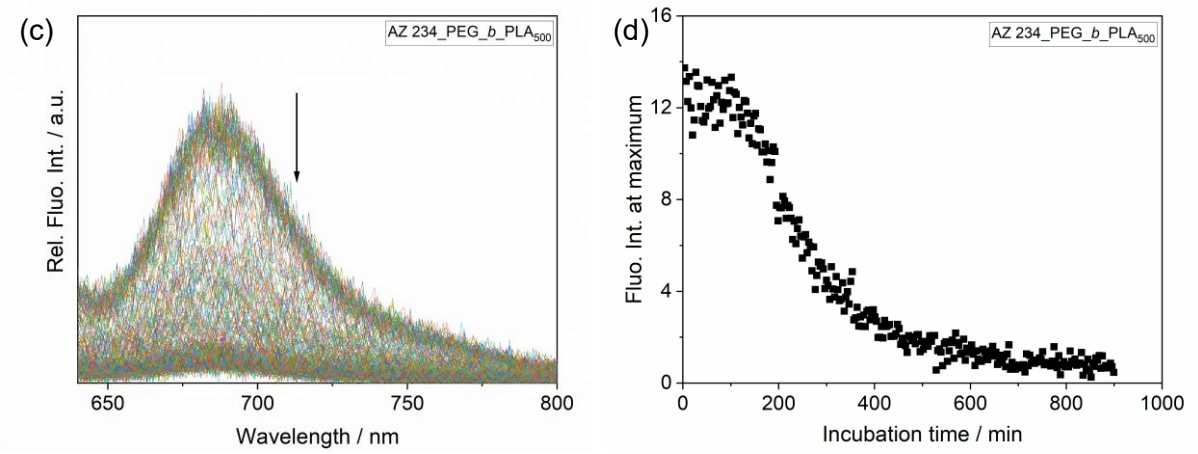

Figure S2. Fluorescence kinetics of **ATTO 594** and **AZ 234** dye release from PEG_{114}-*b*-PLA_{500} assemblies. (a) Fluorescence spectra of **ATTO 594**-loaded vesicles over time ($\lambda_{exc.}$= 585 nm), (b) Change in fluorescence intensity at the emission maximum as a function of incubation time for **ATTO 594**, (c) Fluorescence spectra of **AZ 234**-loaded vesicles over time ($\lambda_{exc.}$= 630 nm), (d) Change in fluorescence intensity at the emission maximum as a function of incubation time for **AZ 234**.

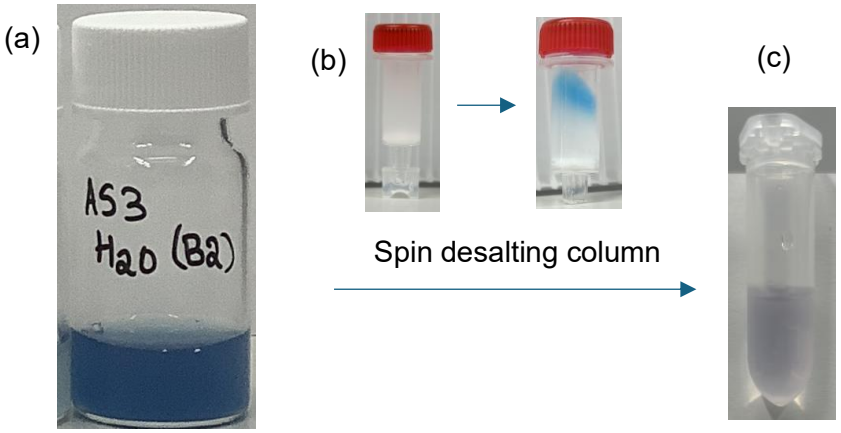

Figure S3. (a) Vesicle suspension of **AS 03** loaded PEG_{114}-*b*-PLA_{500} after 2 days of dialysis, (b) Purification using a Zeba spin desalting column, showing free dye retained within the column after centrifugation, (c) First fraction collected from the column containing purified vesicles.

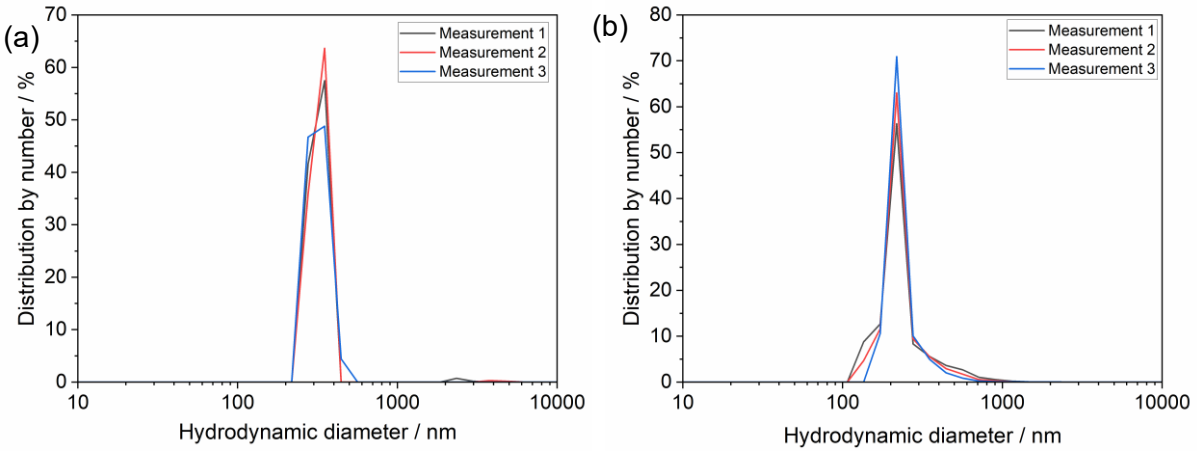

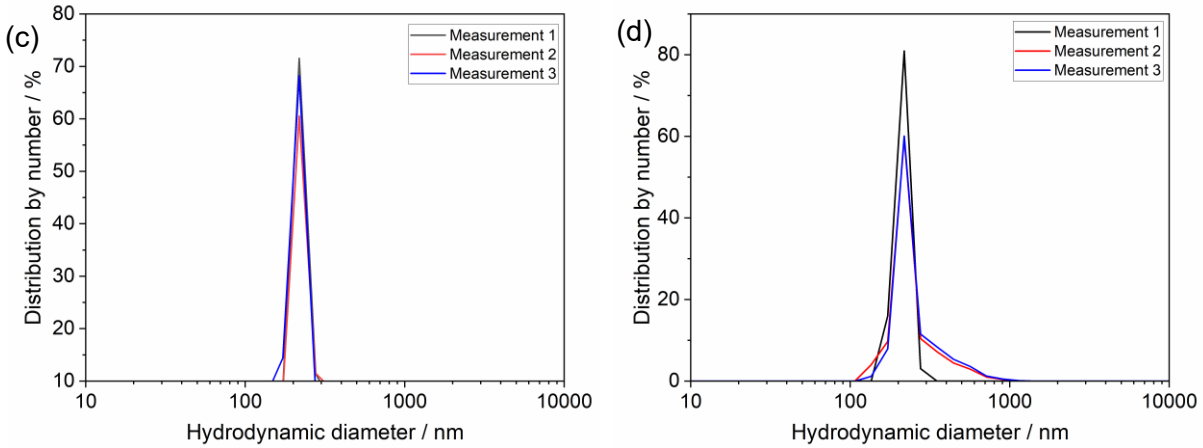

Figure S4. DLS particle size distribution by number of (a) **AS 02**, (b) **AS 03**, (c) **AS 07**, and (d) **AS 13** loaded PEG_{114}-*b*-PLA_{500} vesicles.

Chapter 7: pH-responsive Chitosan-Based Hydrogels for Detecting Wound Infections

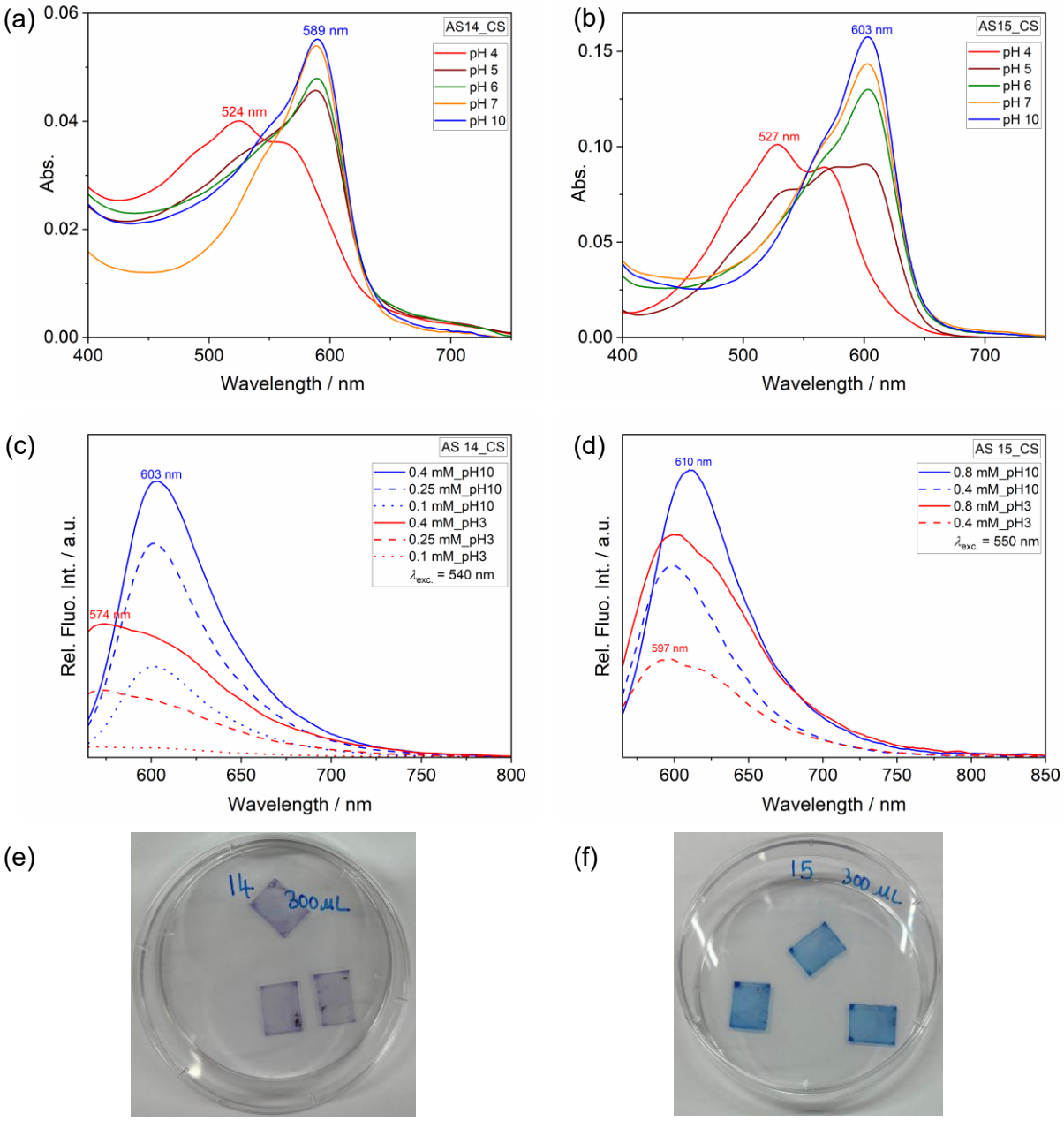

Figure S1. Absorption spectra of spin-coated films at different pH values for (a) **AS 14-CS** (14 mM) and (b) **AS 15-CS** (20 mM), corresponding photographic images of (e) **AS 14-CS** and (f) **AS 15-CS** films washed with PBS, pH 7.4. Fluorescence spectra at pH 3 and pH 10 for films with varying dye loadings for (c) **AS 14-CS** and (d) **AS 15-CS**. An increase in dye concentration led to higher fluorescence intensity; however, fluorescence quenching was observed at 14 mM and 20 mM loadings for both films.

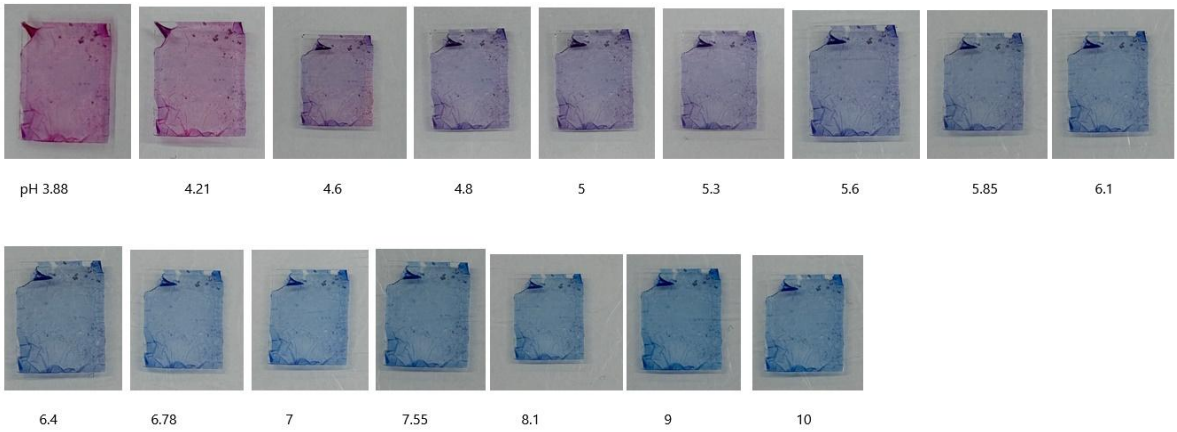

Figure S2. Photographic images of AS 15-CS spin-coated film (20 mM) at different pH.

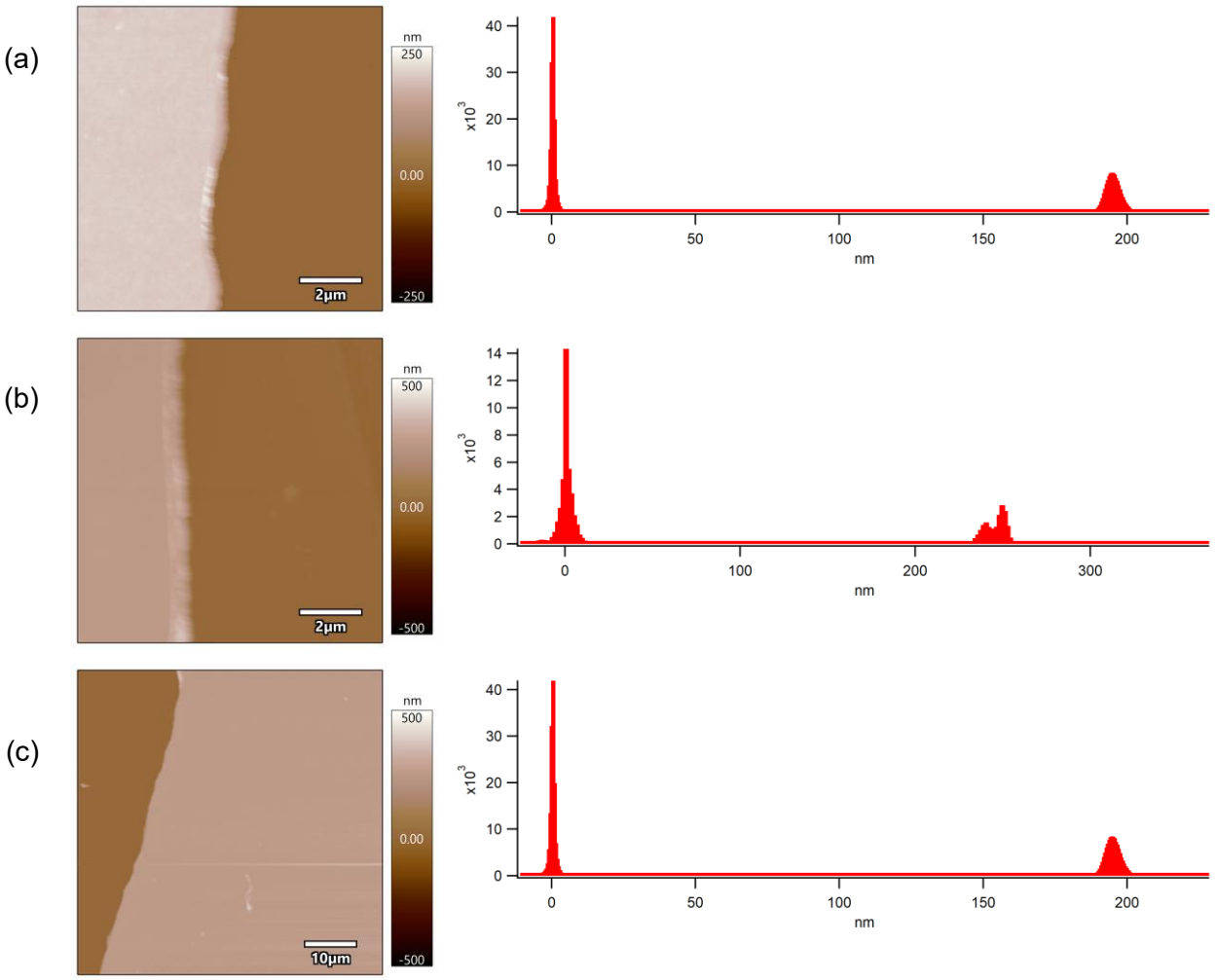

Figure S3. AFM micrographs of the surface (left) and corresponding height distribution profiles (right) for (a) non-modified CS, (b) **AS 14-CS**, and (c) **AS 15-CS**.

Table S1: Assignments of key bands observed in the ATR-FTIR spectra of non-modified hydrogel, **AS 14-CS**, and **AS 15-CS**.

Assignment	Band position (cm^{-1}) Reference Chitosan	Band position (cm^{-1}) CS	Band position (cm^{-1}) AS 14-CS	Band position (cm^{-1}) AS 15-CS
N-H (amide II)	1550–1565	1563	1574	1578 &1546
NH_2	1590–1610	1588	------	------
C=O (amide I)	1620–1665	1651	1650 &1630	1650

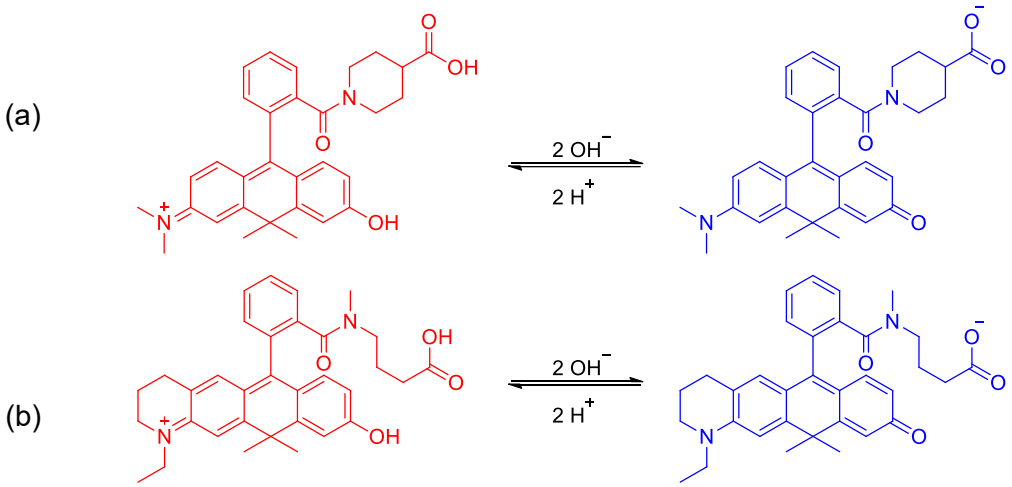

Figure S4. Protonation-deprotonation equilibria of (a) **AS 14** and (b) **AS 15**. Structures shown in red correspond to the protonated forms, while structures in blue represent the deprotonated forms.

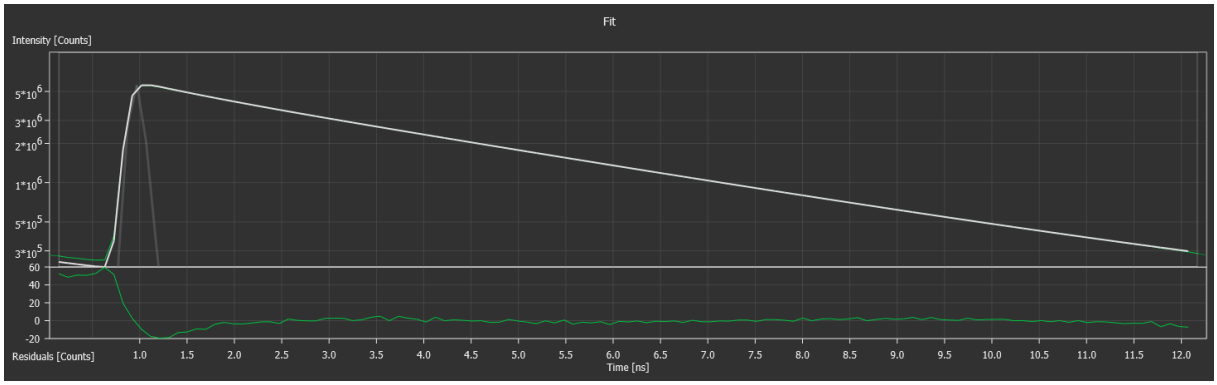

Figure S5. Fluorescence decay of **AS 15-CS** basic film fitted with a bi-exponential model. Residuals indicate good fit quality.

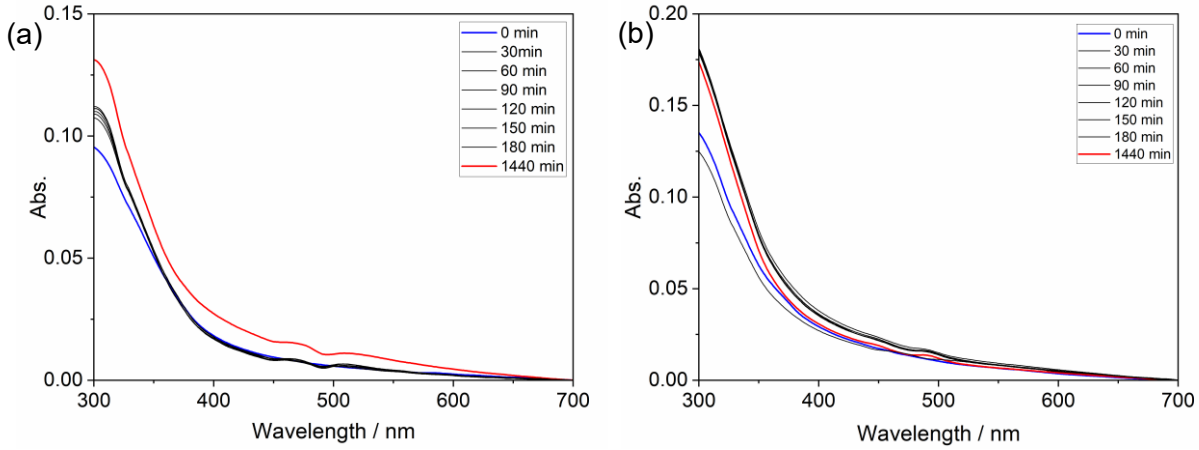

Figure S6. Absorption spectra of unmodified CS film washed with (a) pH 4 buffer and (b) pH 10 buffer.

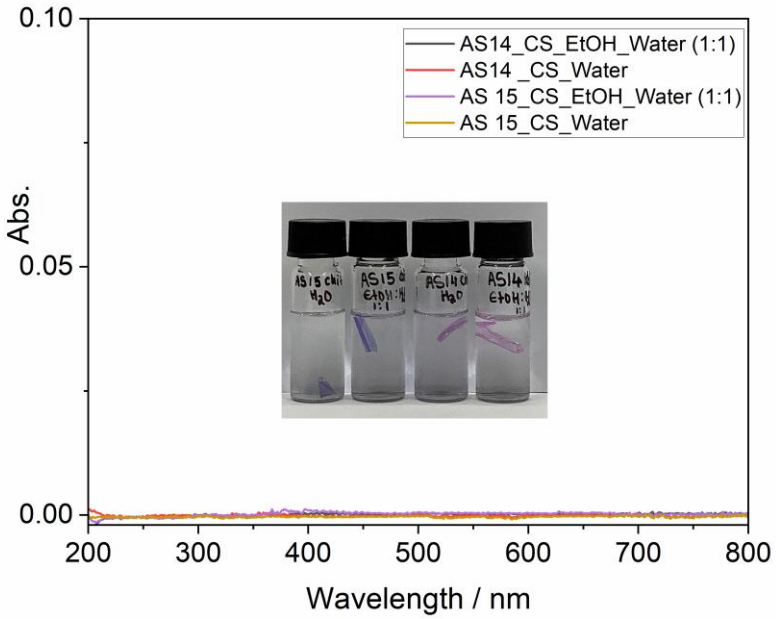

Figure S7. Absorption spectra of solutions obtained after immersing films for 24 h (measured in a 1 mm cuvette), showing the absence of dye release from **AS 14-CS** and **AS 15-CS** films. The inset shows photographs of the films immersed in the corresponding solutions.

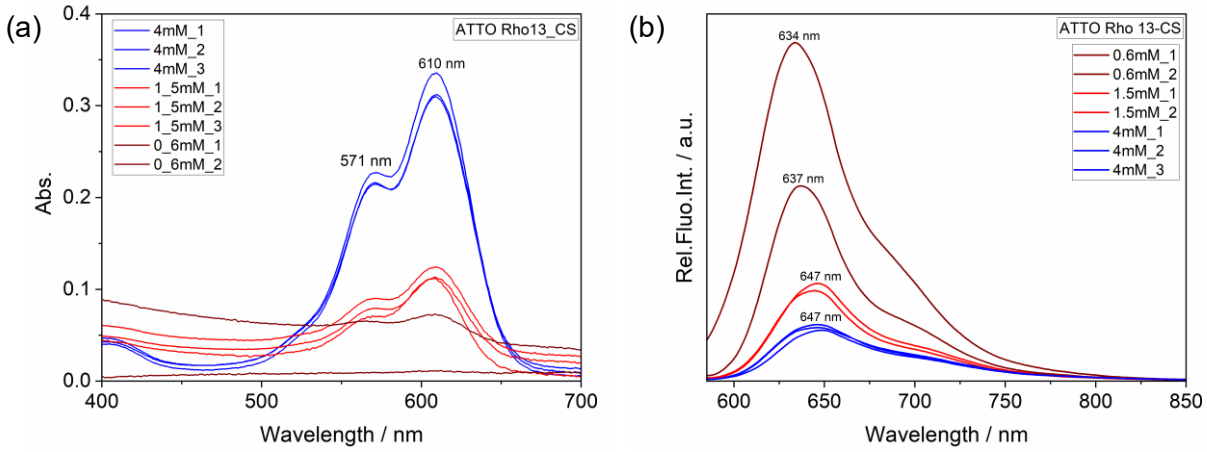

Figure S8. (a) Absorption and (b) emission spectra of **ATTO Rho13-CS** films prepared by spin coating at different dye concentrations.

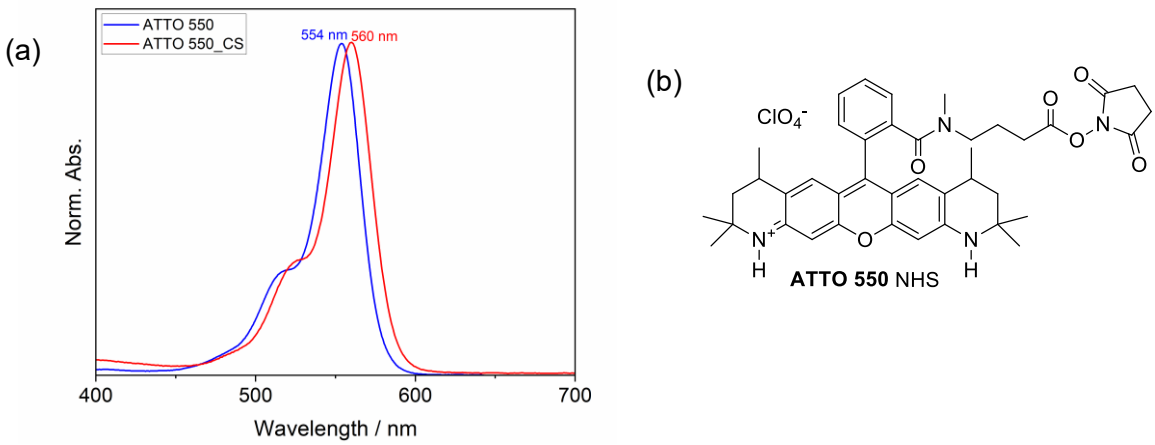

Figure S9. (a) Normalized absorption spectra of **ATTO 550** in PBS and **ATTO 594-CS** films, and (b) the chemical structure of ATTO 550 NHS ester.

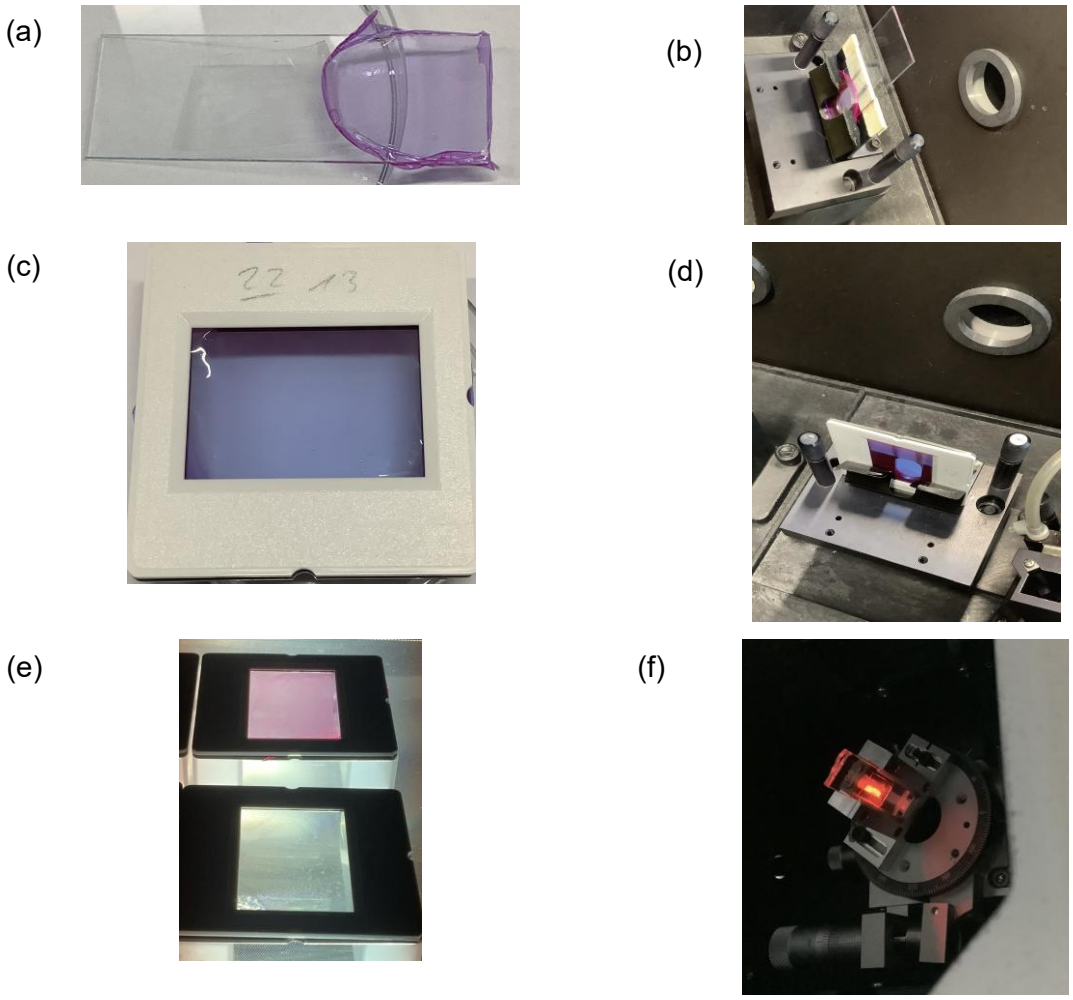

Figure S10. Photographic images of the experimental setup. (a) Modified CS film attached to a microscopic slide. (b) Placement of the slide in the UV-Vis sample holder. (c) Modified CS film is mounted on a 35 mm slide mount. (d) Placement of the mounted film in the UV-Vis sample holder. (e) CS films on a slide mount positioned horizontally on an overhead projector for photostability measurements. (f) Spin-coated coverslip was attached to a 1 mm cuvette and placed in the fluorescence spectrometer sample holder.

Acknowledgements

I would like to express my sincere gratitude to all those who have supported and contributed to this thesis.

First, I am deeply grateful to my supervisor, Dr. Jutta Arden Jacob, for her kindness, encouragement, and support throughout this journey. I sincerely thank Dr. Alexander Zilles for guiding me, introducing me to key concepts of fluorescent dyes, and helping me understand them; providing direction whenever I felt lost; and offering constructive criticism that shaped my work. I am also thankful to my university supervisor, Prof. Dr. Holger Schönherr, for bridging industry and academia, for his valuable suggestions regarding my PhD, and for his generosity. Without the support of these three individuals, this work would not have been possible.

I would like to extend my thanks to everyone at ATTO-TEC GmbH for welcoming me as their first international colleague and for their constant support. I appreciate the kindness and patience shown when I struggled with the German language. I am especially grateful to Dr. Norbert Kemnitzer for his curiosity about my culture and for always asking after my well-being, and to Dr. Phil Marvin Pithan for teaching me 2D NMR analysis and providing valuable advice on scientific communication.

My sincere thanks go to Nicola Cusick for teaching me about polymers, for her friendship, and for our collaborative work in polymer chemistry, including DLS and FESEM measurements. I am also thankful for the comfortable environment she created for me in the university laboratories. I extend my gratitude to all PC I members for their helpfulness during my time at the university.

I would like to thank Dr. Thomas Paululat for NMR measurements, Xin Jiang for access to the FESEM, Prof. Dr. Ulrich Jonas for access to the FTIR, Winny Chelangat and Aysha Awan for FESEM measurements, Dr. Jan Erik Hoffmann for Confocal fluorescence microscopy measurements, and Joshua Schumacher for AFM measurements.

I am grateful to the supervisors and fellow ESRs of the STIMULUS consortium. The summer schools and workshops were both intellectually stimulating and personally enjoyable, and I always looked forward to our next gathering. I would especially like to thank Bhavana Sathish for her constant companionship during these events, and Muhammad Atif for being my travel partner.

I also gratefully acknowledge funding from the European Union's Horizon 2020 research and innovation program under the Marie Skłodowska-Curie grant agreement No. 955664, which supported my research for three years, and from ATTO-TEC GmbH for covering the remaining.

Next, I wish to thank those who made this distant place feel like home and who encouraged me to preserve the lively spirit. Vaisakh Krishnan, thank you for your love and support over the years, and for listening to my research stories, even if you don't understand most of them. Thank you also for leaving everything behind and moving to Europe for us. I am grateful to Vivek Vijayan, Arshal Joseph, Sruthi Venu, Akshara Mariya Josy, and Josepaul Paulachan for bringing joy into my life in Siegen, and to Sreedharshini Jayantth, Jayantth Ganesh, and Ramprasad Chandramohan for warmly welcoming me into your circle of friends. Our weekend meetups, dance practices, and cooking sessions always gave me the energy to start a new week.

To my dear IISER friends, who have been part of my life for five wonderful years and are now spread across the US, Europe, and India: thank you for the relaxing trips that gave me a break from the stress of research and for keeping our bond alive through countless video calls despite the distance. I am especially grateful to my girls' group, the "Samarpanites," for our close friendship.

I would also like to thank my brother, Aswin Syam, for pursuing his master's degree in Germany, which gave us the chance to meet more often and helped me feel connected to home. Finally, I owe my deepest gratitude to my parents for their unconditional support, for never restricting my decisions, and for giving me the freedom I needed throughout my education. I know how lonely it must feel to have both children far away, and one of my greatest motivations to complete this PhD was the thought of seeing your proud and happy faces. Thank you for your constant love and encouragement, and for calling me every day, even if only to ask the same question.